Unione Europea
Fondo Sociale Europeo

Ministero dell'Università
e della Ricerca

Università degli Studi
di Palermo

Dipartimento di Scienze Fisiche e Astronomiche
Dottorato di Ricerca in Fisica – XVIII ciclo

THE INTERACTION BETWEEN THE SUPERNOVA REMNANT SHOCK FRONTS AND THE INTERSTELLAR MEDIUM: MODELS AND OBSERVATIONS

Marco Miceli

Palermo, Dicembre 2006

Supervisore: Prof. Fabio Reale

Coordinatore: Prof. Natale Robba

Abstract

This thesis is devoted to the study of supernova remnants (SNR) and of their complex interaction with the interstellar medium and the circumstellar material. I analyze X-ray observations of two supernova remnants, the young $W49B$ and the middle-aged $Vela$, and I model in detail the shock-cloud hydrodynamic interaction in specific regions of the Vela SNR.

The study of supernova remnants allows us to probe the physical and chemical properties of the interstellar medium (ISM). Moreover, SNRs drive the mass and energy exchange in the ISM, thus playing a fundamental role for its evolution. In young, ejecta-dominated SNRs (like W49B) the X-ray emission is associated with the ejected material expelled at supersonic speed during the SN explosion. The ejecta are heated up to X-ray emitting temperatures by the reverse shock, or by the reflected shock, produced by the interaction of the remnant with a large ambient ISM cloud. In middle-aged SNRs (like Vela), instead, where the mass of the swept-up medium is larger than the ejected mass, the X-ray emission is associated with the interaction of the shock front with the inhomogeneities (clouds) of the interstellar medium.

In the framework of ejecta-dominated remnants, I report on an *XMM-Newton* EPIC observation of the Galactic supernova remnant W49B. The analysis of the X-ray data allows us to obtain new important constraints on the physical scenario and on the dynamics of the supernova explosion (e. g. nucleosynthesis processes, energy of the explosion, etc), and on the interaction of the supernova ejecta with an ambient molecular cloud. The X-ray morphology of the remnant exhibits a bright elongated nebula, and, on its eastern end, a sharp perpendicular structure aligned with the radio shell. I produce line images and equivalent width maps, and I perform a spatially resolved spectral analysis on selected homogeneous regions. The X-ray spectra of W49B are characterized by strong K emission lines from Si, S, Ar, Ca, and Fe. Spectra are described well by two thermal components in collisional ionization equilibrium and are dominated by the emission from the ejecta. A high overabundance of Ni is found in the bright central region and the previous detection of Cr and Mn line emission is confirmed. I also observe spatial anisotropy in temperature and abunances, with the highest values found in the east and the lowest in the west. The most natural interpretation is that

the remnant is the result of an asymmetric bipolar explosion with the eastern jet being hotter and more Fe-rich than the western jet. The eastern jet is confined by interaction with ambient molecular clouds. Both the comparison of the observed abundances with yields for hypernova and supernova nucleosynthesis model and the estimates of the energy of the ejecta do not directly support the association of W49B with a γ-ray burst, although it remains possible. W49B seems then to be the result of an aspherical jet-like supernova explosion of normal energy (10^{51} erg).

In the framework of middle-aged SNRs, I focus on the Vela SNR. Vela is the nearest supernova remnant, so it is possible to study at high spatial resolution the interaction of the main shock front with the inhomogeneities of the ambient medium. I first analyze an *XMM-Newton* EPIC observation of a bright knot, named FilD, in the northern rim of the Vela SNR, where both X-ray and optical emission are visible. The X-ray emitting plasma is described well by an optically-thin plasma in collisional ionization equilibrium with two thermal components at $\sim 10^6$ K and $\sim 3 \times 10^6$ K, respectively. The analysis of the X-ray emission of FilD seems to indicate that both components may be associated with ISM inhomogeneities heated by a transmitted shock front, although thermal conduction between the cloud and the hotter intercloud medium can also provide an efficient "channel" of heating for the FilD cloud.

For a higher level of diagnostics, I perform a detailed hydrodynamic "forward" modeling of the interaction of the Vela SNR shock with an ISM cloud. I solve numerically the hydrodynamic conservation equations and I synthesize the X-ray emission that can be directly compared with the data. The impact of a shock front at 6×10^6 K on an elliptical cloud 30 times denser than the ambient medium describes well the shock-cloud interaction processes in the Vela FilD region in terms of spectral properties and morphology of the X-ray and optical emission. The bulk of the X-ray emission in the FilD knot (i. e. the X-ray component at $\sim 10^6$ K) originates in the cloud material heated by the transmitted shock front and the hot component at $\sim 3 \times 10^6$ K is also associated with the cloud material, which "evaporates" (i. e. approaches the density and temperature of the intercloud medium), as an effect of thermal conduction, in the intercloud medium. The FilD optical emission is associated with thermal instabilities, while the X-ray emission associated with the reflected shock front is negligible.

Finally, I perform a combined analysis of three *XMM-Newton* observations (including the FilD observation) of the northern region of the Vela shell (pointing the regions named RegNE and FilE), which allows us to study a large area of the remnant ($\gtrsim 11$ pc^2, at 250 pc). The data analysis reveals a double regime in the shocked interstellar medium. There are indications of hot, rarefied plasma, heated at relatively high temperatures (some million degrees) and of large, dense, shocked clouds, heated at lower temperatures, close to small, unresolved, dense cloudlets that determine the presence of a soft diffuse and faint emission. According to the results of the spectral analysis, it is possible that RegNE is a shrapnel of ejecta. However, preliminary hydrodynamic modeling shows that the spectral properties of RegNE can be the result of the interaction of a shock front at at 6×10^6 K (i. e. the same temperature as that used for FilD) with a cloud only 10 times denser than the intercloud medium. Even the lack of optical emission associated with the X-ray knot is explained by such a model.

Contents

Chapter 1

Introduction

Supernova remnants (SNRs) are powerful sources of mass and energy for the interstellar medium (ISM) and their emission and evolution are deeply influenced by the complex interaction between the blast wave shock generated during the SN explosion and the ISM inhomogeneities. A very large amount of kinetic energy ($\sim 10^{51}$ erg) and mass (several solar masses) are released in a supernova explosion and this event strongly modifies the physical and chemical properties of the ambient environment. As the shock expands in the surrounding medium, the ISM is heated, compressed, and ionized. Moreover, the interaction with a SNR shock enriches the interstellar gas of heavy elements (e. g. Mg, Si, Ca, and Fe), released during the evaporation of the interstellar dust grains fragmented by collisions with post-shock high temperature protons. The chemical composition of the ISM is also significantly altered by the fragments of the progenitor star (ejecta) expelled at supersonic speed in the supernova explosion. The ejecta, in fact, spread the heavy elements synthesized during the life of the progenitor star and during its death (through the explosive nucleosynthesis processes) in the interstellar galactic medium. Therefore SNRs set up the ISM conditions for the future generations of stellar populations. All these effects are very relevant, since about 1/10 of the total volume of the galactic ISM has been shocked by a SNR, according to the estimates of Cox & Smith (1974).

On the other hand, the interstellar gas is a multi-phase medium, where many components, with very different values of temperatures and densities, are present, as shown in Fig. 1.1. The intrinsic inhomogeneity of the interstellar medium influences the evolution of the supernova remnants because the speed and the direction of the expanding shock wave depend on the density field of the pre-shock medium (see Sect. 1.2 and Sect. 1.4). While propagating in a "cloudy" environment, the shock drives different thermal conditions in the shocked plasma, thus producing the patchy and irregular characteristic morphology of SNRs. The study of SNRs is therefore a powerful diagnostic tool to obtain information about the relevant properties of the interstellar medium (e. g. morphology, spatial distribution, and dimension of the inhomogeneities, density, chemical abundances, etc.)

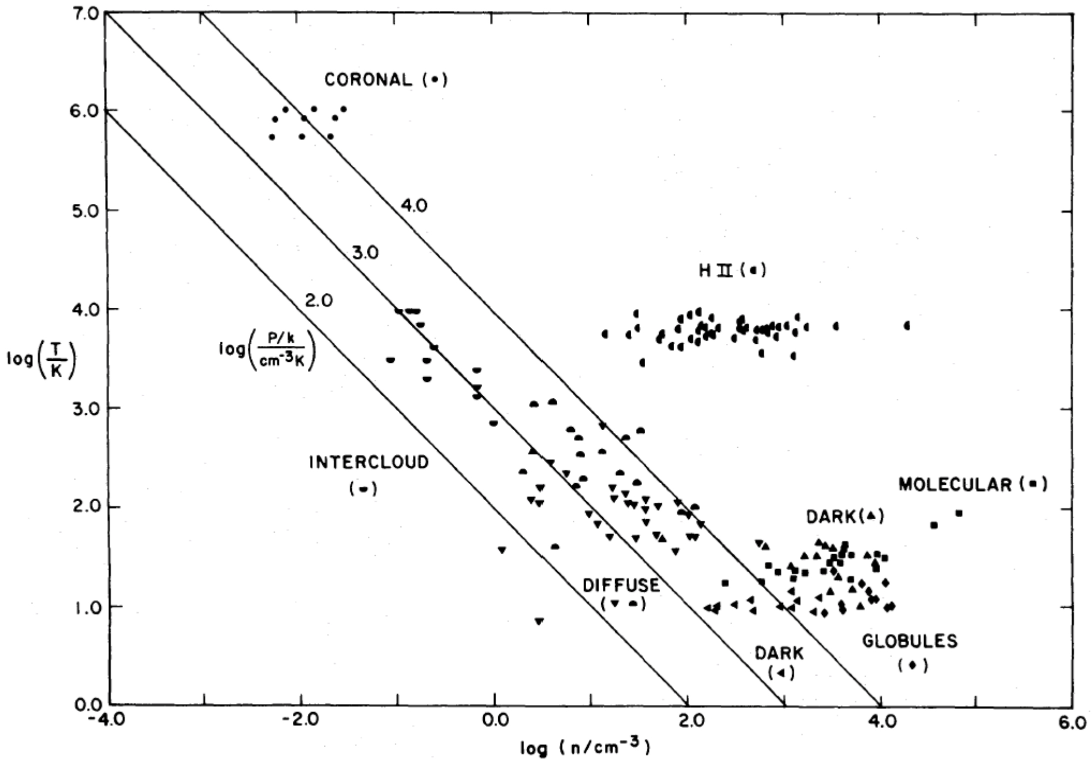

Figure 1.1: Interstellar gas temperature and density (with isobaric lines superimposed), based on seven galactic surveys (from Myers 1978).

Moreover, the interaction of the SNR shock with local inhomogeneities (*clouds*) allows us to study the physics of the shocks and the many different physical processes involved in the interaction, like thermal conduction and radiative cooling, or the formation of transmitted and reflected shocks and of hydrodynamic (HD) and thermal instabilities. The expansion of the remnants in a cloudy environment may also yield to a higher SN heating efficiency, HE, (i. e. the percentage of the SN initial energy not radiated and transferred to the ISM) with respect to the value $HE \sim 0.1$ estimated by Thornton et al. (1998) for an expansion in a cloudless medium.

The study of SNRs is therefore related with many different astrophysical topics, like star formation and evolution, nucleosynthesis, ISM evolution, and also with several physical issues related to the shocks and to the physics of the post-shock medium, whose multi-wavelength electromagnetic emission extends from the radio band up to the gamma rays with both thermal and non-thermal components. A complete study of SNRs then requires a multi-wavelength approach to the analysis of the observations and a proper modeling of the shock-cloud interaction, that is necessary to understand the details of the heating processes and the physical origin of the observed emission.

In this thesis I report on the study of the interaction of the SNR shock fronts with the inhomogeneities of the ISM both through the analysis of observations and through hydrodynamic modeling.

This Chapter is organized as follows: in Sect. 1.1 I briefly describe the mechanisms of the SN explosions and their effects on the chemical evolution of the ISM, in Sect. 1.2 I review the basic properties of the shocks, and in Sect.1.3 I describe the evolution of the SNRs. Section 1.4 is dedicated to the interaction of the SNR shocks with the ISM inhomogeneities and to a brief review of the results obtained by the numerical and analytical models of the interaction (Sect. 1.4.1), to the important time-scales (1.4.2), and to the results of the analysis of X-ray and optical observations (Sect. 1.4.3). Section 1.5 is dedicated to the classification of the SNRs, and, finally, the contents of the thesis and its aims are presented in Sect. 1.6.

1.1 SN explosions and nucleosynthesis

One interesting challenge in astronomy is to understand how the chemical elements have been synthesized in the evolution of the universe. Just after the big bang the universe was predominantly composed only of H and He (plus a very small amount of Li, Be, and B). Heavier elements, up to Fe, are synthesized during the evolution of the stars, while higher-Z elements are produced in the SN explosions.

SNe are classified on the basis of their optical spectra, as reported, for example, in Filippenko (1997). A very wide variety of photometric and spectroscopic properties has been observed and the classification is not always straightforward. However, despite the large amount of SN classes, the origin of all the supernova explosions is related to only two physical systems: exploding white dwarfs in binary systems, that generate Type Ia supernovae, and isolated massive stars with Zero Age Main Sequence (ZAMS) mass 8 $M_\odot < M_{ZAMS} \lesssim 130$ $M_\odot$, that are instead linked to all other types (see, for example, Hashimoto et al. 1993). At the end of their life, the stars in this mass range produce a collapsing Fe core which reaches nuclear density, thus releasing its gravitational energy ($\sim 10^{53}$ erg). About the 99% of this energy is deposited in the neutrinos. A central compact object (neutron star, NS, or black hole, BH) will result, while the envelope is ejected in the surrounding medium.

The detailed calculation of the chemical abundances in the ejecta is a very complicated task. A proper treatment should include a complete HD modeling of the Fe core collapse, of the leakage of the neutrinos produced in the nuclear reactions, of the neutrino-heating process, etc., and it has not yet been provided. Very important results, however, have been obtained by performing complete hydrodynamic and explosive nucleosynthesis calculations with an artificially induced shock wave, obtained by depositing a given amount of energy deduced by the observations in the progenitor star (see, for example, Thielemann et al. 1996 and references therein). The model yields clearly depend (among many other different parameters) on the ZAMS mass of the progenitor star and on the amount of the deposited energy. Figure 1.2 shows the distribution of the isotopic composition of the ejecta as a function of the total enclosed mass (i. e. the mass of the ejecta plus that of the compact object, behind the ejecta), obtained by Nakamura et al. (1999) for a star with $M_{ZAMS} = 20\ \mathrm{M}_{\odot}$ and for an explosion energy[1] 10^{51} erg. Notice the large amount of Ni present in the inner layers of the ejecta.

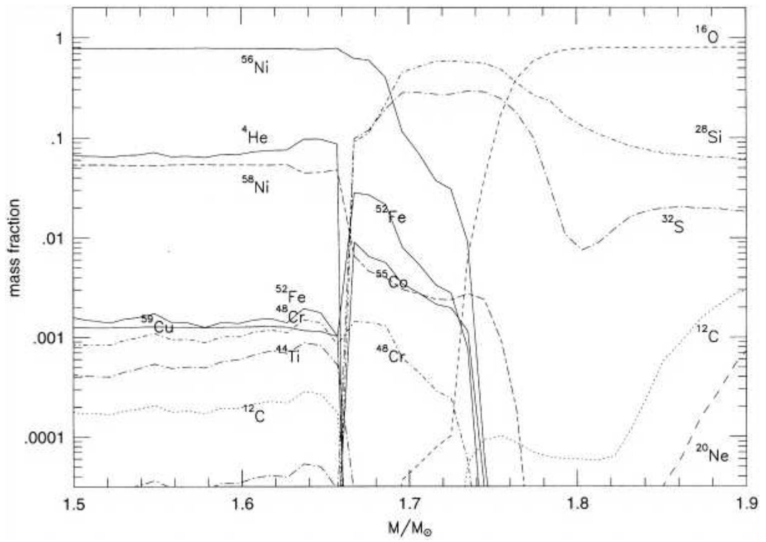

Figure 1.2: Distribution of the isotopic composition of the ejecta as a function of total enclosed mass for a star with $M_{ZAMS} = 20\ \mathrm{M}_{\odot}$ and for an explosion energy 10^{51} erg. From Nakamura et al. 1999.

Besides the large range in the mass of the exploding stars, also a large spread in the kinetic energy of the ejecta has been recently observed. In particular, a new class of supernovae, the *hypernovae*, characterized by highly energetic explosions ($\gtrsim 10^{52}$ erg), has been identified. In the hypernovae the kinetic energy of the ejecta is more than one order of magnitude higher than that of normal core-collapse SNe. The most luminous and powerful of these objects, the Type Ic supernova SN 1998bw (with an estimated energy $E \sim 3 \times 10^{52}$ erg, Iwamoto et al. 1998), was linked to the gamma-ray burst GRB 980425 by Galama et al. (1998), allowing us to understand the physical origin of the gamma-ray bursts[2].

[1]In what follows we will not consider the energy deposited in the neutrinos and we will refer only to the "visible" energy.

[2]For a complete review on GRBs and their associations with hypernovae see Mészáros (2006) and references therein.

The predictions on the nucleosynthesis yields in hypernovae are further complicated by the strong indications of aspherical jet-like explosions that have been found in many cases (see, for example, Wang et al. 2003, Mazzali et al. 2001, and, for a review on hypernovae, Nomoto et al. 2003). The evidence of jet-like explosions in hypernovae supports their link with GRBs, since a spherically symmetric GRB would require an extremely high energy (several times the solar rest mass). Moreover this scenario is in agreement with the collapsar model proposed by MacFadyen & Woosley (1999). According to this model the collapse of a massive rotating Fe core generates a BH and supersonic jets that propagate through the star (The nebular spectrum of SN 1998bw is reproduced by such a model well). As shown by Khokhlov et al. (1999), this mechanism produces a highly aspherical explosion with bipolar fast jets. Nucleosynthesis features in such hyper-energetic and highly aspherical supernovae present important differences from normal supernova explosions, as shown by Maeda & Nomoto (2003) and Nomoto et al. (2006). In particular, these works have shown that Fe-rich materials are ejected at high velocities along the jet axis, while O-rich materials occupy the central region. Moreover, the abundance ratios (Zn, Co, Ti)/Fe are larger and the ratios (Mn, Cr)/Fe are smaller than in normal spherical SNe.

1.2 SNR shocks

The study of SNRs is based on the analysis of the interaction of the blast wave shock produced in the SN explosion with the ambient environment. The basic description of the physics of the shock is provided by Landau & Lifshitz (1959), who show that, in the reference frame of a longitudinal discontinuity (with infinitesimal width), which propagates along the x direction in a homogeneous medium, the hydrodynamic equations of mass, momentum and energy can be written (in integral form) as:

$$[\rho v_x] = 0 \tag{1.1}$$

$$[P + \rho v_x^2] = [\rho v_x v_y] = [\rho v_x v_z] = 0 \tag{1.2}$$

$$[\rho v_x (1/2 v^2 + h)] = 0 \tag{1.3}$$

where v is the bulk velocity of the gas, ρ and P are its density and pressure, and h is the enthalpy per unit volume, while the square brackets indicates the differences between the pre-shock and post-shock values. Equations 1.1-1.3 are known as Rankine−Hugoniot equations. In a simple contact discontinuity we have $\rho v_x = 0$ (i. e. there is no a jump in the velocity and there can be no flux of mass across the density discontinuity), while in the case of a shock, $\rho v_x \neq 0$, then:

$$[v_y] = [v_z] = 0 \tag{1.4}$$

$$[(1/2v^2 + h)] = 0 \tag{1.5}$$

The intensity of a shock is quantified by its Mach number $\mathcal{M}$, defined as the shock speed in units of the pre-shock sound speed. From these equations, Landau & Lifshitz (1959) show that, in the case of an adiabatic, strong (i. e. $\mathcal{M} >> 1$) shock we have, for a perfect gas:

$$\frac{\rho_1}{\rho_0} = \frac{\gamma + 1}{\gamma - 1} \tag{1.6}$$

$$\frac{P_1}{P_0} = \frac{2\gamma\mathcal{M}^2}{(\gamma + 1) - \frac{\gamma - 1}{\gamma + 1}} \tag{1.7}$$

$$\frac{T_1}{T_0} = \frac{(\gamma - 1)P_1}{(\gamma + 1)P_0} \tag{1.8}$$

where T is the temperature, γ is the specific heats ratio, and 1 and 0 indicate the post- and pre-shock values, respectively. These equations show that the ratio of densities on either side of the shock front does not depend on $\mathcal{M}$, and is equal to 4, if $\gamma = 5/3$. The post-shock temperature and pressure are instead much higher than the corresponding pre-shock values, since they increase by a factor $\mathcal{M}^2$. While the material passes through the shock front, there is an increase, δs, of its entropy per unit volume. This entropy variation is associated with the dissipative processes that take place *inside* the shock front. Notice, however, that the amount of the differences between the pre-shock and post-shock values of ρ, P, and T do not depend on the specific nature of the dissipative processes, but only on the conservation of mass, momentum, and energy, imposed by the HD equations.

The primary shock generated in a SN explosion propagates at a speed higher than that of the ejecta by about a factor 4/3. Since the characteristic speed of the ejecta is of the order of 10^4 km s^{-1} and the speed of sound is of the order of a few km s^{-1} (assuming a pre-shock temperature $T = 10^3$ K), the SNR shocks originate with a very high Mach number ($\mathcal{M} \gtrsim 1000$). This allows us to use the equations 1.6–1.8. Notice that, for $\mathcal{M} = 1000$ and $T_0 = 10^3$ K, we obtain a post-shock temperature $T_1 \sim 10^8$ K, therefore it is not surprising that SNRs are intense X-ray sources.

1.3 SNR evolution

In the first phase of the SNR evolution, as long as the mass of the interstellar material swept up by the shock is much less than the mass of the stellar ejecta, the expansion of the remnant is essentially free and its development depends only on the initial conditions. This phase can be very interesting because it allows us to obtain information on the explosion mechanisms, by studying the velocity field of the ejecta, their chemical composition, etc. In the very early phases, in fact, line emission from the radioactive isotopes generated in the supernova explosion contributes significantly to the total brightness of the remnant. However, although the remnant is radiating both thermal X-ray and synchrotron radiation, the initial energy of the SNR is almost unaffected.

When the swept-up mass becomes comparable to the ejected mass, the expansion slows and the remnant enters a phase known as adiabatic expansion, or Sedov-Taylor phase. In this phase the dynamics of the expansion are determined by the total mass of the expanding gas (i. e. ejecta + swept-up ISM) and if we assume an uniform ambient medium, the evolution of the remnant is described by the simple similarity solution discussed by Sedov (1959). According to the Sedov model we can assume the expansion to be adiabatic and radial and, by imposing the conservation of the kinetic energy of the swept-up mass (with pre-shock mass density ρ_0)

$$\frac{d}{dt}\left(\frac{1}{2}\rho_0\frac{4}{3}\pi r_{sed}^3 v_{sed}^2\right) = 0 \tag{1.9}$$

we obtain the classical Sedov relationships that describe the temporal evolution of the SNR radius, r_{sed}, and of its velocity, v_{sed}

$$r_{sed}(t) \propto t^{2/5} \tag{1.10}$$

$$v_{sed}(t) \propto t^{-3/5} \tag{1.11}$$

since the post-shock temperature T_1 is proportional to v^2 (Eq. 1.7 and Eq. 1.8), we also have $T_1 \propto r^{-3}$. The Sedov model predicts a deceleration of the shock front.

During its expansion, the shock front is followed by the ejecta that are decelerated because of the high pressure of the swept-up post-shock ISM in front of them. In the outer edge of the ejected shell, in fact, the pressure is higher than in the inner shell. The outer shells of the expanding ejecta are then decelerated first and the density increases at the boundary of the expanding ejecta. As shown by McKee (1974), this deceleration determines the formation of a reverse shock wave which propagates backward into the remnant. The mechanism that produces the formation of the reverse shock is the following: as the shell expands in the ambient medium, a rarefaction wave propagates back into the shell (this processes is similar to what happens in the Riemann shock tube problem), thus lowering the internal pressure. The pressure is further reduced by the adiabatic expansion losses associated with the spherical diverging flow. The pressure inside the shell is then significantly lower than that behind the blast wave shock and a compression wave begins to propagate back into the shell interior. Because of the low sound speed in the interior, the compression wave steepens into a shock front (the reverse shock) which compresses the ejecta and heats them up to X-ray emitting temperatures. The analysis of the X-ray observations of SNRs therefore allows us to study the physical and chemical properties of the ejected material. Figure 1.3 shows a schematic representation of this scenario.

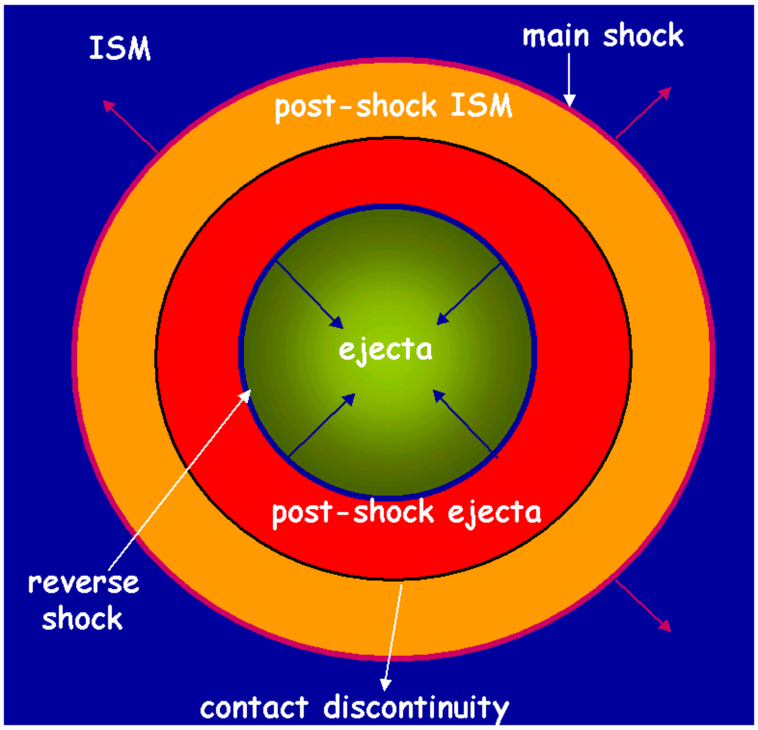

Figure 1.3: Schematic representation of a SNR. As the main blast wave shock propagates in the unperturbed ISM, followed by the ejecta (that are behind the contact discontinuity), the reverse shock propagates inwards, thus shocking the ejecta.

Notice, however, that we have not taken into account several important aspects yet. First of all, the expansion takes place in an inhomogeneous environment and we have to consider how the interaction of the shock front with the ISM inhomogeneities affects the evolution of the remnants (see Sect. 1.4). As shown by Dwarkadas (2005), the evolution is also influenced by the presence of the CircumStellar Material (CSM), which is the result of the strong wind activity of the progenitor star that has modified the local environment. Moreover, as explained in this section, the Sedov model assumes an adiabatic expansion, while in many regions of middle-aged SNRs the radiative cooling can be locally very efficient. As observed in the Tycho SNR (Hwang et al. 2002), the ejecta can also penetrate the forward shock because of Rayleigh-Taylor and Richtmyer-Meshkov instabilities (Kane et al. 1999) and this effect can be enhanced by the clumpy structure of the ejecta (Hamilton 1985) and of the ISM (Jun et al. 1996). Finally, there are examples of remnants where the spatial distribution of the ejecta and the explosion itself are very far from the spherical symmetry. As pointed out in Sect. 1.1, aspherical jet-like explosions are characteristic features of hypernovae and have been investigated as possible mechanisms for $\gamma-$ray bursts (GRB). Notice, however, that an aspherical explosion does not necessarily imply a GRB, because a high explosion energy ($\gtrsim 10^{52}$ erg) is also required. A galactic SNR whose X-ray emission has a highly aspherical morphology and is associated with the ejecta is W49B, which will be presented in detail in this thesis (see Sect. 1.6.1 and Chapter 2).

1.4 Shock-cloud interaction

The first evidence that SNR shocks propagate in an inhomogeneous medium were obtained in the early 70s by observing optical and X-ray images of the CasA remnant (van den Bergh 1971) and of the Cygnus Loop (Cox 1972). Figure 1.4 shows a beautiful Hubble Space Telescope (HST) image of a small portion of the Cygnus Loop, where the filamentary structure of the optical emission is clearly visible.

The effect of the inhomogeneities on the SNR expansion would be negligible if the average distance between two clouds were much larger than their characteristic dimension and if the clouds "absorbed" only a small fraction of the total energy of the remnant. As shown by McKee & Cowie (1975), both these conditions imply a cloud filling factor (i. e. the fraction of the volume occupied by the clouds) $f << 1$. Instead, as shown by the optical and X-ray observations of SNRs, a high degree of inhomogeneity and an intrinsic complexity in the structure of the ISM are present. The interstellar gas is almost completely organized in clumps with different values of density and whose size may range between 10^{-3} pc and a few parsec.

Silk & Solinger (1973) and Sgro (1973) have shown that the interaction of the shock front with an ISM cloud drives the formation of a transmitted shock which propagates through the cloud and of a reflected shock which propagates backward in the intercloud medium (which has already been shocked by the primary shock), as shown in Fig. 1.5.

McKee & Cowie (1975) (hereafter MC) have studied analytically this process, assuming adiabatic conditions and a cloud with uniform density. Letting ρ_c and v_c be the pre-shock cloud density and the velocity of the transmitted shock, respectively, and if ρ_0 and v_{ic} are the pre-shock intercloud density and the velocity of the main shock, MC have shown that, in the reference frame of the pre-shock ISM:

$$\rho_c v_c^2 \sim \rho_0 v_{ic}^2 \tag{1.12}$$

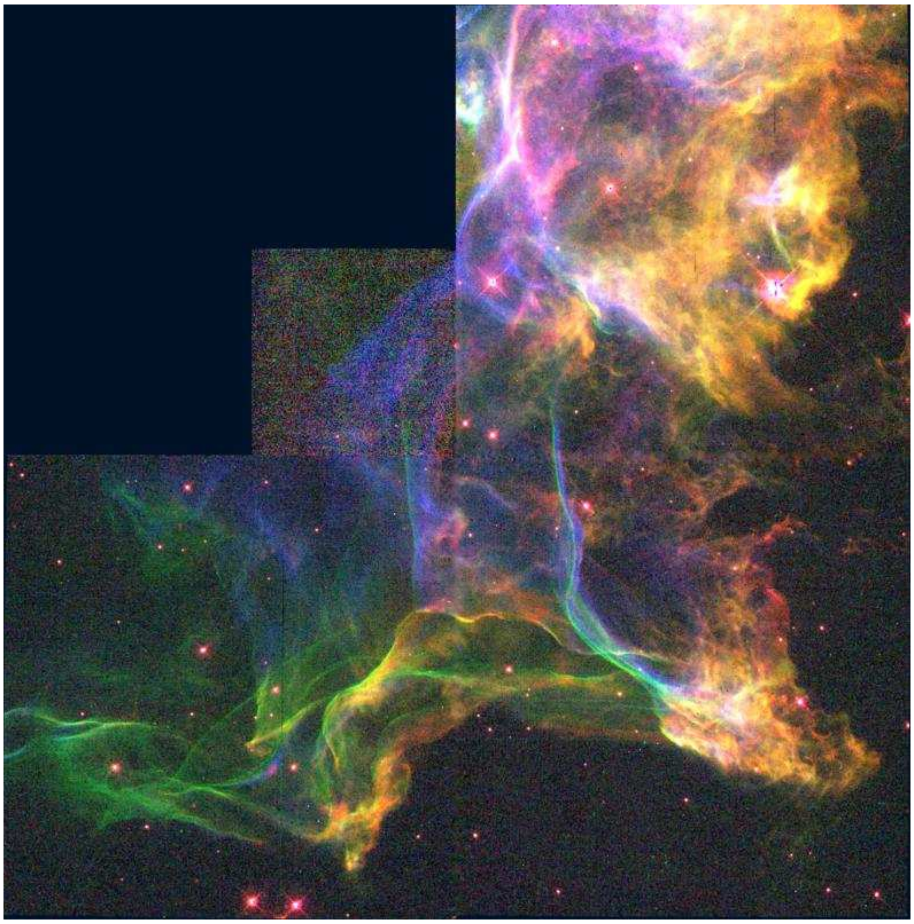

Figure 1.4: HST color-composite image of a portion of the Cygnus Loop taken with the Wide Field and Planetary Camera 2 (WFPC2). The field of view is $\sim 2'40''$. The interaction of the shock with an inhomogeneous medium drives different thermal conditions in the shocked gas: blue shows emission from doubly ionized oxygen, red from singly ionized sulfur, and green from hydrogen. From http://hubblesite.org/newscenter/newsdesk/archive/releases/1995/11/image/a, Credit: Jeff Hester (Arizona State University) and NASA.

Therefore, since the post shock temperature in the cloud is proportional to v_c^2 (see Eq. 1.7 and Eq. 1.8), the lower the cloud/intercloud density contrast, the higher is the temperature of the shocked cloud.

Moreover, indicating with P_4 the pressure of the gas in region 4 of Fig. 1.5 and with P_1 the pressure in region 1 of Fig. 1.5, if we change the density contrast between the cloud and the intercloud medium, we invariably have $1 < P_4/P_1 < 3.15$.

1.4.1 Models

The shock-cloud interaction model described above allows us to obtain indications on the global dynamics of the interaction but cannot describe the details of the

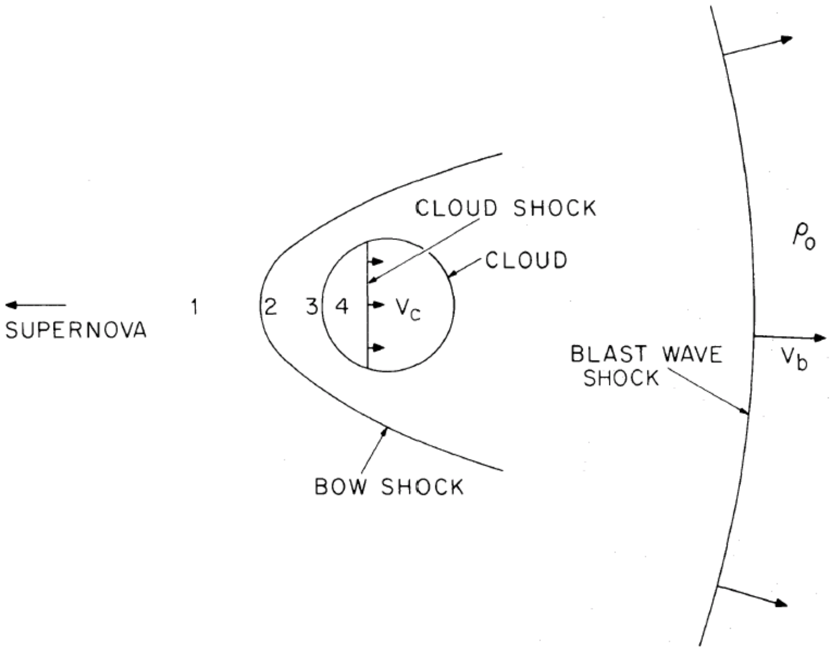

Figure 1.5: Schematic representation of the shock-cloud interaction. In region 1 the gas is shocked by the primary blast wave shock and in region 2 by the reflected bow shock; region 3 indicates the cloud surface; in region 4 the gas is behind the transmitted cloud shock, which propagates (in the left-right direction) at velocity v_c. The primary shock has already engulfed the cloud and propagates at velocity v_b in the intercloud medium (which has pre-shock density ρ_0). From McKee & Cowie 1975.

process. I remark, in fact, that the complex interaction of the SNR shocks with the ISM inhomogeneities involves many physical effects, like purely hydrodynamic effects, radiative losses, thermally conductive supersonic flows, non-equilibrium of ionization, etc. Important results have been obtained by the analytical models of MC and, for example, of Heathcote & Brand 1983, but, because of the complexity of the problem, a deeper insight into the physical scenario can be achieved with a numerical approach to the modeling of the interaction.

Several numerical models have been developed. These models allowed us to ascertain important information on the dynamics of the interaction, but they followed a pure theoretical approach with very few predictions directly comparable with the observations. The first hydrodynamic 2-D models showed the importance of the Kelvin-Helmholtz (KH) and Rayleigh-Taylor (RT) instabilities which develop at the interface between the cloud and the post-shock ambient medium (see, for example, Bedogni & Woodward 1990 and Klein et al. 1994). The 3-D models presented by Stone & Norman (1992) and Xu & Stone (1995) have shown that these instabilities are very efficient in breaking the cloud because of the turbulent mixing with the intercloud medium. All these models, however, do not take into account the effects of radiative losses, thermal conduction and the presence of magnetic fields.

The effects of radiative cooling have been considered in the 2-D models of Mellema et al. (2002) and Fragile et al. (2004). These models show that the radiative cloud fragments into numerous cold cloudlets. Moreover, the efficiency of radiative cooling is enhanced by the presence of an ambient magnetic field, as shown by Fragile et al. (2005) (where, however, the thermal conduction is not taken into account).

A complete model which takes into account the combined effects of thermal conduction and radiative cooling (exploring two different physical regimes, characterized by different density ratios cloud/ambient medium and different Mach numbers) has been recently proposed by Orlando et al. (2005). This work has shown that, when radiative losses dominate, the shocked cloud is fragmented into cold and dense cloudlets, while when the efficiency of thermal conduction is higher than that of radiative cooling, the "evaporation" of the cloud in the intercloud medium is induced: the high-pressure cloud material, heated through thermal conduction with the hotter intercloud medium, expands and approach the density and temperature values of the intercloud medium. In both cases, however, thermal conduction suppresses the hydrodynamic instabilities that would develop at the cloud boundaries. Thermal conduction and radiative cooling are therefore competing effects. The dynamics of the shock-cloud interaction can enhance or reduce the degree of inhomogeneity of the ISM. When radiative losses dominates, the cooling induces the formation of small and dense knots whose density contrast with the intercloud medium is much higher than that of the pre-shock cloud. On the other hand, if thermal conduction is more efficient, the ISM inhomogeneities are smoothed because of the evaporation of the shocked cloud in the intercloud medium and the ISM becomes more homogeneous.

Despite these large theoretical efforts, however, no detailed comparison with the observations has yet been provided. Although comparisons with the observations are present, for example, in Hamilton & Sarazin (1984) and in White & Long (1991), these models are very simplified and do not include at the same time all the relevant physical effects.

Indeed, the comparison between detailed models and observations is not straightforward, because the real interstellar clouds may have a very complex morphology, and are often seen in projection with other shocked clouds, so that many overlapping shocks (not necessarily correlated) are present in the same field of view. Moreover, it is difficult to derive from the observations the physical parameters of the problem that are necessary to set up the simulations and it is also difficult to ascertain the evolutionary stage of the interaction, in order to compare the data with the appropriate temporal frame of the numerical simulation. It is also necessary to take into account the instrumental response of the detectors and the effects of the interstellar absorption.

Recently, an observation-oriented numerical model has been presented by Patnaude & Fesen (2005) to describe the shock-cloud interaction in a small, isolated cloud along the southwestern limb of the Cygnus Loop. However, no observable quantities are produced from this model and only a simple qualitative comparison between the model density plot and the overall morphology of the Hα emission is presented.

To overcome these limitations, our group at the Osservatorio Astronomico di Palermo has started a long-term project which will lead to accurate and complete numerical models and to a self-consistent methodological approach for comparison with high resolution multi-wavelength observations of SNRs. The project consists in performing accurate and complete hydrodynamic simulations and in synthesizing observables (e. g. X-ray images and spectra) directly from the model. This work has two important guide-lines: i) a theoretical aspect which consists in understanding the effects and the role of the different physical processes on the evolution of the system and on the electromagnetic emission of the shocked cloud, and ii) an observation-oriented aspect which aims at the proper interpretation of specific X-ray and optical observations (i. e. to understand the physical origin of the observed multi-wavelength emission, to obtain information about the density and temperature profiles of the shocked clouds, etc.). First important results in the framework of item i) have been recently obtained by Orlando et al. (2006). This work has shown the non-trivial relationship between the complex pattern of shocks and the emerging X-ray emission in the case of a pure hydrodynamic treatment of the shock-cloud interaction and also in the case of a more complete approach which takes into account radiative cooling and thermal conduction (see Fig. 1.6). Item ii) is a main issue of this thesis and the achieved results are discussed in detail in Chapter 4.

1.4.2 Time scales

An important time-scale for the evolution of the shock-cloud interaction is the cloud crushing time τ_{cc} (Klein et al. 1990), defined as the characteristic time for the transmitted shock to cross the cloud. For a spherical cloud with radius R_c:

$$\tau_{cc} = \frac{R_c}{v_c} \sim \frac{R_c \chi^{1/2}}{v_{ic}} \tag{1.13}$$

where $\chi = \rho_c/\rho_0$ is the cloud/intercloud density contrast and where we have used Eq. 1.12.

As we have seen in the previous section, the evolution of the system strongly depends on the relative efficiency of thermal conduction and radiative cooling; hence it is useful to estimate the characteristic time-scales of these two processes.

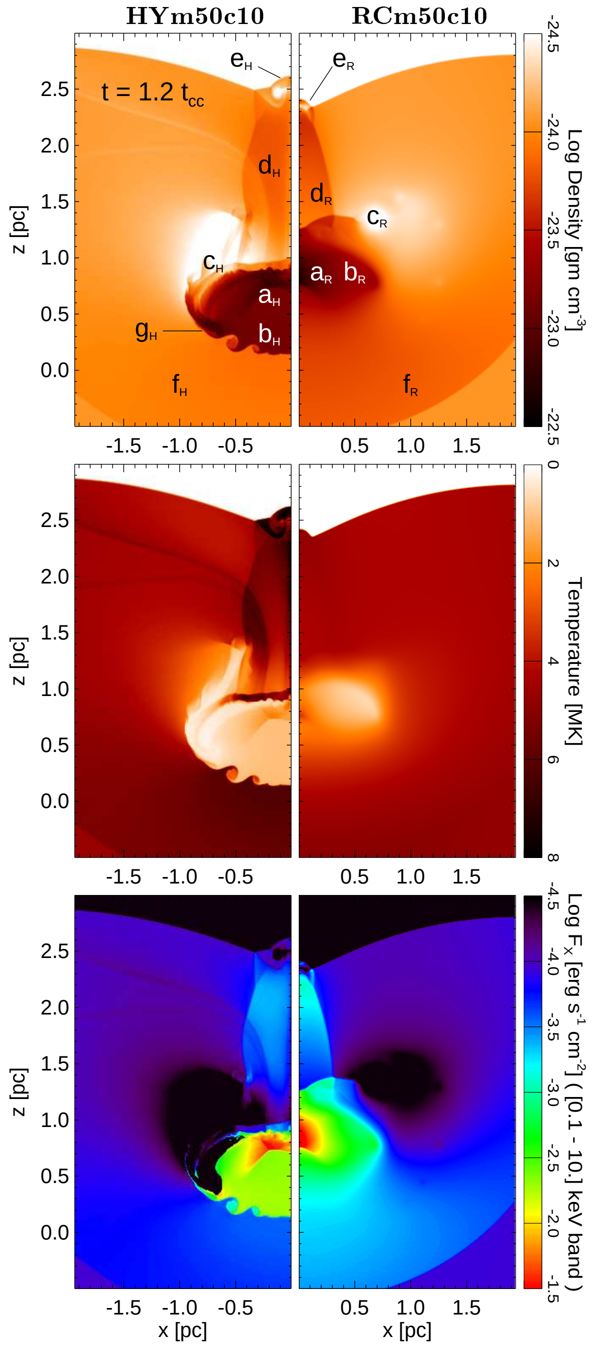

Figure 1.6: 2-D slices in the $(x,\ z)$ plane of density (*upper panels*), temperature (*middle panels*), and X-ray emission in the $0.1-10$ keV band (*lower panels*), derived for the interaction of a shock front with $\mathcal{M}=50$ and an ISM cloud 30 times denser than the intercloud medium, neglecting (model HYm50c10, *left panels*) and considering (model RCm50c10, *right panels*) the effects of thermal conduction and radiative cooling. From Orlando et al. (2006).

Since for an optically thin plasma we have:

$$\left(\frac{dE}{dt}\right)_{rad} = \frac{1}{\gamma-1}\frac{dP}{dt} = n_e n_H \Lambda(T) \tag{1.14}$$

where $\Lambda(T)$ is the radiative losses function per unit emission measure (Raymond & Smith 1977, Mewe et al. 1985), $n_e = \rho/m_e$ and $n_H = \rho/m_H$ are the electron and hydrogen number density, and

$$E = \epsilon + \frac{1}{2}|\mathbf{v}|^2 \; , \qquad \epsilon = \frac{P}{(\gamma - 1)\rho} \; , \tag{1.15}$$

then, the radiative cooling time-scale is defined as:

$$\tau_{rad} = \frac{P}{(\gamma-1)n_e n_H \Lambda(T)} \sim 2.5 \times 10^3 \frac{T^{3/2}}{n} \tag{1.16}$$

where the last equation has been obtained in the approximation $n_e n_H \Lambda(T) \sim 1.6 \times 10^{-19} T^{-1/2}$ (Raymond et al. 1976 and Raymond & Smith 1977), valid if 10^5 K $< T < 10^7$ K. Considering the thermal conduction, where, according to Spitzer (1962),

$$\left(\frac{dE}{dt}\right)_{cond} = \nabla \cdot [\kappa(T)\nabla T] \sim \frac{2}{7}\kappa(T)\frac{T}{l^2} \tag{1.17}$$

where l is the characteristic length of temperature variation and $\kappa(T) = 5.6 \times 10^{-7} T^{5/2}$ erg s^{-1} K^{-1} cm^{-1}, the thermal conduction time-scale is:

$$\tau_{cond} = \frac{7nk}{2(\gamma-1)}\frac{l^2}{\kappa(T)} \sim 2.6 \times 10^{-9} \frac{nl^2}{T^{5/2}} \tag{1.18}$$

The ratio of the time-scales is therefore:

$$\frac{\tau_{rad}}{\tau_{cond}} \sim 10^{12} \frac{T^4}{(nl)^2} \tag{1.19}$$

Note that, by equating this ratio to 1, we derive the Field length scale $L_F = 1.3 \times 10^6 T^2/n$ (Field 1965), i.e. the maximum scale on which the conduction dominates the radiative cooling.

Orlando et al. (2005) derived the relationship between these time-scales (and the cloud-crushing time) as a function of the cloud/intercloud density contrast, χ, and of the shock Mach number, $\mathcal{M}$, for a cloud of 1 pc radius. This relationship is shown in Fig. 1.7. The figure shows that there is a range of χ and $\mathcal{M}$ values where thermal conduction dominates (i. e. $\tau_{cond} < \tau_{rad}$) and the cloud evaporates in the intercloud medium. If we increase the density contrast and/or reduce the Mach number we instead have $\tau_{rad} < \tau_{cond}$ and thermal instabilities determine the fragmentation of the shocked cloud in dense cloudlets.

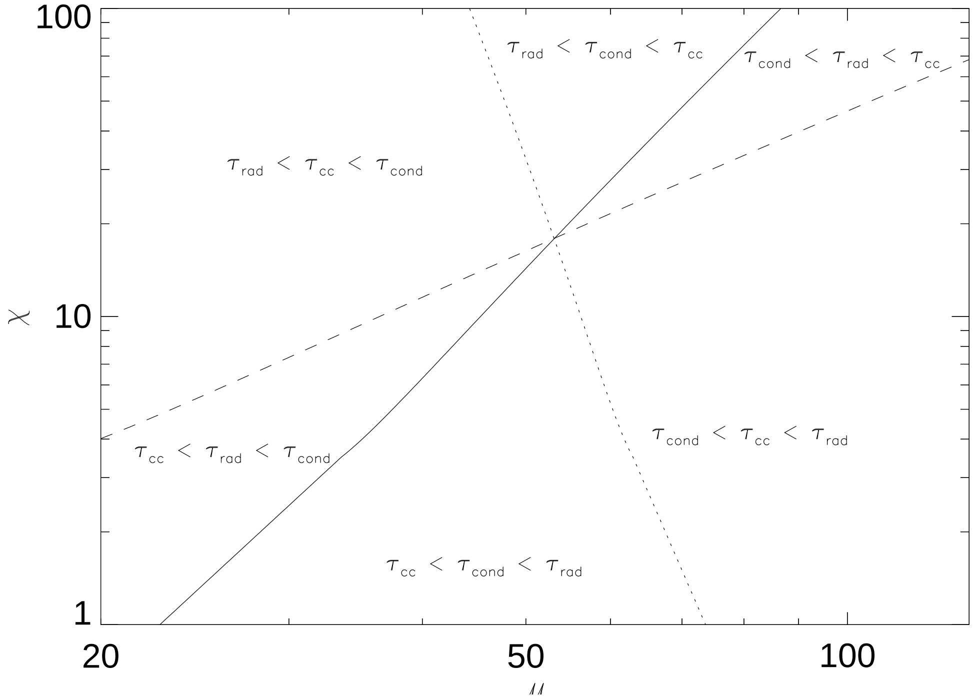

Figure 1.7: Relationship between the radiative time-scale, τ_{rad}, the conductive time-scale τ_{cond}, and the cloud-crushing time τ_{cc} in the $\chi - \mathcal{M}$ parameter-space for the impact of a shock with Mach number $\mathcal{M}$ with a spherical cloud (of 1 pc radius) χ times denser than the intercloud medium. The lines are the locii where $\tau_{rad} = \tau_{cond}$ (solid line), $\tau_{rad} = \tau_{cc}$ (dashed line), and $\tau_{cond} = \tau_{cc}$ (dotted line). From Orlando et al. (2005).

1.4.3 X-ray and optical emission

As we have seen, the difficulties in interpreting the observed emission of SNRs arise because many different processes may occur at the same time in the same object and observations are affected by superposition effects if the spatial resolution is not high enough (a cloud with a diameter of 0.1 pc, at 1 kpc, covers in the sky a circle of 20" radius). Notice also that the presence of the inhomogeneities determines complicated local variations of the thermodynamical parameter of the emitting plasma and this implies large spatial variations in the spectral properties of the source.

Several authors (see, for example, Decourchelle et al. 1997, Bocchino et al. 2000, and Patnaude et al. 2002) have shown how the combined study of X-ray and optical observations of SNRs provides important information about the shock-cloud interaction process and about the physical and chemical conditions of the post-shock medium (temperature, chemical composition, morphology of the clouds, etc.). From the analysis of past optical and X-ray observations, three different physical scenarios have been proposed to explain the details of the shock-cloud interaction and of the observed emission. These scenarios all associate the optical emission with slow radiative shocks propagating in a dense ($n \sim 10$ cm^{-3})

and cool ($T \sim 10^4 - 10^5$ K) environment, while X-ray emission originates from hotter and less dense regions.

A first scenario associates the optical emission with a transmitted shock travelling through dense clouds and explains the X-ray emission with the evaporation of the inhomogeneities engulfed by the main blast wave. This model has been applied in the past to observations of different SNRs (Fesen et al. 1982, Charles et al. 1985, Craig et al. 1997) and to describe the composite SNR G327.1-1.1 (Bocchino & Bandiera 2003). More recently this scenario has been invoked for other remnants. Byun et al. (2006) have shown that, in the supernova remnant HB21, the interaction of the shock front with dense infrared emitting molecular cloud is driving the evaporation of the clouds and their X-ray emission. In this remnant, in fact, sensitive ^{12}CO $J = 1 - 0$ observations have revealed that small broad-line clouds are spatially related with X-ray bright regions observed with the *ROSAT* satellite. Chen et al. (2004) revealed several signatures of the cloud evaporation by analyzing a *Chandra* X-ray observation of the SNR 3C 391. In particular, this scenario can account for the highly clumpy structure and the uniform temperature and density distribution over almost all of the remnant. Another indication of the cloud evaporation in 3C 391 is that the density of the X-ray emitting plasma, derived from the spectral analysis, is much lower than the mean ambient cloud density.

A second class of interpretations points out the importance of the overpressured regions in the post-shock flows and associates the X-ray emission with the intercloud medium heated by reflected shocks. When the clouds are very large and dense, thermal conduction is less efficient (see Eq. 1.19 and Fig. 1.7) and the effects of the evaporation can be neglected. In this case all the X-ray emission originates in the plasma heated by the reflected shock. According to this scenario the X-ray emission is localized "behind" the optical emission, which is associated with the shock transmitted into the inhomogeneities. The simple comparison between the morphology of the optical and X-ray emission can give clear indications, as shown in Fig. 1.8, left panel. This scenario has been extensively adopted for the Cygnus Loop. For example, the comparison between optical and *ROSAT* X-ray observations has shown that the X-ray emission in the southeastern rim of the Cygnus Loop is associated with a reflected shock (Graham et al. 1995). This conclusion has been recently confirmed by the analysis of a *Chandra* observation of the same region carried on by Levenson & Graham (2005). Also in the northern and eastern part of the remnant the results of the spectral analysis of two *ASCA* observations revealed the presence of a hot X-ray emitting component (at $\sim 3.5 \times 10^6$ K) that has been associated with the plasma behind the reflected shock (Miyata & Tsunemi 2001). This hot component has a temperature higher (about a factor of 2) than that predicted by the Sedov model and so it cannot be associated with the main shock. In the eastern part of the Cygnus Loop, however, Miyata & Tsunemi (2001) also found a cooler component (at $\sim 6 \times 10^5$ K) associated by the authors with the cloud material heated by the transmitted shock. A *Chandra* observation of the western limb of the remnant revealed a similar scenario (Levenson et al. 2002). In this region, in fact, both the transmitted and the reflected shocks seems to be visible in X-rays, as shown in Fig. 1.8, right panel. All these results concur on associating the emission of the Cygnus Loop with the interaction of the shock with the large and dense walls of a cavity in the surrounding medium.

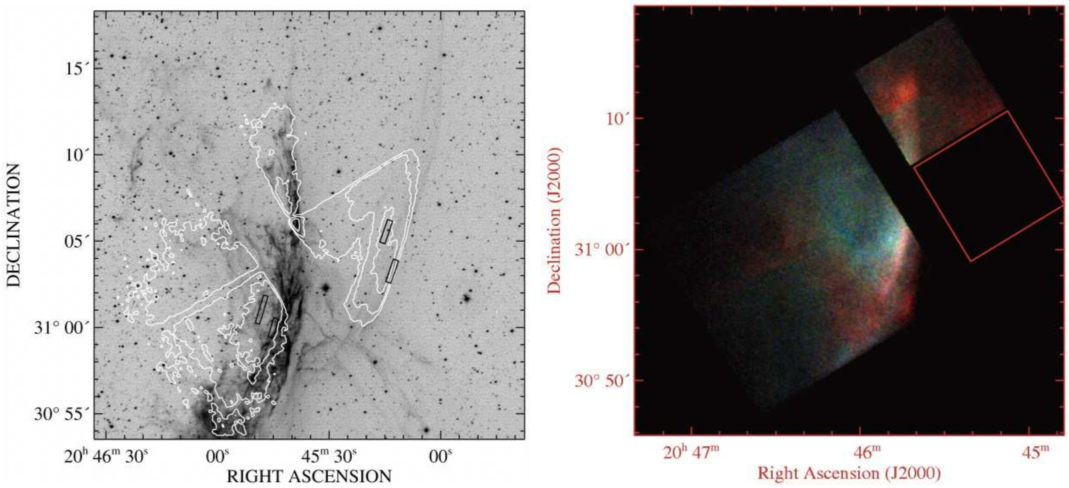

Figure 1.8: *left panel:* Hα image of the western limb of the Cygnus loop where contours of the X-ray emission are superimposed (in white). From Levenson et al. (2002). *Right panel: Chandra* X-ray emission of the same region in the $0.3 - 0.6$ keV (red), $0.6 - 0.9$ keV (green), and $0.9 - 2$ keV (blue) energy bands. The soft emission is associated with the transmitted shock, while the harder emission originates behind the reflected shock. From Levenson et al. (2002).

A third interpretation is based on the propagation of transmitted shocks through inhomogeneities with an inwards increasing density profile. These shocks can account for the observed X-ray emission when the cloud/intercloud density contrast is low (see Eq. 1.12) and/or when the primary blast wave shock is fast. This scenario was proposed by Bocchino et al. (2000) to explain the optical and X-ray emission of two regions in the northern rim of the Vela SNR in which the main blast wave seems to interact with a small isolated cloud (FilD region) and with a cavity wall (FilE region). The detailed study of new observations of these regions and the numerical modeling of the shock-cloud interaction in the FilD knot are main arguments of this thesis and are extensively discussed in Sect. 1.6.2, Chapter 3, and Chapter 4). As we have seen, the association of the X-ray emission with the transmitted shock has been adopted also to explain the soft X-ray emitting component observed in different regions of the Cygnus Loop (see also Patnaude et al. 2002 and Levenson et al. 2003).

1.5 SNR classification

Supernova remnants are classified into four broad categories, based primarily on their radio and X-ray morphology: Shell-like, Crab-like (Plerionic), Composite, and Mixed-morphology.

- Sheel-like remnants are characterized by an almost spherical, limb-brightened morphology. The X-ray emission can be both thermal (Cas A), or non-thermal (SN 1006).
- Crab-like remnants presents a bright central region, plerion or pulsar wind nebula, that is a synchrotron nebula powered by the relativistic wind of the central energetic pulsar.
- Composite remnants are shell-like remnants containing non-thermal plerions (e. g. the Vela SNR).
- Mixed-morphology SNRs have center-filled *thermal* X-ray emission and shell-like radio morphology. They show quite flat temperature profiles and a higher central density than would be expected from the Sedov model (Rho & Petre 1998).

1.6 Contents of the thesis

In this thesis I aim at studying the complex interaction of the SNRs with the ISM and the effects of this interaction on the evolution of the physical and chemical properties of the galactic medium. As explained in this chapter, the different evolutionary stages of a remnant allow us to study different aspects of the interaction.

In particular, in young SNRs, where the ISM swept-up mass is lower than (or comparable to) the mass of the ejecta, the X-ray emission is often associated with the ejecta heated by the reverse shock (or by a reflected shock, if a large molecular cloud is present). The study of the young, ejecta-dominated SNRs is therefore a powerful diagnostic tool to study the ejecta, thus obtaining information on the dynamics of the supernova explosions and on their contribution to the chemical evolution of the Galaxy. Moreover, in the early phases of its expansion, the shock front interacts with the CSM, and the emerging radiation allows us to understand how massive stars influence the local environment with their winds.

On the other hand, in middle-aged SNRs, the bulk of the emission is associated with the shocked ISM and the contribution of the ejecta becomes negligible. In this case it is possible to study the dynamics of the interaction of the shock front with the ISM inhomogeneities and the evolution of the shocked interstellar clouds.

To obtain a complete description it is therefore necessary to study both these evolutionary stages. To this end I focus on two different remnants: i) the bright SNR W49B, which is a clear prototype of the ejecta-dominated SNRs, where clear signatures of the interaction of the ejecta with ambient molecular clouds are visible and ii) a specific region (the northern rim) of the Vela SNR, which is the nearest middle-aged SNR, where it is possible to study the details of the shock-cloud interaction and the physical origin of the observed X-ray and optical emission.

1.6.1 The supernova remnant W49B

The galactic supernova remnant W49B is one of the brightest ejecta-dominated SNRs observed in X-rays. It has a center-filled morphology in X-rays and a shell-like morphology in the radio band. According to Rho & Petre (1998), W49B is similar to mixed-morphology supernova remnants, but its classification is uncertain. In the radio band, W49B is one of the 10 galactic sources with the highest surface brightness at 1 GHz (Moffett & Reynolds 1994). The diameter of the radio shell is $\sim 4'$, while its distance D_{W49B} is still uncertain. On the basis of HI absorption analysis of Radhakrishnan et al. (1972), and considering the corrections by Moffett & Reynolds (1994), $D_{W49B} \sim 8$ kpc, but Brogan & Troland (2001) have shown that this estimate, although perfectly consistent with the new VLA data, is not supported by very clear evidence and that the range of possible D_{W49B} values is quite large, being ~ 8 kpc $< D_{W49B} \lesssim 12$ kpc. This upper limit is consistent with a possible association of W49B with the star forming region W49A (which is at 11.4 kpc, according to Gwinn et al. 1992), although thare are a few indications that W49B is closer to us. In what follows, however, we will use $D = 8$ kpc.

In the X-ray band, W49B was first detected with the *Einstein Observatory* (Pye et al. 1984). The discovery of intense Fe XXV K line emission by *EXOSAT* (Smith et al. 1985) indicated that the X-ray emission of W49B is thermal and dominated by the ejecta. This result has been further confirmed by analysis of the *ASCA* spectrum (Fujimoto et al. 1995, Hwang et al. 2000). Ejecta-dominated remnants are expected to be relatively young, and while the age of W49B has not yet been determined accurately, published age estimates are in the range of $\sim 1000 - 4000$ yr (Pye et al. 1984, Smith et al. 1985, Hwang et al. 2000). The low resolution images of Si, S, and Fe K emission lines obtained with *ASCA* may indicate that the iron emission is confined to the inner part of the remnant, while silicon and sulfur emission appears to originate in the outer regions, as shown in Fig. 1.9. This result has been interpreted by Fujimoto et al. (1995) as evidence of a stratified distribution of the elements.

The analysis of the same *ASCA* data carried out by Hwang et al. (2000)

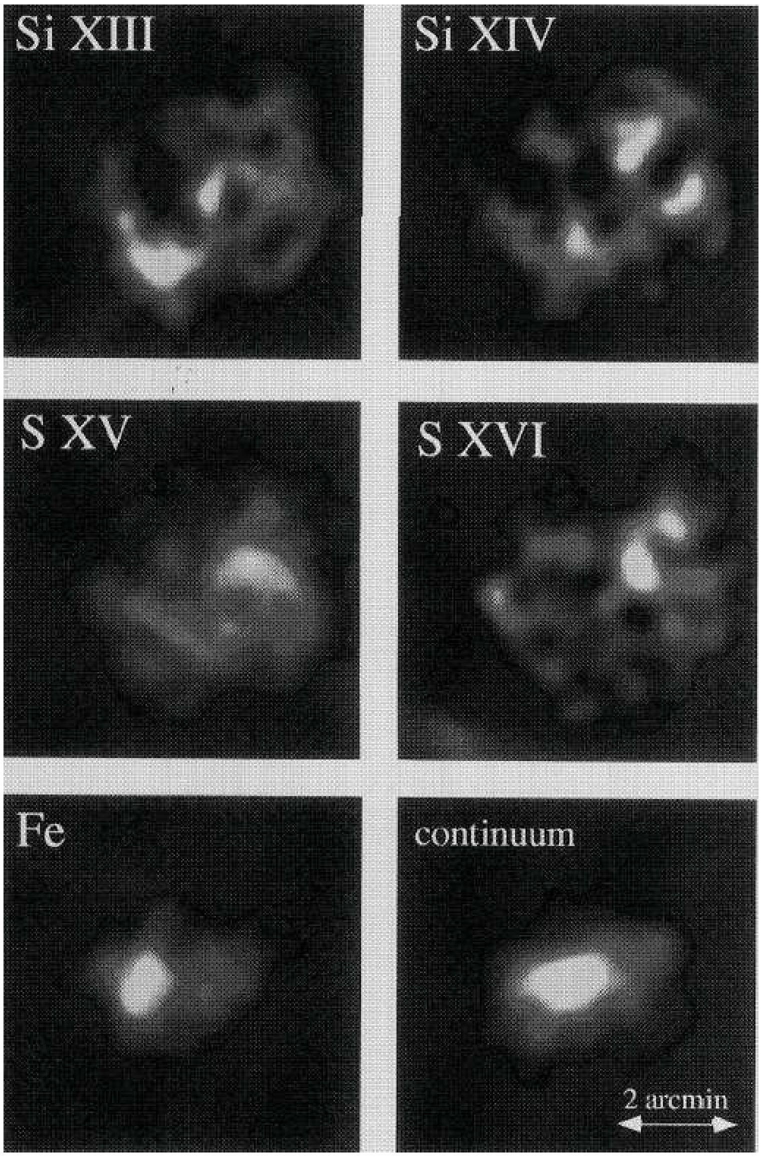

Figure 1.9: Narrow-band images of W49B and continuum image in the 4−6 keV band obtained with *ASCA* by Fujimoto et al. (1995). The contribution of the continuum is subtracted in the Si and S images (in the Fe band this contribution is negligible).

showed that broadband modeling of the remnant's global spectrum requires two thermal components and significant overabundances of Si, S, Ar, Ca, Fe with respect to the solar values.

Recently, the comparison between data obtained in X-rays with the *Chandra* satellite and in the infrared with the Palomar observatory have revealed new details of the morphology of W49B (Keohane et al. 2006). Figure 1.10 shows these new data. The molecular hydrogen IR emission at 2.12 μm (in red, in Fig. 1.10) reveals the presence of a shocked molecular H_2 cloud that clearly confines the remnant at East. The circular distribution of the molecular cloud around the

SNR has probably been shaped by strong stellar winds from the progenitor star pushing out the ambient interstellar material to its current location and forming a cavity. The [Fe II] emission at 1.64 μm (in green) reveals instead a barrel-shaped structure with four coaxial rings of warm gas. This structure has been interpreted as residuals of a strong stellar winds from the progenitor star. The molecular cloud has density $n_{H_2} \sim 2-3\times10^3$ cm^{-3} and temperature $T_{H_2} \sim 1.2-2\times10^3$ K, while the [Fe II] structure has density $n_{FeII} \sim 1.6-8\times10^2$ cm^{-3} and temperature $T_{FeII} \sim 0.7-1.0\times10^3$ K (Keohane et al. 2006). The *Chandra* X-ray emission

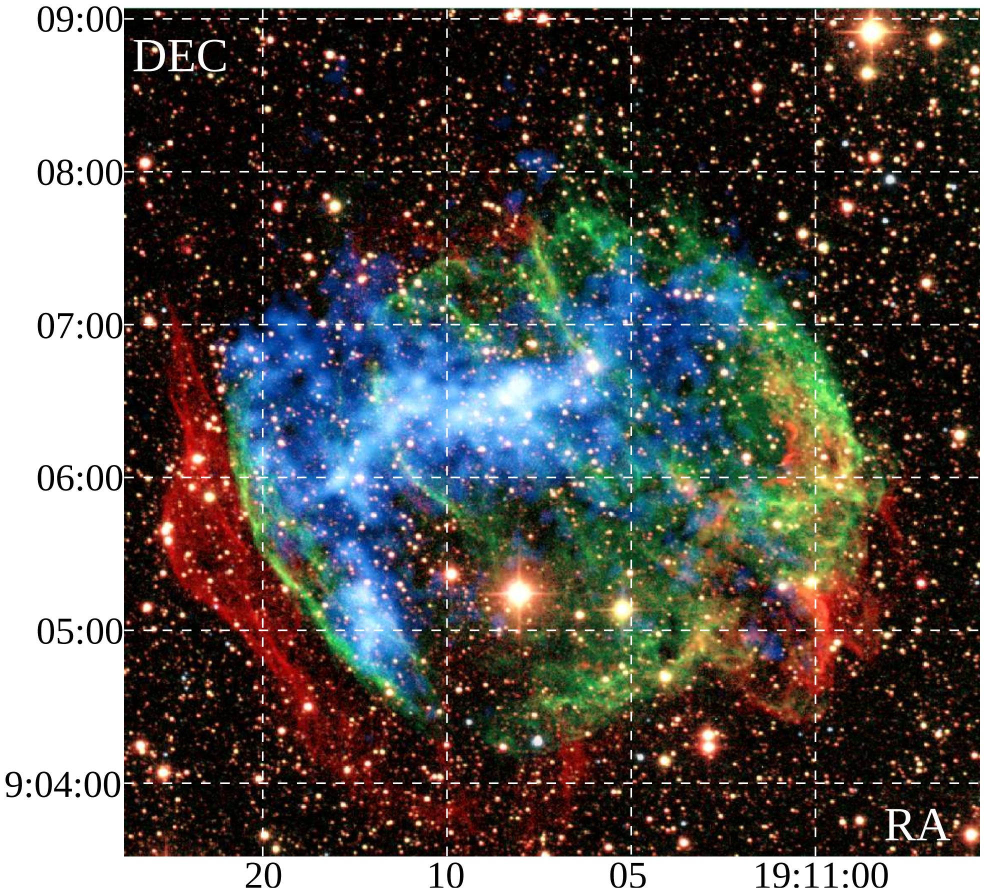

Figure 1.10: Color composite *Chandra* X-ray image (in blue), infrared 2.12 μm molecular hydrogen (in red), and 1.64 μm [Fe II] (in green) images of W49B (from http://chandra.harvard.edu/press/04_releases/press_060204.html).

in the Fe K line band (in blue) shows the presence of an elongated structure in the Fe K emission (interpreted by the authors as a jet). This simple qualitative consideration together with the nondetection of a neutron star associated with the remnant, have been considered as making W49B consistent with theoretical predictions for a collapsar and thus a candidate for a gamma-ray burst remnant.

1.6.2 The Vela SNR and its northern rim

The Vela SNR is the nearest middle-aged SNR. Its distance is ~ 250 pc (Bocchino et al. 1999, Cha et al. 1999) and at this distance one arcmin corresponds to only 0.07 pc. Therefore, the Vela SNR represents a privileged laboratory for the study of the shock-cloud interaction. The age of this SNR has been estimated to be $\sim 10^4$ yr, in good agreement with the characteristic age (~ 11200 yr, Taylor et al. 1993) of the pulsar PSR B0833-45, which is associated with the remnant (Weiler & Panagia 1980 and Weiler & Sramek 1988). The X-ray emission of the remnant is quite soft and its total flux in the $0.1-2.4$ keV band is 2.9×10^{-8} erg cm^{-2} s^{-1} (Lu & Aschenbach 2000). Figure 1.11 shows the $0.1-2.4$ keV image of the Vela SNR obtained with the *ROSAT* satellite.

Lu & Aschenbach (2000) analyzed the *ROSAT* observation of the Vela to perform a spatially resolved spectral analysis of the whole remnant. The spectra have been extracted from square regions of $8.75'$ edge length and have been described with two thermal components of an optically-thin thermal plasma in collisional ionization equilibrium, CIE. The spatial distribution of the temperatures of the two components is shown in Fig.1.12, where the contour levels of the count image are superimposed. Notice that the two brightest regions have the lowest temperatures.

Although the bulk of the X-ray emission of the Vela SNR is associated with the post-shock ISM, there are also indications of X-ray emitting ejecta. Aschenbach et al. (1995) identified 6 "shrapnels" (labelled Shrapnel A-F), that are protruding features with a characteristic boomerang shape beyond the primary blast wave. The biggest and brightest shrapnel is Shrapnel D, which is clearly visible in Fig. 1.11, in the eastern part of the shell at $\alpha\sim 9^h00^m00^s$ and $\delta=-45°30'00''$. The opening angle of these boomerang-like structures seems to suggest supersonic motion in tenuous matter. Moreover, their central axis intersect near the center of the Vela SNR. Because of these indications, the shrapnels have been associated with fragments of supernova ejecta, although an alternative interpretation associates them with "break-outs" of the main shock produced by the interaction with ISM inhomogeneities that make the shock non-spherical. Recently, the results of the analysis performed by Katsuda & Tsunemi (2005) on an *XMM-Newton* observation of the Shrapnel D revealed that O, Ne, and Mg are significantly overabundant with respect to the corresponding solar values. These results clearly confirm the association of shrapnel D with a fragment of SN ejecta. Strong indications of the interaction of the shrapnel with an interstellar cloud have also been found. An *XMM-Newton* observation of Shrapnel A was also analyzed by Katsuda & Tsunemi (2006). The morphology of this shrapnel is characterized by a bright knot and a faint trailing wake with a structure in temperature which decreases toward the center of the shell, as in shrapnel D. In this case, however,

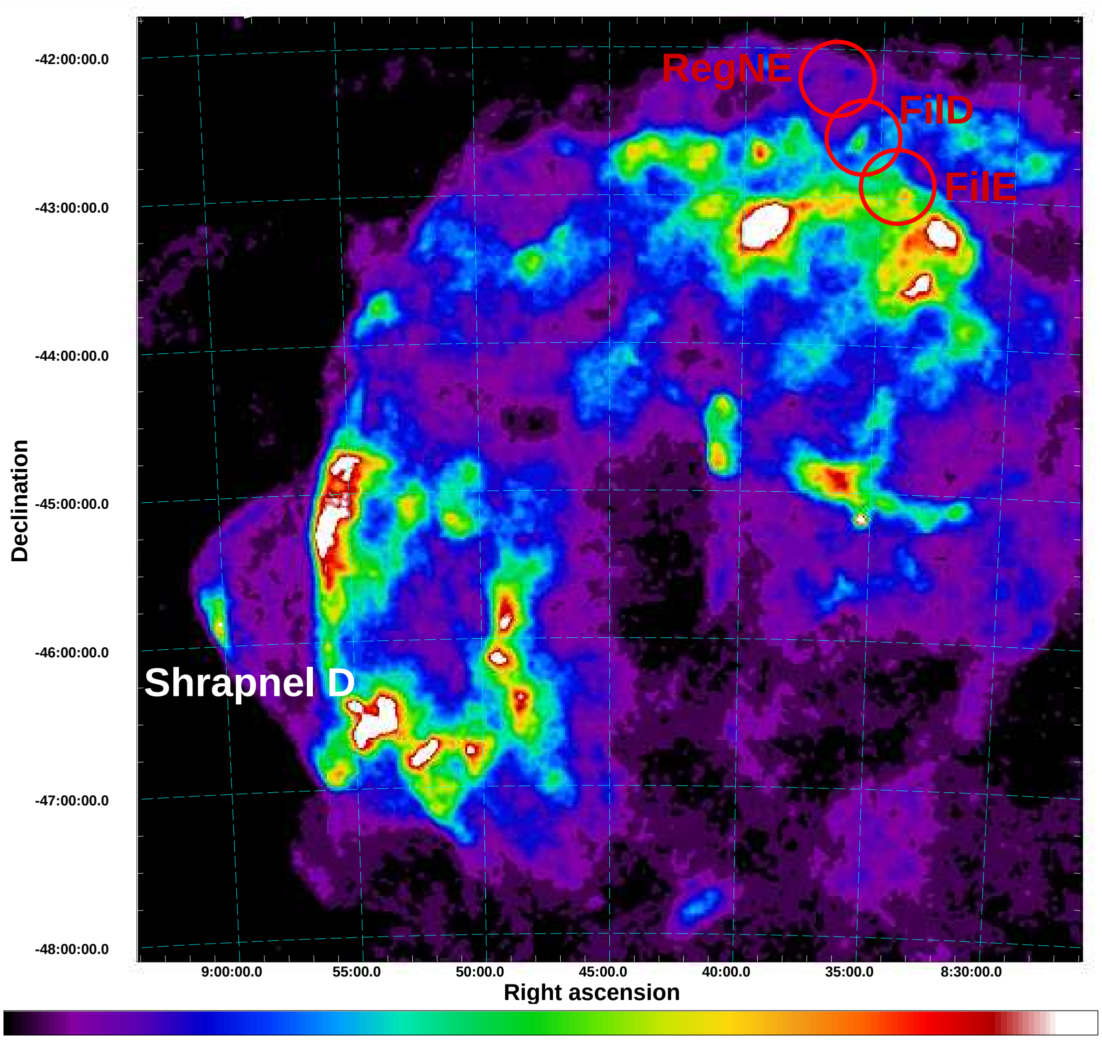

Figure 1.11: *ROSAT* All-Sky-Survey image of the Vela SNR in the $0.1 - 2.4$ keV band. The color scale ranges between 0 and 30 counts, the bin-size is $45''$ and the image has been smoothed by a gaussian distribution with $\sigma = 67.5''$. The red circles indicate the *XMM-Newton* EPIC fields of view of the three observations pointing the regions named RegNE, FilD, and FilE, that are analyzed and discussed in this thesis.

the C and Si abundance resulted to be oversolar, while the abundances of O, Ne, Mg, and Fe are lower than their solar values. This may indicate that Shrapnel A is an ejecta fragment strongly contaminated by the mixing with the local ISM.

As for the study of the interaction of the shock front with the ISM clouds, the Vela SNR, unlike the Cygnus Loop (which has been almost completely covered by several *Chandra* and *XMM-Newton* observations), has not yet been systematically studied, although it has the great advantage of a smaller distance. In the optical band, the Vela SNR is characterized by long filaments that, on large spatial scale (some degrees), have a complex correlation with the X-ray and radio emission (Bock et al. 1998, Moriguchi et al. 2001). It is necessary to study this

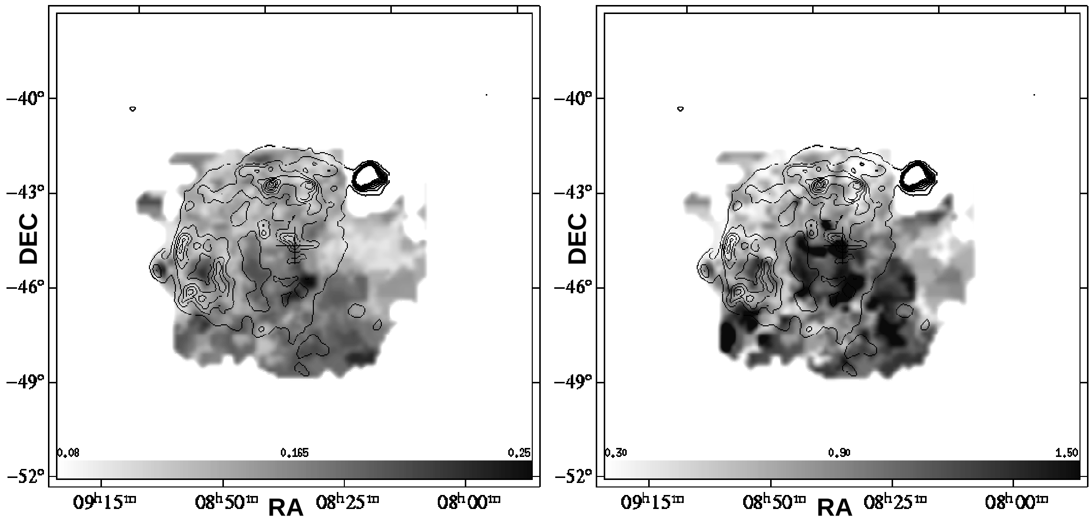

Figure 1.12: Spatial distribution of the temperatures of the cool (*left panel*) and hot (*right panel*) X-ray emitting components in the Vela SNR. The gray scale is linear and the temperature is expressed in keV. The contour levels of the count image are superimposed. From Lu & Aschenbach (2000).

correlation at spatial scales comparable with those of the filament (few arcminutes) to get crucial information on the dynamics of the interaction of the blast wave shock with the ISM inhomogeneities.

The northern rim of the Vela SNR presents all the characteristic features of a complex interaction between the blast wave shock and several inhomogeneities of the ambient medium. A close-up view of this part of the shell is shown in Fig. 1.13, where the radio contour levels at 843 MHz are superimposed on the Hα (upper panel) and $0.1 - 2.4$ keV X-ray emission (lower panel). The figure shows the complex relationship between the emission in these three bands. The evidence for the interaction of the shock front with ISM clouds has been pointed out by the combined analysis of $ROSAT$, optical, and UV observations of the regions FilD and of FilE (for the localization of these region, see Fig. 1.11), discussed by Bocchino et al. (1994, 1997, 1999, 2000). In particular, in FilD there is clear evidence for the interaction of the shock front with a relatively small ($\sim 2 \times 10^{18}$ cm) and isolated cloud. As for FilE, instead, the $ROSAT$ All-Sky Survey indicates the presence of a large limb-brightened structure corresponding to a long and bright Hα filament and this suggests the interaction of the shock with a large (several pc) inhomogeneity at a larger projected distance from the main shock front than FilD. The analysis of the X-ray emission of these regions showed that the observed spectra are described significantly better by a 2-component optically thin thermal plasma in CIE than by a single-temperature model or a non-equilibrium of ionization (NEI) model. In the FilD knot the two components, with temperatures $1.10 \pm 0.06 \times 10^6$ K and $6^{+6}_{-3} \times 10^6$, have been

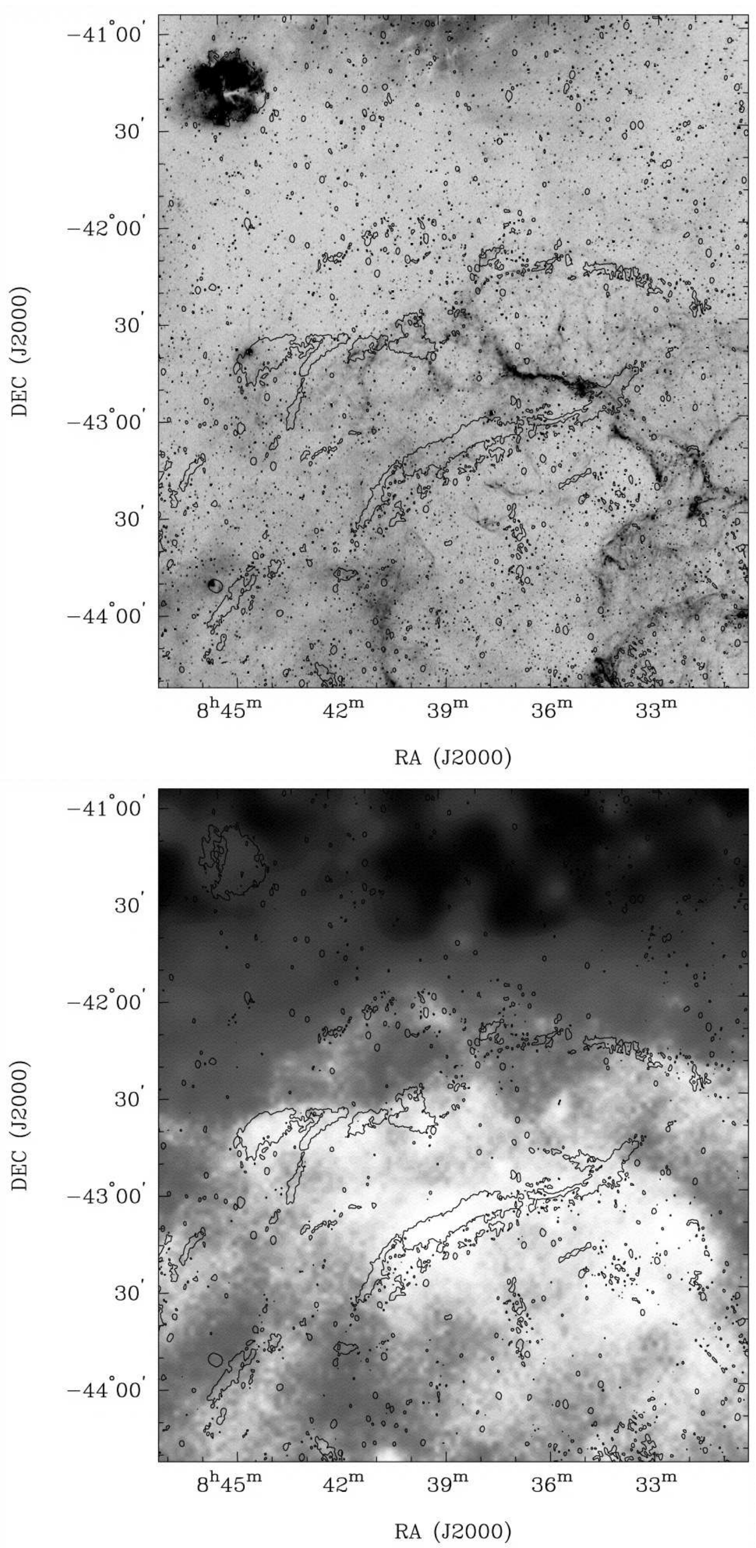

Figure 1.13: 843 MHz radio contour level (at 4 mJy beam-1) on Hα (*upper panel*) and X-ray (*lower panel*) images. The Hα image is from the MSSSO Hα Survey, while the X-ray image has been obtained in the $0.1 - 2.4$ keV band with the *ROSAT* satellite. From Bock et al. (1998).

associated with the shocked plasma of the cloud behind the transmitted shock front and with the intercloud medium, respectively (Bocchino et al. 1999). However, the evaporation scenario is also consistent with the data. The emission in FilE seems instead associated with a recent encounter of the shock with a cavity wall. The instrumental characteristics of the *ROSAT* PSPC detector did not allow the authors to describe the shock-cloud interaction univocally or to get detailed information about the morphology of the emitting plasma and about its chemical abundances. Although important information and indications have been obtained, it was then not possible to discriminate unambiguously between the three different mechanisms of X-ray and optical emission described in Sect. 1.4.3.

1.6.3 Aims of the thesis

In the framework of the study of relatively young, ejecta-dominated SNRs, I present the analysis of an *XMM-Newton* EPIC observation of W49B. My aim is to exploit the high sensitivity of *XMM-Newton* to obtain deep insights into the spatial distribution of the elements and into the physical conditions in the remnant. In particular it is important to test the hypothesis of radial stratification in the abundances of the ejecta made by Fujimoto et al. (1995). Another crucial aspect is to understand the physical origin of the remnant, thus discriminating between a jet-like hypernova explosion (related to a GRB) and a spherical (or aspherical) SN explosion. I also aim at obtaining information on the interaction of the supernova remnant with the ambient interstellar clouds and with the circumstellar material. The results are presented in Chapter 2 (see also Miceli et al. 2006a).

To study the interaction of the shock front with the ISM inhomogeneities, that determine the bulk of the emission in middle-aged SNRs, I also focus on the Vela SNR. In particular, In Chapter 3, I present the analysis of an *XMM-Newton* EPIC observation of the FilD region (see also Miceli et al. 2005a,b). The aim of this work is to study the shock-cloud interaction process in this region of the Vela shell and to discriminate among the different scenarios described in Sect. 1.4.3. Important issues are to obtain a detailed description of the ISM clouds and of their morphology and internal structure and to study the physical and chemical properties of the shocked plasma.

As shown in Sect. 1.4.1, to obtain detailed information on the physical scenario, it is necessary an accurate modeling of the shock-cloud interaction. To this end, I have pursued an accurate "forward" modeling of the interaction of the Vela SNR shock with an isolated ISM cloud. In Chapter 4 I present a detailed hydrodynamic model of the shock-cloud interaction in the Vela FilD region (see also Miceli et al. 2006b). My approach consists in synthesizing observable quantities from the model (for example, maps of X-ray surface brightness and spectra), comparing them directly with the *XMM-Newton* EPIC data and with optical observations of the FilD region. I also perform on the synthesized products the same analysis I carried on for the EPIC data. The aims of this work are: i) the proper interpretation of the X-ray observation (i. e. to understand the physical origin of the different spectral components, to ascertain the evolutionary stage of the interaction, to obtain information about the density and temperature profiles of the emitting plasma); ii) to address the role of the different physical processes (transmitted and reflected shocks, thermal conduction, radiative cooling) in the evolution of the system and to understand how these processes influence the X-ray and optical emission; iii) to obtain a key for the interpretation of other X-ray observations of middle-aged SNRs.

In Chapter 5 I show the results of the preliminary analysis of two new *XMM-Newton* observation of the FilE and RegNE regions in the northern rim of the Vela shell. RegNE is near to the main shock, which lies at only $25'$. Here is the region in which we expect the occurrence of non-equilibrium of ionization. The FilE observation is complementary with respect to the other two, in the sense that it allows us to address a different physical scenario, that is the interaction of the shock with a dense cavity wall.

Chapter 2

The supernova remnant W49B

In this chapter I report on the analysis of an *XMM-Newton* observation of the bright galactic SNR W49B (see also Miceli et al. 2006a), which has been introduced in Sect. 1.6.1. Most of this work has been performed at the DSM/DAPNIA/ Service d'Astrophysique of the Commissariat à l'Energie Atomique (CEA) in Saclay (France), where I spent six months in the framework of a scientific collaboration with Dr. Anne Decourchelle and Dr. Jean Ballet.

The chapter is organized as follows: Sect. 2.1 presents the EPIC data and describes the data processing procedure, Sect. 2.2 presents the X-ray results in terms of the global spectrum (2.2.1), imaging (2.2.2), and spatially resolved spectral analysis (2.2.3). Section 2.3 discusses the results in the context of observations at other wavelengths and SN models and provides possible scenarios for the physical origin of the remnant.

2.1 The Data

The *XMM-Newton* data presented here consist of two observations: Observation ID 0084100401 and 0084100501 (PI A. Decourchelle) performed on 3 April 2004 and 5 April 2004 with the EPIC MOS (Turner et al. 2001) and EPIC pn (Strüder et al. 2001) cameras. EPIC cameras are CCD detectors with spectral resolution $E/\Delta E \sim 20-50$ in the $0.1-10$ keV band. The field of view (FOV) has a diameter of $\sim 30'$, and the pixel size is $1.1''$ (MOS) and $4.1''$ (pn), while the mirror PSF width is $6'' - 15''$ FWHM–HEW. The *XMM-Newton* mirror assembly is subject to vignetting, so there is a decrease in effective area with increasing in off-axis angle. A description of the *XMM-Newton* telescope and of the instrumental characteristics of the EPIC cameras is provided in Appendix A.

Both observations have the pointing coordinates α (2000) $= 19^h11^m13^s$ and δ (2000) $= 9°7'1''$. The relevant information about the data are summarized in Table 2.1. A third data set (0084100601, with the same pointing coordinates) is heavily contaminated by proton flares, so it was not used for the analysis.

Table 2.1: Relevant information about the data.

OBS_ID	CAMERA	t_{exp} (ks)*	Mode	Filter
0084100401	MOS1	18.6/15.8	Large Window	medium
0084100401	MOS2	18.7/16.0	Large Window	medium
0084100401	pn	17.0/12.9	Full Frame	medium
0084100501	MOS1	18.7/16.8	Large Window	medium
0084100501	MOS2	18.7/16.3	Large Window	medium
0084100501	pn	17.0/14.6	Full Frame	medium

* Unscreened/Screened exposure time.

The data were processed using the Science Analysis System (SAS V6.1.0). To create light curves, images, and spectra, were selected events with PATTERN[1]$\leq$ 12 for the MOS cameras, PATTERN$\leq$ 4 for the pn camera, and FLAG$=0$ for both. To eliminate the contamination by soft proton flares, I screened the data by applying a count-rate limit on the light curves at high energies ($10-12$ keV for MOS and $12-14$ keV for the pn camera). With a $\delta t = 100$ s binning for the light curves, I set the count-rate limit at 18 counts per bin for the MOS cameras, and 22 counts per bin for the pn camera. The exposure times are given in Table 2.1. For each camera I merged the screened event files of the two observations using the task $MERGE$.

All the images presented here are superpositions of the MOS1, MOS2, and pn images (obtained using the $EMOSAIC$ task) and are background-subtracted, vignetting-corrected, and adaptively smoothed. Despite being relatively small in extent compared to the *XMM-Newton* field of view, W49B has a high X-ray brightness that contaminates the local background. For this reason, I used the high signal-to-noise background event files E1_fm0000_M1.fits, E1_00fm00_M2.fits, E1_0000fm_PN.fits (obtained using the medium filter) described in detail in Read & Ponman (2003). The exposure and vignetting corrections were performed by dividing the superposed count images by the corresponding superposed exposure maps (produced using the task $EEXPMAP$). The pn exposure maps were scaled by the ratio of the pn/MOS effective areas to make MOS-equivalent superposed count rate images. I smoothed the images adaptively to a signal-to-noise ratio of 10 using the task $ASMOOTH$. The background-subtracted count images and the background- and continuum-subtracted line images (Sect. 2.2.2) were smoothed while accounting for their variances. The resulting template was then applied to

[1]For the definition of PATTERN and FLAG, see Appendix A

smooth the associated exposure maps before performing the image division. The continuum under the lines was estimated by scaling a continuum band adjacent to the line emission using the continuum spectral slope derived from the global remnant spectrum. The energy ranges chosen for the lines and the continua are listed in Table 2.2. In all the line bands, the background is $\lesssim 0.5\%$ of the total signal, except for the $7.65 - 8.0$ keV band where it is $\sim 3.6\%$ of the total signal. In the continuum band $4.4 - 6.2$ keV, the background amounts to $\sim 1.3\%$. In all the images North is up and East is to the left.

For spectral analysis, I processed the event files with the *EVIGWEIGHT* task (Arnaud et al. 2001) to correct for vignetting effects. For the background subtraction, I used the same background event files used for the images. Once extracted the source spectrum form a specific region in the FOV, I extracted the corresponding background spectrum from the same region (in the detector coordinates) of the background event file. The background-subtracted spectra were rebinned to achieve a signal-to-noise ratio per bin $> 5\sigma$, and the spectral fits were performed simultaneously on the MOS1, MOS2, and pn spectra in the $1-9$ keV band using XSPEC (Arnaud 1996). The chosen on-axis response files are m1,2_medv9q20t5r6_all_15.rsp for MOS1,2 spectra and epn_ff20_sdY9_medium.rsp for pn spectra. All the reported errors are at 90% confidence, as calculated according to Lampton et al. (1976).

2.2 X-ray emission

The broadband ($1 - 9$ keV) X-ray morphology of W49B obtained with the EPIC cameras is shown in Fig. 2.1 (left panel). For comparison, the VLA radio image obtained at 327 MHz by Lacey et al. (2001) is also presented in Fig. 2.1 (right panel). The X-ray surface brightness of W49B has its maximum at the center of the remnant, and shows an elongated jet-like structure extending for $\sim$ 5 pc along its East-West axis (labelled b, see Fig. 2.1) .

At the eastern end of the remnant, there is a bright, sharp X-ray structure (labelled a, see Fig. 2.1), running perpendicular to the X-ray jet-like region and parallel to the radio shell (labelled α, see Fig. 2.1). I remind the reader that the eastern side of W49B is bounded by a large molecular cloud, detected in the 2.12 μm molecular-hydrogen narrow-band image (Fig. 1.10). The X-ray structure b lies between two radio structures (β and γ) that are parallel to the radio shell (α) and to the H_2 emission. The positions of these structures (β and γ) are almost coincident with two coaxial ring-like structures observed in the 1.64 μm [Fe II] image of W49B (Fig. 1.10). The X-ray structures a (east) and c (west) lie outside these radio structures. No intense X-ray emission has been detected in the south western region of the shell, where copious radio and [Fe II] emission

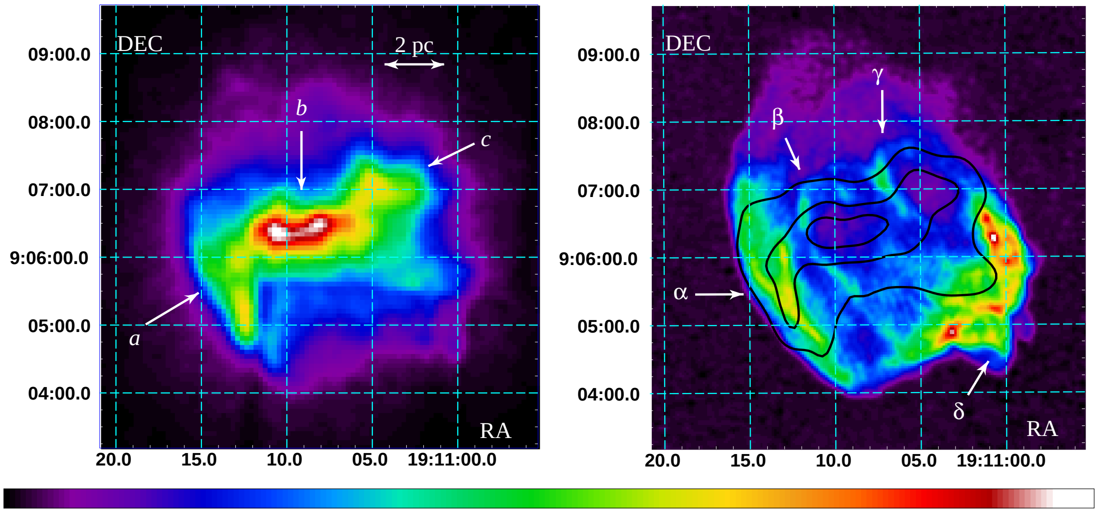

Figure 2.1: *Left panel:* Vignetting-corrected EPIC count-rate image of W49B in the $1-9$ keV band. The image is adaptively smoothed (with signal-to-noise ratio 10) and background-subtracted. The 2 pc scale has been obtained assuming a distance of 8 kpc. The count-rate per pixel ranges between 0 and 7.2×10^{-3} s^{-1} bin^{-1} (bin size= 4″). *Right panel:* Radio image of W49B at 327 MHz (angular resolution 6″) obtained by Lacey et al. (2001). I have superimposed in black the X-ray contour levels derived from the $1-9$ keV EPIC image at 25%, 50%, and 75% of the maximum. The color bar has a linear scale.

are observed (δ, see Fig. 2.1). According to Lacey et al. (2001), there is evidence of stronger interstellar absorption in this direction. It is reasonable to conclude, however, that no hard X-ray emission is present in this region.

2.2.1 Global spectrum

The impressive EPIC spectrum of W49B integrated over the whole SNR in the $1-9$ keV energy band is shown in Fig. 2.2. The spectrum is dominated by intense emission lines of He-like and H-like ions of Si, S, Ar and Ca and by a huge Fe K emission line blend. The Fe K line complex in W49B has the largest equivalent width ever observed in a supernova remnant. A phenomenological modeling of the global spectrum (2 bremsstrahlung for the continuum + narrow Gaussians for the lines) allows us to derive the line energies reported in Fig. 2.2. The emission feature observed at $\sim$ 7.8 keV corresponds to a possible blending of Fe XXV and Ni XXVII K emission lines and is discussed in Sect. 2.2.4. The continuum above 2.3 keV is described well by a thermal bremsstrahlung model with $kT = 1.69$ keV and $N_H = 5.3 \times\ 10^{22}$ cm^{-2}; this model has been used to estimate the continuum under the lines given in Table 2.2. Unlike the *ASCA* spectrum (Hwang et al. 2000), the *XMM-Newton* global spectrum cannot be accurately fit by a two-component thermal model (reduced $\chi^2 \sim 2.4$). This indicates that the emission originates from physically inhomogeneous regions. Spatially resolved spectral analysis of homogeneous regions is required to correctly reproduce the spectra with 2-component models, as discussed in Sect. 2.2.3.

In the analysis of the *ASCA* global spectrum of W49B, Hwang et al. (2000) found evidence of the presence of two new emission line features (at ~ 5.7 keV and ~ 6.2 keV) that are not included in the currently available atomic database for X-ray spectral modeling. These were attributed to the He-like Cr transitions (forbidden line at 5.655 keV; resonance line at 5.682 keV) and the He-like Mn transitions (forbidden line at 6.151 keV; resonance line at 6.181 keV). The *XMM-Newton* data confirm this detection: modeling the global spectrum of the remnant in the $4.4-6.4$ keV band with a thermal bremsstrahlung continuum, I find a clear excess in the residuals corresponding to these transitions. These lines can be reproduced by adding two Gaussian components to the bremsstrahlung model to determine the line energy and flux. I find, respectively for Cr and Mn, line centroid energy $E_{Cr} = 5.66 \pm 0.01$ keV and flux $F_{Cr} = 2.5 \pm 0.4 \times 10^{-5}$ photons cm^{-2} s^{-1}, $E_{Mn} = 6.19^{+0.01}_{-0.04}$ keV and $F_{Mn} = 1.0 \pm 0.3 \times 10^{-5}$ photons cm^{-2} s^{-1}, in good agreement with the values reported by Hwang et al. (2000) ($E_{Cr} = 5.69^{+0.02}_{-0.03}$ keV and $F_{Cr} = 3.0^{+0.8}_{-1.1} \times 10^{-5}$ photons cm^{-2} s^{-1}; $E_{Mn} = 6.17 \pm 0.05$ keV and $F_{Mn} = 1.3^{+1.4}_{-0.6} \times 10^{-5}$ photons cm^{-2} s^{-1}). The addition of the Cr Gaussian leads to a reduction of χ^2, $\delta\chi^2 = 111$ for 616 d.o.f.; adding the Mn Gaussian gives an additional $\delta'\chi^2 = 28$ (to be compared with the values obtained with the *ASCA* spectrum: $\delta\chi^2 = 20$ for 61 d.o.f. and $\delta'\chi^2 = 10$). I find no indication of the presence of the Ti Heα line (at 4.97 keV), obtaining an upper limit for the flux $F_{Ti} < 3.6 \times 10^{-6}$ photons cm^{-2} s^{-1}, which is more stringent than the one reported from ASCA ($F_{Ti} < 2 \times 10^{-5}$ photons cm^{-2} s^{-1}, Hwang et al. 2000). The flux of the Cr and Mn lines contributes $\sim 3\%$ of the total flux in the $4.4 - 6.4$ band.

2.2.2 Imaging

The spatially resolved spectral study of the emission in the different lines provides information about the spatial distribution of the synthesized elements and the chemical composition of the X-ray emitting plasma. As explained in Sect. 1.6.1, Fujimoto et al. (1995) argued (on the basis of low angular resolution *ASCA* images) that the sulfur emission, unlike the iron emission, was associated with the outer envelope of the remnant and not related to the bright $4-6$ keV continuum emission from the center.

To investigate both this claim and the suggested radial stratification of the elements, I produce background- and continuum-subtracted line images of S, Ar, Ca, Fe, and Ni lines (see Fig. 2.3 and Table 2.2). The Si emission line images shown in Fig. 2.6 are discussed in Sect. 2.2.3. The S H-like line image is very similar to the S He-like line image and therefore is not shown in the figure. All

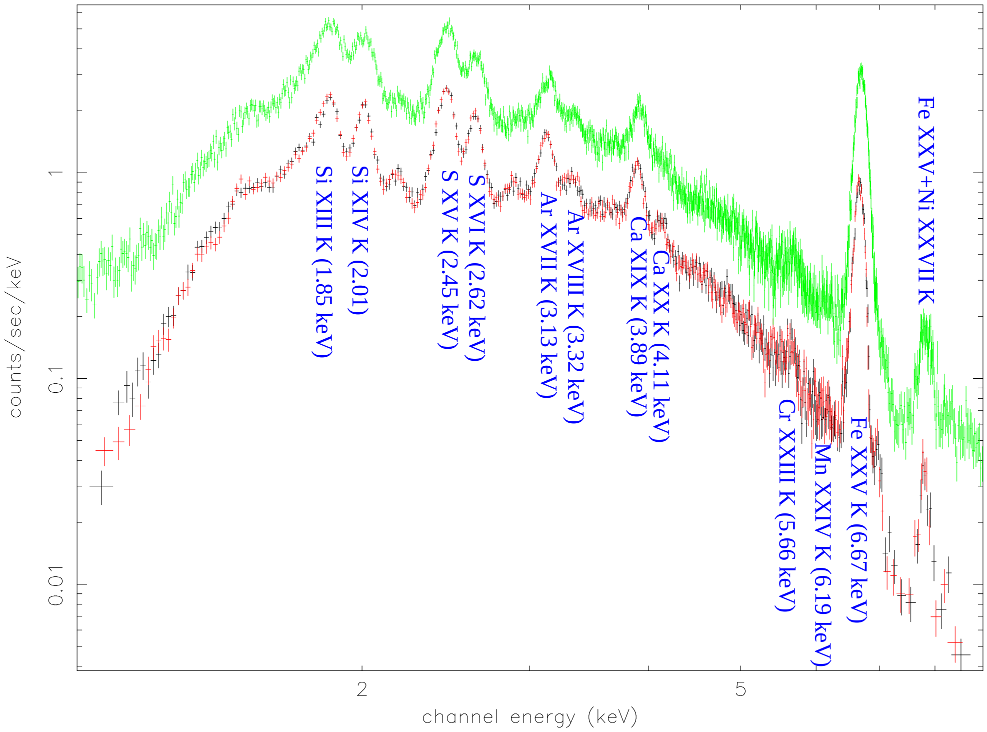

Figure 2.2: pn (upper) and MOS (lower) global spectra of W49B in the $1-9$ keV energy band, extracted from a circular region covering the entire remnant (of radius $3.3'$ corresponding to ~ 7.7 pc). Line energies have been determined using narrow Gaussian components on top of a thermal bremsstrahlung continuum. Note that to reproduce the continuum at energies below the Si K lines, an additional bremsstrahlung component is required.

the line images present a bright centrally elongated morphology similar to the $4.4-6.2$ keV continuum emission, as shown in Fig. 2.3. Overall, there are no significant differences between the morphologies in the Si, S, Ar, Ca, and Fe lines[2] (although some detailed structures may differ as I discuss later). This result does not agree with the line-imaging results obtained for the lower-Z elements with *ASCA* data (see Fig. 1.9).

A detailed analysis of the Fe K line image in Fig. 2.3 (lower left panel) shows that the iron emission differs from that of lower-Z elements in the western part of the remnant. In particular, regions 6 and 7 do not have significant Fe line emission, while they do have significant emission from Si, S, Ar, and Ca. The lower statistics Fe XXV+Ni XXVII image of Fig. 2.3 (lower right panel) presents a morphology that is fully consistent with the Fe K image.

[2]All the images in Fig. 2.3 are adaptively smoothed to a signal-to-noise ratio 10. Therefore, where the signal is high (as in the case of the Fe K line), the images are convolved with gaussians with low sigmas, while in the case of weak lines (e. g. the Fe XXV+Ni XXVII K blend) the images are convolved with gaussians with large sigmas. This explains why the Fe line image morphology appears to be slightly narrower than the others.

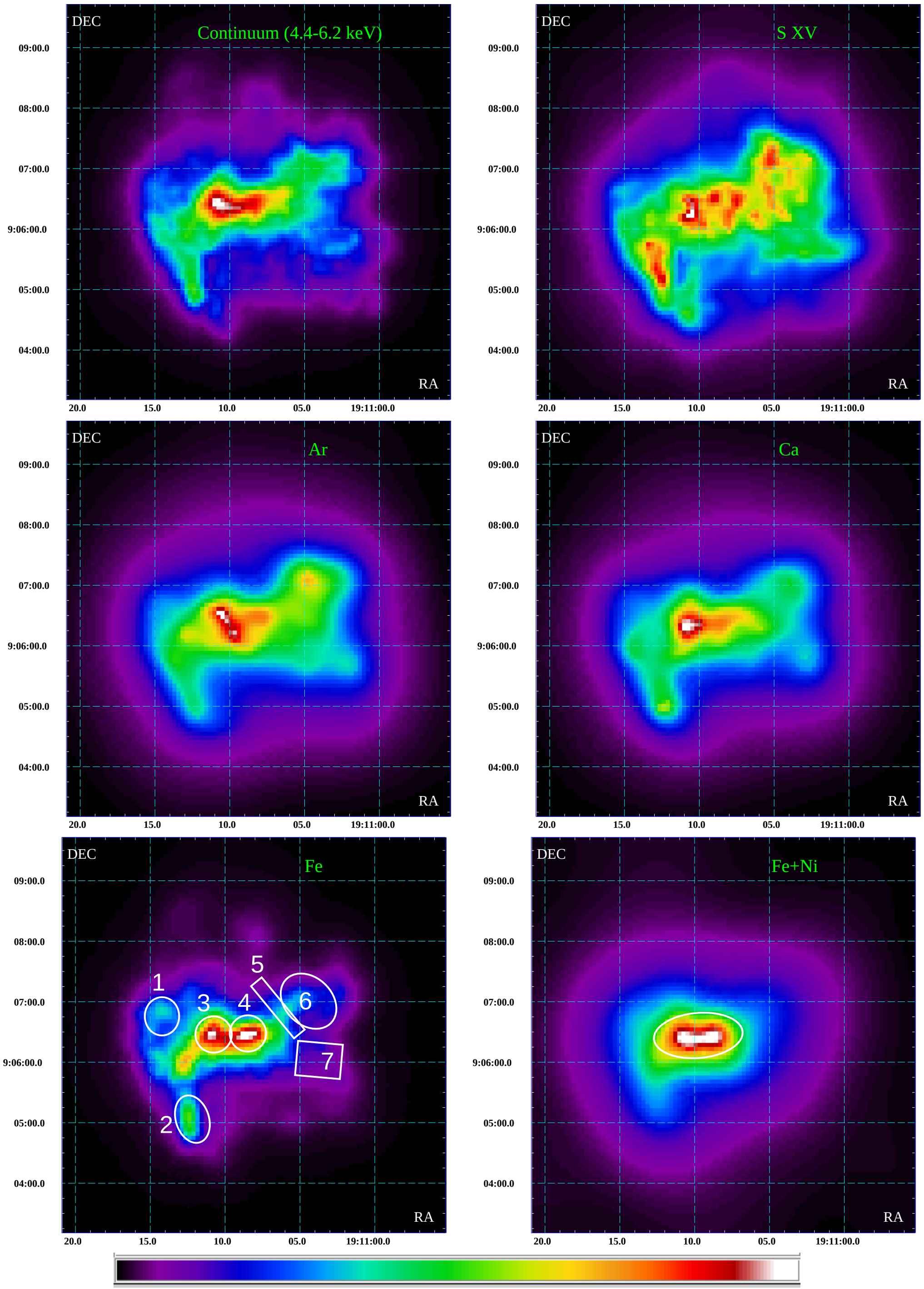

Figure 2.3: Vignetting-corrected and continuum-subtracted EPIC count-rate images of the continuum ($4.4-6.2$ keV, *upper left*), S XV K ($2.35-2.53$ keV, *upper right*), Ar XVII K ($3.05-3.2$ keV, *central left*), Ca XIX K ($3.8-4.0$ keV, *central right*), Fe XXV K ($6.45-6.9$ keV, *lower left*), and Fe XXV+Ni XXVII K ($7.65-8.0$ keV, *lower right*). All images are adaptively smoothed with signal-to-noise ratio 10. The 7 regions selected for spatially resolved spectral analysis are shown in the Fe XXV K line image, while the ellipse in the Fe XXV+Ni XXVII K line image indicates the region used for the detection of the Ni line (Sect. 2.2.4). The count-rates per pixel (bin size= $4''$) range between 0 and: 8.6×10^{-4} s^{-1} bin^{-1} (continuum); 3.4×10^{-4} s^{-1} bin^{-1} (S); 1.7×10^{-4} s^{-1} bin^{-1} (Ar); 1.9×10^{-4} s^{-1} bin^{-1} (Ca); 7.0×10^{-4} s^{-1} bin^{-1} (Fe); 2.1×10^{-5} s^{-1} bin^{-1} (Fe+Ni). The color bar has a linear scale.

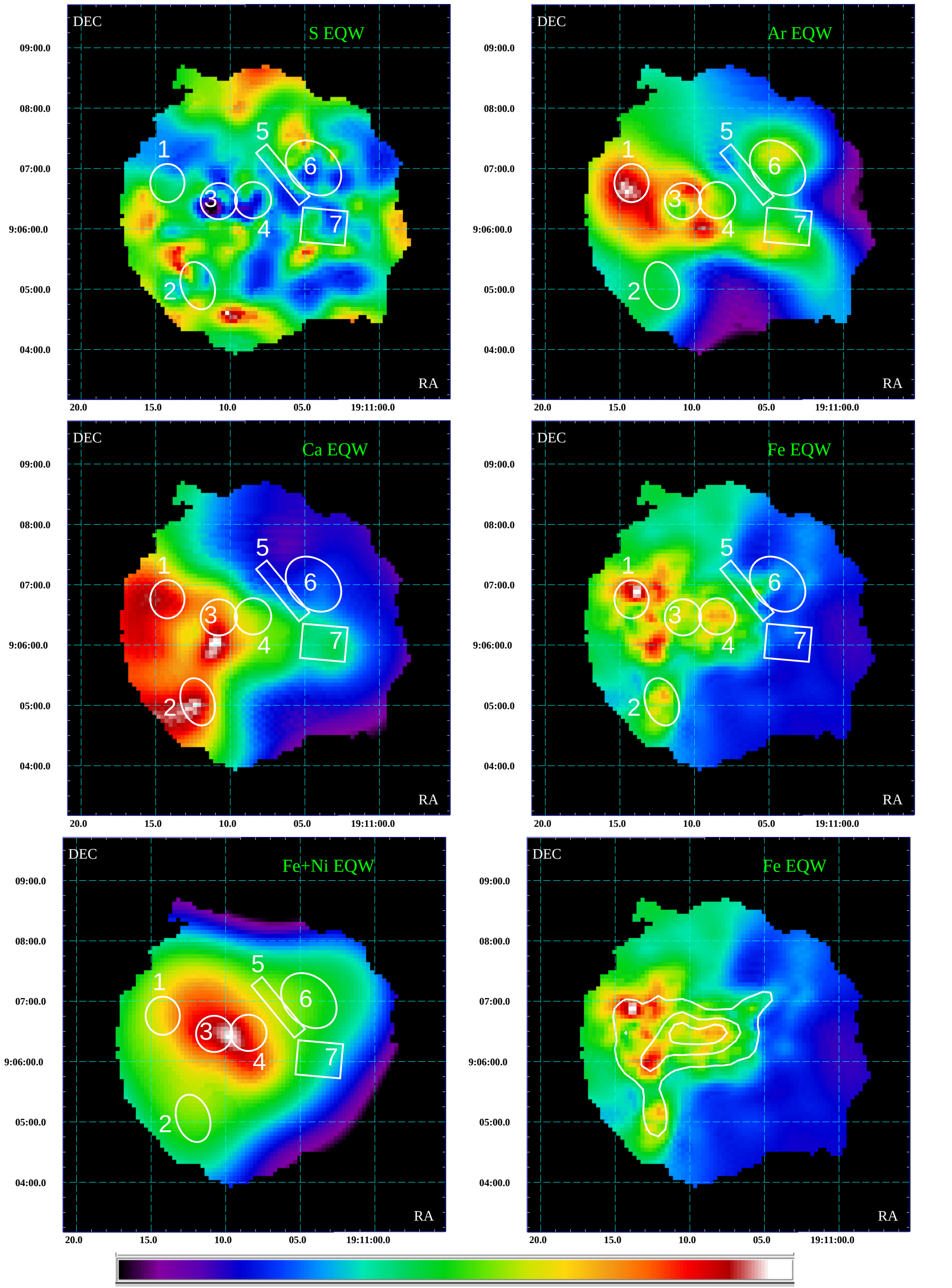

Figure 2.4: Equivalent width maps of the S He-like and H-like line emission in the 2.35 – 2.7 keV band (*upper left*), of the Ar XVII K blend (3.05 – 3.2 keV, *upper right*), of Ca XIX K (2.35 – 2.7 keV, *central left*), of Fe XXV K (6.45 – 6.9 keV, *central right*), and of the Fe XXV+Ni XXVII K emission lines in the 7.65 – 8.0 keV band (*lower left*). In the *lower right* panel I have overlaid the 75%, 50%, and 25% contour levels of the corresponding line image (Fig. 2.3, lower left panel) on the Fe XXV K equivalent width map. The ranges of the equivalent width maps are: 0.245 – 0.6 keV (S), 0.07 – 0.13 keV (Ar), 0.085 – 0.18 keV (Ca), 0 – 12.1 keV (Fe), 0.315 – 1.4 keV (Fe+Ni).

Table 2.2: Parameters used for the production of the line images of Fig. 2.3 and the equivalent width maps of Fig. 2.4.

Emission line	Line energy band (keV)	Cont. energy band (keV)
S XV Kα	$2.35 - 2.53$	$2.75 - 3.0$
S XVI Kα	$2.58 - 2.7$	$2.75 - 3.0$
Ar XVII Kα	$3.05 - 3.2$	$2.75 - 3.0$
Ca XIX Kα	$3.8 - 4.0$	$3.45 - 3.7$
Fe XXV Kα	$6.45 - 6.9$	$4.4 - 6.2$
Fe XXV+Ni XXVII K	$7.65 - 8.0$	$7.05 - 7.5$

To disentangle higher element abundances in the bright line image structures from higher emission measure (which might be caused by either higher density or higher emission volume), I produced equivalent width maps as shown in Fig. 2.4. The equivalent width of a line is defined as the ratio of the continuum-subtracted line flux and of its underlying continuum. Since both these terms depend linearly on the emission measure, this dependence is not present in their ratio. The equivalent width maps therefore depend linearly on the abundances (the higher the equivalent width, the higher is the abundance of the element), but are also affected by the temperature, column density, and ionization age. These images were constructed by dividing the background- and continuum-subtracted line images by the corresponding underlying continuum. Before the division, the estimated continuum map was adaptively smoothed using the same template as used for the background- and continuum-subtracted line images. As explained in Sect. 2.1, the underlying continuum is estimated from continuum regions adjacent to the line emission, under the assumption that the continuum has a uniform spectral slope over the entire SNR. As shown in Fig. 2.4, the S map is clearly different from the other maps, but the equivalent width images of Ar, Ca, Fe, and Fe+Ni all show similar features. In particular, all these maps show higher equivalent widths in the central and eastern parts of the remnant than in the western part, with maxima corresponding approximately to regions 1 and 3. This is particularly true for iron. In the Ar map there is an indication of non-negligible equivalent widths in the western regions 6 and 7.

As the S H-like and He-like line images are very similar, I use the combined $2.35 - 2.7$ keV band to improve the statistics of the sulfur equivalent width map as shown in Fig. 2.4 (upper left panel). The map appears patchy and shows no clear structures. Given the relatively low line energies, the map may be affected by local variations of N_H, as we shall see in Sect. 2.2.3.

In conclusion, the line emission maps of all the observed elements show a centrally elongated bright structure in good agreement with the morphology of the continuum. The equivalent width images indicate that Ar, Ca, and Fe may be more abundant in the central and eastern parts of the remnant than in the West. The high values of the equivalent width are therefore not restricted to the jet-like structure, but extend to the eastern side of the remnant, as illustrated in Fig. 2.4 (lower right panel), where I show the contours of the iron line image superimposed on the iron equivalent width map. A clear drop-off of the equivalent width is observed towards the western side. This effect is particularly strong for iron, and is less pronounced for the lower-Z elements, which show significant equivalent widths in the west. While I thus find an East/West abundance anisotropy, I find no clear evidence of radial stratification of the elements.

The image analysis also allows us to obtain information about the thermal structure of the source. To this end, I produce a MOS median photon energy (MPE) map, that is an image where each pixel holds the median energy of the detected MOS photons in the continuum band $4.4 - 6.2$ keV. This map provides information about the spatial distribution of the spectral properties of the plasma, because the harder the spectrum (i. e. the higher is the continuum temperature), the higher is the local MPE. To produce this map, I consider the MOS1 and MOS2 event files in the continuum energy band $4.4 - 6.2$ keV, with a bin size of $6''$ (so as to collect more than 10 counts per pixel everywhere in the remnant). For each pixel, I calculate the median energy of the photons and then I smooth the map with a gaussian distribution by using the following procedure: for each pixel k of the MPE map we define its weight as $W_k = C_k\ e^{\frac{-(i-k)^2}{\sigma^2}}$, where C_k is the number of photons detected in that pixel, the i index runs over all the other pixels and $\sigma = 12''$. The smoothed median energy value at the i pixel is then $SMPE_i = \Sigma_k\ (W_k\ MPE_k)/\Sigma_k\ (MPE_k)$. The W49B MPE map is shown in Fig. 2.5 and suggests a higher continuum median photon energy in the eastern side of the remnant than in its western end.

2.2.3 Spatially resolved spectral analysis

To quantify the equivalent width map results for the element distributions, I perform a spatially resolved spectral analysis so as to study in detail the physical and chemical characteristics of the plasma in different parts of the remnant. In particular, I analyze the spectra extracted from the seven fairly homogeneous regions shown in Fig. 2.3 (lower left panel) and in Fig. 2.4. While this set of regions does not cover the entire remnant, it does allow us to study the spatial variations of the spectral properties in the X-ray emitting plasma. In order to analyze spectra extracted from physically uniform regions, the shape and size of the seven regions were chosen in order to have a sufficient number of photons and very small fluctuations of the median photon energy ($\sim 1\%$) in each region.

Regions 1 and 2 are located on the X-ray eastern, elongated structure along

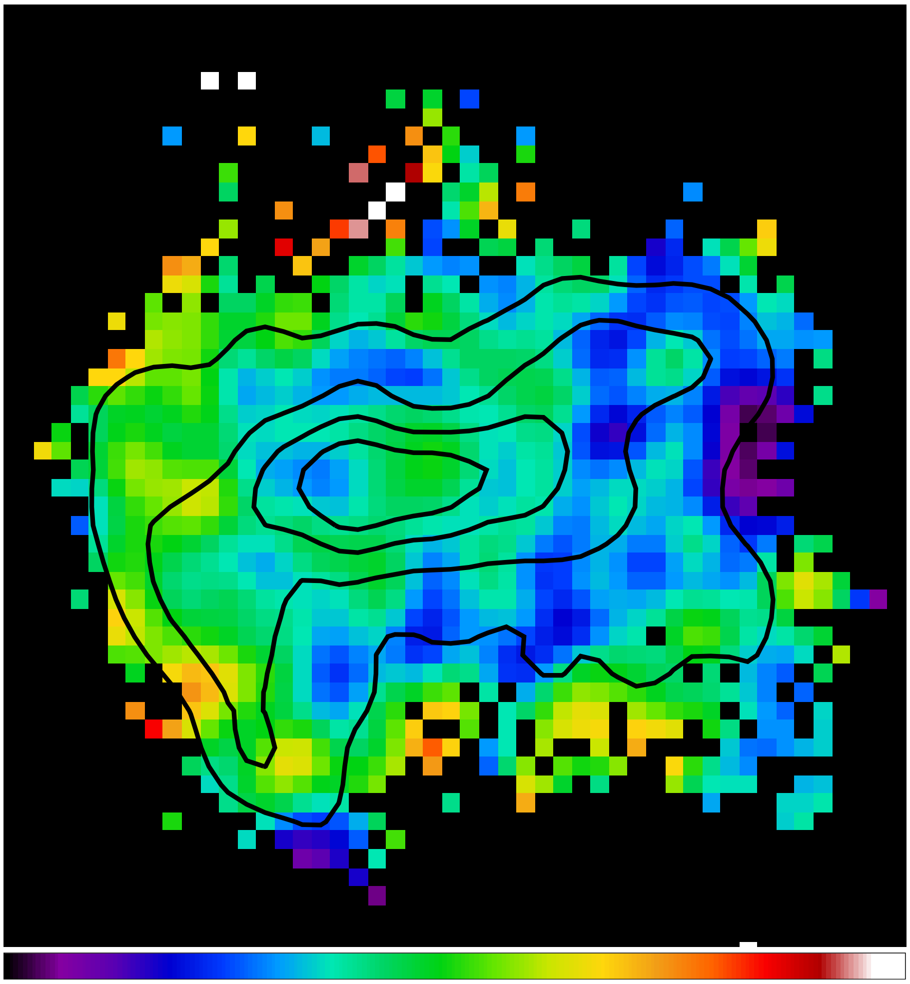

Figure 2.5: MOS median photon energy map of the continuum emission (bin size= 6″). In each pixel the local median photon energy of the photons detected by the MOS cameras in the continuum energy band 4.4 − 6.2 keV is reported. I superimposed, in black, 4 contour levels indicating where the median is computed over more than 10, 20, 30, and 40 counts (from the outer to the inner level, respectively). The pixels where the median is computed with less than 4 photons have been masked out. The color bar has a linear scale and ranges between 4.85 keV and 5.25 keV.

the radio shell (labelled a/α in Fig. 2.1), at its northern and southern ends, respectively. They both exhibit high values in the equivalent width maps. Regions 3 and 4 cover the brightest part of the centrally elongated X-ray structure: region 3 corresponds to the maximum of the continuum emission in the 4.4 − 6.2 keV band (Fig. 2.3, upper left panel), and region 4 corresponds to the highest Fe K line emission region (Fig. 2.3, lower left panel). Region 5 follows the western radio structure γ (Fig. 2.1). Region 6 covers the western X-ray structure c and, finally, region 7 lies on the faint south western structure that is seen in the continuum and K line emission of S, Ar, Ca, but not of iron.

Spectral modeling and results

I first model the extracted spectra using XSPEC with a single MEKAL model of an optically-thin thermal plasma in collisional ionization equilibrium (Mewe et al. 1985, Mewe et al. 1986, Liedahl et al. 1995). Good fits to the spectra require non-solar abundances for Si, S, Ar, Ca, and Fe. All other element abundances were fixed at their solar values. To account for the contribution from the Cr line (Sect. 2.2.1), I add a narrow Gaussian component with fixed energy; it was not necessary to account for the Mn line. I also add a systematic 5% error term to reflect the estimated 5-10% uncertainties in the calibration of the instrumental effective area. The reduced χ^2 values obtained using the two MOS and the pn cameras range from 1.3 (with 354 d.o.f.), for region 5, to 1.7 (445 d.o.f.) for region 2. Above 2 keV, the models describe the continuum and emission line spectra quite well, but these single-temperature models severely underpredict the Si XIII Kα line (at $\sim$ 1.85 keV), as illustrated in Fig. 2.7 (left panel). The best-fit parameters for these fits are thus not reported here. The same problem was encountered by Hwang et al. (2000) in the modeling of the *ASCA* global spectrum and, more recently, by Keohane et al. (2006) in the modeling of the *Chandra* spectra of several region of W49B. I find that the quality of the fits does not significantly improve if a single non-equilibrium of ionization (NEI) model is used instead and this conclusion has been subsequently confirmed also by the analysis of the *Chandra* spectra performed by Keohane et al. (2006).

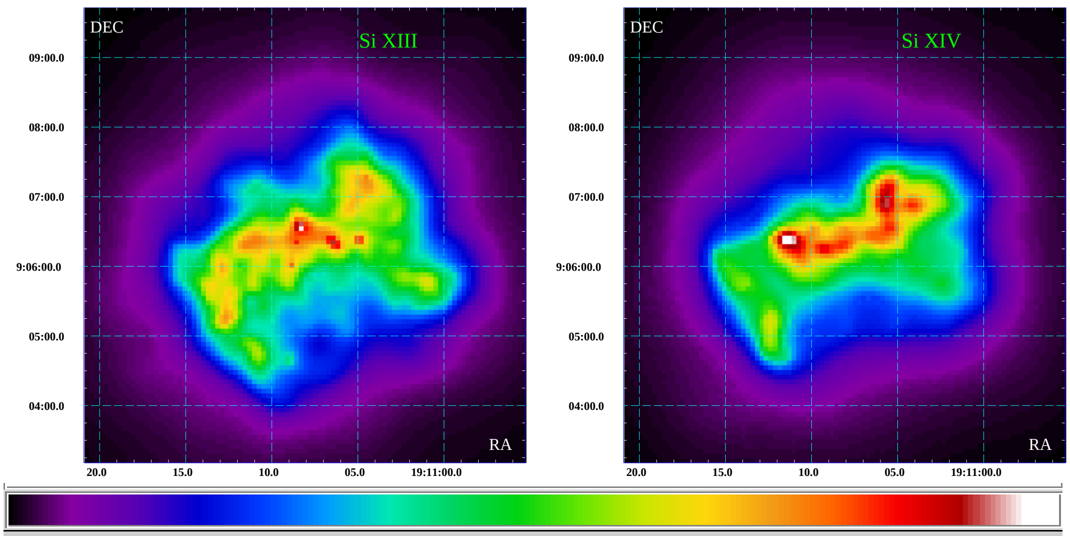

Figure 2.6: Vignetting-corrected and continuum-subtracted EPIC count-rate image of the Si XIII Kα ($1.77-1.9$ keV, *left panel*) and Si XIV Kα ($1.96-2.06$ keV, *right panel*). The images are adaptively smoothed with signal-to-noise ratio 10. The count-rates per pixel (pixel size= $4''$) range between 0 and 2.3×10^{-4} s^{-1} bin^{-1} for Si XIII and 1.7×10^{-4} s^{-1} bin^{-1} for Si XIV. The color bar has a linear scale.

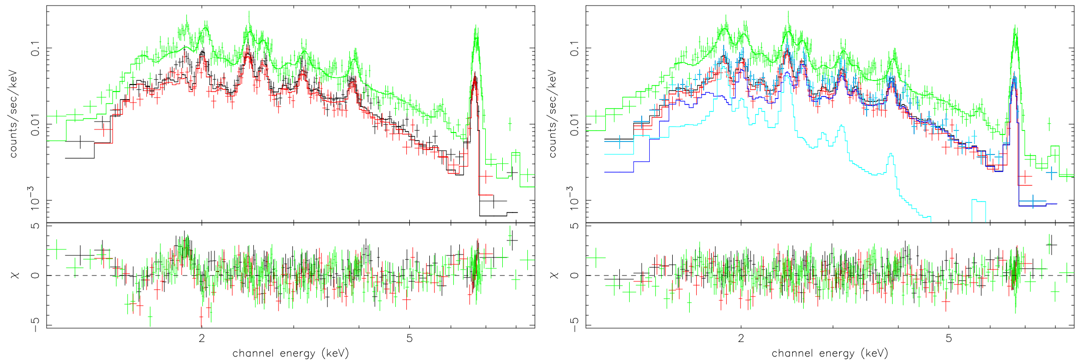

Figure 2.7: pn (upper) and MOS (lower) spectra of region 2 with the corresponding best-fit model and residuals obtained with one thermal component (left panel) and with two thermal components (right panel). The contribution of the two components for the MOS camera is indicated in the right panel in cyan for the cooler component and blue for the hotter component.

I obtain a good description of the spectra by adding a second thermal MEKAL component in CIE. I require the two components to have the same abundances and to be absorbed by the same interstellar column density. The spectra are also well-described if the soft component has solar abundances and is in non-equilibrium of ionization (PSHOCK model). In this case the temperatures of the two components (NEI+CIE) are comparable to those obtained for the two CIE components, but the fits give somewhat higher chi-squared values. For example, in region 2: $\chi^2_{NEI+CIE} = 529.7$ (with 442 d.o.f.) and $\chi^2_{2CIE} = 506.7$ (443); in region 4: $\chi^2_{NEI+CIE} = 821.2$ (673) and $\chi^2_{2CIE} = 793.5$ (674); in region 6: $\chi^2_{NEI+CIE} = 1064.1$ (843) and $\chi^2_{2CIE} = 1059.3$ (844). I therefore adopt the two CIE component model hereafter, while cautioning the reader that the high interstellar absorption complicates the description of the soft component and hence the discrimination between these two models.

Figure 2.7 shows a representative spectrum, extracted from region 2, with the best-fit model and residuals for two thermal components (right panel) and, for comparison, a single thermal component (left panel). The best-fit parameters for all seven spectral regions are given in Table 2.3.

The values of $N_{\rm H}$ in the different spectral regions range approximately from 4.2×10^{22} cm^{-2} to 4.9×10^{22} cm^{-2} (compared with the global $N_{\rm H} = 5.0^{+0.3}_{-0.2} \times 10^{22}$ cm^{-2} estimated by Hwang et al. 2000). To produce the line and the equivalent width images (see Sect. 2.2.2), I estimate the continuum contribution under the lines by assuming a uniform absorbed slope of the continuum based on the global spectrum of W49B. For low energy lines, spatial variation of the column density over the remnant can thus introduce errors in the line and equivalent width images. In particular, where $N_{\rm H}$ is higher than its global averaged value, we may overestimate the continuum under the line and hence underestimate the equivalent width. We observe this kind of effect in the S equivalent width image (Fig. 2.4, upper left panel), where there is a minimum in region 3 with a mean value of 0.32 keV, corresponding to the highest value of the column ($N_{\rm H} = 4.8^{+0.1}_{-0.2} \times 10^{22}$ cm^{-2}), and a higher mean equivalent width of 0.4 keV in region 2, which has a lower column ($N_{\rm H} = 4.22^{+0.08}_{-0.05} \times 10^{22}$ cm^{-2}).

Variations in column density may also affect the Si images, but in this case there is no clear relationship between such variations and inhomogeneities in the equivalent width map. This probably indicates that other effects are also present. As explained above, a single temperature model provides a good overall description of the spectra in the $1-9$ keV band, but fails to reproduce the observed Si line flux in the narrow energy range $1.7-1.9$ keV. It is therefore possible that the Si He-like emission originates predominantly in a plasma with different physical conditions than the one responsible for the other emission lines. As shown in Fig. 2.6, the He-like line morphology resembles that of the Si H-like emission, as well as the S, Ar, and Ca line emission. The Si equivalent width maps (not presented here) have irregular patchy features at odds both with those seen for the other elements and with the spatially resolved spectral analysis. This is probably because the continuum of the hard component is not negligible at low energies, even though the Si He-like line emission itself is associated with the soft thermal component (see the right panel of Fig. 2.7).

I find larger variations for the temperature of the hotter component kT_2 (1.75$-$3.3 keV) than for the cooler component kT_1 ($0.7-1.05$ keV), but there is no radial temperature structure (see Table 2.3). The temperature of the hotter component is at a maximum in region 1 at kT_2, and decreases significantly moving southward along the X-ray elongated a structure to region 2. This temperature also decreases towards the western side of the remnant (from region 3 to region 6), in agreement with the trend highlighted by the median photon energy map of the continuum shown in Fig. 2.5. The difference between the continuum surface brightness of region 3 (i. e. the brightest region in the continuum band $4.4-6.2$ keV) and region 4 is caused by the higher temperature in region 3, and not by differences in the emission measure.

In Table 2.3, the parameter EM indicates the values of the emission measure per unit area, which is the product of the square of the particle density times the extension of the plasma along the line of sight. These values are in the range $0.3-1.7\times\ 10^{20}$ cm^{-5} for the cooler component, and $0.4-3.5\times\ 10^{20}$ cm^{-5} for the hotter component. In region 6 we have the highest values for both EM_1 and EM_2. Associated with the decreasing trend of T_2, we note that the corresponding emission measure EM_2 is slightly higher in region 6 than in regions 3 and 4.

I use the best-fit values of temperature and emission measure to derive the plasma density (indicated with n in Table 2.3) and the volume filling factor (f) of each component, obtained as in Bocchino et al. (1999). These quantities were derived by assuming pressure equilibrium between the two components and assuming that in each spectral region the extension of the X-ray emitting plasma is equal to the length of the chord intercepted by the radio shell (approximated as a sphere with angular radius $\phi = 2.15'$) along the line of sight. The filling factor of the cool component is $\lesssim 0.1$, and the densities of the two components are almost uniform across the remnant.

I find significant element overabundances in all the spectral regions: all the elements have fitted abundances > 1.5 (at 90% confidence level) with respect to their solar value. This attests to the origin of the emission in the ejecta. Moreover, higher abundance values are found for the central and eastern regions compared to the western regions, in good agreement with the results of our image analysis. All abundances are lower in regions 5, 6, and 7, with the largest decrease observed for the Fe abundance, as expected. For example, the ratio $(Ar/Ar_\odot)/(Fe/Fe_\odot)$ is 0.7 ± 0.1 in region 4 and 1.8 ± 0.3 in region 6, while the ratio $(Ca/Ca_\odot)/(Fe/Fe_\odot)$ is 1.2 ± 0.2 in region 4 and $1.8^{+0.3}_{-0.2}$ in region 6. This agrees with the considerations discussed at the end of Sect. 2.2.2, where regions 6 and 7 show low equivalent widths for iron, but non-negligible line emission and line equivalent widths for the lower-Z elements. All the abundances reported in Table 2.3 are given as the ratio of the number density of the respective element to the number density of hydrogen expressed in units of the solar value of this ratio. In a pure-ejecta plasma (where hydrogen emission is negligible), this ratio would be ill-defined, and the spectral shape would only depend on the relative abundances of the heavy elements. I verified that this is not the case for our fits. In fact, if we scale all the abundances by the same factor f, we obtain significantly higher χ^2 values for $f \gtrsim 1.5$. Therefore the abundances in Table 2.3 are well-defined and above solar. In Sect. 2.3 these abundances will be compared with the predictions of the supernova nucleosynthesis models introduced in Sect. 1.1

In each spectral region I also obtain another χ^2 minimum with $kT_1 \sim 0.2$ keV. This value agrees with the results obtained with the *ASCA* data by Hwang et al. (2000) and Kawasaki et al. (2005). In this case, however, I find very high values for the emission measure per unit area of the cool component ($EM_1 \gtrsim 10^{22}$ cm^{-5}), which would imply unrealistically high values for the filling factor ($f_1 \sim 0.5$) and the density ($n_1 \sim 50$ cm^{-3}). In what follows, I therefore only discuss the results presented in Table 2.3.

2.2.4 Evidence of Ni overabundance

Thanks to the high *XMM-Newton* effective area at high energies, it is possible to detect a strong emission feature at ~ 7.8 keV, with possible contributions from both Fe XXV and Ni XXVII. The Ni XXVII emission line has been previously detected in only one SNR, Cas A (Bleeker et al. 2001, Willingale et al. 2002). This emission blend can be used to set constraints on the Ni abundance in W49B. Since

Table 2.3: Best-fit parameters for the spectra extracted in the seven regions shown in Fig. 2.3 (lower left panel), described with two thermal components in collisional ionization equilibrium. All errors are at the 90% confidence level.

Parameter	Region 1	Region2	Region 3	Region 4	Region 5	Region 6	Region 7
$N_{\rm H}$ (10^{22} cm^{-2})	4.5 ± 0.1	$4.22^{+0.08}_{-0.05}$	$4.8^{+0.1}_{-0.2}$	4.5 ± 0.1	$4.3^{+0.2}_{-0.1}$	4.61 ± 0.05	$4.36^{+0.08}_{-0.09}$
kT_1 (keV)	$0.90^{+0.08}_{-0.06}$	$0.75^{+0.03}_{-0.05}$	$0.92^{+0.06}_{-0.08}$	0.8 ± 0.1	$0.96^{+0.09}_{-0.09}$	$0.78^{+0.06}_{-0.04}$	$0.82^{+0.09}_{-0.06}$
EM_1^* (10^{20} cm^{-5})	$0.5^{+0.2}_{-0.1}$	$1.16^{+0.1}_{-0.09}$	1.2 ± 0.2	$1.3^{+0.3}_{-0.3}$	$0.8^{+0.3}_{-0.2}$	$1.1^{+0.4}_{-0.2}$	$0.92^{+0.1}_{-0.05}$
kT_2 (keV)	$3.0^{+0.4}_{-0.2}$	$2.19^{+0.1}_{-0.06}$	2.6 ± 0.2	$2.35^{+0.12}_{-0.09}$	$2.2^{+0.2}_{-0.2}$	$1.77^{+0.03}_{-0.09}$	2.00 ± 0.04
EM_2^*(10^{20} cm^{-5})	0.5 ± 0.1	1.1 ± 0.1	$1.8^{+0.1}_{-0.1}$	$1.95^{+0.1}_{-0.08}$	1.4 ± 0.3	$2.2^{+0.3}_{-0.1}$	1.3 ± 0.1
$Si/Si_\odot$	2.2 ± 0.4	$3.4^{+0.2}_{-0.4}$	3.7 ± 0.4	2.9 ± 0.3	$2.4^{+0.3}_{-0.5}$	2.3 ± 0.1	$2.1^{+0.3}_{-0.2}$
$S/S_\odot$	4.1 ± 0.5	4.1 ± 0.3	$4.6^{+0.3}_{-0.6}$	$3.6^{+0.3}_{-0.4}$	$2.7^{+0.3}_{-0.5}$	$2.4^{+0.2}_{-0.1}$	2.8 ± 0.3
$Ar/Ar_\odot$	$5.6^{+1.1}_{-0.9}$	3.8 ± 0.6	$4.9^{+0.8}_{-0.6}$	$4.1^{+0.3}_{-0.7}$	2.6 ± 0.6	2.8 ± 0.3	$3.4^{+0.3}_{-0.5}$
$Ca/Ca_\odot$	8 ± 1	$6.6^{+0.9}_{-0.8}$	7 ± 1	$6.9^{+0.7}_{-0.9}$	$4.7^{+0.8}_{-0.9}$	$4.4^{+0.4}_{-0.5}$	$5.2^{+0.5}_{-0.7}$
$Fe/Fe_\odot$	$5.2^{+0.6}_{-0.4}$	5.1 ± 0.3	$5.1^{+0.4}_{-0.6}$	$5.6^{+0.4}_{-0.3}$	$2.6^{+0.2}_{-0.3}$	$2.5^{+0.1}_{-0.2}$	$1.6^{+0.2}_{-0.1}$
χ^2/d.o.f.	298.8/244	506.7/443	800.0/646	793.5/674	403.2/352	1059.3/844	566.3/434
f_1	$0.08^{+0.03}_{-0.04}$	$0.11^{+0.04}_{-0.03}$	0.08 ± 0.04	0.08 ± 0.03	$0.10^{+0.06}_{-0.05}$	$0.09^{+0.06}_{-0.04}$	$0.11^{+0.04}_{-0.03}$
n_1 (cm^{-3})	6^{+3}_{-2}	7^{+2}_{-1}	7^{+4}_{-2}	8 ± 2	5^{+3}_{-2}	7^{+4}_{-2}	$5.5^{+3}_{-0.9}$
n_2 (cm^{-3})	$1.8^{+0.3}_{-0.2}$	$2.5^{+0.2}_{-0.1}$	2.6 ± 0.2	$2.6^{+0.3}_{-0.1}$	2.3 ± 0.2	$3.0^{+0.8}_{-0.2}$	2.3 ± 0.2

* Emission measure per unit area.

the photon statistics for the seven individual spectra do not allow us to resolve the features in the $7.65 - 8.0$ keV band in detail, I extract the spectrum from the larger elliptical region shown in Fig. 2.3 (lower right panel). This region covers the area of highest surface brightness in the $7.65 - 8.0$ keV band. I fit the spectrum in the $1 - 9$ keV band with the 2-component thermal model used for the spatially resolved spectral analysis. Table 2.4 gives the best-fit parameters derived both by fixing the Ni abundance to the solar value (second column) and by fitting the Ni abundance as a free parameter (third column). We can reproduce the Fe XXV and Ni XXVII K line blends better by fitting for the Ni abundance. The F-test gives the probability that the improvement of the fit is insignificant as $< 10^{-17}$. We can conclude that there is convincing evidence of Ni overabundance ($Ni/Ni_{\odot} = 10^{+2}_{-1}$) in the centrally jet-like structure of W49B. Notice that, since Ni is not synthesized during the stellar evolution, the observed Ni overabundance is the result of the explosive nucleosynthesis processes (Sect. 1.1).

Table 2.4: Best-fit parameters for the spectrum extracted from the elliptical region shown in Fig. 2.3 (lower right panel) and reproduced by two thermal components in collisional ionization equilibrium. All errors are at the 90% confidence level.

Parameter	$Ni/Ni_{\odot} = 1$	Ni thawed
$N_{\rm H}$ (10^{22} cm^{-2})	$4.60^{+0.06}_{-0.03}$	$4.68^{+0.06}_{-0.02}$
kT_1 (keV)	$0.87^{+0.04}_{-0.02}$	$0.86^{+0.02}_{-0.05}$
EM_1^* (10^{20} cm^{-5})	$1.13^{+0.04}_{-0.02}$	$1.1^{+0.1}_{-0.2}$
kT_2 (keV)	$2.35^{+0.02}_{-0.03}$	$2.2^{+0.2}_{-0.1}$
EM_2^* (10^{20} cm^{-5})	$1.79^{+0.06}_{-0.04}$	$1.82^{+0.06}_{-0.05}$
$Si/Si_{\odot}$	$3.3^{+0.1}_{-0.3}$	3.3 ± 0.2
$S/S_{\odot}$	3.7 ± 0.1	$3.7^{+0.1}_{-0.2}$
$Ar/Ar_{\odot}$	$4.2^{+0.4}_{-0.2}$	$4.2^{+0.3}_{-0.4}$
$Ca/Ca_{\odot}$	6.3 ± 0.5	6.4 ± 0.5
$Fe/Fe_{\odot}$	$5.5^{+0.1}_{-0.2}$	$6.0^{+0.1}_{-0.2}$
$Ni/Ni_{\odot}$	1	10^{+4}_{-1}
χ^2/d.o.f.	1678.8/1327	1584.3/1326

* Emission measure per unit area.

2.2.5 Overionization

Through their analysis of the *ASCA* global spectrum, Kawasaki et al. (2005) claimed the presence of "overionized" plasma in W49B. In particular, they measured the intensity ratio of the H-like to the He-like Kα lines of Ar and Ca to obtain the ionization temperature T_z, and found that T_z is higher than the electron temperature T_e estimated from the continuum of the X-ray spectrum. According to Kawasaki et al. (2005), this result can be interpreted in the framework of this simplified scenario: in a young remnant in the Sedov phase (see Sect. 1.3), the expanding shock front heats the ambient ISM to X-ray emitting temperatures and bright X-rays appear along the outer rim, while the hot gas within the post-shock interior is rarefied compared to the shell regions. As the remnant evolves, the hot interior plasma gradually approaches a uniform temperature via thermal conduction with the cooler outer regions. If in W49B the conductive time-scale (see Sect. 1.4.2) is shorter than the time necessary to reach CIE conditions, we would observe a higher degree of ionization than that corresponding to the plasma temperature in equilibrium conditions. Notice, however, that this interpretation does not take into account many important aspects, like the presence of ejecta and of reflected or reverse shocks.

To verify the presence of overionized plasma, I perform the same analysis by modeling the *XMM-Newton* global spectrum in the $2.75-6.0$ keV band. I model the continuum and estimate T_e with a zero metallicity VMEKAL component and include four narrow Gaussian components to model the Ar and Ca lines and a fifth Gaussian component for the Cr line. I consider absorption column densities of $N_H = 4.6 \times 10^{22}$ cm^{-2} and $N_H = 5.23 \times 10^{22}$ cm^{-2} (the value adopted by Kawasaki et al. 2005). For those column densities, I obtain electron temperatures of $kT_e = 1.80 \pm 0.03$ keV and $1.66^{+0.02}_{-0.01}$ keV, respectively. I find no evidence of overionization for Ar, given the respective ionization temperatures of $kT_z = 1.68 \pm 0.07$ and $kT_z = 1.64^{+0.08}_{-0.05}$. For Ca, the ionization temperature does seem higher than the continuum temperature: $kT_z = 2.0^{+0.1}_{-0.05}$ with $N_H = 4.6 \times 10^{22}$ cm^{-2} and $kT_z = 2.04^{+0.1}_{-0.08}$ with $N_H = 5.23 \times 10^{22}$ cm^{-2}. However, I caution the reader that these estimates may not be reliable because the global spectrum originates from physically non-uniform regions of W49B that have different temperatures and abundances. A case in point is that the estimates of the electron temperatures obtained from the global spectrum are significantly lower than those obtained from our spatially resolved spectral analysis of homogeneous regions (see Sect. 2.2.3 and kT_2 values in Table 2.3). I therefore repeat my analysis for the more uniform central region indicated by a white ellipse in the lower right panel of Fig. 2.3. This is where the overionization effects are expected to be strongest in the scenario proposed by Kawasaki et al. (2005). My analysis shows that these effects are not present. Using the same model described above in the 2.75-6.0 keV band, I find the results shown in Table 2.5. Given that kT_z is always slightly lower than or consistent with kT_e, we can conclude that there is no indication of overionization in the central region of W49B.

The absence of overionized plasma is also supported by the fact that, in W49B, there is no observational evidence that the conductive time scale is shorter than

Table 2.5: Electron temperature (kT_e) and ionization temperature (kT_z) for Ar and Ca in the central region indicated by a white ellipse in the lower right panel of Fig. 2.3. All errors are at the 90% confidence level.

Temperature	$N_{\rm H} = 4.6 \times 10^{22}$ cm^{-2}	$N_{\rm H} = 5.23 \times 10^{22}$ cm^{-2}
kT_e (keV)	2.4 ± 0.1	$2.25^{+0.08}_{-0.1}$
kT_z^{Ar} (keV)	$1.9^{+0.1}_{-0.2}$	1.8 ± 0.1
kT_z^{Ca} (keV)	$2.3^{+0.1}_{-0.3}$	2.2 ± 0.2

the ionization time scale. The amount of the non-equilibrium of ionization effects is indicated by the τ_{NEI} parameter, which is the time integral of the plasma density, calculated from the shock impact

$$\tau_{NEI} = \int_0^t n dt \sim nt \; . \tag{2.1}$$

The plasma reaches the CIE conditions at $\tau_{NEI} = \tau_{eq} \gtrsim 10^{12}$ s/cm^{-3}. As for thermal conduction, we can calculate the product of the conductive time scale (see eq. 1.18) times the plasma density, using our best-fit values for density ($n \sim 2.5$ cm^{-3}) and temperature ($T \sim 2.3$ keV) in the central region of W49B and assuming the characteristic length of temperature variation to be comparable with the radius of the radio shell (i. e. $2.15'$, corresponding to $\sim 1.5 \times 10^{19}$ cm at 8 kpc). We then obtain $\tau_{cond}\, n \sim \tau_{eq} \sim 10^{12}$ s/cm^{-3}, which suggests that the plasma is in collisional ionization equilibrium.

2.3 Discussion

On the basis of low angular-resolution *ASCA* line images, Fujimoto et al. (1995) argued for stratification of the SN ejecta in W49B, with iron confined to the inner region and lower-Z elements (Si and S) forming an outer envelope. This hypothesis was supported by the analysis of the global spectrum, with the intensity ratios of Lyα and Heα giving different ionization ages for Si, S, Ar, and Ca. Hwang et al. (2000) pointed out that, while this conclusion is compatible with the *ASCA* spectrum, no difference in the ionization ages is required if the data are modeled with a two-component thermal plasma. The analysis of *XMM-Newton* data presented here allowed us to discriminate between these two scenarios. The spatially resolved spectral analysis has shown that a correct fit of the spectra requires two thermal components and that these two components are compatible with collisional ionization equilibrium, both at the center and in the outer parts of the remnant. Moreover, as explained in Sect. 2.2.2, the line images and equivalent width maps exclude a radial stratification of the elements in the ejecta, with

Fe K emission confined to the inner part of the X-ray emitting region and lower-Z emission lines originating in an outer shell. In fact, both the central jet-like structure and the eastern sharp structure of the SNR have high abundances of Ar, Ca and Fe, while the western part has lower abundances.

The physical conditions of the plasma are not uniform in W49B. The highest temperatures are found in the northern end of the sharp eastern structure (labelled *a*) and in the central jet-like structure (labelled *b*). The lowest temperatures are found in the western part of W49B and in the south eastern zone. Assuming pressure equilibrium between the two components, no significant variations in the plasma density across the remnant are observed.

The observed X-ray emission originates in the SN ejecta, and Si, S, Ar, Ca, Fe, and Ni are all highly overabundant with respect to their solar values. They have almost the same values in structures *a* and *b*, and are lower (but still overabundant) in structure *c*. No clear evidence of X-ray emission from the shocked ambient medium is present. In fact, the results of the spatially resolved spectral analysis suggest that both the X-ray emitting components are associated with overabundant plasma. This agrees with the similarity of the morphology between the Si He-like emission blend (associated with the cooler component) and the other emission blends (associated with the hotter component). As explained in Sect. 2.2.3, however, the high absorption column inhibits the possibility of a detailed study of the soft component in that it is not easy to determine its morphology. Furthermore, the contribution of the hot component is significant even below 1.7 keV, so that it is not possible to produce a broad band clean image of the soft component. We therefore cannot rule out the possibility that the soft component (whose flux amounts to only the $\sim 10\%$ of the total flux) may be associated with the shocked circumstellar or interstellar medium. Figure 2.8 shows the map of the ratio Si He-like/Si H-like emission (i. e. the count-rate image in the $1.77 - 1.9$ keV energy band divided by the count-rate image in the $1.96 - 2.06$ keV energy band). The Si He-like/Si H-like ratio is enhanced in the outer parts of the remnant (with two maxima in the northern and southeastern parts of W49B), while it is almost uniform in the jet-like central region and at its eastern and western ends. If we associate the cool component (i. e. the Si He-like emission) with the ISM (or with the CSM) and the Si H-like emission with the ejecta, this may indicate that the ejecta are mainly distributed along the elongated jet-like structure, while the shocked ambient material totally embeds the remnant. On the other hand, the Si He-like/Si H-like ratio reaches its maxima in regions with low surface brightness where the statistics are not good enough to make these features completely reliable.

It is interesting to consider to what extent the complex morphology of W49B, and the inhomogeneities in temperature and abundance, are caused by the dynamics of the SN explosion or by the remnant's interaction with its environment.

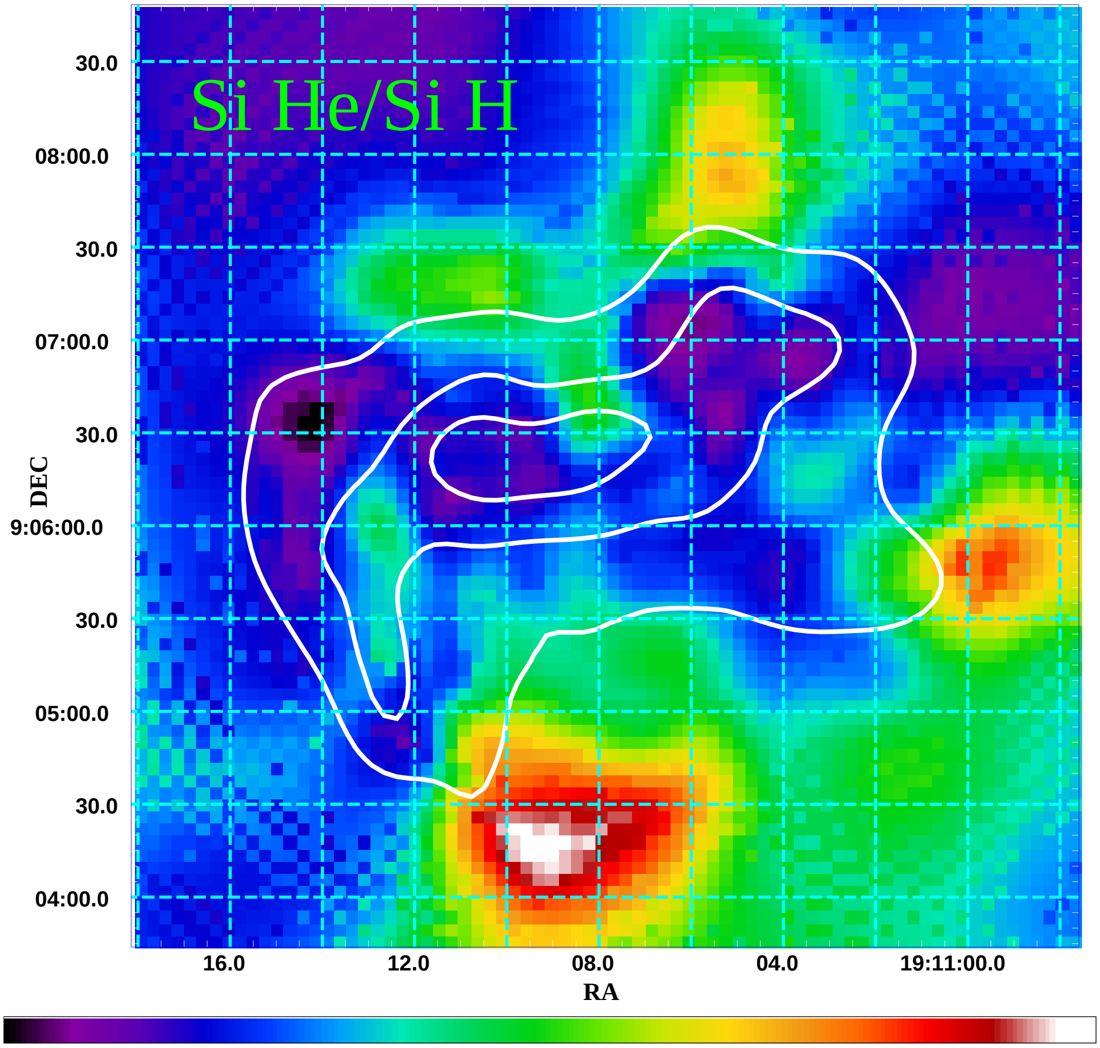

Figure 2.8: *XMM-Newton* EPIC image of the count-rate in the $1.77 - 1.9$ keV energy band divided by the count-rate in the $1.96 - 2.06$ keV energy band. The image is vignetting-corrected, adaptively smoothed (with signal-to-noise ratio 10) and background-subtracted. The color bar ranges between 1 and 2.2. I have superimposed in white the X-ray contour levels derived from the $1 - 9$ keV EPIC image at 25%, 50%, and 75% of the maximum.

Recent 2.12 micron infrared imaging observations have revealed a shocked molecular H_2 cloud that confines the remnant (see Sect. 1.6.1 and Fig. 1.10). The circular distribution of the molecular cloud around the SNR has probably been shaped by strong stellar winds from the progenitor star pushing out the ambient interstellar material to its current location and forming a cavity. Infrared [Fe II] observations at 1.64 μm reveal a barrel-shaped structure with four coaxial rings of warm gas, which has been interpreted as residuals of a strong stellar wind (Keohane et al. 2006).

The morphology of the eastern region of W49B has clearly been shaped by the ambient molecular cloud. Despite their similar abundance values, the eastern

a and central b regions have very different morphologies. The fact that region a is almost perpendicular to region b is probably due to its confinement by the large H_2 cloud to the east. Since the density of the molecular cloud is $n_{H_2} \sim 2-3\times10^3$ cm^{-3} (according to the estimates of Keohane et al. 2006), the H_2 cloud is about three order of magnitude denser than the ejecta (whose density is reported in Table 2.3). The cloud then acts as a wall that prevents the expansion in the East direction. The [Fe II] observations show that the cavity is an inhomogeneous environment for the supernova remnant expansion (see Fig. 1.10).

In contrast, there are no observed interstellar structures that might have shaped the elongated structure of the central X-ray region b, confining the ejecta in the North and South direction. This central structure thus may have been produced directly by the supernova explosion or by a peculiar configuration of pre-existing structures in the ambient stellar wind material.

The central elongated morphology seen in the *Chandra* Fe K image has been originally attributed to a bipolar jet and taken as evidence that W49B is a $\gamma-$ray burst (GRB) remnant (Keohane et al. 2004[3]). The presence of such an elongated morphology, however, does not necessarily reflect a jet-like explosion. A similar elongated central bright structure has been observed with *Chandra* in the G292.08+1.8 remnant, but Park et al. (2004) showed that its emission is associated with normal chemical composition plasma that originates in shocked dense circumstellar material rather than in shocked ejecta. Unlike for G292.08+1.8 SNR, our analysis suggests that the X-ray emission in the central X-ray region b of W49B is dominated by ejecta, although we cannot rule out the possibility that the soft component comes from solar abundance material. The scenario proposed for G292.08+1.8 can nevertheless be invoked for W49B. It is possible that the jet-like X-ray emission reflects the morphology of the ambient medium across the remnant. While no dense structures are visible toward the North and South of W49B (as shown in the infrared image of Fig. 1.10), we may assume the ambient medium to be enhanced in the central zone, forming a torus-like structure all across W49B. According to this scenario, the cold component may be associated with the thin belt of material heated by the transmitted shock travelling into the ISM structure. This would explain the low values of the filling factor of the soft component. The hot component is associated with the ejecta interacting with the reflected shock. In this case, only the material expelled in the plane of the torus is interacting with the the reverse shock and heated by it, as shown in the schematic representation of Fig. 2.9 (lower panel).

Another possibility is that the elongated structure is associated with a bipolar ejecta jet interacting with the cavity wall visible at the eastern end of the remnant (upper panel of Fig. 2.9). In this case we have to assume that the density contrast

[3]See also http://chandra.harvard.edu/press/04_releases/press_060204.html

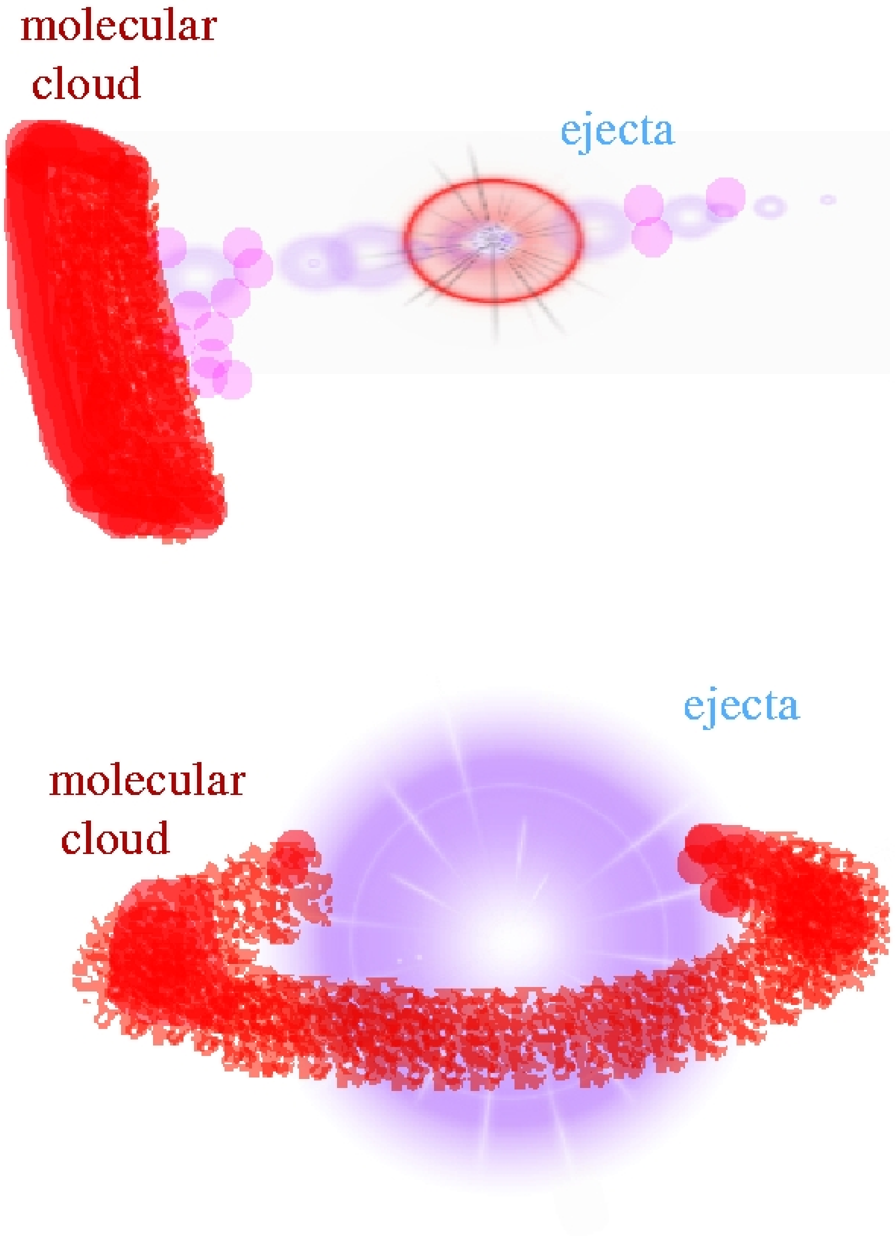

Figure 2.9: Schematic representation of the two possible physical scenarios associated with W49B: Aspherical jet-like explosion (*upper panel*) or spherical explosion in an inhomogeneous environment (*lower panel*).

has driven a very strong reflected shock that has now reached the center of W49B. Moreover, I have found that structures a and b have similar abundance values and, therefore, that a could be considered as the head of the eastern jet. The scenario that emerges is that this jet has been distorted to deviate mostly southwards by its impact with the H_2 wall. In this framework, we would have a highly anisotropic bipolar jet, where the eastern arm is significantly more extended, hot and Fe-rich than the western one.

We can estimate the mass of the X-ray emitting ejecta in both these scenarios. The spectral analysis has shown that the hard component is clearly associated with the ejecta, therefore, for the mass estimates, I will refer only to this component. The mass estimates, however, would at maximum double by associating also the soft component with the ejecta, since the emission measure of the soft component is similar to that of the hot component (within a factor of two, see Table 2.3). Notice also that we assume the mass density to be $\rho = \mu m_H n_H$, with $n_e = n_H$ and with $\mu = 1.26$. This μ value corresponds to cosmic abundances, therefore, since in the hard component we find significant metal overabundances, our estimates can be considered as lower limits of the mass of the ejecta. In the case of aspherical jet-like explosion we can assume, for the sake of simplicity, that the ejecta are distributed into a cylinder of radius $R_{jet} = 0.55'$ and height $H_{jet} = 3.6'$ (shown in the left panel of Fig. 2.10), with volume $V_{jet} \sim 1.27 \times 10^{57}$ cm^3 at 8 kpc. Since the emission measure per unit area in the central region of the remnant is 1.8×10^{20} cm^{-5} (cfr. Table 2.4), we derive a mean density of the ejecta $n_{jet} \sim 4.8$ cm^{-3} and then a total mass $M_{jet} \sim 6$ M$_\odot$. On the other hand, in the case of a spherical explosion, we would observe only the ejecta heated by the reflected shock generated by the impact of the main shock with the circumstellar torus. We can therefore assume that the ejecta are distributed into the cylinder shown in the right panel of Fig. 2.10 (with radius $R_{sph} = 1.8'$, height $H_{sph} = 1.1'$ and volume $V_{sph} \sim 4.1 \times 10^{57}$ cm^3 at 8 kpc). Taking the emission measure per unit area (EM) of this region into account, we obtain a density $n_{sph} = \sqrt{EM/2R_{sph}} \sim 2.6$ cm^{-3} and an X-ray emitting mass $M_{sph} \sim 10$ M$_\odot$. It is also possible that the ejecta do not occupy all the cylindric volume, but only a small fraction of it. For example, we can assume the ejecta to occupy a torus with outer radius R_{sph} and inner radius gR_{sph} with $0 < g < 1$. This assumption, however, does not alter very much our mass estimate, since, in this case, we would have a mass $M'_{sph} = M_{sph}\ (1-g^2)/\sqrt{1-g}$, i. e., for example, $M'_{sph} = 0.875\ M_{sph}$ for $g = 0.75$. In the spherical explosion scenario, M_{sph} would be only a small fraction of the total ejected mass (the fraction interacting with the reflected shock). In fact, by assuming the ejecta to be distributed into a sphere of 1.8' radius, we obtain $M^{tot}_{sph} \sim 25$ M$_\odot$. This would imply a very high (maybe unrealistic) zero age main sequence mass M_{ZAMS} of the progenitor star, given that, before the SN explosion, massive stars lose a very large amount of their mass ($\sim 75\%$, as shown by Dwarkadas 2006) through stellar winds. As an example, notice that the bright hypernova SN Ic 1998bw has very massive ejecta

($\sim$ 10 $M_\odot$) and $M_{ZAMS} \sim 40$ $M_\odot$ (Iwamoto et al. 1998). We then conclude that the aspherical explosion scenario seems to be preferable according to the mass estimates.

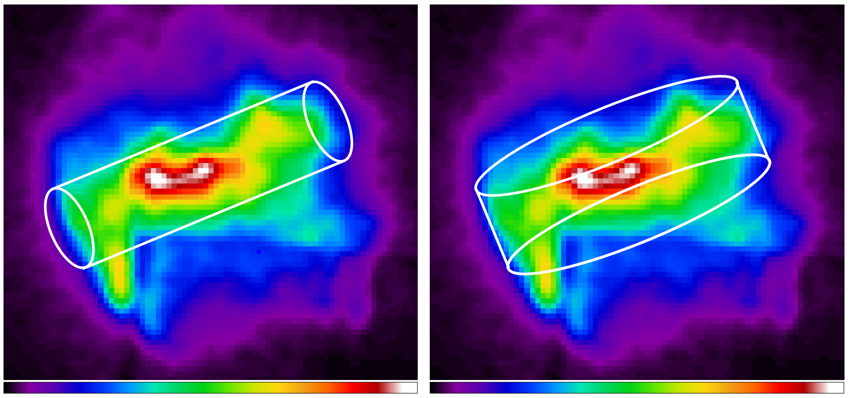

Figure 2.10: Same as left panel of Fig. 2.1 where I have superimposed the cylindric volumes used to estimate the mass of the X-ray emitting ejecta for a jet-like explosion (*left panel*) and for a spherical explosion (*right panel*).

As explained in Sect. 1.1, there is a link between very energetic jet-like explosions (or hypernovae) and $\gamma-$ray bursts, although a bipolar explosion does not necessarily imply a GRB, because a high explosion energy ($\gtrsim 10^{52}$ erg) is also required.

To investigate the possibility that W49B is a GRB remnant, I compare the abundance values found in the *a* region (see Table 2.4) with those obtained from models of explosive nucleosynthesis in bipolar explosions by Maeda & Nomoto (2003). In particular, I compare the expected and observed ratios $(X/X_\odot)$ / $(Fe/Fe_\odot)$ for $X = Si$, S, Ar, Ca, Cr, Mn, and Ni (for Cr and Mn I assume the same ratios as observed for Ar, in agreement with the estimates given in Hwang et al. 2000). None of the models can reproduce the entire observed abundance pattern. The hypernova models with zero-age main-sequence progenitor mass $M_{ZAMS} = 40M_\odot$ and explosion energy $E > 10^{52}$ erg strongly disagree with the observed values (with very large discrepancies for the Si, S, and Ar abundances). I obtain better results with the less energetic aspherical supernova models 25A ($E = 6.7 \times 10^{51}$ erg and $M_{ZAMS} = 25M_\odot$) and 25B ($E = 0.6 \times 10^{51}$ erg and $M_{ZAMS} = 25M_\odot$). I also find relatively good agreement with the spherical explosion model 25Sa ($E = 1 \times 10^{51}$ erg and $M_{ZAMS} = 25M_\odot$). The predicted values of these three models, of the best hypernova model ($E = 3.2 \times 10^{52}$ erg and $M_{ZAMS} = 40M_\odot$), and my observational findings are summarized in Fig. 2.11. While the hypernova model predictions are completely different from the observed abundance pattern, there is good overall agreement for Ar through Ni for all the other models, but the observed abundances of Si[4] and S are not well reproduced.

[4]The poor agreement for the Si abundance may be due to the possible association of the

The observed abundance pattern in W49B does not favor a hypernova explosion of sufficient energy to generate a GRB.

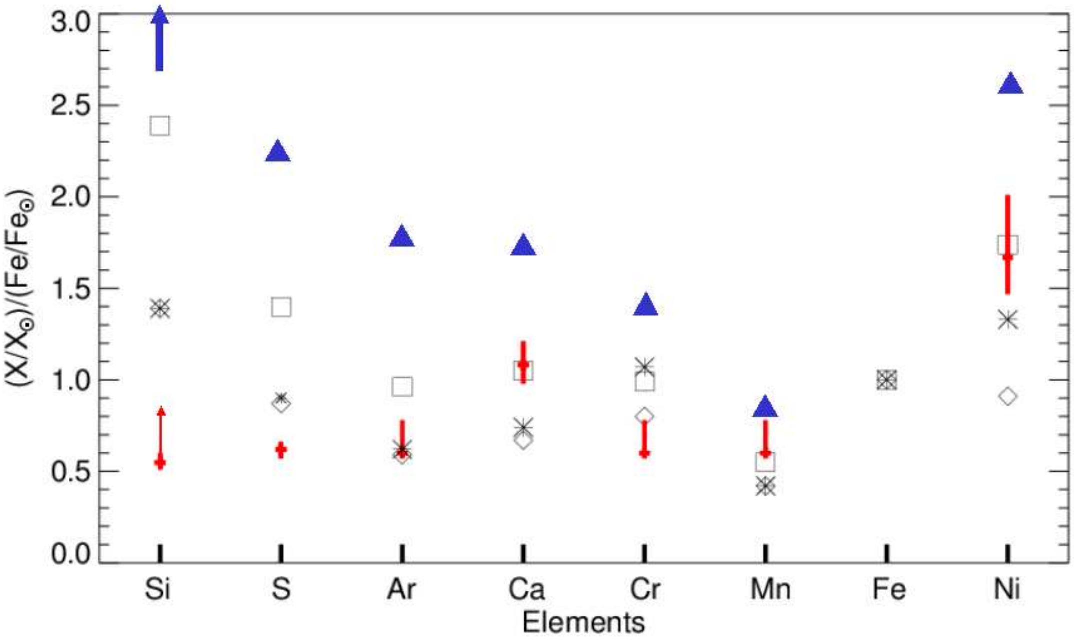

Figure 2.11: Elemental abundances in the central jet-like region of W49B (red crosses, see Table 2.4), normalized to the Fe abundance relative to the solar values (Anders & Grevesse 1989), compared with the yields obtained from the aspherical supernova models 25a (boxes) and 25b (diamonds), from the aspherical hypernova model 40C (blue triangles), and from the spherical supernova model 25Sa (stars) of explosive nucleosynthesis by Maeda & Nomoto (2003). The Cr and Mn abundances in the central region have been derived from the Ar abundance following Hwang et al. (2000).

An independent way to ascertain whether W49B is the result of a hypernova explosion consists in estimating the total energy of the remnant in the case of aspherical jet-like explosion. Assuming that the ejecta have been shocked by a reverse shock, we can derive the relative velocity of the ejecta with respect to the reverse shock, v_r. In fact, as shown in McKee & Hollenbach (1980),

$$T_s = \left(\frac{v_r}{839\ \mathrm{km\ s^{-1}}}\right)^2 \times 10^7 \mathrm{K} \tag{2.2}$$

where T_s is the post-shock temperature of the plasma. The spectral analysis allows us to derive the electron post-shock temperature $T_e \sim 2.3$ keV (see Table 2.4), which is always $\leq T_s$. If we assume the ion temperature to be of the same order of T_e, we obtain the lower limit $v_r > 1350$ km/s. I remind the reader that this is the speed of the ejecta in the reference frame of the reverse shock and is therefore larger than the speed of the ejecta in the reference frame of the

soft component (where the Si He-like line originates) with the CSM: in this case the observed abundance is an average between the ejecta Si abundance and the CSM Si abundance.

unperturbed ambient ISM. In fact, given the mass of the shocked ejecta, it is reasonable to conclude that the reverse shock is moving towards the center of the remnant. Notice that this is true also if we assume the ejecta to be heated by the reflected shock generated by the interaction of the main shock front with the dense molecular cloud. The v_r value is remarkably in agreement with the estimate of the X-ray forward shock velocity with respect to the unperturbed medium, $v_s \sim 1200$ km/s, derived by Keohane et al. (2006). Taking our M_{jet} estimate into account, we then derive a kinetic energy $K_{ej} \sim 1.2 \times 10^{50}$ erg. Notice that, according to Rakowski (2005), it is reasonable to assume that $0.1 < T_e/T_s < 1$ (for shock velocity < 5000 km/s). In the case $T_e = 0.1\ T_s$, we then obtain the upper limit $v_r < 4300$ km/s and then $K_{ej} < 1.2 \times 10^{51}$ erg. The internal energy $U_{jet} = (3/2) n_{jet} k T_s V_{jet}$ is in the range $3.4 \times 10^{49} - 3.4 \times 10^{50}$ erg (for $T_e/T_s = 0.1 - 1$) and is even lower. The total energy of the remnant[5] is then of the order of some 10^{50} erg and, in any case, lower than 1.5×10^{51} erg. Although our estimates of mass and velocity are quite rough, it would be necessary for the velocity of the ejecta to be one order of magnitude larger than v_{jet}, or for the total mass to be two orders of magnitude larger than M_{jet} to obtain 10^{52} erg. This result, together with the observed abundance pattern, concur in excluding the possible association of W49B with a hypernova (and a GRB), although this association cannot be definitely ruled out especially given the emergence of the class of underenergetic GRBs associated with SNe (Mazzali et al. 2006).

[5]In the case of the spherical explosion scenario we find $K_{sph} \sim 2 \times 10^{50} - 2 \times 10^{51}$ erg and $U_{sph} \sim 6 \times 10^{49} - 6 \times 10^{50}$ erg.

Chapter 3

Shock-cloud interaction in the Vela SNR. The FilD region observed with *XMM-Newton*

In this chapter I report on the analysis of an *XMM-Newton* EPIC observation of the FilD knot (see also Miceli et al. 2005a,b). FilD is a bright region in the northern rim of the Vela SNR and it has been introduced in Sect. 1.6.2. In this region there is a clear signature of the interaction of the shock front with an isolated cloud. Because of the good combination of sensitivity, spectral, and spatial resolution of the *XMM-Newton* telescope, the analysis of the X-ray emission in this region can give important information about the physical properties of the X-ray emitting plasma. This allows us to obtain a more complete description of the post-shock conditions of the FilD cloud than that obtained with the past observations of the FilD region performed with the *ROSAT* satellite (Bocchino et al. 1997, 1999, 2000). Moreover, the achieved results can also give important constraints for the setup of the hydrodynamic model of the shock-cloud interaction in this region described in Chapter 4.

The chapter is organized as follows: in Sect. 3.1 I present the EPIC data, in Sect. 3.2 I describe the morphology of the X-ray emission, identifying the physically different emitting regions visible in the field of view (FOV), and I present the results of the spatially resolved spectral analysis. In Sect. 3.3 I study the thermal structure of the source, show the 3-D map of the plasma, and discuss the shock-cloud interaction in the FilD knot, emphasizing the presence of a multi-phase shocked medium.

3.1 Data processing

The *XMM-Newton* EPIC observation of Vela FilD presented here is a Guaranteed Time Observation, obtained in virtue of the participation of the INAF – Osservatorio Astronomico G. S. Vaiana di Palermo on the development of the EPIC cameras. The observation has been performed with the EPIC MOS (Turner et al. 2001) cameras and with the EPIC pn (Strüder et al. 2001) camera on 9 November 2001. A description of the *XMM-Newton* telescope and of the instrumental characteristics of the EPIC cameras is provided in Appendix A. The pointing coordinates of the observation are: α (2000) $= 8^h35^m44^s$, δ (2000) $= -42°35'29''$.

Table 3.1 summarizes the main information about the data.

Table 3.1: Relevant information about the data.

CAMERA	t_{exp} (ksec)^I	Mode	Filter	N_{ph}^{II}
pn	26.8/11.5	Ext. Full Frame	medium	291115
MOS1	31.1/25.2	Large Window	medium	203113
MOS2	31.1/25.2	Large Window	medium	207807

I. Unscreened/Screened exposure time.

II. Number of events in the whole field of view ($0.3 - 10$ keV).

Data have been processed with the Standard Analysis System (SAS V5.4.1) pipeline. To eliminate the contamination by soft proton flares I removed the time intervals which showed anomalous background enhancements. In particular, I extracted the background light curve with a bin size of 10 s, at energy > 10 keV and I eliminated time intervals with high counts (> 30 for pn data and > 15 for MOS1 and MOS2 data). Table 3.1 shows the unscreened and screened exposure time, t_{exp}; the pn observation is strongly contaminated by proton flares ($\sim 57\,\%$ of the total exposure). There was also a further screening of the data, obtained by excluding some residual hot pixels (especially from the MOS1 observation)

The X-ray sources present in the EPIC field of view and not correlated with the Vela SNR have been removed. Detection of these sources was performed on the summed data set (MOS1+MOS2+pn), using the Wavelet Transform algorithm *PWXDETECT* (Damiani et al. 1997a,b). In this way I found position, extension, and X-ray flux of 21 sources; 10 among them have an optical counterpart in the USNO-A2.0 archive. All the detected sources have a significant signal in the energy range $1 - 10$ keV, so their contribution has been subtracted only in this band. Since the Vela emission covers the entire FOV, it was not possible to isolate a region where the local background could be extracted. The contribution of the incident photon X-ray background was derived from the EPIC public observation 0106260201, whose FOV is wholly outside the Vela SNR shell, and pointed toward the source RXJ0806.4-4123, which is only $\sim 5°$ distant from our observation. In the $0.3 - 2$ keV band (where our analysis is focussed) the count-rate contribution of this background is between ~ 5 % and ~ 15 % of the total signal. In particular, in a $4''$ bin, the mean $0.3 - 2$ keV MOS count-rate of the photon background is $R \sim 8.6 \times 10^{-6}$ s^{-1} with a mean photon energy $\overline{E} \sim 670$ eV; I used these values to compute the background-subtracted $\overline{E}$ vs. CR plot described in Sect. 3.2.2. and to extract pn and MOS background spectra for the spectral analysis. As for the non-photon background, which is probably associated with a residual flux of soft protons, I found that above 1 keV the non-photon background amounts to $> 95\%$ of the total signal for the pn camera and $> 70\%$, for the two MOS cameras and that: i) In the $0.3 - 0.5$ keV band the non-photon background contribution is too low to be estimated; ii) in the $0.5 - 1$ keV band it amounts to $2 - 12$ % of the total signal for the pn camera, and iii) in the $0.3 - 2$ keV band it is negligible.

Spectral analysis was performed in the energy band $0.3 - 1.1$ keV using XSPEC. I selected events with PATTERN[1] ≤ 12 for the MOS cameras, PATTERN≤ 4 for the pn camera, and FLAG$= 0$ for all the cameras. The Ancillary Response Files (ARF) were generated with the SAS *ARFGEN* task, and the event files were processed using the *EVIGWEIGHT* task (Arnaud et al. 2001) to correct vignetting effects. I summed the MOS1 and MOS2 spectra summing the exposure times, averaging the ARFs (weighted for the corresponding exposure times), and using the MOS1 response file for the analysis of the summed spectrum. Spectra were rebinned to achieve a signal-to-noise ratio per bin $> 5\sigma$ and the fittings were performed simultaneously on the pn and MOS-summed spectra. All the errors are calculated according to Lampton et al. (1976) at 90% confidence level. As shown in Sect. 3.2.3, the best fit parameters are not significantly influenced by the choice of the background.

3.2 The data analysis

3.2.1 The region morphology

To reduce statistical fluctuations in the images, I implement a weighted average of the pn, MOS1, and MOS2 count-rate maps in three different bands: $0.3 - 0.5$ keV, $0.5 - 1$ keV, and $0.3 - 2$ keV. The first two bands were chosen to understand how the emission is distributed in the FOV at different energies, while the image in the $0.3 - 2$ keV band allows me to make a comparison between the EPIC and the past *ROSAT* PSPC observations. All images are MOS-equivalent. Therefore,

[1]For the definition of PATTERN and FLAG, see Appendix A

in the weighted sum, each camera contributes with its count-rate, scaled by the factor $A_{eff}^{MOS}/A_{eff}^{cam}$, where A_{eff} is the effective area of the camera. Since this ratio depends on the spectral distribution of the incoming photons, I have taken the thermal spectrum of the source into account. I estimate that in all these images the relative statistical error of the count-rate in each bin is $< 18\%$.

Fig. 3.1 shows the count-rate images (vignetting corrected) in the $0.3 - 0.5$ keV band and $0.5 - 1$ keV band; these images are adaptively smoothed through the convolution with gaussians having $4 \leq \sigma_{min} \leq 24''$. North is up and East is on the left. Notice that, assuming a distance of 250 pc (see Sect. 1.6.2), the diameter of the EPIC FOV corresponds to an extension of ~ 2.1 pc. There are

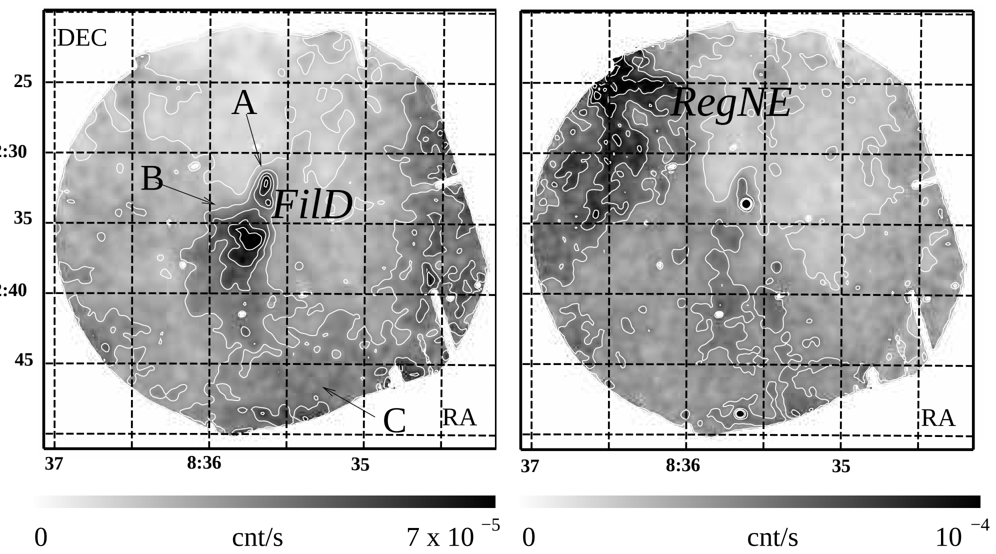

Figure 3.1: Adaptively smoothed count-rate images (MOS equivalent) in the $0.3 - 0.5$ keV band (*left*) and $0.5 - 1$ keV band (*right*). These images are a weighted average of the pn, MOS1, and MOS2 images. Eight contour levels, equispaced between 0% and 100% (included) of the peak value ($\sim 7.1 \times 10^{-5}$ cnt s^{-1} bin^{-1} and $\sim 10^{-4}$ cnt s^{-1} bin^{-1} respectively), are shown; the bin is $4''$.

striking differences in the morphology of the emission in these two bands. The FilD complex, in the middle of the FOV, is clearly visible in the soft band (Fig. 3.1, left panel), and its internal structure is resolved in good detail with *XMM-Newton*. FilD looks composed by two bright parts (A and B in Fig. 3.1). South of FilD there is a wide region, labelled C, that extends westwards. As shown in the *ROSAT* observation RP500015 (Bocchino et al. 1999, Fig. 2b), region C stretches beyond the EPIC FOV. FilD is barely visible in the hard band (*right panel*), where another large structure is present. This bright structure, named RegNE, has a slightly higher count-rate than FilD in the $0.3 - 2$ keV band (Fig. 3.2) and was not visible in the past *ROSAT* PSPC observation. The analysis of two new *XMM-Newton* observations of RegNE and of the southwestern (C) structure is described in Chapter 5.

It is interesting to note how EPIC data relate to the optical observations of the FilD region. Figure 3.3 shows a color composite optical image of FilD (from Bocchino et al. 2000), where I have superimposed the X-ray contour levels of the EPIC observation in the $0.3 - 0.5$ keV band. The FOV of this observation is indicated by the white square in the left panel of Fig. 3.2. A larger scale image of the Hα emission in this region and its relationship with the morphology of the X-ray knot is shown in the next chapter (Fig. 4.2), where I present the hydrodynamic model of the shock-cloud interaction in FilD and I discuss the physical origin of the X-ray and optical emission. In the southwestern part

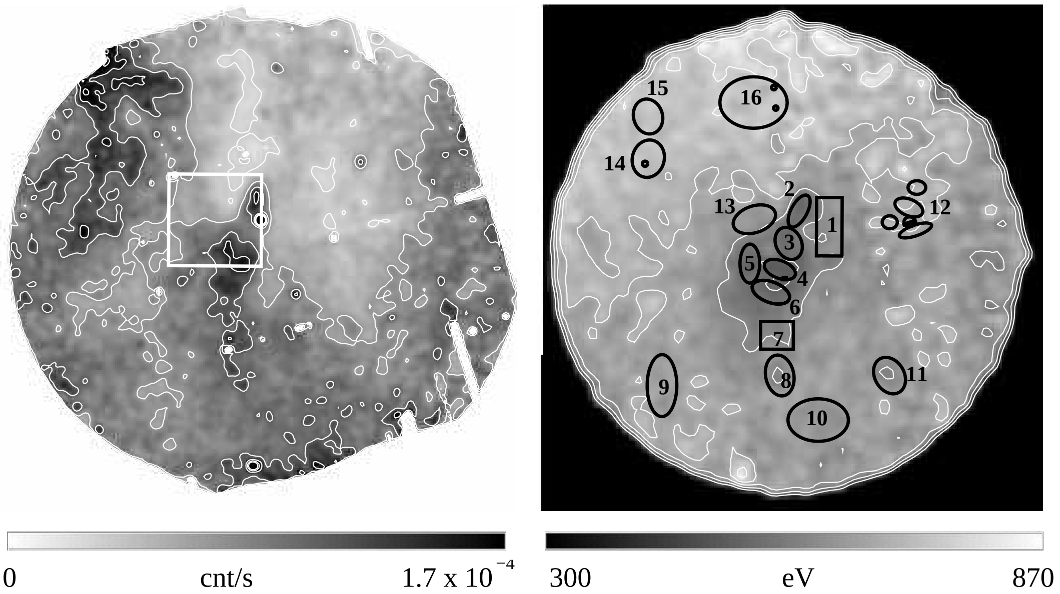

Figure 3.2: *Left*: Adaptively smoothed count-rate images (MOS equivalent) in the $0.3-2$ keV band (bin size= $4''$); Eight contour levels, equispaced between 0% and 100% (included) of the peak value ($\sim 1.7 \times 10^{-4}$ cnt s^{-1} bin^{-1}) are shown. The white square indicates the field of view of Fig. 3.3. *Right*: Mean energy map (smoothed with $\sigma = 20''$, bin size= $10''$). In each pixel the local mean photon energy of the photons detected by the MOS cameras between 0.3 keV and 2 keV is reported. I superimposed 6 contour levels equispaced between 0.5 keV and 0.85 keV. The 16 subregions selected for spectral analysis are also shown.

of the image of Fig. 3.3 there is a clear relationship between optical and X-ray emission: maximum X-ray emission contour levels, in fact, are just outside the optical filament which follows a path that "grazes", without crossing, the two FilD regions with the highest X-ray surface brightness (A and B in Fig. 3.1). This kind of relationship between optical and X-ray emission, also observed by Patnaude et al. (2002) in the southwestern region of the Cygnus Loop, suggests that a transmitted shock is propagating through a cloud with an inwardly increasing density profile, generating optical emission in the inner and denser part of the

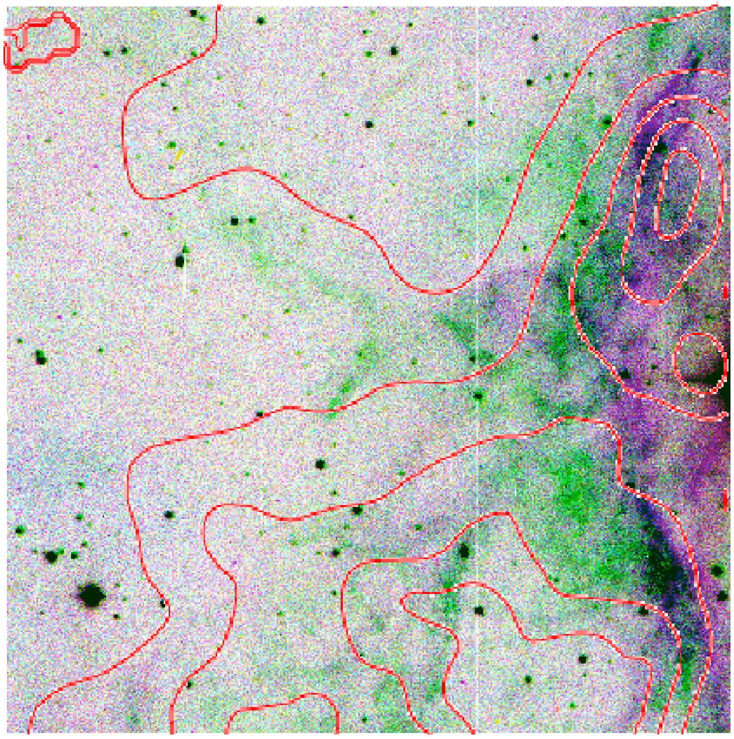

Figure 3.3: Color composite optical image of FilD (from Bocchino et al. 2000): the $H\alpha$ emission is reported in green, and the [OIII] emission in violet. The $5.7' \times 5.7'$ field of view is indicated by the white square in the left panel of Fig. 3.2. I superimposed (in red) X-ray contour levels derived from EPIC observation in the $0.3-05$ keV band.

cloud and X-ray emission in the outer part.

3.2.2 Analysis of the photon energy map

The *XMM-Newton* data allows me to study the distribution of photon energies across the FOV and to produce, as done for W49B, a high resolution mean photon energy ($\overline{E}$) map (i.e., an image where each pixel holds the mean energy of the detected MOS photons), shown in Fig. 3.2, right panel. As explained in Sect. 2.2.2, this map provides information about the spatial distribution of the spectral properties of the plasma; in particular, high $\overline{E}$ values indicate hard spectra (and high temperatures). To realize this map, I consider the MOS1 and MOS2 event files in the $0.3-2$ keV band; a bin size of $10''$ allows me to collect more than 10 counts per pixel everywhere. For each pixel, I calculate the mean photon energy and then I smooth the map with a gaussian distribution with $\sigma = 20''$ (the error on each value of $\overline{E}$ is ~ 10 eV). The map clearly shows that $\overline{E}$ has a minimum in the FilD region and a maximum in RegNE.

The large inhomogeneities in the count-rate and mean energy maps suggest that the blast wave shock propagates in a complex environment, generating dif-

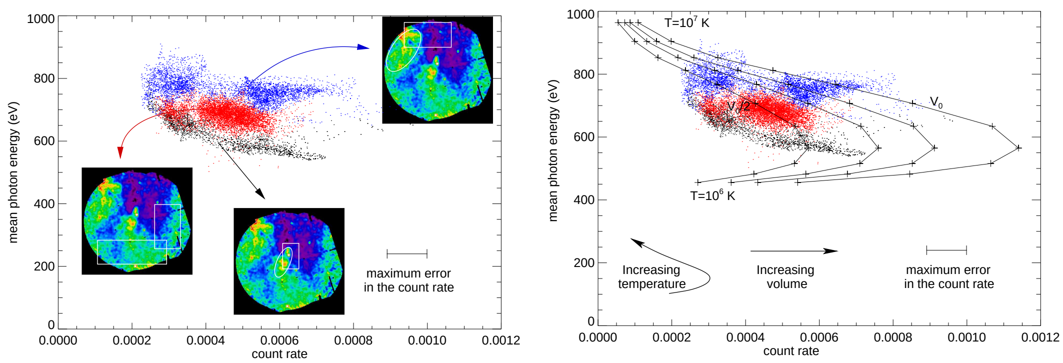

Figure 3.4: *Left panel*: $\overline{E}$ vs. count-rate scatter plot for the pixels of Fig. 3.2. The colors of the points codify the three different regions indicated in the field of view. Errors in $\overline{E} \sim 10$ eV, bin size= $10''$. *Right panel*: Same as left panel where I have superimposed the expected $\overline{E}$ vs. CR values for an optically thin plasma with different temperatures (equispaced in $\log T$ from 10^6 K to 10^7 K) and volumes. In each curve the volume is fixed and ranges between $V_0/2 = 4 \times 10^{54}$ cm^3 and V_0. The values have been obtained assuming pressure $P = 3.7 \times 10^{-10}$ dine cm^{-2}, and taking the interstellar absorption ($N_H = 10^{20}$ cm^{-2}) and the EPIC MOS instrumental response into account.

ferent thermal conditions in the shocked plasma. To get information about the distribution of the physical parameters of the plasma and about the geometrical morphology of the inhomogeneities, I investigate the relation between the mean photon energy in a given pixel and the corresponding count-rate, CR. As we shall see in the following, this study allows us to detect different shocked clouds in the FOV.

Figure 3.4 shows the observed $\overline{E}$ vs. CR relation (background subtracted), where each point corresponds to a $10''$ pixel of the mean energy map. The right panel of the figure shows the same graph where I have overlaid the expected $\overline{E}$ vs. CR values for an optically thin plasma with different temperatures (ranging from 10^6 K to 10^7 K) and volumes (between $V_0/2 = 4 \times 10^{54}$ cm^3 and V_0) all having the same pressure $P = 3.7 \times 10^{-10}$ dine cm^{-2} (which corresponds to a density $n = 2.7$ cm^{-3} at $T = 10^6$ K), obtained taking the interstellar absorption (with $N_H = 10^{20}$ cm^{-2}, in agreement with Bocchino et al. 1994, Lu & Aschenbach 2000, and Kahn et al. 1985) and the EPIC instrumental response into account.

The global trend is a decreasing one, and it is similar to what we would observe in the case of pressure equilibrium. It is interesting to note how the different structures present in the FOV are disposed in the graph. The black points correspond to the photons emitted from FilD and an adjacent region; they clearly identify a very narrow strip in the graph, suggesting that FilD and the surrounding fainter regions are part of a single structure. We can then suppose that FilD is a largely isobaric structure formed by components with different temperatures and/or extensions along the line of sight. The red points, corresponding to the southwestern region, distinctly identify a different flatter trend, with a higher $\overline{E}$, hence a higher mean temperature along the line of sight and a higher value of pressure and/or volume. This region seems therefore to be physically different from FilD. Finally, the events detected in the northeastern region of the FOV (blue) have the highest mean energy and the decreasing trend is less marked. These points do not overlap with the points either of FilD or of the southern region, suggesting that we are observing three physically different ISM inhomogeneities.

Note that the $\overline{E}$ vs. CR scatter-plot can also give indications on the physical scenario associated with the X-ray emission. In fact, a plasma heated by a reflected shock would yield an increasing trend in the $\overline{E}$ vs. CR scatter-plot, because the hotter plasma behind the reflected shock front is also more compressed since it was shocked twice. Therefore, in the reflected shock case, the plasma with the higher temperature should also have a higher emission measure (and then a higher CR), as we shall see in Chapter 4. Thus the $\overline{E}$ vs. CR trend, visible in Fig. 3.4, may suggest that we are observing ISM clouds heated by a transmitted shock.

3.2.3 Spectral analysis

The analysis above allows us to define spatial regions in the FOV with homogeneous physical properties across the plane of the image. It is then possible to perform a spatially resolved spectral analysis on them to obtain the physical parameters. I analyze the spectra extracted from the 16 subregions indicated in the right panel of Fig. 3.2. These subregions cover all the significant structures in the FOV, identified on the basis of the mean photon energy map of Sect. 3.2.2, and their shape and size are chosen so as to have enough photon statistics (> 2000 counts per subregion) and very small fluctuations of the mean photon energy ($< 4\%$), which is almost uniform in each subregion. In this way it is possible to probe the different spectral features between regions whose extension is only a few arcminutes and which do not have internal spectral inhomogeneities *across the plane of the image*. Subregions $1-6$ are located on FilD; subregions $7-12$ cover the south western structure; subregion 13 is in the "transition zone" between FilD and RegNE which is covered by subregions 14 and 15; subregion 16 corresponds to the northern area with very low surface brightness.

A single temperature model both in Collisional Ionization Equilibrium (CIE) or Non-Equilibrium of Ionization (NEI) is rejected in all the regions except for RegNE. All the extracted spectra are described well (at 95 % confidence level) by two MEKAL components of an optically-thin thermal plasma in CIE (Mewe et al. 1985, Mewe et al. 1986, Liedahl et al. 1995), with non-solar Ne and Fe abundances and modified by the interstellar absorption of Morrison & McCammon (1983). Figure 3.5 shows a representative spectrum, extracted from subregion 7, with its best fit model.

The elements whose lines mainly contribute to the observed spectra are O, Ne, and Fe. In particular in all spectra the K-shell line complexes of O VII (at 0.56 keV), O VIII (at 0.65 keV), and Ne IX (at 0.92 keV) are visible. As for the O abundance, I find in each subregion $O/O_{\odot} = 0.9 \div 1.1$ so I tie this abundance to 1. The blending between the Fe XVII L-lines and the Ne IX lines generates an entanglement between the best fit values of the abundances of Ne and Fe, and the statistics is not enough to discriminate between these two values in most of the regions. To overcome this problem I focus on the subregions 14, 15, and 16 where the signal to noise ratio is best at energies of ~ 0.9 keV. In these subregions the mean value of the ratio $(Ne/Ne_{\odot})/(Fe/Fe_{\odot})$ is 4.4 and I assume that this ratio remains the same in the other subregions. Therefore, in all spectral fittings, I left the model Fe abundance free and link the Ne abundance to it, so as to have $(Ne/Ne_{\odot})/(Fe/Fe_{\odot}) = 4.4$.

It was not possible to obtain a good estimate of the N_H parameter ($N_H \simeq 1.5^{+3.5}_{-1.5} \times 10^{20}$ cm^{-2}), so it was fixed to 1×10^{20} cm^{-2}, which is a typical value in this part of the Vela SNR (Bocchino et al. 1994, Lu & Aschenbach 2000, and Kahn et al. 1985).

The influence of the background on the spectral best-fit parameters is negligible. In Table 3.2.3, I report the best fit parameters obtained from the spectral analysis of subregions 4, 10, and 16, with the subtraction from source spectra of the background of the EPIC observation 0106260201 and of the EPIC observations of the Galactic Plane Survey[2]. The table shows that the choice of the photon background does not significatively influence the values of the best-fit parameters.

I also check for the presence of NEI effects. In all the extracted spectra, the fittings of the cooler component with the PSHOCK non-equilibrium of ionization model (Borkowski et al. 2001) reveal that the plasma has reached the collisional ionization equilibrium. As explained in Sect. 2.2.5, the amount of the NEI effects is indicated by the τ_{NEI} parameter, and the plasma reaches the CIE conditions at $\tau_{NEI} \gtrsim 10^{12}$ s/cm^{-3}. In all the spectral subregions, the best-fit values of the τ_{NEI} parameter for the cooler component are a few 10^{13} s/cm^{-3} (their lower limits are always larger than some 10^{11} s/cm^{-3}), and the best-fit temperatures and emission measures are the same as those obtained with the MEKAL model. As for the hotter component, the statistics are too low to infer significant information on NEI effects in the FilD and in the southwestern region, while in RegNE (subregions 14 and 15) the spectra are described well by the non-equilibrium of ionization model with a temperature of $\sim 7 \times 10^6$ K. The results obtained in this region with the

[2] 10 EPIC observations of the Galactic Plane Survey, pointing galactic longitude 319°, and galactic latitude between 0° and 3°.

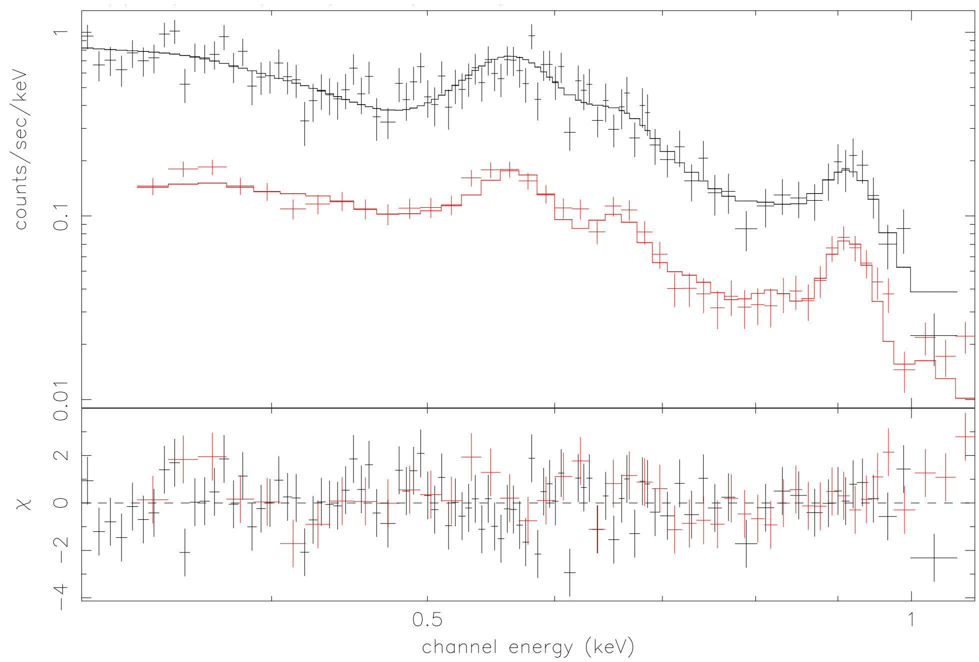

Figure 3.5: pn (upper) and MOS-summed (lower) spectra extracted from subregion 7 (indicated in Fig. 3.2) with the corresponding best fit model and residuals.

CIE and NEI conditions are reported in Table 3.3. Assuming NEI conditions for the hotter component, the temperature of RegNE is a bit higher, and comparable to the inter-cloud temperature (see Fig. 3.11). This is at odds with the patchy morphology of the emission of this region, which seems to suggest that RegNE cannot be associated with the inter-cloud medium. A more detailed study of NEI conditions in RegNE, discussed in Chapter 5, shows that also in RegNE the plasma seems to have reached the collisional ionization equilibrium .

The findings of the spatially resolved spectral analysis are shown in detail in Figures 3.6−3.8. The achieved results can be summarized as follows:

1. In the subregions 14 and 15, spectra can be modelled with only one thermal component.

2. The temperatures T_I and T_{II} of the two components are both rather uniform in the FOV (Fig. 3.7) with mean values (between the subregions): $\overline{T}_I = 1.14 \pm 0.02 \times 10^6$ K (cooler component) and $\overline{T}_{II} = 3.0 \pm 0.1 \times 10^6$ K (hotter component).

Table 3.2: Best fit parameters, obtained from the spectral analysis of subregions 4, 10, and 16 of Fig. 3.2 with subtraction from source spectra of the background of the EPIC observation 0106260201 (left column) and of the background of the 10 EPIC observations of the Galactic Plane Survey (GPS, right column).

subregion 4	0106260201	GPS
T_I (10^6 K)	$1.14^{+0.05}_{-0.04}$	$1.15^{+0.04}_{-0.05}$
T_{II} (10^6 K)	3.4 ± 0.5	$3.5^{+0.8}_{-0.6}$
$n_I^2 L_I$ (10^{18} cm^{-5})	$7^{+1.2}_{-1.4}$	$7^{+1.2}_{-1.1}$
$n_{II}^2 L_{II}$ (10^{18} cm^{-5})	$0.28^{+0.09}_{-0.07}$	$0.28^{+0.09}_{-0.1}$
$Ne/Ne_\odot$	$1.3^{+0.7}_{-0.5}$	$1.3^{+1}_{-0.6}$
χ^2 (d. o. f.)	102.1 (85)	93.0 (85)
subregion 10	0106260201	GPS
T_I (10^6 K)	$1.05^{+0.04}_{-0.06}$	$1.01^{+0.07}_{-0.08}$
T_{II} (10^6 K)	$3.3^{+0.2}_{-0.3}$	$3.1^{+0.3}_{-0.1}$
$n_I^2 L_I$ (10^{18} cm^{-5})	$4.5^{+0.8}_{-0.7}$	$5.1^{+1.5}_{-0.9}$
$n_{II}^2 L_{II}$ (10^{18} cm^{-5})	$0.52^{+0.05}_{-0.04}$	$0.54^{+0.04}_{-0.06}$
$Ne/Ne_\odot$	$1.2^{+0.4}_{-0.3}$	$1.4^{+0.4}_{-0.2}$
χ^2 (d. o. f.)	181.0 (157)	176.9 (157)
subregion 16	0106260201	GPS
T_I (10^6 K)	1.3 ± 0.2	$1.2^{+0.1}_{-0.6}$
T_{II} (10^6 K)	2.9 ± 0.2	$2.8^{+0.2}_{-0.4}$
$n_I^2 L_I$ (10^{18} cm^{-5})	$0.16^{+0.6}_{-0.03}$	$0.19^{+0.15}_{-0.05}$
$n_{II}^2 L_{II}$ (10^{18} cm^{-5})	0.14 ± 0.01	$0.14^{+0.03}_{-0.01}$
$Ne/Ne_\odot$	$2.0^{+0.5}_{-0.2}$	$2.2^{+0.5}_{-0.4}$
χ^2 (d. o. f.)	189.1 (169)	185.5 (169)

Table 3.3: Best-fit parameters of the spectral analysis of subregions 14 and 15 with the MEKAL CIE model and with the PSHOCK NEI model.

MEKAL	subregion 14	subregion 15
Temperature (10^6 K)	$2.58^{+0.09}_{-0.1}$	$2.73^{+0.13}_{-0.1}$
n^2L (10^{17} cm^{-5})	$11.3^{+0.5}_{-0.5}$	$11.2^{+0.7}_{-0.6}$
$Fe/Fe_\odot$	$0.64^{+0.14}_{-0.11}$	$0.54^{+0.13}_{-0.14}$
χ^2(d. o. f.)	146.4(125)	158.7(134)
PSHOCK	subregion 14	subregion 15
Temperature (10^6 K)	7^{+2}_{-2}	7^{+2}_{-3}
n^2L (10^{17} cm^{-5})	$2.3^{+1}_{-0.5}$	$2.5^{+2}_{-0.4}$
$Fe/Fe_\odot$	$0.49^{+0.07}_{-0.07}$	$0.50^{+0.09}_{-0.10}$
τ_{NEI} (s/cm^3)	$6^{+4}_{-2} \times 10^{10}$	$8^{+5}_{-3} \times 10^{10}$
χ^2(d. o. f.)	131.2(124)	145.6(133)

3. Both components present large variations of the emission measure per unit area, as shown in Fig. 3.8.

4. A third MEKAL component in the model does not improve the description of the data.

3.2.4 Ne and Fe abundances

Figure 3.6 shows the best-fit values of $Ne/Ne_{\odot}$ in the 16 subregions versus the mean MOS count-rate (for a bin size of $10''$) in the corresponding subregion. The Fe abundances can be deduced from the condition $(Ne/Ne_{\odot})/(Fe/Fe_{\odot}) = 4.4$.

In 10 subregions I find Ne abundances significantly higher than solar, with an average $\overline{Ne}/Ne_{\odot} = 1.7 \pm 0.2$ over all the subregions. Typically, the Ne overabundance is associated with overabundances of O, Mg, Si, and Fe and represents a clear signature of the ejecta, as shown, for example, by the analysis of the *XMM-Newton* observation of the Vela Shrapnel D performed by Katsuda & Tsunemi (2005) (see also Sasaki et al. 2001 and Miyata et al. 2001). However, this is not the case, since Fe is underabundant and the O abundance is solar. Moreover, in the FilD region the Ne abundance is not as high as in the Shrapnel D, where $\overline{Ne}/Ne_{\odot} \gtrsim 8$. Analogous O, Ne, and Fe abundances ($Ne/Ne_{\odot} = 1.7^{+0.9}_{-0.3}$, $O/O_{\odot} = 0.8^{+0.3}_{-0.2}$ and $Fe/Fe_{\odot} = 0.50^{+0.22}_{-0.04}$) were found in a small region of the Cygnus Loop by Miyata & Tsunemi 2001. Notice, however, that the solar Ne abundance is still not well determined. The analysis of the X-ray spectra of a sample of nearby solar-like stars has recently shown that in the solar neighborhood the neon-to-oxygen ratios is more than 2 times higher than that currently estimated for the Sun (Drake & Testa 2005). This suggests that the solar Ne abundance may be underestimated, and this indication is supported by other works (see Cunha et al. 2006 and references therein). Therefore, the slight Ne overabundance detected in FilD may not be "real", but only the result of a poor determination of the Ne abundance in the Sun.

In all the analyzed subregions the Fe is underabundant with an average value $\overline{Fe}/Fe_{\odot} = 0.39 \pm 0.05$. According to Vancura et al. (1994) (VAN), the fraction of Fe locked up in the pre-shock ISM grains is 0.98, so in the X-ray emitting plasma at the shock front we have $Fe/Fe_{\odot} = 0.02$. VAN used a numerical model to describe the evolution of the grain destruction which generates the release of Fe in the interstellar gas in the post-shock region. However, assuming the typical values of this zone of the Vela shell, shock inter-cloud velocity $v_{ic} = 700$ km/s, and inter-cloud density $n_{ic} = 0.05$ cm^{-3} (Sect. 3.3.4), this model predicts that the observed Fe abundance can be obtained only after ~ 20000 yr, i. e. about two times the age of the Vela SNR. In conclusion, it is difficult to explain the observed Ne and Fe abundances, and it is necessary to obtain more information about the value and the spatial distribution of the abundances of these elements

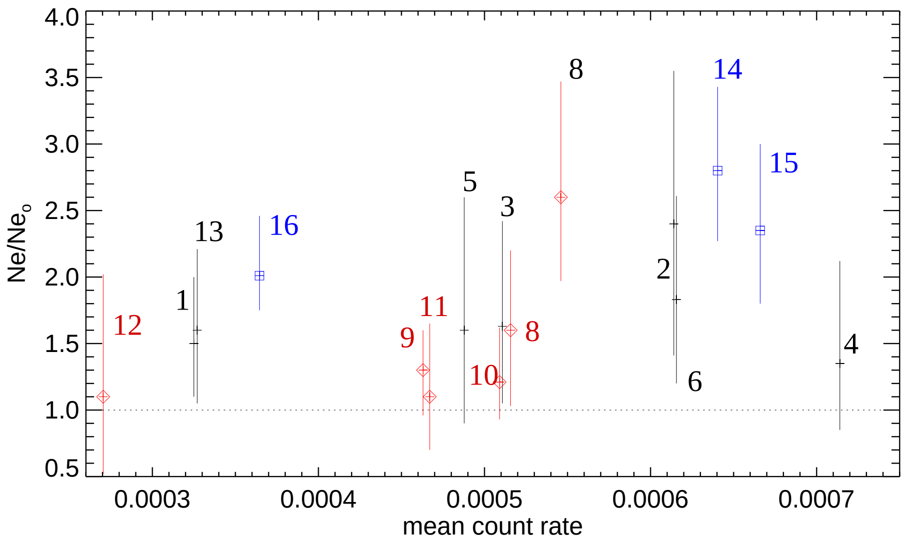

Figure 3.6: Best fit Ne abundances in units of the solar photospheric abundance (the errors are at 90% confidence level) versus the mean MOS count-rate (in bin of 10″) for the 16 subregions of Fig. 3.2. The Fe abundances can be deduced from the condition $(Ne/Ne_{\odot})/(Fe/Fe_{\odot}) = 4.4$. Cross≡FilD subregions; diamonds≡southwestern subregions; squares≡RegNE and North subregions.

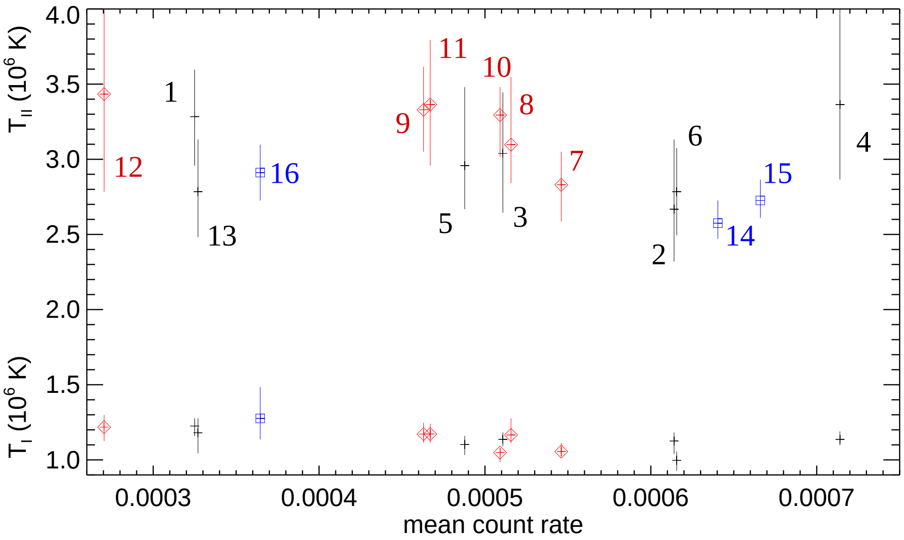

Figure 3.7: Best fit values of T_I (cooler component) and T_{II} (hotter component) versus the mean MOS count-rate (in bin of 10″) for the 16 subregions of Fig. 3.2. In subregions 14 and 15 (whose spectra are well described by one component) only T_{II} is indicated. T errors are at 90% confidence level, while the maximum errors in the count-rate are 3×10^{-6} s^{-1}. Symbols as in Fig. 3.6.

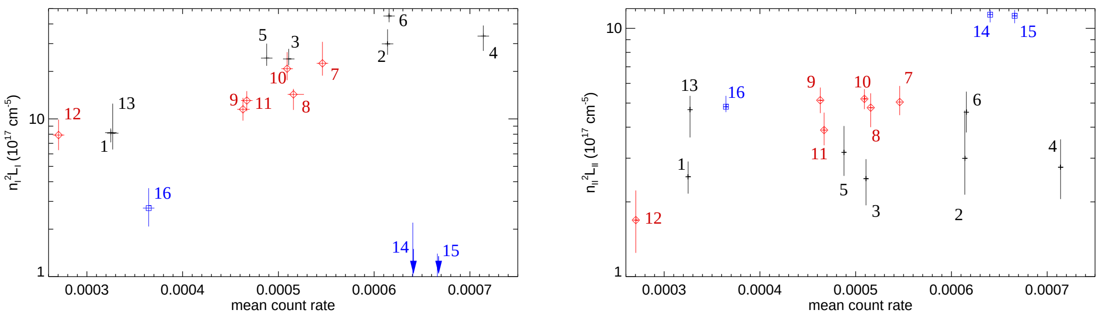

Figure 3.8: Best fit values of the emission measure per unit area (i. e. the product of the square of the density n of the plasma times its geometric extension along the line of sight L) of the cooler component, *left panel*, and of the hotter component, *right panel*, vs. the mean MOS count-rate (in bin of $10''$) for the 16 subregions of Fig. 3.2. For subregions 14 and 15 (whose spectra are well described only by the hotter component), an upper limit to the cooler component is reported. Errors as in 3.7, symbols as in Fig. 3.6.

in the Vela SNR. Preliminary results on this issue will be provided in Chapter 5, where a large-scale (and high-resolution) description of the northern rim of the Vela shell is presented.

3.3 The physical interpretation

3.3.1 Thermal structure of the region

As pointed out in the previous section, the observed spectra are described well by two thermal components at $\sim 10^6$ K and $\sim 3 \times 10^6$ K. Since in each subregion the mean photon energy is almost uniform (maximum variations of $\sim 25 - 30$ eV), two distinct components necessarily indicate two different thermal phases of the interstellar medium intercepted *along the line of sight.* Since the emission measures per unit area are highly inhomogeneous, we can conclude that the EPIC data reveal for the first time that both these phases are associated with the ISM inhomogeneities (therefore, in what follows, I will use the term “clouds” to indicate these hot, X-ray emitting structures). This is at variance with ROSAT data, which suggested (Bocchino et al. 1999) an association of the hotter thermal component with the inter-cloud medium. Clouds can so be described as two-temperature structures.

Assuming that the temperature of the shocked plasma is mainly determined by the local density (the post-shock temperature increases with the shock Mach number, $\mathcal{M} \propto n^{-1/2}$, as shown in eq. 1.7, eq. 1.8, and eq. 1.12), we conclude that, since the temperature of each component is uniform in the FOV, the density of each phase is also similar for all the observed clouds. Therefore, differences in surface brightness imply differences in the extension of the two phases along the line of sight. The two components of the X-ray emission can be related to two different parts of the ISM clouds with different densities: a core, which corresponds to the cooler and denser component, and a hotter and less dense corona, which reasonably surrounds the core.

Figures 3.7 and 3.8 show the best-fit temperatures and emission measures versus the mean MOS count-rate (for a bin size of 10″) in the corresponding subregion. It is then possible to conclude that the trend in the $\overline{E}$ vs. CR scatter plot of Fig. 3.4 can be determined by the relative dimensions of the cores and of the coronae.

3.3.2 Density of the cores and of the coronae

An upper limit to the density of the cloud cores (and hence of the coronae) is the density n_{opt} of the optical filament of Fig. 3.3. The multi-wavelength study of the FilD region performed by Bocchino et al. (2000) has shown that $n_{opt} = 3.2 - 8.2$ cm^{-3}, so we can infer that the density of the X-ray emitting plasma is $\lesssim 5$ cm^{-3}.

Considering the lower limits (at 90% confidence level) of the emission measure (shown in Fig. 3.8) and an upper limit for the extension along the line of sight, L_{max}, it is possible to get an estimate of the lower limits of n_I and n_{II}. The shocked inhomogeneities cannot extend beyond the Vela SNR, so the length of the chord intercepted by the Vela shell along the line of sight represents the maximum extension L_{max} of the clouds in this direction. By approximating the Vela shell as a sphere with radius $r_{Vela} \approx 5.06 \times 10^{19}$ cm, in FilD $L_{max} \approx 5.8 \times 10^{19}$ cm and $n_I > 0.32$ cm^{-3}, while, in RegNE, $L_{max} \approx 5.1 \times 10^{19}$ cm and $n_{II} > 0.14$ cm^{-3}.

On the other hand, we may assume that FilD has an average extension along the line of sight comparable to its size in the plane of the image ($L_{FilD} \sim 2 \times 10^{18}$ cm) and, in this way, we obtain a best guess value for $n_I \sim 1.5$ cm^{-3}. In the same way, setting $L_{RegNE} \sim 3 \times 10^{18}$ cm, we obtain a best guess value for $n_{II} \sim 0.55$ cm^{-3}. Notice that these values indicate pressure equilibrium between cores and coronae.

An independent estimate of a lower limit of n_I can be obtained from the evidence that the cloud cores have reached the collisional ionization equilibrium. Modelling the cooler component of the spectra with the PSHOCK non-equilibrium model (Borkowski et al. 2001), I obtain best-fit values of $\tau_{NEI} \approx 2 \times 10^{13}$ s/cm^{-3} with a lower limit (for subregion 4) of 2×10^{11} s/cm^{-3}, so:

$$\tau_{NEI} = \int_{t_{FilD}}^{t_{Vela}} n_I(t)dt = \overline{n}_I(t_{Vela} - t_{FilD}) > 2 \times 10^{11} \quad \text{s/cm}^3 \tag{3.1}$$

where $(t_{Vela} - t_{FilD})$ is the elapsed time since the shock reached FilD, and $\overline{n}_I$ is the average density in this period. Assuming the Sedov model describes the evolution of the shock in the inter-cloud medium, we have:

$$t_{Vela} - t_{FilD} = \int_{r_{FilD}}^{r_{Vela}} \frac{dr}{v(r)} = t_{Vela} \left[1 - \left(\frac{r_{FilD}}{r_{Vela}} \right)^{5/2} \right] . \qquad (3.2)$$

If FilD and the center of the Vela shell lie on a same plane, normal to the line of sight, $r_{FilD} \approx 4.1 \times 10^{19}$ cm , therefore $t_{Vela} - t_{FilD} \approx 4500$ yr and, from eq. (3.1), $\overline{n}_I > 1.4$ cm^{-3}. Conversely, by putting $\overline{n}_I = 5$ cm^{-3}, it is possible to obtain a lower limit for $t_{Vela} - t_{FilD}$, in this way we infer that FilD was shocked at least 1300 yr ago.

A similar useful estimate of a lower limit for n_{II} is not possible, because in the coronae there is no a univocal signature of CIE and the hotter component can also be described with a NEI model, as shown in Sect. 3.2.3. The results can be summarized as follows:

$$\textbf{Cores:} \quad \begin{cases} n_I \approx 1.5 \ (0.32 \div 5) \quad (\mathrm{cm}^{-3}) \\ \overline{n}_I \gtrsim 1.4 \quad (\mathrm{cm}^{-3}) \end{cases}$$

$$\textbf{Coronae:} \quad n_{II} \approx 0.55 \ (0.14 \div 5) \quad (\mathrm{cm}^{-3})$$

It is worth noting that the association of the two spectral components with two physical phases of the cloud is only a schematic representation of a more complicated scenario. It is reasonable to think that in the post-shock medium there is a wide distribution of temperatures and densities and that each components contribute to the total observed spectrum. Because of the limited spectral response of the CCD detectors, we can only resolve two well-defined "averaged" regimes that seems to be typical of all the shocked structures in this region of the Vela. In Chapter 4, where the HD modeling of the FilD cloud is discussed, I'll show the details of this link between spectral components and physical regions of the shocked cloud.

3.3.3 3D map of the plasma

Merging the results of the spectral analysis with the related images, I derive the three-dimensional structure of the observed ISM clouds with resolution down to less than 0.1 pc. These maps are based on the assumption that the observed X-ray emission at any position in the field of view can be described with two-component thermal models having the same temperatures values, but different emission measure weights. The two temperatures were computed as mean values over all the spectral subregions presented in Sect. 3.2.3, also assuming the same Ne/Fe ratio anywhere. This approach allows me to derive maps of the extensions along the line of sight of the cores (L_I) and of the coronae (L_{II})

In each pixel, the MOS count-rates R_s, in the $0.3-0.5$ keV band, and R_h, between 0.5 keV and 1 keV are:

$$R_s = \Lambda_s^{MOS}(\overline{T}_I)\frac{n_I^2 L_I \Omega}{4\pi} + \Lambda_s^{MOS}(\overline{T}_{II})\frac{n_{II}^2 L_{II}\Omega}{4\pi} \tag{3.3}$$

$$R_h = \Lambda_h^{MOS}(\overline{T}_I)\frac{n_I^2 L_I \Omega}{4\pi} + \Lambda_h^{MOS}(\overline{T}_{II})\frac{n_{II}^2 V_{II}\Omega}{4\pi} \tag{3.4}$$

where $\Lambda_{s,h}^{MOS}(T)$ is the function of radiative losses per emission measure folded with the *XMM-Newton* MOS response (in the corresponding energy band) and Ω is the solid angle subtended by a pixel. The $\Lambda_{s,h}^{MOS}(T)$ values were calculated with the simulation of a MOS observation (in the soft and in the hard band) of an isothermal plasma with temperature $\overline{T}_{I,II}$, abundances $\overline{Fe}/Fe_\odot$ and $\overline{Ne}/Ne_\odot$ and with $(n_I^2 L_I \Omega/4\pi) = 1$. In this way I find: $\Lambda_s^{MOS}(\overline{T}_I) = 20.08$ cm^5 s^{-1}; $\Lambda_h^{MOS}(\overline{T}_I) = 14.21$ cm^5 s^{-1}; $\Lambda_s^{MOS}(\overline{T}_{II}) = 53.53$ cm^5 s^{-1}; and $\Lambda_h^{MOS}(\overline{T}_{II}) =$ 191.02 cm^5 s^{-1}.

Solving the system of eqs. (3.3) and (3.4) for $n_{I,II}^2 L_{I,II}$ we obtain:

$$n_I^2 L_I = \left(\frac{4\pi}{\Omega}\right)\frac{R_h\Lambda_s^{MOS}(\overline{T}_{II}) - R_s\Lambda_h^{MOS}(\overline{T}_{II})}{\Lambda_s^{MOS}(\overline{T}_{II})\Lambda_h^{MOS}(\overline{T}_I) - \Lambda_s^{MOS}(\overline{T}_I)\Lambda_h^{MOS}(\overline{T}_{II})} \tag{3.5}$$

$$n_{II}^2 L_{II} = \left(\frac{4\pi}{\Omega}\right)\frac{R_s\Lambda_h^{MOS}(\overline{T}_I) - R_h\Lambda_s^{MOS}(\overline{T}_I)}{\Lambda_s^{MOS}(T_{II})\Lambda_h^{MOS}(\overline{T}_I) - \Lambda_s^{MOS}(\overline{T}_I)\Lambda_h^{MOS}(\overline{T}_{II})}\ . \tag{3.6}$$

Notice that eqs. (3.3) and (3.4) hold only if the count-rate in each pixel does not depend on the count-rate in the adjacent pixels, so the angular extension of the pixels has to be larger than that of the PSF. For this reason I realize two MOS count-rate images (in the $0.3-0.5$ keV and $0.5-1$ keV bands respectively) by rebinning with a pixel-size of $16''$. I then apply eqs. (3.5) and (3.6) at each pixel of these images and thereby obtain a high resolution map of n^2L for the two components. From this map it is possible to know the emission measure of the plasma with a spatial resolution $\lesssim 0.05$ pc. It is important to remark that the results obtained from eqs. (3.5) and (3.6) are consistent with the findings of the spectral analysis; for example, in subregion 14 (where we expect the largest differences, since T_{II} is significantly different from $\overline{T}_{II}$) the best fit value of $n_{II}^2 L_{II}$ is $1.13 \pm 0.05 \times 10^{18}$ cm^{-5}, while from the n^2L map we obtain that, in this subregion, the mean value of $n_{II}^2 L_{II}$ is $\sim 1.09 \times 10^{18}$ cm^{-5}.

Assuming given values for the density of the cloud cores and of the cloud coronae, (for example, the estimate $n_I = 1.5$ cm^{-3} and $n_{II} = 0.55$ cm^{-3}, reported in Sect. 3.3.2), it is then possible to derive the extension along the line of sight of the two components for each pixel of the n^2L map. Figs. 3.9 and 3.10 show the 3-D structure of the cores (in white) and of the coronae (in transparent blue), presented from two different angle-shots.

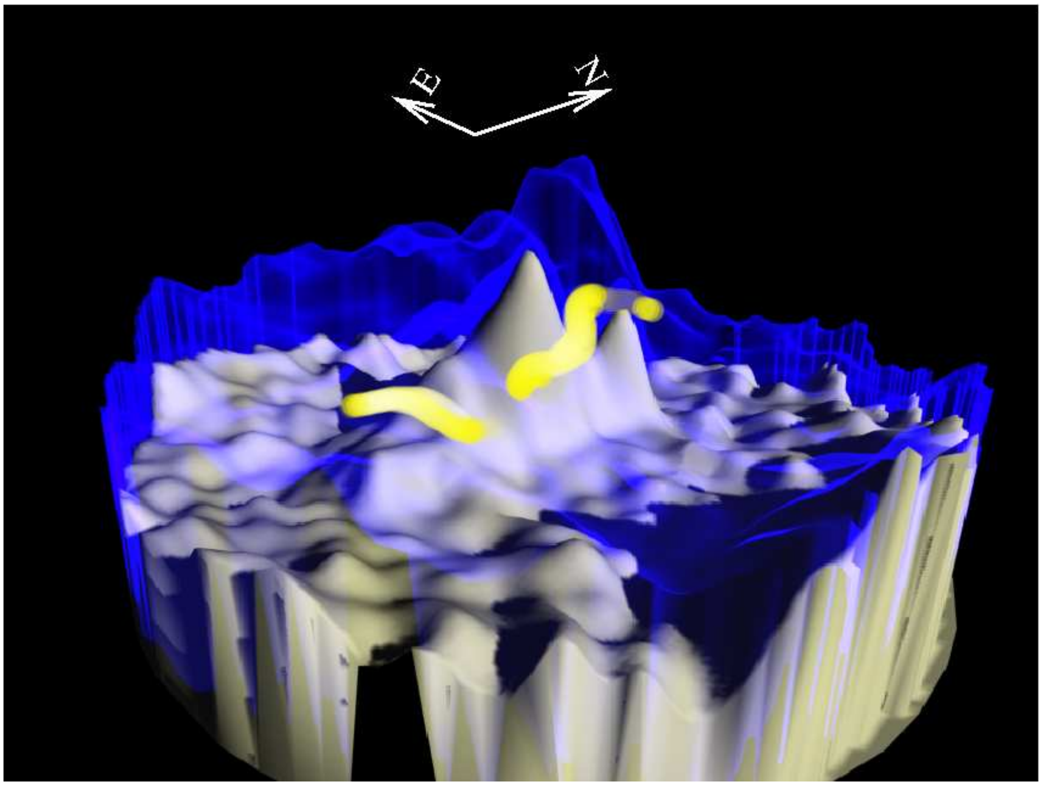

Figure 3.9: 3-D map of the observed ISM clouds. The height of the features is proportional to the extension along the line of sight of the cores (L_I, in white) and of the coronae (L_{II}, semi-transparent blue). North and East are also indicated. In this image the structure of FilD is visible; the optical filament of Fig. 3.3 lies between the two peaks, corresponding to subregions 2 and 4 of Fig. 3.2 and its morphology is sketched in yellow (see also Fig. 4.2). Assuming $n_I = 1.5$ cm^{-3} and $n_{II} = 0.55$ cm^{-3}, the maximum value for L_I is $\sim 4.4 \times 10^{18}$ cm and for L_{II} is $\sim 4.7 \times 10^{18}$ cm (for other values of density L scale as $1/n^2$).

In the map, the large core of FilD is surrounded by a very thin corona and the two white peaks correspond to the two bright parts of FilD (A and B in Fig. 3.1 and subregions 2 and 4 of Fig. 3.2). In RegNE the core is nearly absent (I remind that the spectra extracted in RegNE are described well by a single, hot, thermal component) and the corona is very thick. It is possible that the core of RegNE lies outside of the EPIC FOV, but, as we shall see in Chapter 5, a new *XMM-Newton* observation of RegNE (where the whole knot is inside the FOV) confirms that in this region there is no evidence for a cold component. As for the southwestern structure, it has a smaller core and a thicker corona than FilD.

I also derive an estimate of the mass of the X-ray emitting plasma in FilD. The dimensions of its core are $\sim 2.4 \times 10^{18}$ cm and $\sim 1.1 \times 10^{18}$ cm (on the plane of the observation) and $6.8 \times 10^{18}/n_I^2$ cm (along the line of sight), while its corona has about the same extension on the plane of the observation; but it is an order of magnitude less thick, so the mass of FilD, for $n_I = 1.5$ cm^{-3}, is $\sim 10^{31}$ g (the mass of the corona is $\sim 7 \times 10^{29}$ g). The dimensions of RegNE

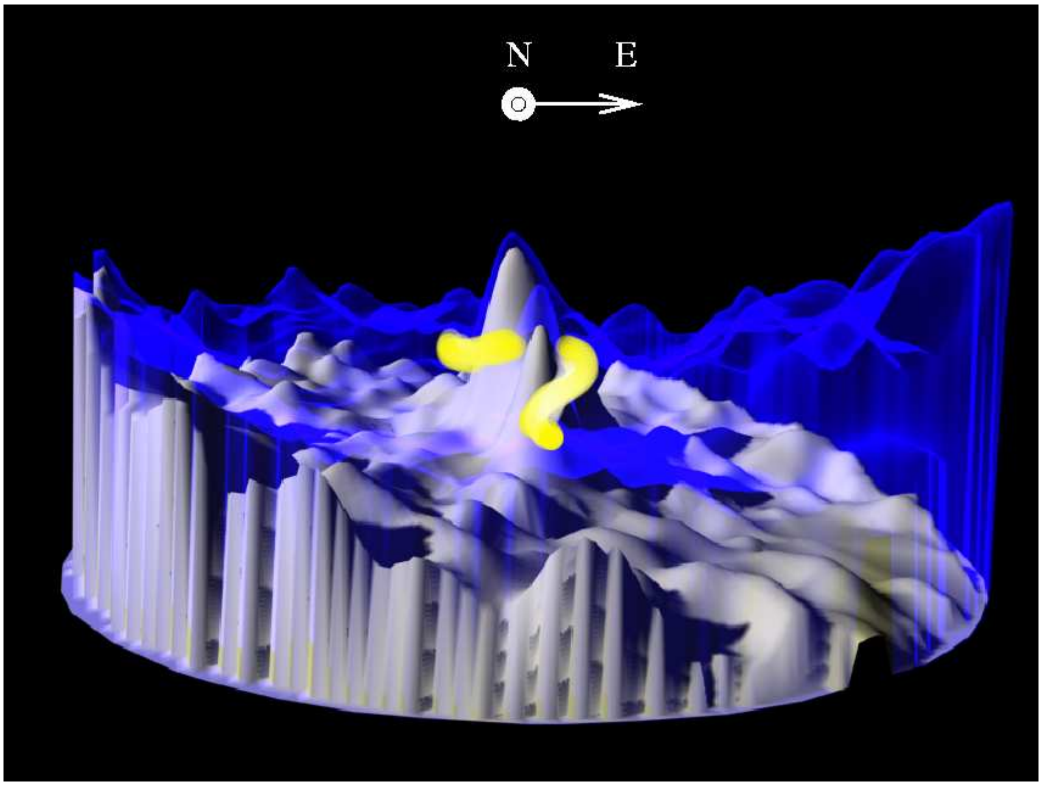

Figure 3.10: Same as Fig. 3.9 from a different angle-shot. The large corona of RegNE is visible in close-up.

are $\sim 1.4 \times 10^{18}$ cm and $\sim 3.3 \times 10^{18}$ cm, on the plane of the observation, and $\sim 1 \times 10^{18}/n_{II}^2$ cm, along the line of sight. Note that with other guesses of the n_I value, assuming pressure equilibrium, the extensions along the line of sight of cores and coronae scale with the same factor ($L \propto 1/n^2$); hence, the relative size of the inhomogeneities does not change.

3.3.4 Shock-cloud interaction

In this section I discuss the dynamics and evolution of the shock-cloud interaction in the observed region in light of my new results.

First of all, since there is neither enhancement of the X-ray emission "behind" the optical filament nor inhomogeneities in the plasma temperature and density, the reflected shock model (see Sect. 1.4.3) is not compatible with the data. This result is further supported by the trend of the points in the $\overline{E}$ vs. CR scatter-plot, as explained in Sect. 3.2.2.

Cloud crushing time

As shown in Sect. 1.4.2, the cloud crushing time is $\tau_{cc} \sim (R_c\chi^{1/2})/v_{ic}$ where, for FilD, we can assume a radius $R_c \approx 1.2 \times 10^{18}$ cm. To obtain an estimate of cloud/intercloud density contrast χ, I find an upper limit for the inter-cloud density n_{ic}. This value was obtained introducing a third hotter MEKAL component in the analysis of the spectra of the subregions 12 and 16, where there are no distinct signatures of the presence of significant inhomogeneities, and considering the upper limit of its emission measure. In this way I obtain $n_{ic} \lesssim 0.06$ cm^{-3}. Since the density of FilD is ~ 1.5 cm^{-3} (Sect. 3.3.2), $\chi \approx 30$.

Since there is no significant emission behind the main shock it is not possible to directly measure the shock velocity in the intercloud medium, v_{ic}. However, it can be estimated by using the Sedov model (Sect. 1.3), where

$$v(ic) = \frac{2r_{Vela}^{5/2}}{5t_{Vela}} r_{FilD}^{-3/2} \tag{3.7}$$

where r_{Vela} and t_{Vela} are the radius and the age of the Vela SNR, and r_{FilD} is the distance between the FilD knot and the center of the shell. We know that $r_{FilD} > 4.1 \times 10^{19}$ cm (Sect. 3.3.2) and $r_{FilD} < 5.0 \times 10^{19}$ cm. This upper limit is obtained from eq. 3.1, with $t_{Vela} - t_{FilD} \gtrsim 1300$ yr and then from eq. (3.2). Therefore $v_{ic} = 5.7 - 7.8 \times 10^7$ cm/s. In this way we get

$$2700 < t_{cc} < 3700 \quad \text{yr}.$$

I have already pointed out (Sect. 3.3.2) that FilD was shocked less than 4500 yr ago. Moreover, assuming $n_I = 1.5$ cm^{-3}, we obtain that the time elapsed from the shock impact is about 4200 yr; hence, we are observing the shock-cloud interaction at $\gtrsim 1\ t_{cc}$.

Thermal conduction and radiative cooling

As explained in Sect. 1.4.1, the evolution of the shocked ISM clouds, apart from dragging, is governed by the competition of radiative cooling and thermal conduction with the surrounding medium, so it is important to estimate the efficiency of both these processes to describe the scenario of the shock-cloud interaction. The radiative and conductive time-scales have been defined in Sect. 1.4.2. To estimate the radiative time-scale (eq. 1.16) in the FilD region, I calculate $\Lambda(T)$ in the $0.01 - 50$ keV band for core and corona, following Mewe et al. 1985, Mewe et al. 1986, Liedahl et al. 1995. I find: $\Lambda(\overline{T}_I) \approx 1.0 \times 10^{-22}$ erg s^{-1} cm^3 and $\Lambda(\overline{T}_{II}) \approx 3.4 \times 10^{-22}$ erg s^{-1} cm^3. As for the conductive time-scale (eq. 1.18), since in the observed inhomogeneities I detect only two temperatures, we can reasonably approximate the temperature scale-heights l with the extensions of the clouds. The dimensions of FilD and of RegNE are reported in Sect. 3.3.3; the southwestern structure extends beyond the EPIC FOV, so it is not possible to estimate its dimensions.

I then estimate τ_{rad} and τ_{cond} for the cores and the coronae of FilD and of RegNE for all the permitted values of the density (Sect. 3.3.2), assuming pressure equilibrium between cores and coronae. The coronae are heated through thermal conduction from the hotter and less dense inter-cloud medium; on the other hand, they lose their thermal energy through radiative losses and thermal conduction towards the cooler cores. Notice that, since the inter-cloud medium is hotter and less dense than the coronae, Eq. (1.18) predicts that the heating of the coronae is more efficient than their cooling through thermal conduction.

In FilD, for all the permitted values of density, I find $\tau_{rad} \approx 4 \times 10^5$ yr and $\tau_{cond} \approx 2 \times 10^3$ yr: the radiative cooling is negligible (its time-scale is more than an order of magnitude higher than the age of the Vela SNR), so the FilD corona gains thermal energy by means of thermal conduction from the inter-cloud medium. This heating produces the progressive evaporation of the corona.

The FilD core is heated through thermal conduction from the surrounding hotter corona. On the other hand, it loses thermal energy through radiative losses and, if we assume that the optical filament lies inside FilD, through thermal conduction toward the optical filament. The radiative and conductive cooling time-scales are invariably of the same order ($\tau_{rad}/\tau_{cond} = 0.8 \div 1.5$) and are $\sim 5\times10^4$ yr ($\sim 10^5$ yr, for $n_I = 1.4$ cm^{-3}, and $\sim 2\times10^4$ yr, for $n_I = 5$ cm^{-3}). The heating time-scale is shorter and corresponds to the thermal conduction cooling time-scale of the FilD corona ($\sim$ 2000 yr). It is possible to estimate whether this core is gaining or losing energy: the heating rate is $H \propto (n_{II}kT_{II}V_{II})/\tau_{cond}$, where V_{II} is the volume of the FilD corona and τ_{cond} is the conductive time-scale of the corona; the cooling rate is $C \propto (n_I kT_I V_I)/\tau_{rad}$, where V_I is the volume of the core and τ_r is its radiative cooling time-scale. The ratio C/H is always lower than 0.22, so we conclude that there is a net heating of the FilD core. As for RegNE, where the core is nearly absent, for all the permitted values of density, $\tau_r \approx 500\tau_c$. Hence, the radiative cooling is also negligible in this cloud.

These conclusions are not significantly affected by NEI. As shown in Sect. 3.2.3, we cannot rule out the possibility that the hotter component has not reached CIE conditions yet. However, since the temperature in non-equilibrium of ionization is higher than in CIE, the thermal conduction to the cores is more efficient, so the time-scale for the heating of the cores is lower and the evaporation rate of the coronae is higher than in CIE.

3.3.5 The physical scenario in FilD

As we pointed out in the previous sections, the thermal conduction between the cores and the coronae and especially between the coronae and the inter-cloud medium is a very efficient process. On the other hand, the estimated value of t_{cc} (Sect. 3.3.4) and the presence of an optical filament within the FilD core (and into the southwestern structure) indicate that a transmitted shock is propagating through a cloud. Notice, however, that, although the reflected shock scenario can be rejected, it is difficult to explain the peculiar orientation of the optical filament in the FilD cloud as the result of a simple transmitted shock. In fact, while in the southwestern structure the optical emission runs parallel to the inferred direction of the transmitted shock front planes (i. e. perpendicular to the radius of the shell), the orientation of the FilD optical filament is almost aligned with the radius of the Vela shell (see also Fig. 4.2).

The emerging scenario is that the observed X-ray emission comes from the cloud plasma heated "internally" by the transmitted shock and "externally" by the thermal conduction from the hotter inter-cloud medium. In the inner and denser part of the cloud, the shock is radiative and the plasma cools off through radiative optical emission, while in the cores and in the coronae there is a net heating of the plasma which evaporates in the inter-cloud medium in a few 10^3 yr. Fig. 3.11 is a schematic representation of the structure of the FilD cloud, which summarizes all the ISM phases we identified on the basis of optical and X-rays data.

The detailed interpretation of these results is, however, not straightforward. It is possible that cores and coronae are pre-existing phases of the ISM clouds, that may be a chaotic mix of dense and tenous gas, or may have a density profile that smoothly decreases in the outer parts. Another possibility is that the formation of the coronae is induced by thermal conduction. The hot X-ray emitting component may then be the results of the interaction with the shock front and coronae may be associated with the cloud material that is evaporating in the intercloud medium. It is difficult to discriminate between these scenarios only on the basis of the observation analysis and it is also difficult to obtain a convincing explanation of the physical origin of these components and to understand the differences in the relative weight of core and corona that we observe in FilD and in RegNE. Also the physical origin of the optical emission is not completely clear. A deeper physical insight into these important issues, obtained with detailed hydrodynamic modeling, will be presented in Chapter 4 and in Chapter 5.

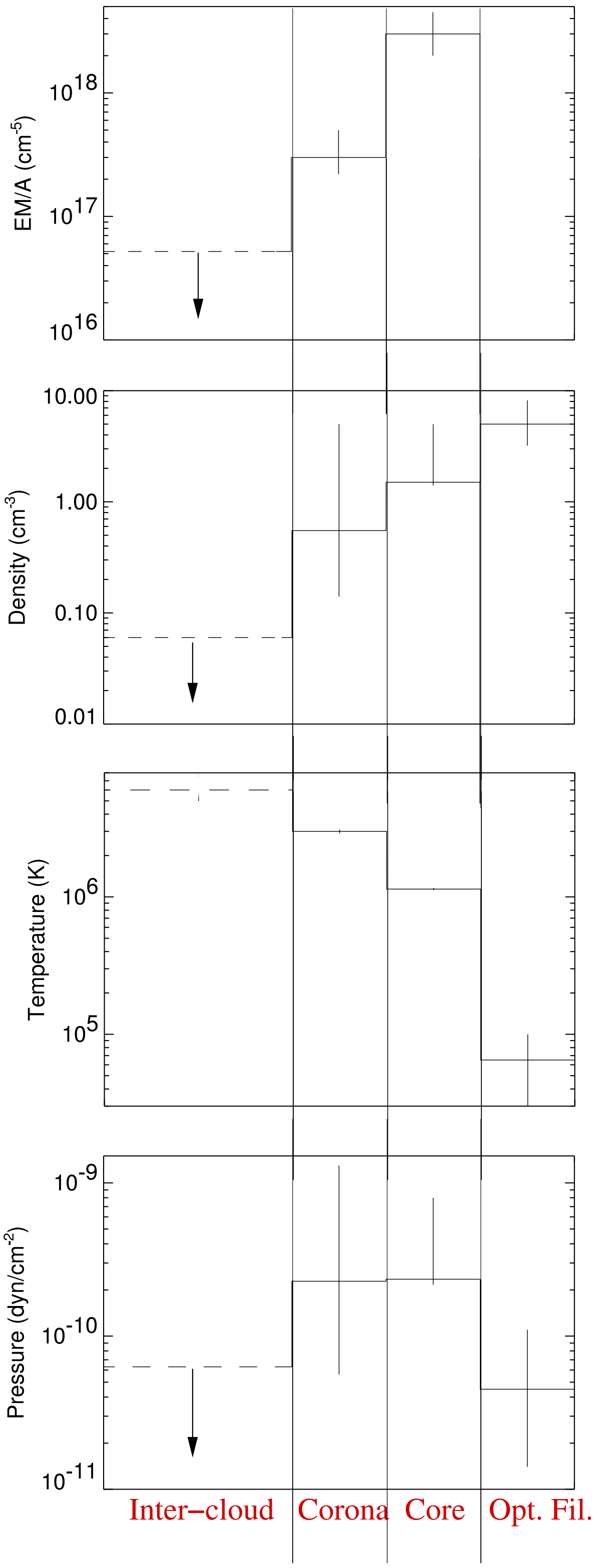

Figure 3.11: Schematic view of the FilD post-shock structure. The derived values of emission measure per unit area (in the $0.3 - 1.1$ keV band), particle density, temperature and pressure are reported for the different ISM phases together with their error bars (at 90 % confidence level). The values for the optical filament are taken from Bocchino et al. (2000), the inter-cloud temperature has been derived using the Sedov model.

Chapter 4

Shock-cloud interaction in the Vela SNR. Hydrodynamic modeling of the Vela FilD region

In this chapter I present the accurate modeling of the interaction of the Vela SNR shock front with the FilD cloud (see also Miceli et al. 2006b). As pointed out in Sect. 1.4.1, because of the intrinsic complexity of the system under study, a detailed modeling is required to interpret the results of the observation analysis and to understand the physical origin of the observed emission. Moreover, no detailed comparison between models and observations has yet been provided. To this end, FilD is an ideal "laboratory ", because, as I showed in Chapter 3, it is a nearby, bright (both in X-rays and in the optical band) and isolated (no other clouds are seen in projection) shocked cloud, whose X-ray emission has been studied in great detail.

The chapter is organized as follows: in Sect. 4.1 I present the modeling approach and its aims (Sect. 4.1.1), I discuss the constraints for the simulations (Sect. 4.1.2) and the model equations (Sect 4.1.3) and setups (Sect. 4.1.4); the results are presented in Sect. 4.2 and discussed in Sect. 4.3.

4.1 Hydrodynamic modeling

4.1.1 The forward modeling approach

The methodological approach followed to model the shock-cloud interaction in the Vela FilD region is described by the flowchart shown in Fig. 4.1.The starting point is the observation, studied through an accurate data analysis. To describe the observed system, I then define the physical model, including all the relevant physical effects. The model corresponds to a set of conservation equations, which we need to solve. To describe the evolution of the system, we need time-dependent compressible fluid equations, shown in Sect. 4.1.3, which are non-linear partial differential equations. The results of the observation analysis (i. e. the post-shock conditions) constrain the values of the physical parameters for the model setup. Once defined initial conditions and parameters, the model equations are solved by performing detailed and accurate numerical simulations. The simulation results consist in space distributions of plasma temperature, density, and velocity, sampled at regular time intervals. From each set of distributions we are able to synthesize a corresponding spectrally-resolved map of X-ray emission and spectra. After filtering it through the instrumental response, the synthesized maps and spectra can be directly compared with the *XMM-Newton* EPIC data (and with optical observations of the FilD region) and it is also possible to perform on the synthesized products the same analysis carried on for the EPIC data. We call this approach "forward modeling"

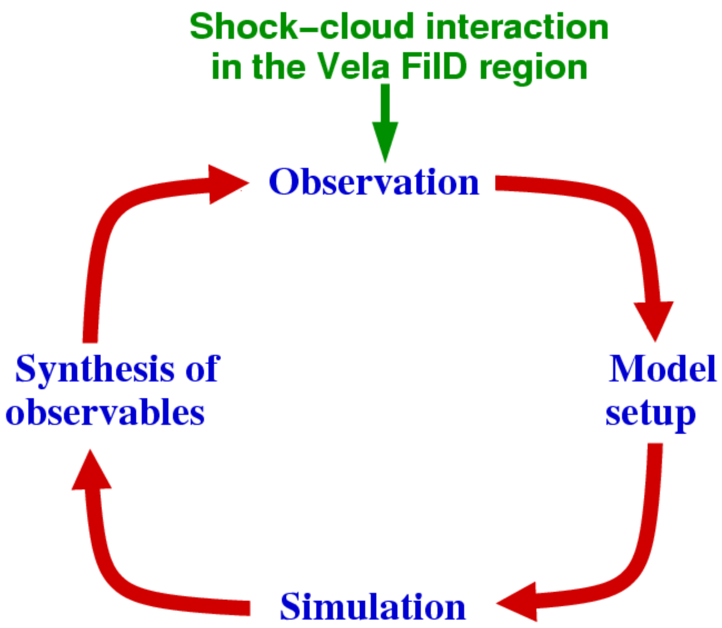

Figure 4.1: Flowchart of the methodological approach for the modeling of the shock-cloud interaction in the Vela FilD region.

The aims of this work are: i) the proper interpretation of the *XMM-Newton* observation (i. e. to understand the physical origin of the two spectral components, to ascertain the evolutionary stage of the interaction, to obtain information about the density and temperature profiles of the emitting plasma); ii) to understand the role of the different physical processes (transmitted and reflected shocks, thermal conduction, radiative cooling) in the evolution of the system; iii) to obtain a key for the interpretation of future X-ray observations of middle-aged SNRs.

The open issues are related, in particular, to the causes of the presence of the two X-ray emitting components and to their association with physical (pre-shock or post-shock) phases of the clouds and with specific heating processes. Do both components originate in the plasma behind the transmitted shock? Are these components associated with different pre-shock phases of the FilD cloud, or are they a result of the shock-cloud interaction (maybe related with the cloud evaporation)? Moreover, as explained in Sect. 3.3.5, it is difficult to understand the origin of the optical filament. Optical filaments in SNRs are usually associated with the plasma behind the transmitted shock which travels through dense interstellar clouds, because they are typically aligned with the transmitted shock front planes. In the FilD region, instead, the filament is almost aligned along the South-North direction and, therefore, it is perpendicular to the plane of the incident shock front, as shown in Fig. 4.2, where the X-ray emission contour levels are superimposed on an Hα image of the FilD region.

4.1.2 Constraints from the observations

Fig. 4.3 shows the *XMM-Newton* EPIC MOS count rate images of the FilD region in the $0.3-0.5$ keV, $0.5-1$ keV, and $0.3-2$ keV energy bands. With respect to the images presented in Sect. 3.2, these image are rebinned to a bin size $10.4''$ and do not include the EPIC pn contribution. The images are adaptively smoothed to a signal-to-noise ratio of 10 and vignetting-corrected as in Miceli et al. (2006a). The *XMM-Newton* images show that shape and size of the FilD X-ray knot are similar in the three energy bands. I remind the reader that the extension of the X-ray emitting knot is $\sim (2 \times 1 \times 1) \times 10^{18}$ cm.

As shown in Sect. 3.2.3, the X-ray spectra in the FilD region are described well by two thermal components in collisional ionization equilibrium at $\sim 1{\times}10^6$ K and $\sim 3{\times}10^6$ K, respectively and the emission measure (EM) of the cooler component is about one order of magnitude larger than that of the hotter component (Fig. 3.8). The post-shock density of the cooler component (core) is $n_I = 1.5-5$ cm^{-3} and the corona post-shock density is about three times lower. The inhomogeneity of the surface brightness in the FilD region is determined by different volume distributions along the line of sight of the two components. In particular, the surface brightness increases with the EM per unit area of the soft component. Moreover, in Sect. 3.3.4, I estimated that the shock velocity in the intercloud medium is $v_{ic} = 5.7-7.8 \times 10^7$ cm/s. Therefore, according to Eq. 2.2, the shock temperature is $T_{sh} = 4.6-8.6 \times 10^6$ K. I also derived the mean abundances of O ($\overline{O}/O_\odot \approx 1.0$), Fe ($\overline{Fe}/Fe_\odot = 0.39 \pm 0.05$), and Ne ($\overline{Ne}/Ne_\odot = 1.7 \pm 0.2$). Finally, I estimated that FilD was shocked $\sim 1300-4500$ yr ago. I will use these results as constraints for the modeling.

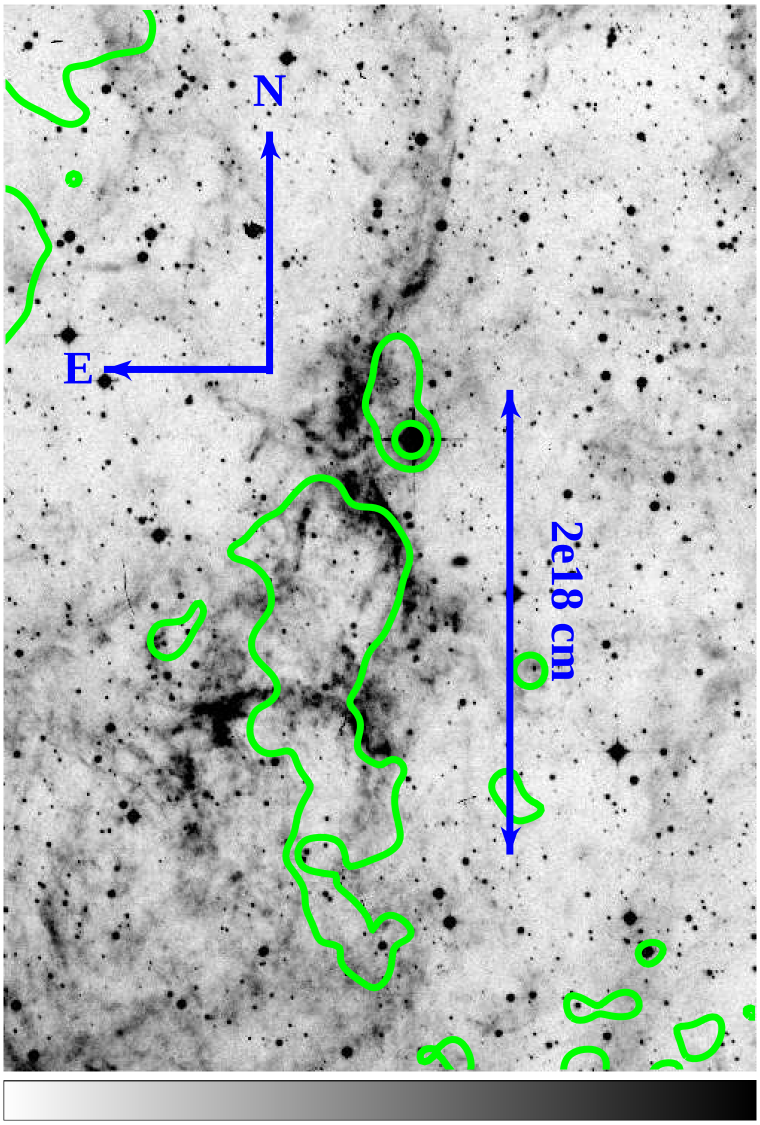

Figure 4.2: Vela FilD Hα emission (from AAO/UKST H-alpha survey). I have superimposed, in green, the X-ray contour levels at a count rate 2.4 times higher than the minimum, derived from the EPIC observation in the $0.3 - 2$ keV band (Fig. 3.2).

4.1.3 The model equations

I model the impact of a plane-parallel SNR shock on an isolated uniform cloud in pressure equilibrium with the ambient (intercloud) isothermal medium (Fig. 4.4). The plane-parallel approach is justified because, as clearly shown in Fig. 1.11, the FilD cloud is small (< 1 pc) with respect to the curvature radius of the Vela shell (~ 15 pc). The shock-cloud interaction is described by means of a two-dimensional hydrodynamic model. We solve the time-dependent compressible fluid equations of mass, momentum, and energy conservation. Since the analysis of the X-ray emission of FilD has shown that it is important to include the

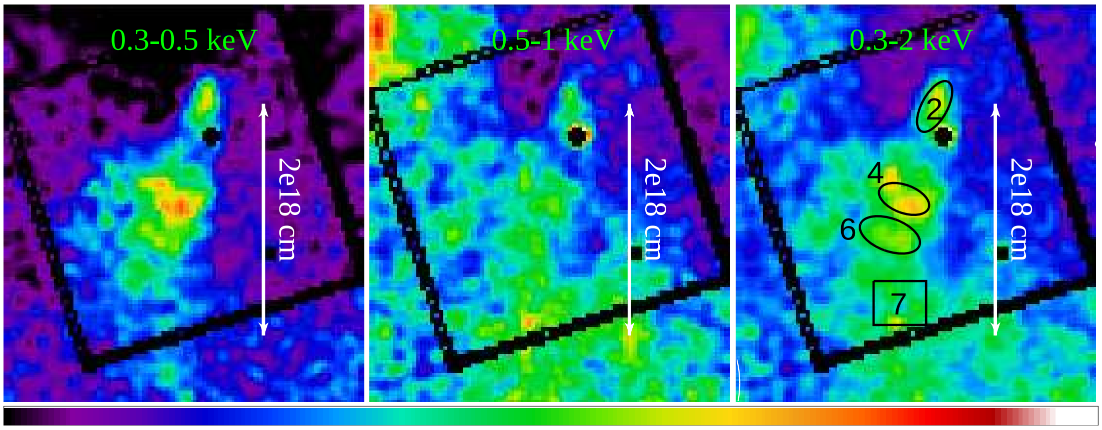

Figure 4.3: *XMM-Newton* EPIC MOS count rate images of the Vela FilD knot, observed in different energy bands. I smoothed the images adaptively to a signal-to-noise ratio of 10. The bin size is $10.4''$, corresponding to 3.9×10^{16} cm, assuming a distance $D = 250$ pc. The color bar has a linear scale and the count rates range between 1.2×10^{-4} s^{-1} bin^{-1} and 6×10^{-4} s^{-1} bin^{-1}, in the $0.3 - 0.5$ keV and $0.5 - 1$ keV images, and between 2.4×10^{-4} s^{-1} bin^{-1} and 1.2×10^{-3} s^{-1} bin^{-1}, in the $0.3 - 2$ keV images.

radiative cooling of the plasma and thermal conduction between the different phases of the emitting material (Sect. 3.3.4), the model equations are:

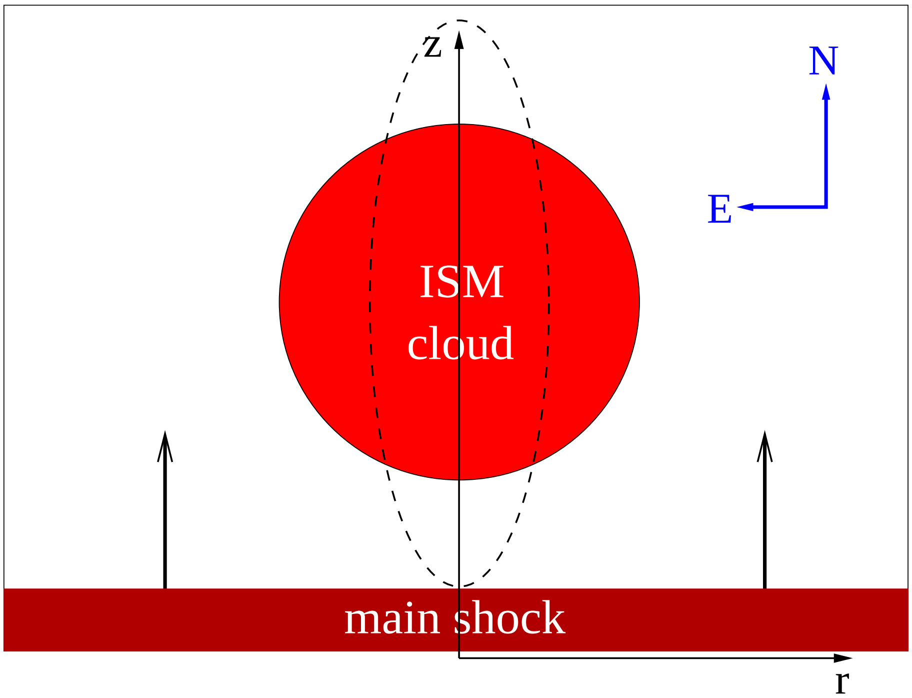

Figure 4.4: Schematic representation of the initial conditions of the simulations. The system consists of a planar shock-front which interacts with a spherical/ellipsoidal (dashed line) isolated ISM cloud. The $(r,\ z)$ plane is also indicated.

$$\frac{\partial \rho}{\partial t} + \nabla \cdot \rho \mathbf{v} = 0 \tag{4.1}$$

$$\frac{\partial \rho \mathbf{v}}{\partial t} + \nabla \cdot \rho \mathbf{v}\mathbf{v} + \nabla P = 0 \tag{4.2}$$

$$\frac{\partial \rho E}{\partial t} + \nabla \cdot (\rho E + P)\mathbf{v} = -\nabla \cdot \mathbf{q} - n_e n_H \Lambda(T) \tag{4.3}$$

with

$$E = \epsilon + \frac{1}{2}|\mathbf{v}|^2 \ , \qquad P = (\gamma - 1)\rho\epsilon \ , \tag{4.4}$$

where $\mathbf{v}$ is the bulk velocity of the gas, t is the time, P the pressure, T the temperature, n_e and n_H are the electron and hydrogen number density, respectively (we assume $n_e = n_H$), $\rho = \mu m_H n_H$ is the mass density ($\mu = 1.26$, assuming cosmic abundances), $\Lambda(T)$ is the radiative losses function per unit emission measure (Raymond & Smith 1977, Mewe et al. 1985), and q is the conductive flux, defined following Dalton & Balbus (1993) as

$$q = (1/q_{spi} + 1/q_{sat})^{-1} \ , \tag{4.5}$$

where q_{spi} and q_{sat} are the classical (Spitzer 1962) and saturated (Cowie & McKee 1977, Dalton & Balbus 1993) conductive flux, respectively

$$q_{spi} = -\kappa(T)\nabla T \ , \tag{4.6}$$

$$q_{sat} = -\text{sign}(\nabla T) 5\phi\rho c_s^3 \tag{4.7}$$

with $\kappa(T) = 5.6 \times 10^{-7} T^{5/2}$ erg s^{-1} K^{-1} cm^{-1}, $\phi = 0.3$ (in agreement with the values suggested by Giuliani 1984 and Borkowski et al. 1989 for a fully ionized cosmic gas), and where $c_s = \sqrt{2kT_e/\mu m_H}$ is the isothermal sound speed. Here I briefly discuss these two conductive regimes. The Spitzer thermal conduction is a diffusive process due to the diffusion of hot electrons. The dependence of $\kappa(T)$ on $T^{5/2}$ in Eq. 4.6 derives from the relationship $\kappa(T) \propto \lambda_e$, where λ_e is the electron mean free path

$$\lambda_e = t_{eq}\left(\frac{3kT_e}{m_e}\right)^{1/2} \tag{4.8}$$

where $t_{eq} \propto T^{3/2}$ is the electron-electron equipartition time, which indicates the time in which collisions produce a large alteration in the original velocity distribution and is defined as the mean time in which electron-electron deflections gradually deflect a test electron by 90°. Whereas λ_e is of the same order as the temperature scale-height, l (or lower, as in the shock transition zone), the test electron does not follow a random walk and the diffusive Spitzer model is not applicable. In this case we apply the saturated conduction, where the heat flux is $q_{sat} = (3/2)n_e kT_e v_{char}$, where $v_{char} = \alpha\sqrt{kT_e/m_e}$ is the characteristic speed of the electrons and differs form the thermal speed because of the α parameters. This parameter includes the effects of the electrostatic fields that impede the free streaming of the electrons. By putting $\alpha = 20/3\ \phi\sqrt{2m_e/\mu m_H}$ we then obtain, after some algebra, Eq. 4.7 (we are assuming ions and electrons to have the same temperature). Equation 4.5 assures a smooth transition between these two regimes. Notice that the saturated thermal conduction in the shock transition zone may determine the formation of a "conductive precursor" of the shock front. In fact, because of thermal conduction, the plasma immediately behind the shock front can heat the pre-shock medium thus producing a shock precursor. I here show that this "conductive front" does not move faster than the shock front. The speed of the conductive front has to be of the same order of v_{char}, and, since $\phi = 0.3$, $v_{char} = 160 \times T^{1/2}$ m/s. Also the shock front velocity is proportional to $T^{1/2}$ and is $v_{shock} = 270 \times T^{1/2}$ m/s (see Eq. 2.2 and McKee & Hollenbach 1980), therefore the conductive front does not overtake the shock front.

Finally, I add to the set of equations 4.1-4.3, the equation:

$$\frac{\partial C_{\rm cl}}{\partial t} + \nabla \cdot C_{\rm cl}\mathbf{v} = 0 \qquad (4.9)$$

where $C_{\rm cl}$ is the mass fraction of the cloud inside the computational cell. Therefore, by definition, the pre-shock cloud material has $C_{\rm cl} = 1$, while $C_{\rm cl} = 0$ in the intercloud ambient medium. By adding this equation we can follow the time evolution of the cloud material which can be identified by this passive (zero mass) tracer. The tracer can be considered as a "color" that marks the cloud material, because it does *not* modify the dynamics of the system.

The numerical solutions

The set of equations has been solved numerically by using the advanced hydrodynamic simulation tool *FLASH* (Fryxell et al. 2000), upgraded to include thermal conduction and radiative losses from an optically thin thermal plasma (see Orlando et al. 2005). The FLASH code is based on a directionally split Piecewise-Parabolic Method (PPM) Riemann solver (Woodward & Colella 1984), and uses adaptive mesh refinement (PARAMESH, MacNeice et al. 2000), particularly appropriate to describe the moving steep gradients at the boundaries of the shock front. The code is made parallel with Message Passing Interface (MPI) directives for efficient execution on high performance computers and is structured into a collection of components called FLASH modules. The FLASH code is described in more detail in Appendix B.

The simulations presented in this chapter have been performed on the IBM pSeries p4 and p5 systems at the Consorzio Interuniversitario CINECA (Bologna, Italy) in the framework of the INAF / CINECA Agreement. The IBM pSeries p5 high performance computer at the CINECA (IBM SP5/512) is an IBM SP cluster of 512 IBM Power 5 processors (clock 1.9 GHz), with 64 nodes and 1.2 TB RAM memory, with a peak performance of 3.89×10^{12} floating-point operations per second (3.89 TFlop/s). The simulations were also performed on a Linux cluster at the Sistema di Calcolo per l'Astrofisica Numerica SCAN of the INAF - Osservatorio Astronomico G. S. Vaiana di Palermo. This machine is a Linux Cluster EXADRON with 24 AMD Opteron 250 processors (clock 2.2 GHz), 12 IB nodes, and a total RAM memory of 48 Gb.

The total computational time (summed on all the processors) is $\sim$ 9000 CPU hours.

4.1.4 The model setup

I show results of four simulations with different model setups. The setup of the physical parameters is dictated by the results of the analysis of the X-ray data. The relevant parameters are: the cloud/intercloud density contrast, the shock temperature, and the cloud dimension. Table 4.1 shows the initial physical parameters of the four setups. In all the setups the intercloud pre-shock temperature is 10^4 K and the intercloud pre-shock density is 0.05 cm^{-3}. In setup Sph1 and Sph2 the cloud is spherical, whereas in setup Ell1 and Ell2 we consider an ellipsoidal cloud, with the semimajor axis b_{cl} aligned with the incident shock velocity. The Mach number $\mathcal{M}$ (i. e. the shock speed in units of the intercloud isothermal sound speed) and the density contrast χ (i. e. the ratio cloud/intercloud density) are $\mathcal{M}_{S1E1} = 50$, $\chi_{S1E1} = 20$ (for setup Sph1 and Ell1); $\mathcal{M}_{S2E2} = 57$, $\chi_{S2E2} = 30$ (for setup Sph2 and setup Ell2). The shock temperature is then 4.6×10^6 K (for $\mathcal{M} = 50$) and 6.6×10^6 K (for $\mathcal{M} = 57$), according to our estimates ($T_{sh} = 4.6 - 8.6 \times 10^6$ K, see Sect. 3.3.4 and Sect. 4.1.2). According to the results of Orlando et al. (2005), for these Mach values, radiative cooling dominates over thermal conduction (see Fig. 1.7). This implies the local formation of thermal instabilities in structures with dimensions $L > L_F = 1.3 \times 10^6 T^2/n$ ($L_F \sim 10^{16}$ cm, for $T = 2 \times 10^5$ K and $n = 5$ cm^{-3}), which is the critical Field length (Field 1965), introduced in Sect. 1.4.2. Notice, however, that the results reported in Orlando et al. (2005) were derived for an impact of a SNR shock with a spherical cloud with radius $R = 3.09 \times 10^{18}$ cm, while our clouds are smaller. So we expect lower values of the characteristic length of temperature variations, l, in our simulations. Since the characteristic conductive time-scale is proportional to the inverse of the square of the temperature scale-height (Eq. 1.18), smaller clouds imply a higher efficiency of thermal conduction, which may inhibit the formation of thermal instabilities.

Table 4.1: Physical parameters of the model setups. In all the setups the intercloud pre-shock temperature is 10^4 K and the intercloud pre-shock density is 0.05 cm^{-3}. The setups marked in boldface are those discussed in detail in this chapter.

Model setup	**Sph1**	Sph2	Ell1	**Ell2**
Cloud morphology	**Sphere**	Sphere	Ellipsoid	**Ellipsoid**
Cloud Radius/semiaxis (10^{18} cm)	$\boldsymbol{R_{cl} = 2}$	$R_{cl} = 3.09$	$a_{cl} = c_{cl} = 1,\ b_{cl} = 3.09$	$\boldsymbol{a_{cl} = c_{cl} = 1,\ b_{cl} = 3.09}$
Cloud density (cm^{-3})	$\boldsymbol{n_{cl} = 1}$	$n_{cl} = 1.5$	$n_{cl} = 1$	$\boldsymbol{n_{cl} = 1.5}$
Density contrast	**20**	30	20	**30**
Cloud mass ($\mathrm{M}_\odot$)	$\boldsymbol{M_{cl} = 0.035}$	$M_{cl} = 0.196$	$M_{cl} = 0.032$	$\boldsymbol{M_{cl} = 0.047}$
Shock temperature (10^6 K)	$\boldsymbol{T_{sh} = 4.6}$	$T_{sh} = 6$	$T_{sh} = 4.6$	$\boldsymbol{T_{sh} = 6}$
Mach number	**50**	57	50	**57**

The cloud pre-shock density is 1 cm^{-3}, for setup Sph1 and Ell1, and 1.5 cm^{-3}, for setup Sph2 and Ell2. Since we are in the strong shock limit ($\mathcal{M} >> 1$), we can apply Eq. 1.6 to derive an indication of the cloud post-shock density. We then obtain 4 cm^{-3} (Sph1 and Ell1) and 6 cm^{-3} (Sph2 and Ell2), according to our estimates of the density of the cloud cores and of the optical emitting medium (see Fig. 3.11).

To describe the interaction of the shock front with a spherical or ellipsoidal cloud, the simulations can be performed in a cylindrical 2-D coordinate system (r, z), assuming axial symmetry (see Fig.4.4). The computational domain extends over 1.5×10^{19} cm in the r direction and over 2×10^{19} cm in the z direction. I use reflection boundary conditions at $r = 0$ and zero-gradient boundary conditions (for $\mathbf{v}$, ρ, and p) elsewhere. The shock velocity is parallel to the z axis, which corresponds to the North direction in the *XMM-Newton* observation. The post-shock initial conditions are given in the strong shock limit (Zel'Dovich & Raizer 1967). The finest spatial resolution is $\sim 1.95 \times 10^{16}$ cm, therefore we have more than 100 zones per cloud radius in setup Sph1 and Sph2 and $\gtrsim 150$ and $\gtrsim 50$ zones per semimajor and semiminor axis, respectively, in setup Ell1 and Ell2. The typical time-step is $\sim 5 \times 10^5$ s.

4.1.5 Synthesis of the X-ray emission

The hydrodynamic modeling allows us to simulate the detailed evolution of the temperature and density of the shock-cloud system. From the computed temperature and density we are able to synthesize the X-ray emission detectable with the *XMM-Newton* EPIC-MOS1 camera (Turner et al. 2001), by using the following procedure. From the 2-D maps of n and T we obtain the full 3-D distributions in the cartesian space (x', y', z') (where the y' axis corresponds to the direction of the line of sight and is perpendicular to the (r, z) plane), by applying the symmetry condition: $(r,\ z) \leftrightarrow (x'^2 + y'^2 = r^2,\ z' = z)$. I then derive the emission measure, $EM(x',\ y',\ z')$, and temperature, $T(x',\ y',\ z')$, for each fluid element and the distribution $EM(x',\ z')$ vs. $T(x',\ z')$ (hereafter EMD) integrated along the line of sight (which is parallel to the plane of the shock front), for each (x', z'), in the temperature range $0.58 - 16 \times 10^6$ K (using 145 bins equispaced in $\log T$). From the EMDs, I synthesize the maps of the X-ray emission and the focal plane spectra using the MEKAL spectral code (Mewe et al. 1985, Mewe et al. 1986, Liedahl et al. 1995), with solar abundances for all the elements, but Fe ($Fe/Fe_\odot = 0.39$) and Ne ($Ne/Ne_\odot = 1.7$), according to the results of the data analysis (see Sect. 3.2.3). The source is assumed at a distance $D = 250$ pc, corresponding to the best estimate of the distance of the Vela SNR, which is known with a $\sim 30\%$ uncertainty (see Sect. 1.6.2 and references therein). I filter the emission through the *XMM-Newton* EPIC-MOS1 instrumental response and the interstellar column density at the Vela FilD knot, $N_H = 1 \times 10^{20}$ cm^{-2}

(see Sect. 3.2.3). The exposure time ($t_{exp}^{synth} = 50$ ks, for the MOS1 camera) is the same as that of the *XMM-Newton* observation ($t_{exp}^{obs} \sim 25$ ks for each MOS camera, as shown in Table 3.1).

I have integrated the emission over a cube with edge length 10^{19} cm (centered on the cloud). This length corresponds to the maximum extension of the inter-cloud post-shock medium along the line of sight and was chosen so as to match the minima of the X-ray synthesized surface brightness with those observed with *XMM-Newton*.

The X-ray emission maps have been produced in the same energy bands analyzed in the previous chapter (i. e. $0.3 - 0.5$ keV, $0.5 - 1$ keV, and $0.3 - 2$ keV) and are presented in Sect. 4.2.1 and Sect. 4.2.2. The space binning of all the model X-ray maps is 3.9×10^{16} cm that corresponds to $10.4''$ (i. e. the bin-size of the *XMM-Newton* EPIC images of Fig. 4.3) at 250 pc. Focal plane spectra have been synthesized for different regions of the domain, to perform a spatially resolved spectral analysis. All spectra have been analyzed using XSPEC (the chosen on-axis response file is m1_medv9q20t5r6_all_15.rsp).

4.1.6 Determination of the evolutionary stage of the interaction

I solve the time-dependent model equations over a time range of $\sim$ 6000 yr, for all the model setups. The FilD observation provides only a "snapshot" of the shock-cloud interaction and it is important to determine which stage of the evolution of the physical system corresponds to the observed one. I have developed a procedure for the selection of a time interval where the solutions of the model equations best describe the observed data. This procedure is based on the definition of three quantities:

1. The extension, A, of the synthesized X-ray emitting knot, defined as the area covered by the region with an X-ray surface brightness three times larger than the minimum (in the $0.3 - 2$ keV energy band).

2. The mean photon energy, MPE, of the synthesized X-ray emitting knot, defined as the mean photon energy in the X-ray emitting region with an X-ray surface brightness three times larger than the minimum (in the $0.3-2$ keV energy band).

3. The count-rate, R, in the soft region, defined as the average count-rate in the region with a mean photon energy between the minimum E_{min} and $1.2 \times E_{min}$.

Figure 4.5 shows the temporal evolution ($t = 0$ corresponds to the impact of the shock front with the cloud) of A (upper panel), MPE (central panel), and

R (lower panel), for setup Sph1 (black diamond) and setup Ell2 (red cross). The corresponding observed values are indicated by the horizontal blue lines, while the vertical green lines indicate the formation of optically emitting plasma (i. e. plasma with temperature $\lesssim 10^5$ K and density > 1 cm^{-3}). No optical emission is therefore present on the left of the green line.

The graphs in Fig. 4.5 indicate that, for both setups, we can identify a temporal range, around 3500 ± 500 yr where the synthesized values globally best approach the observed ones. Below $t = 3000$ yr we do not have optical emission, while above 4000 yr the synthesized values have largest deviations from the observed ones. For all the three quantities, the smallest deviations are at ~ 3500 yr, therefore in what follows I report in detail the results at $t = 3400$ yr, for setup Sph1, and $t = 3550$, for setup Ell2. These values are both consistent with the estimate of the time elapsed after the shock impact ($\sim 1300 - 4500$ yr) provided in Chapter 3.

Figure 4.5 also indicates that, for $t \sim 3500$ yr, setup Ell2 reproduces well the observed values of A and MPE, while in setup Sph1 we have a large area of the X-ray emitting knot and a mean photon energy in the bright regions that is larger than the observed one.

4.2 Results

4.2.1 The spherical cloud

The upper panel of Fig. 4.6 shows, for **setup Sph1**, the 2-D cross-sections through the $(r,\ z)$ plane of temperature and density 3400 yr after the impact of the shock front with the spherical cloud (i. e. at the stage of the interaction which best approaches the observed data, as shown Sect. 4.1.6). Figure 4.6 also shows, for comparison, the cross-sections through the $(r,\ z)$ plane of temperature and density 3550 yr after the impact of the shock front with the ellipsoidal cloud (setup Ell2, see Sect. 4.2.2). Figure 4.7 presents the time evolution of temperature and density in setup Sph1, with the n and T cross-sections through the $(r,\ z)$ plane at different times.

As the shock interacts with the cloud, part of it is transmitted through the cloud (with temperature $\sim 10^6$ K and density ~ 4 cm^{-3}) and a reflected shock propagates backwards in the ambient medium. In Fig. 4.6, the plasma behind the reflected bow shock has a density $n \sim 0.6$ cm^{-3} and it is about three times denser than the intercloud post-shock plasma. The pressure behind the transmitted shock front, P^t, the reflected shock front, P^r, and the main shock front, P^{ms}, is: $P^t \lesssim 1\times10^{-9}$ dyne cm^{-2}, $P^r \sim 6.5\times10^{-10}$ dyne cm^{-2}, and $P^{ms} \sim 2.5\times10^{-10}$ dyne cm^{-2}. The thermal conduction between the cloud and the intercloud medium drives a thin hot halo around the cloud. As the primary shock progressively

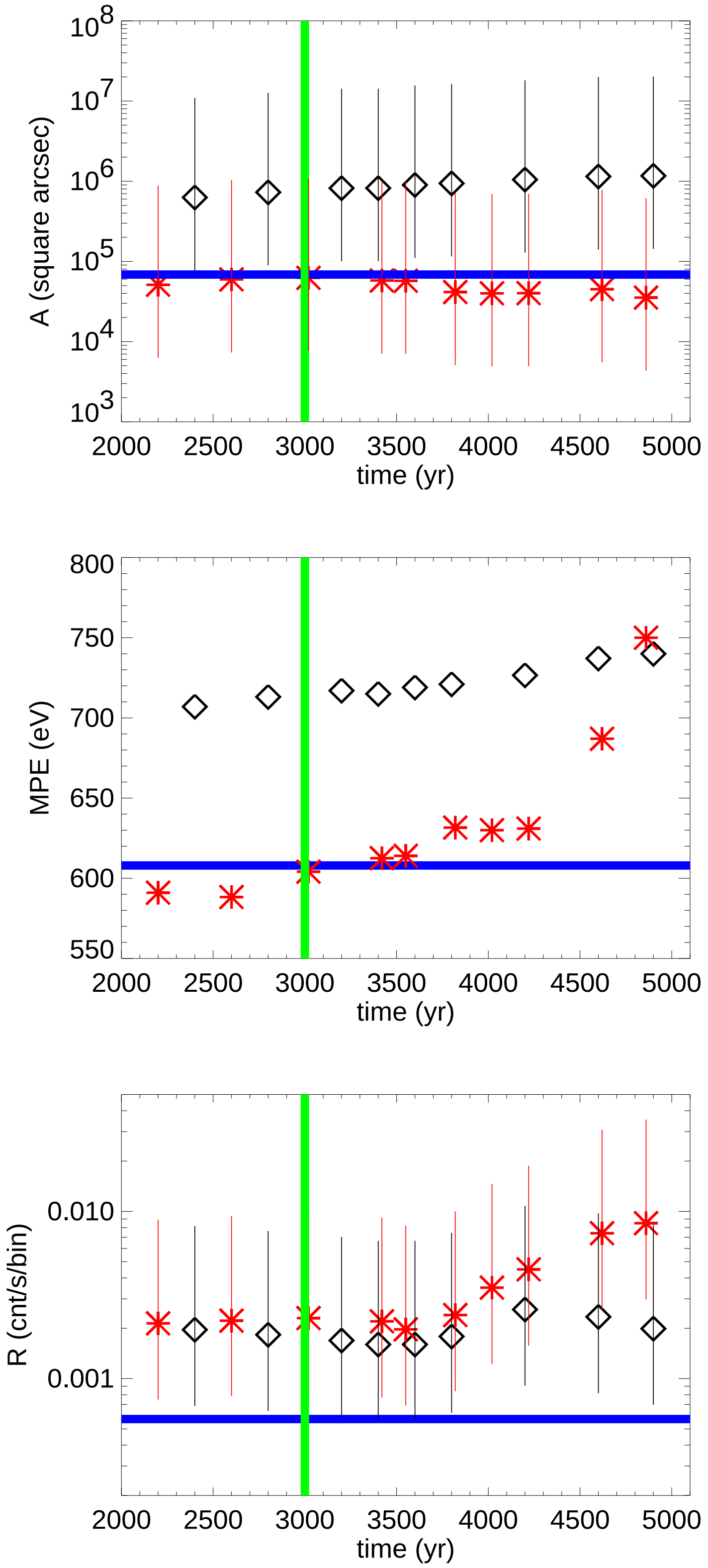

Figure 4.5: Temporal evolution of the quantities A, *upper panel*, MPE, *central panel*, and R *lower panel* (defined in Sect. 4.1.6), for setup Sph1 (black diamond) and setup Ell2 (red cross). The error bars are associated with the $\sim 30\%$ uncertainty in the distance of the Vela SNR. The blue lines correspond to the observed values and the green lines indicate the epoch of the formation of thermal instabilities.

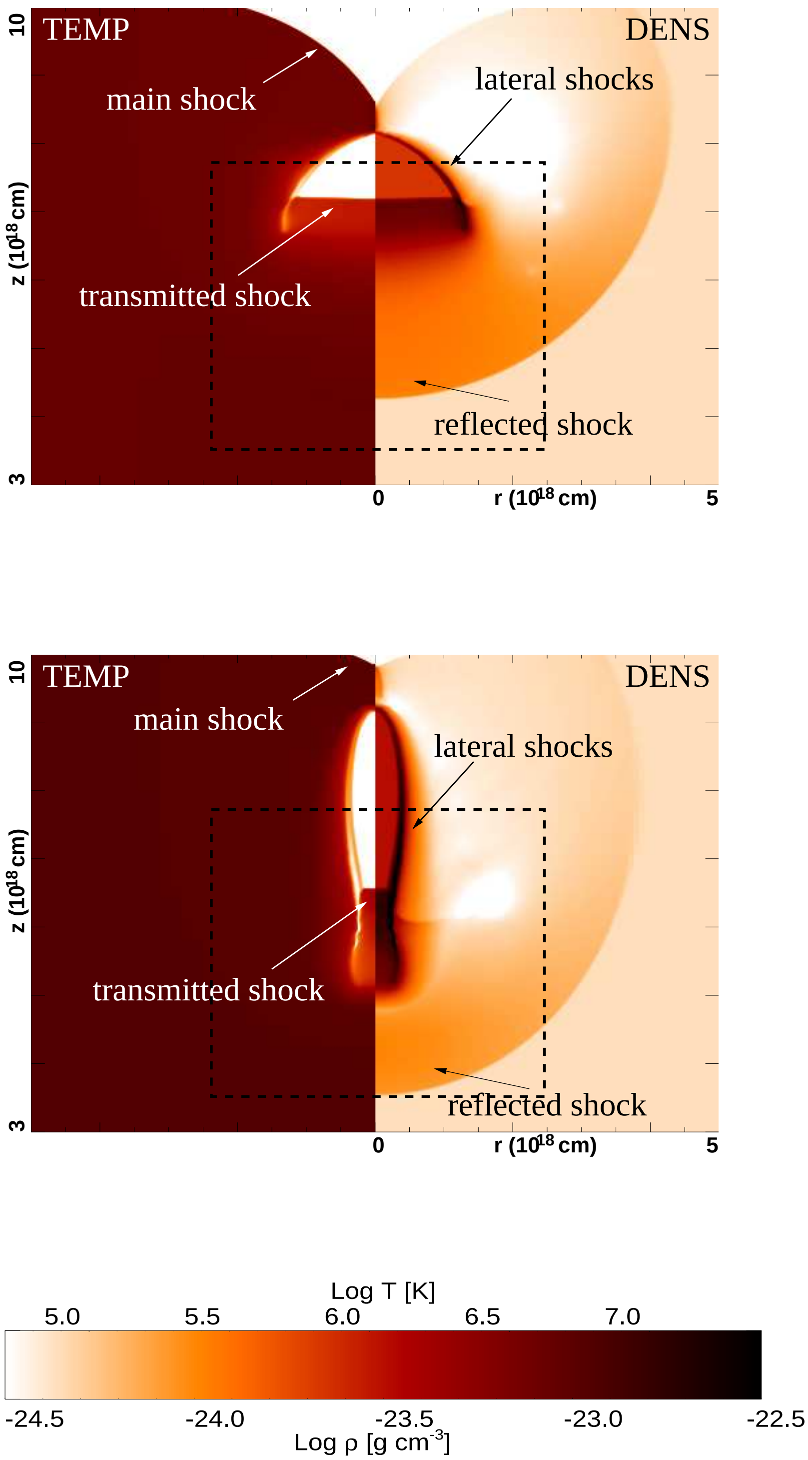

Figure 4.6: *Upper panel:* temperature (on the left) and density (on the right) 2-D cross-sections through the $(r,\ z)$ plane 3400 yr after the impact of the shock front with the spherical cloud (setup Sph1). *Lower panel:* same as upper panel for the ellipsoidal cloud (setup Ell2), 3550 yr after the shock impact. The color bar has a logarithmic scale. The dashed box indicates the field of view of the X-ray count-rate maps showed in Fig. 4.9.

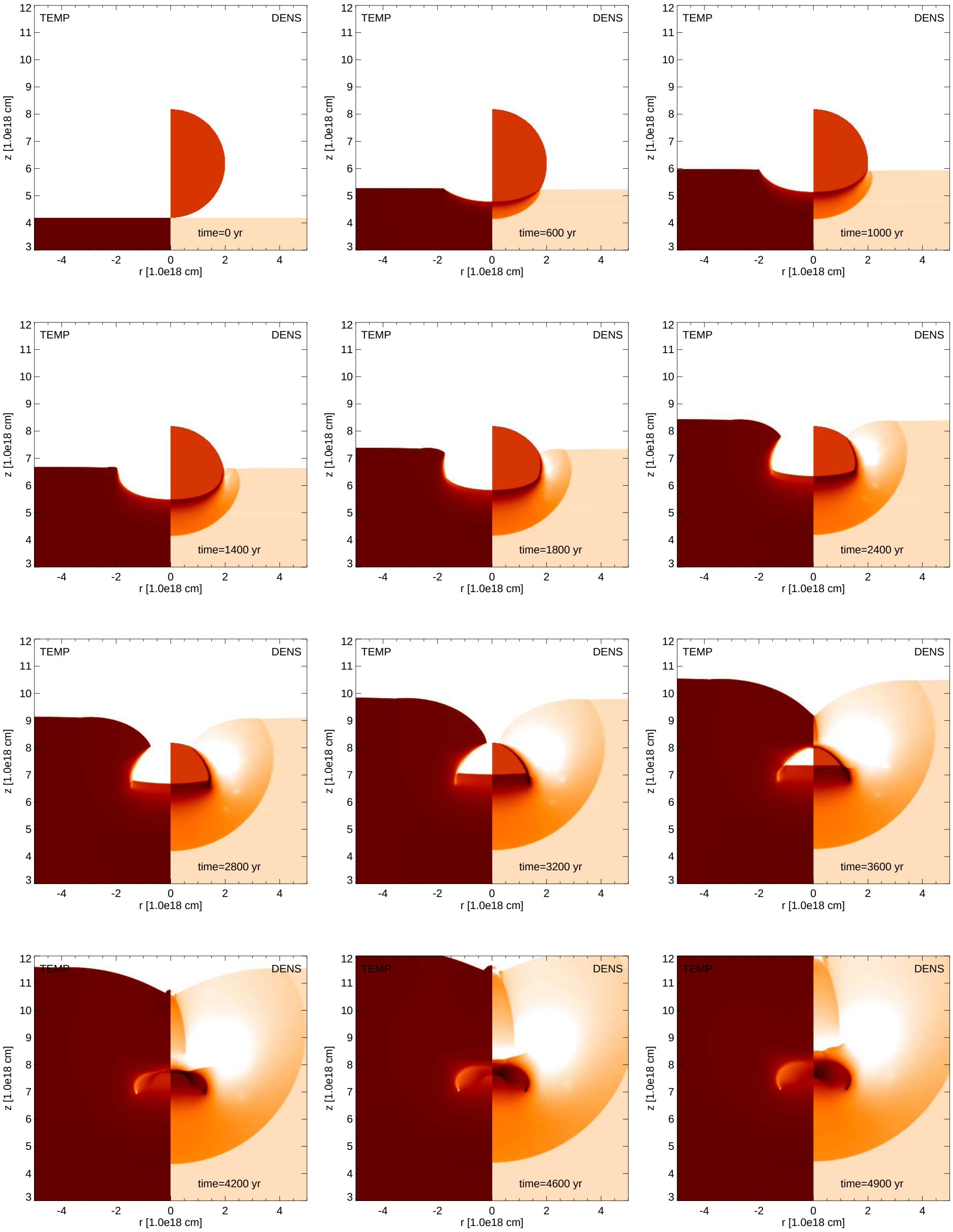

Figure 4.7: Same as upper panel of Fig. 4.6 for different times.

engulfs the cloud, it generates lateral shocks propagating into the cloud.

Figure 4.8 shows the radial (at $z = 7.1 \times 10^{18}$ cm) and axial (at $r = 0$) profiles of density and temperature for setup Sph1, where I have superimposed the estimates of density and temperature for cores and coronae derived from the analysis of the *XMM-Newton* observation of FilD. The shocked cloud is at $r \sim 0 \div 10^{18}$ cm. At the outer edge of the cloud there is a dense (and cold) narrow region (see below) and then, for $r \gtrsim 1.2 \times 10^{18}$ cm, the density and temperature gradually approach the corresponding intercloud values. The axial profiles shows the density and temperature of the plasma behind the main shock front ($z \sim 3 \times 10^{18} \div 4.2 \times 10^{18}$ cm), the reflected shock front ($z \sim 4.2 \times 10^{18} \div 6 \times 10^{18}$ cm), and the transmitted shock front ($z \sim 6 \times 10^{18} \div 7.2 \times 10^{18}$ cm. At $z \sim 7.2 \times 10^{18} \div 8.1 \times 10^{18}$ cm we observe the pre-shock cloud material, at $z \sim 8.1 \times 10^{18} \div 8.6 \times 10^{18}$ cm we observe the northern end of the cloud and the intercloud medium behind the main shock front, while for $z \gtrsim 8.6 \times 10^{18}$ cm we observe the unperturbed intercloud medium.

After $\sim$ 3000 yr, in the regions where the transmitted shock interacts with the lateral shocks, there are dense ($n \sim 5$ cm^{-3}), cold ($T \sim 1 - 2 \times 10^5$ K), and elongated ($L \sim 5 \times 10^{17}$ cm) structures. These structures are larger than the critical Field length and are therefore thermally unstable. They cool off to temperatures of a few 10^4 K, reaching density $n \sim 10$ cm^{-3} in a few hundreds yr (and are visible in Fig. 4.6). These cold and dense structures are also visible in Fig. 4.8. Their density and temperature values are consistent with the characteristic temperature and density of optical filaments in SNRs and with those observed in the FilD region (Bocchino et al. 2000). I caution the reader that the simulations model a plasma where hydrogen is fully ionized and that for very low values of temperature the radiative losses function is not calculated accurately. Therefore the values of temperature and density derived when T approaches the H ionization temperature may not be completely correct. However, the model clearly indicates that thermal instabilities can produce the FilD optical emission.

The upper panels in Fig. 4.9 show the synthesized X-ray maps, for setup Sph1, at the same epoch of Fig. 4.6, derived in the three different energy bands, $0.3-0.5$ keV, $0.5-1$ keV, and $0.3-2$ keV, by following the procedure described in Sect. 4.1.5. The X-ray emission in the $0.3-2$ keV energy band for different times is shown in Fig. 4.10. At $t = 3400$ yr, the synthesized count rate per space bin is, on average, in agreement with the observed one, considering its strong dependence on the source distance D (the synthesized count rate scales as D^{-4}, because the flux scales as D^{-2} and the angular extension of the bin as $D^{-1} \times D^{-1}$) and that the distance of the Vela SNR is known with $\sim 30\%$ uncertainty. Although the overall morphology of the synthesized emission in the $0.3-2$ keV band for setup Sph1 appears similar to the observed one, there are significant differences.

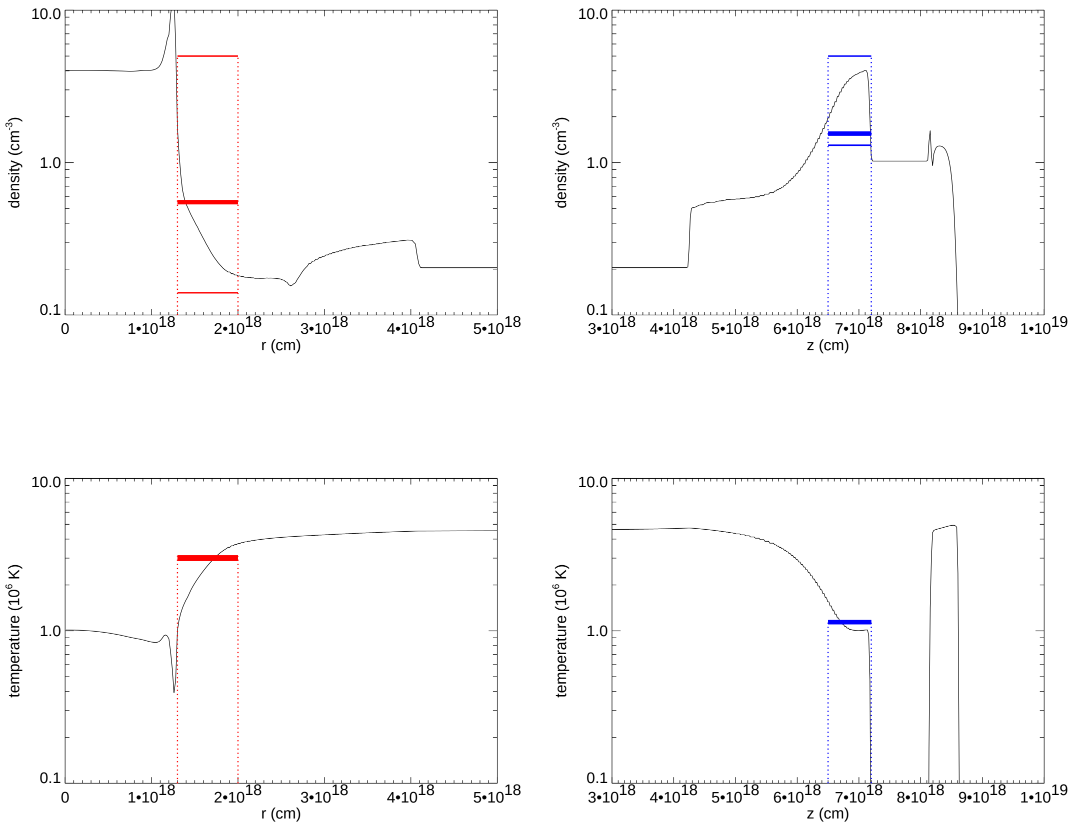

Figure 4.8: Radial (at $z = 7.1 \times 10^{18}$ cm) and axial (at $r = 0$) profiles of density (*upper panels*) and temperature (*lower panels*) 3400 yr after the impact of the shock front with the spherical cloud (setup Sph1, see upper panel of Fig. 4.6). I have superimposed to the corresponding structures the estimates of density and temperature for cores (in *blue*) and coronae (*red*) derived from the analysis of the *XMM-Newton* observation of FilD (with their error bars). The cold and dense spike at $r \sim 1.2 \times 10^{18}$ cm corresponds to a thermal instability.

Great part of the synthesized emission above 0.5 keV, shown in the central upper panel of Fig. 4.9, is clearly associated with the plasma heated by the reflected shock (see Fig. 4.6), while the bulk of the soft X-ray emission in the $0.3-0.5$ keV band originates in the cloud plasma heated by the transmitted shock. The morphology of the synthesized emission below 0.5 keV is then very different from the synthesized emission in the $0.5-1$ keV band. In setup Sph1, therefore, the morphology of the X-ray emitting knot in the broad band $0.3-2$ keV is the result of the superposition of the emission associated with two different physical conditions of the plasma: the cloud material heated by the transmitted shock at North, which contributes with soft emission, and the intercloud material heated by the reflected shock in the central and southern parts of the knot, with harder emission. The extension of the X-ray emitting knot in the $0.3-2$ keV band is significantly larger than that in the $0.3-0.5$ keV band. This result does not match the *XMM-Newton* observation of the FilD knot, which shows that the X-

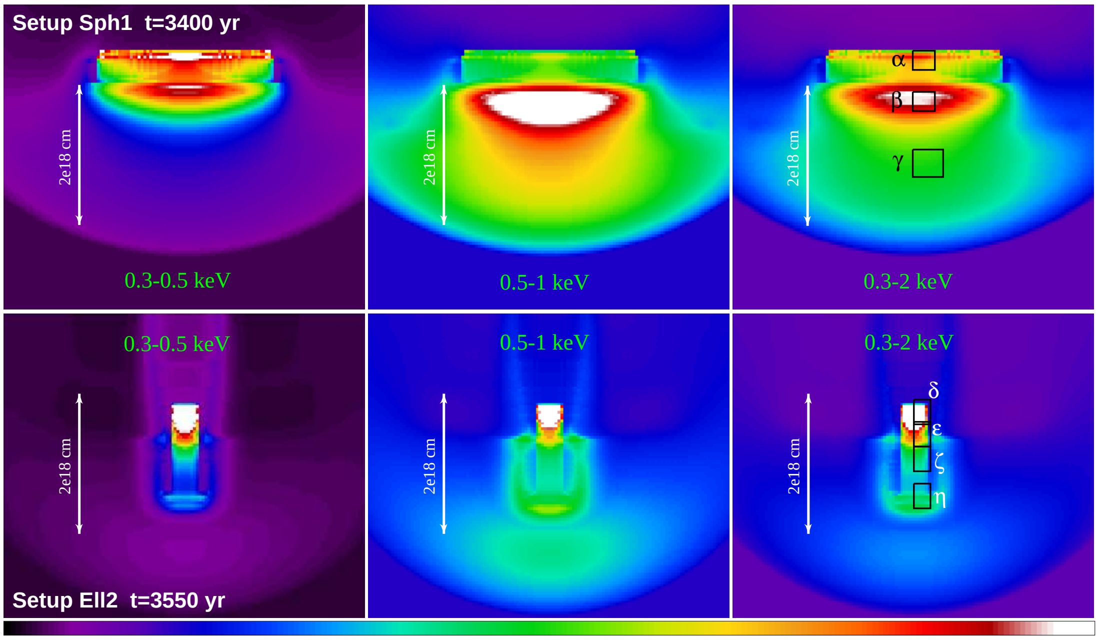

Figure 4.9: Synthesized *XMM-Newton* EPIC MOS count rate images in different energy bands for the interaction of the Vela SNR shock front with a spherical cloud at $t = 3400$ yr after the first impact of the shock with the cloud (setup Sph1, *upper panels*) and with an ellipsoidal cloud at $t = 3550$ yr (setup Ell2, *lower panels*). The field of view of these image is indicated by a dashed box in Fig. 4.6. The bin size of the images is 3.9×10^{16} cm. The color bar has a linear scale between 0 and 1.2×10^{-3} s^{-1} bin^{-1}, in the $0.3-0.5$ keV and $0.5-1$ keV images, and between 0 and 2.4×10^{-3} s^{-1} bin^{-1}, in the $0.3-2$ keV images. The count rate values and the 2×10^{18} cm scale have been obtained assuming a distance $D = 250$ pc. The boxes indicates the regions for the spatially resolved spectral analysis (see Table 4.2).

ray emission in the $0.3-0.5$ keV band has almost the same extension as the ones in the $0.5-1$ keV and $0.3-2$ keV bands (Fig. 4.3).

The upper panel of Fig. 4.11 shows, for setup Sph1, the emission measure of the plasma with $T < 10^5$ K and $n > 3$ cm^{-3} projected in the plane of the sky, which is a proxy of the optical emission. I also superimpose, in green, the corresponding X-ray contour levels at a count rate 2.4 times higher than the minimum, derived from the synthesized X-ray images in the $0.3-2$ keV band shown in Fig. 4.9. The impact of the Vela shock front with the spherical cloud of setup Sph1 produces an optical filament aligned with the incident shock front, at odd with the observation (Fig. 4.2).

To study the distribution of the photon energy across the field of view, I synthesize the MOS mean photon energy map (see Sect. 3.2.2) in the $0.3-2$ keV band. The map is shown in Fig. 4.12 (left panel), where I superimpose the surface brightness contour level at 75% of the maximum in the same energy band.

Table 4.2: Best-fit parameters of the spectral fitting performed simultaneously on the observed MOS spectra and on those synthesized from the hydrodynamic simulations for the spectral regions indicated in Fig. 4.3 and Fig. 4.9. The spectra are described with two thermal components (at temperature T_I and T_{II}) in collisional ionization equilibrium, with an energy-independent multiplicative factor (first row) to take into account the differences in surface brightness between the synthesized and the observed spectra and the different areas of the spectral regions. All the reported errors are at 90% confidence. I compare spectra extracted (synthesized) from regions with similar mean photon energy and/or count rate.

Parameter (setup Sph1*)	Regions $\alpha - 2$	Regions $\alpha - 4$	Regions $\beta - 4$	Regions $\beta - 7$
$factor$	0.37 ± 0.02	0.45 ± 0.02	0.30 ± 0.02	$0.53^{+0.01}_{-0.03}$
T_I (10^6 K)	$0.99^{+0.02}_{-0.03}$	$0.99^{+0.01}_{-0.04}$	$1.44^{+0.06}_{-0.05}$	1.39 ± 0.07
T_{II} (10^6 K)	$3.4{+}0.4_{-0.3}$	3.6 ± 0.4	$3.4{+}0.2_{-0.3}$	3.2 ± 0.2
EM_I/EM_{II}	70 ± 20	70 ± 20	7.2 ± 1.3	$4.8^{+0.8}_{-0.6}$
$Fe/Fe_\odot$	$0.4^{+0.3}_{-0.1}$	0.4 ± 0.1	0.3 ± 0.1	$0.6^{+0.2}_{-0.1}$
Reduced χ^2 (d. o. f.)	1.65 (67)	1.5 (69)	4.51 (78)	2.2 (91)
Parameter (setup Ell2)	**Regions $\delta - 4$**	**Regions $\epsilon - 2$**	**Regions $\zeta - 6$**	**Regions $\eta - 7$**
$factor$	$0.39^{+0.01}_{-0.02}$	0.4 ± 0.2	$1.13^{+0.6}_{-0.5}$	$1.43^{+0.1}_{-0.05}$
T_I (10^6 K)	$1.11^{+0.05}_{-0.03}$	1.04 ± 0.02	$1.00^{+0.04}_{-0.06}$	$1.08 \pm 0. - 5$
T_{II} (10^6 K)	3.5 ± 0.3	3.4 ± 0.2	$3.3^{+0.2}_{-0.4}$	3.5 ± 0.2
EM_I/EM_{II}	40 ± 11	38^{+10}_{-8}	24^{+5}_{-4}	8 ± 3
$Fe/Fe_\odot$	0.5 ± 0.2	$0.4^{+0.2}_{-0.1}$	$0.5^{+0.2}_{-0.1}$	0.4 ± 0.1
Reduced χ^2 (d. o. f.)	1.68 (65)	1.08 (72)	2.65 (80)	2.07 (90)

* In region γ the synthesized spectrum is completely different from the observed ones (reduced $\chi^2 > 10$).

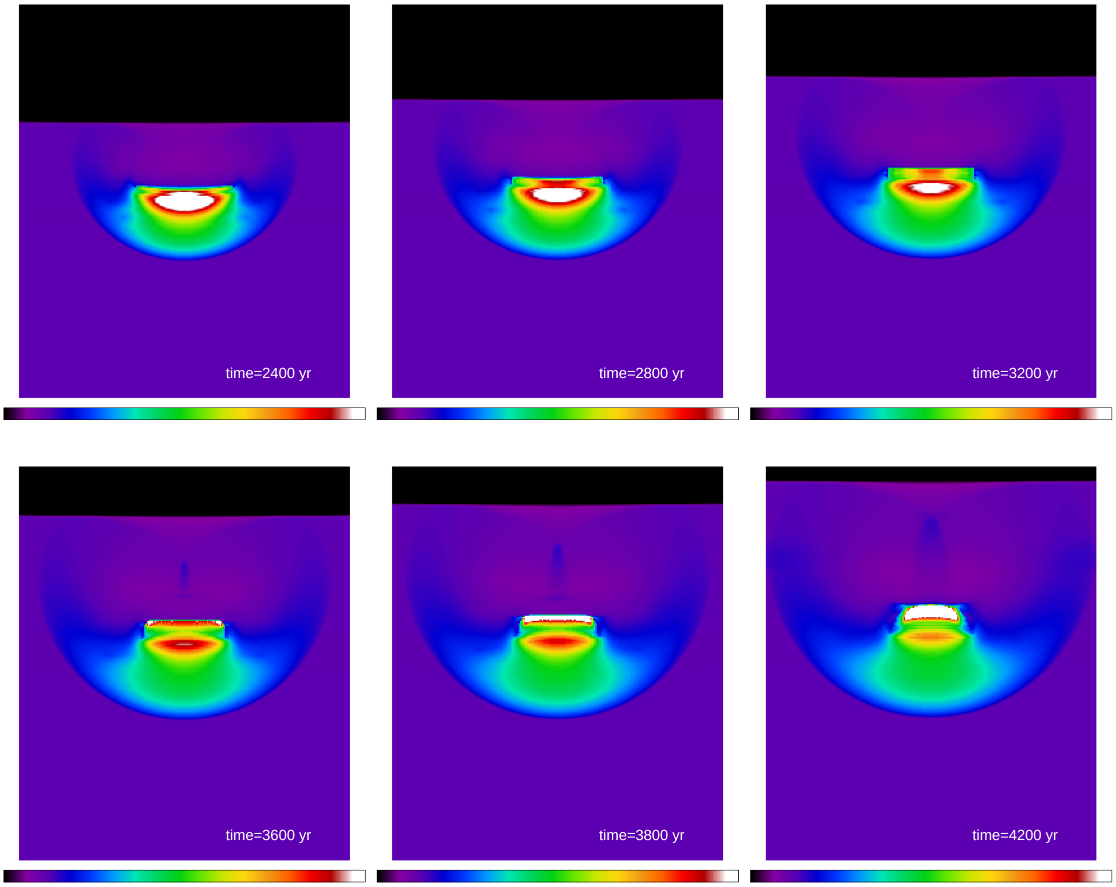

Figure 4.10: Synthesized *XMM-Newton* EPIC MOS count rate images in the $0.3-2$ keV energy band at different times for setup Sph1. The color bar has a linear scale between 0 and 2.4×10^{-3} s^{-1} bin^{-1}. The bin size is 3.9×10^{16} cm.

The brightest region does not correspond to the region with the minimum photon energy[1], at odd with what we observe in the FilD cloud (Fig. 4.12, right panel).

As done for the *XMM-Newton* data, I also perform a spatially resolved spectral analysis. In order to compare the observed spectra with those synthesized from the hydrodynamic simulations, I use the same procedure as that applied for the X-ray data, by defining physically homogeneous regions. The regions are indicated in the upper right panel of Fig. 4.9, for setup Sph1. In each of these regions there are limited fluctuations of mean photon energy ($\lesssim 1.7\%$ in region α, $\lesssim 6\%$ in region β, and $\lesssim 2\%$ in region γ). Region α is in the bright northern part of the X-ray knot, where the emission associated with the transmitted shock dominates and the mean photon energy is low, region β is in the brightest part of the cloud where both transmitted and reflected shocks contribute to the emission, and region γ is located on the South, where we have high values of temperature and of mean photon energy. Part of the regions selected for the analogous spatially resolved

[1]This explains the high MPE values in Fig. 4.5

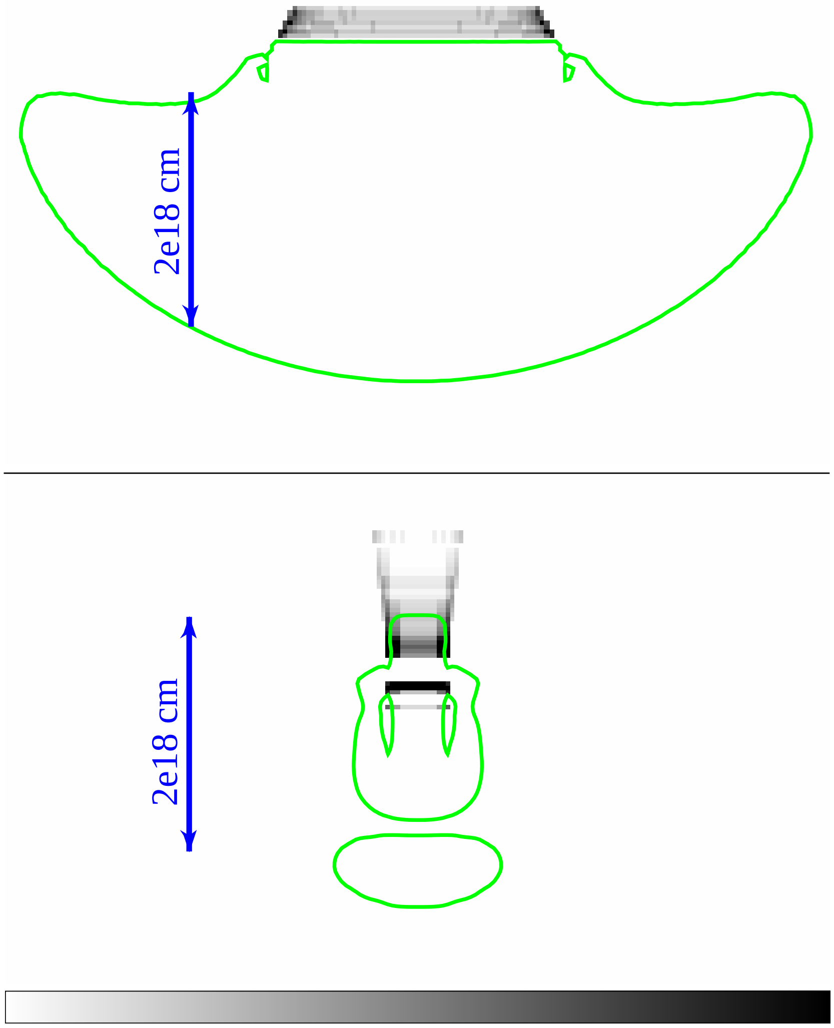

Figure 4.11: Synthesized map (projected in the plane of the sky) of the emission measure of the plasma with $T < 10^5$ K and $n > 3$ cm^{-3}, integrated along the line of sight, 3400 yr after the impact of the Vela shock front with a spherical cloud (setup Sph1, upper panel) and 3550 yr after the impact with an ellipsoidal cloud (setup Ell2, lower panel). As in Fig. 4.2, I have superimposed, in green, the X-ray contour levels at a count rate 2.4 times higher than the minimum, derived from the synthesized X-ray images in the $0.3-2$ keV band shown in Fig. 4.9.

spectral analysis of the *XMM-Newton* data are shown in Fig. 4.3. The spectral fittings were performed simultaneously on the synthesized and the observed MOS spectra. In agreement with the findings of Sect. 3.2.3, I adopt a MEKAL model of an optically-thin plasma in CIE with two thermal components, I fix $N_H = 1\times10^{20}$ cm^{-2}, and I leave the model Fe abundance free and link the Ne abundance to it, so as to have $(Ne/Ne_\odot)/(Fe/Fe_\odot) = 4.4$. I add to the model an energy-independent multiplicative factor to take into account the differences in surface brightness between the synthesized and the observed spectra and the different

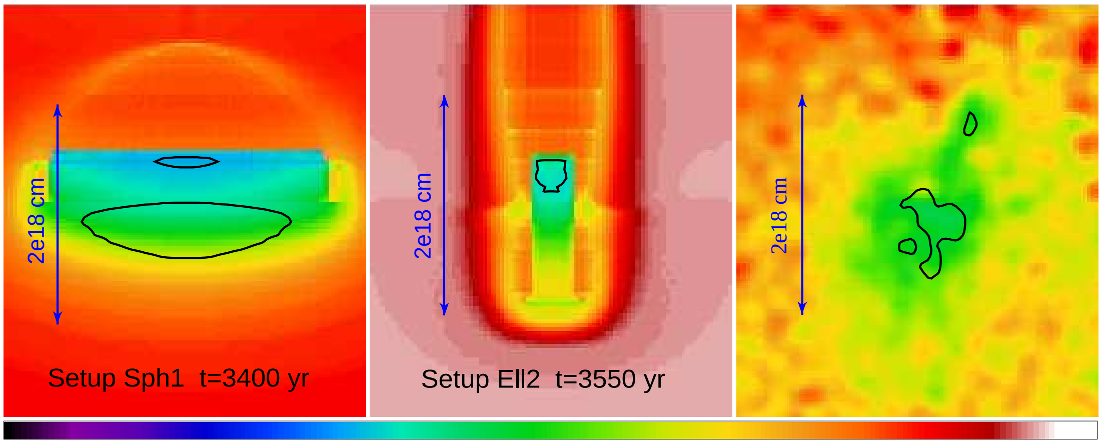

Figure 4.12: Synthesized mean photon energy map for setup Sph1 (3400 yr after the shock impact), *left panel*, setup Ell2 (3550 yr after the shock impact), *central panel*, and observed mean photon energy map in the Vela FilD region, *right panel*. Each pixel holds the mean energy of the EPIC MOS photons in the $0.3-2$ keV energy band. The color scale is linear and ranges between 300 eV and 870 eV. I superimpose (in black) the corresponding contour level at 75% of the maximum count rate in the same energy band.

areas of the spectral regions. The results are summarized in Table 4.2. Notice that, since this spectral model describes well the observed spectra (as shown in Sect. 3.2.3), the χ^2 values of the joint fit of the observed+synthesized spectra in Table 4.2 can be considered as an indication of the agreement between the observed and the synthesized spectra. As shown in the table and in the upper panel of Fig. 4.13, there is a good agreement between the spectrum synthesized in region α and those observed in the FilD regions with low mean photon energy (region 2 and region 4), but if we compare the spectra of region β and region 4 (i. e. the ones with the highest synthesized and observed surface brightness), we have significant differences (see Table 4.2). Instead, the spectrum of region β has similar spectral features to the one observed in region 7, where the count rate is lower than in region 4, but the mean photon energy is higher. The spectrum extracted from region γ, not shown in the table, is completely different and significantly harder than all the observed spectra (see the lower panel of Fig. 4.13), even than those extracted from the RegNE cloud, which is the hardest X-ray emitting region in the EPIC field of view, as shown in Chapter 3.

In **setup Sph2**, the post-shock temperature of the cloud (i. e. the temperature behind the transmitted shock) is $\sim 10^6$ K (as in setup Sph1), while the cloud density is slightly higher than in setup Sph1 ($n \lesssim 6$ cm^{-3}). I synthesize the X-ray count-rate maps and focal plane spectra also for setup Sph2. The emission morphologies in the three energy bands ($0.3-0.5$ keV, $0.5-1$ keV, and $0.3-2$ keV) are very similar to those of setup Sph1. Moreover, the synthesized X-ray

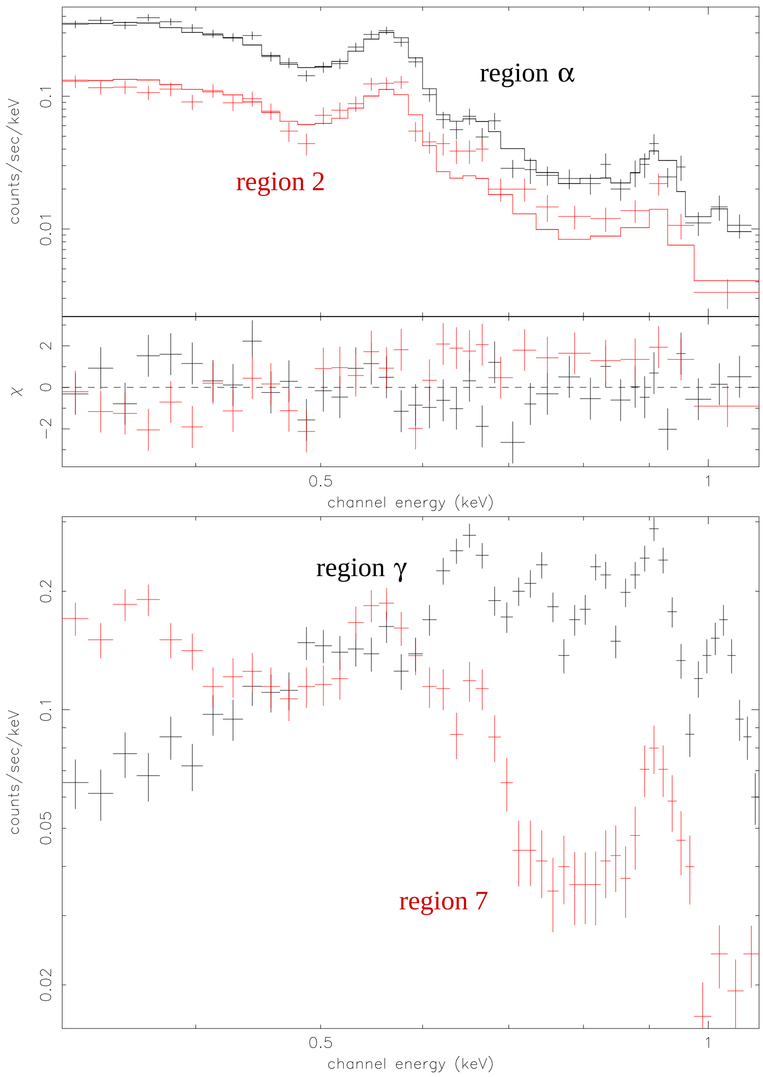

Figure 4.13: *Upper panel*: joint fit of the observed spectrum in region 2 (in red) and of the synthesized spectrum for setup Sph1 in region α (in black) with best-fit model and residuals. For the localization of the regions see Fig. 4.3 and Fig. 4.9. *Lower panel*: Same as above, for region 7 and region γ.

emission presents similar spectroscopic features to setup Sph1 (see Sect. 4.2.1). However, the global X-ray luminosity of setup Sph2 is too high (more than one order of magnitude) with respect to the observed one, therefore this setup will not be discussed in detail.

4.2.2 The ellipsoidal cloud

Setup Ell1 differs from setup Sph1 for the shape of the cloud. However, for setup Ell1, I find that in the evolution of the shock-cloud interaction there are no conditions for optical emission of the plasma[2]. In this case thermal instabilities do not develop and the plasma does not cool off to the characteristic temperatures of the optically emitting regions, while we observe a bright optical filament in the FilD cloud. Therefore, we will not discuss setup Ell1 further.

On the other hand, thermal instabilities leading to optically emitting regions develop in **setup Ell2**, that we discuss in detail in the following. The lower panel of Fig. 4.6 shows the 2-D cross-sections through the $(r,\ z)$ plane of temperature and density 3550 yr after the impact of the shock front with the ellipsoidal cloud. The velocity field of the plasma and the contours of the cloud tracer are shown in Fig. 4.14, where it is possible to appreciate how the cloud material expands in the intercloud medium. As shown in Sect. 4.1.6, this stage of the interaction is the one that best describes the observed data. The temperature and density cross-sections at different times are shown in Fig. 4.15.

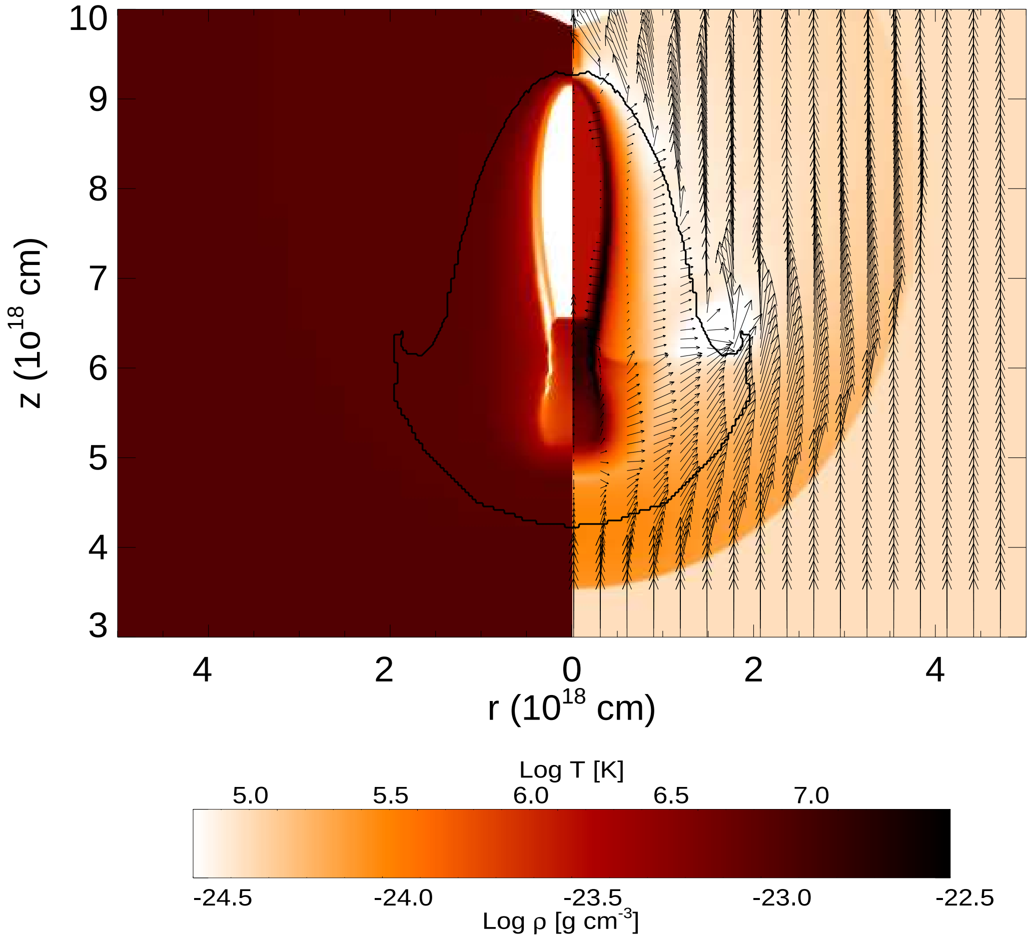

Figure 4.14: Same as lower panel of Fig. 4.6, where I have superimposed the contour of the cloud tracer and, on the right panel, the velocity field. The velocity arrows scale linearly with respect to the maximum velocity (680 km/s). The tracer contour enclose the fluid cell whose content is the original cloud material by more than 90%.

[2]I followed the evolution for ~ 6000 yr.

At $t = 3550$ yr, for setup Ell2, the plasma behind the transmitted shock has temperature $T \gtrsim 10^6$ K and density $n \sim 6 - 7$ cm^{-3}, the plasma behind the reflected bow shock has density $n \sim 0.4 - 0.5$ cm^{-3} and it is about two times denser than the intercloud post-shock plasma. The pressure behind the transmitted shock front, P^t, the reflected shock front, P^r, and the main shock front, P^{ms}, are: $P^t \sim 2 \times 10^{-9}$ dyne cm^{-2}, $P^r \sim 7 \times 10^{-10}$ dyne cm^{-2}, $P^{ms} \sim 3 \times 10^{-10}$ dyne cm^{-2}. In Fig. 4.6, the hot halo around the cloud due to its evaporation in the intercloud medium (see also Fig. 4.14) is also visible. A non-negligible fraction of the cloud material has reached the temperature and density values of the intercloud medium. The cloud evaporation is quite efficient, in fact, after ~ 6400 yr the cloud material is either evaporated in the intercloud medium (i. e. has density lower than 0.6 cm^{-3}), or condensed into cold, optically emitting structures with density larger than 10 cm^{-3}.

Figure 4.16 shows the radial (at $z = 6 \times 10^{18}$ cm) and axial (at $r = 0$) profiles of density and temperature for setup Ell2, where I have superimposed the estimates of density and temperature for cores and coronae derived from the analysis of the *XMM-Newton* observation of FilD. The shocked cloud is at $r \lesssim 2 \times 10^{17}$ cm. At the outer edge of the cloud there is a dense (and cold) narrow region (see below) and then, for $r \gtrsim 3 \times 10^{17}$ cm, the density and temperature gradually approach the corresponding intercloud values. The axial profiles shows the density and temperature of the plasma behind the main shock front ($z \sim 3 \times 10^{18} \div 3.5 \times 10^{18}$ cm), the reflected shock front ($z \sim 3.5 \times 10^{18} \div 5 \times 10^{18}$ cm), and the transmitted shock front ($z \sim 5 \times 10^{18} \div 6.6 \times 10^{18}$ cm). At $z \sim 6.6 \times 10^{18} \div 9.1 \times 10^{18}$ cm we observe the pre-shock cloud material and, at larger z, we observe the northern end of the cloud, the intercloud medium behind the main shock front, and the unperturbed intercloud medium.

The lower panels of Fig. 4.9 show the synthesized X-ray maps in the three energy bands, $0.3 - 0.5$ keV, $0.5 - 1$ keV, and $0.3 - 2$ keV, for setup Ell2. The X-ray emission in the $0.3 - 2$ keV energy band for different times is shown in Fig. 4.17. Also in this case, at $t = 3550$ yr, the synthesized count rate per bin is, on average, consistent with the observed one (considering a $\sim 30\%$ uncertainty for the distance of the Vela SNR), except for a small region in the northern edge of the synthesized X-ray knot. In the other parts of the knot the synthesized count rate per bin is closer to the observed one than setup Sph1. In setup Ell2 the hard X-ray emission from the plasma heated by the reflected shock does not contribute significantly to the broadband emission. In this case, in fact, the X-ray emission in the $0.3 - 0.5$ keV band has almost the same morphology as those in the $0.5 - 1$ keV and $0.3 - 2$ keV bands, just like in our *XMM-Newton* observation. Moreover, the overall morphology of the synthesized emission in all the energy bands is quite similar to the observed one.

Thermal instabilities occur in the narrow sheets at the lateral boundary of

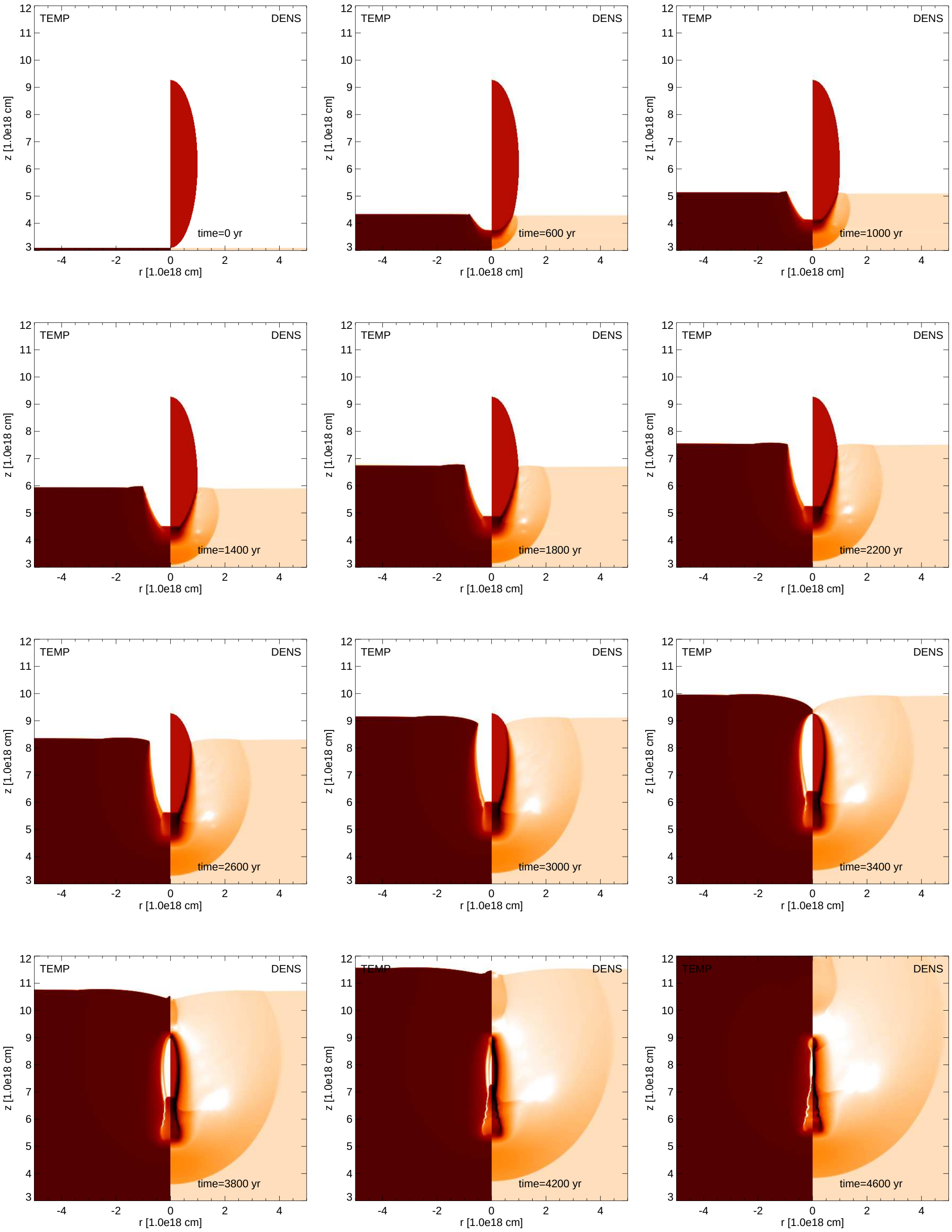

Figure 4.15: Same as lower panel of Fig. 4.6 for different times.

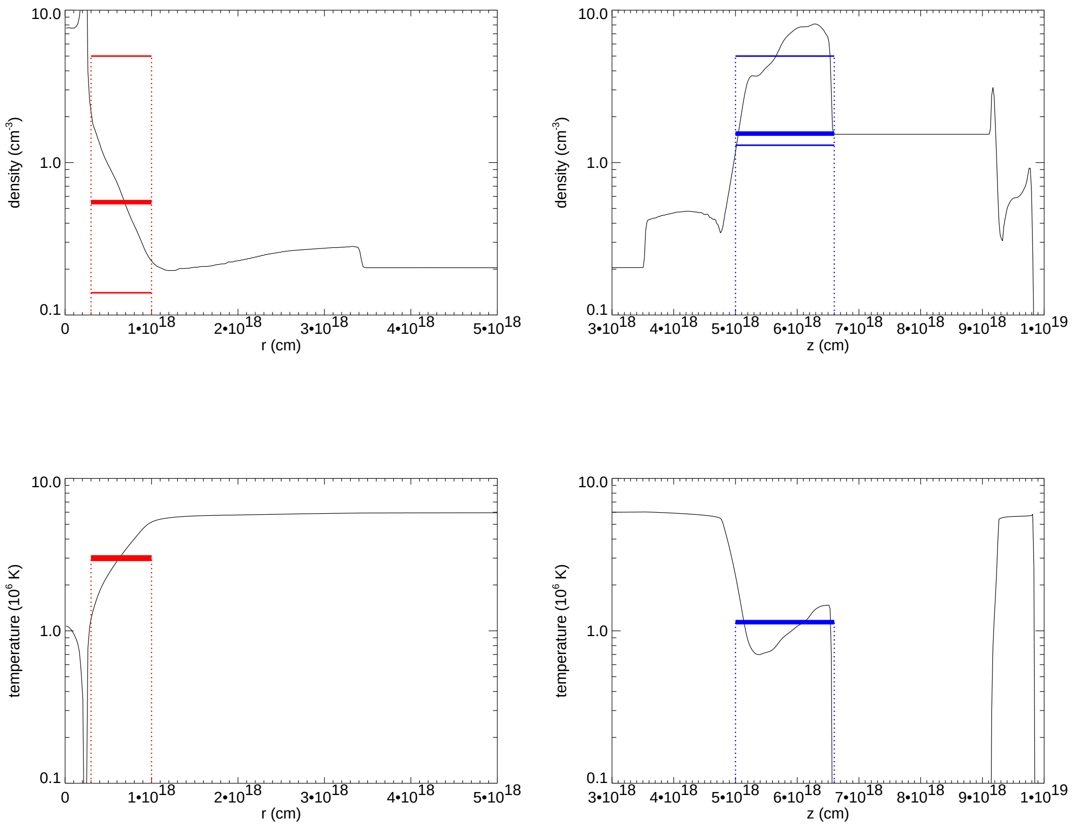

Figure 4.16: Radial (at $z = 6 \times 10^{18}$ cm) and axial (at $r = 0$) profiles of density (*upper panels*) and temperature (*lower panels*) 3550 yr after the impact of the shock front with the ellipsoidal cloud (setup Ell2, see lower panel of Fig. 4.6). I have superimposed to the corresponding structures the estimates of density and temperature for cores (in *blue*) and coronae (*red*) derived from the analysis of the *XMM-Newton* observation of FilD (with their error bars). The cold and dense spike at $r \sim 2 \times 10^{18}$ cm corresponds to a thermal instability.

the cloud ~ 3000 yr after the shock impact, where the lateral shocks (that move toward the center of the cloud, as shown in Figure 4.14) and the transmitted shock interact. There the plasma rapidly cools off to temperatures of a few 10^4 K, reaching density of a few tens cm^{-3}. These cold and dense structures are also visible in Fig. 4.16. The lower panel of Fig. 4.11 shows the emission measure of the plasma with $T < 10^5$ K and $n > 3$ cm^{-3} projected in the plane of the sky for setup Ell2. The similarity with the observations is even more evident: the impact of the Vela shock front with the ellipsoidal cloud produces an optical filament aligned with the shock velocity, with a morphology similar to the observed one.

Fig. 4.12 (central panel) shows the synthesized MOS mean photon energy map in the $0.3-2$ keV band for this setup. I superimposed the surface brightness contour level at 75% of the maximum in the same energy band. In agreement with the observational findings (Fig. 4.12, right panel), the brightest region corresponds to the region with the minimum photon energy. This explains the

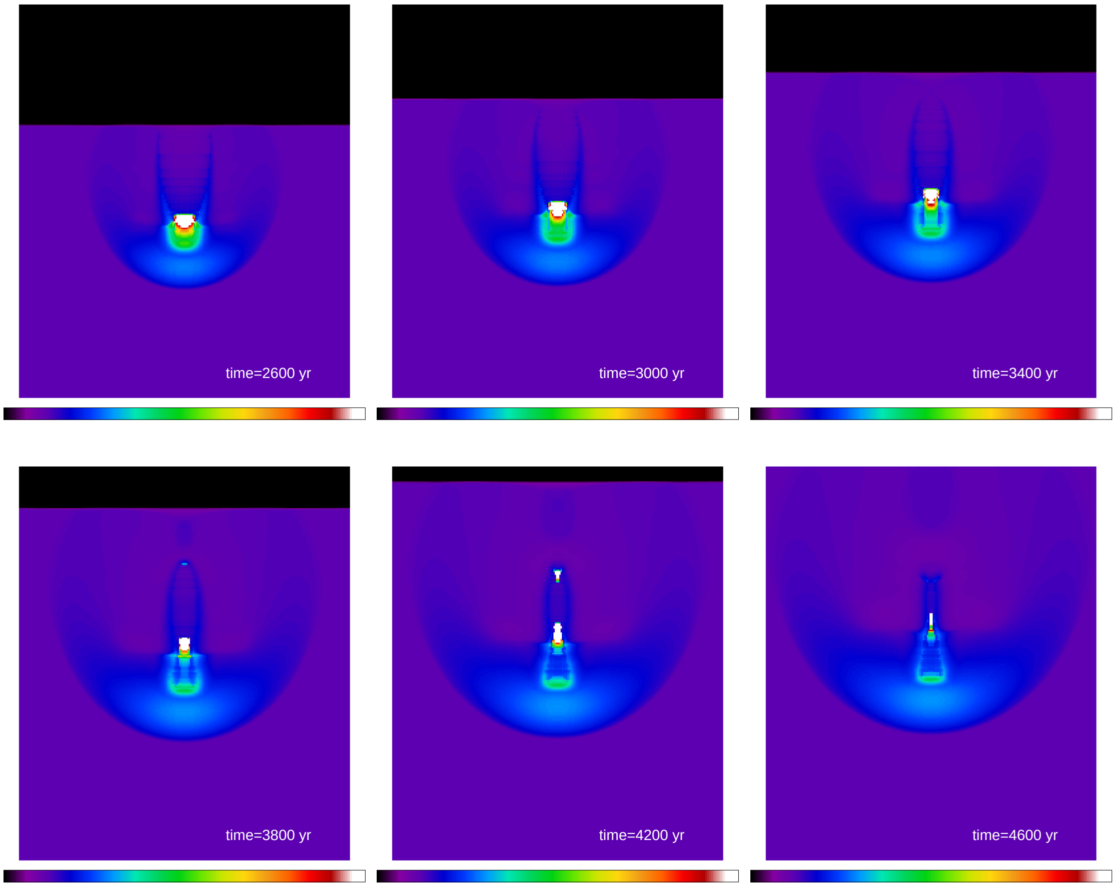

Figure 4.17: Synthesized *XMM-Newton* EPIC MOS count rate images in the $0.3-2$ keV energy band at different times for setup Ell2. The color bar has a linear scale between 0 and 2.4×10^{-3} s^{-1} bin^{-1}. The bin size is 3.9×10^{16} cm.

good agreement between the observed and synthesized MPE shown in Fig. 4.5.

As for the spatially resolved spectral analysis, I define the four spatial regions with homogeneous physical properties shown in Fig. 4.9 (lower right panel). In these regions the fluctuations of the mean photon energy are small ($\lesssim 2\%$ in region δ, $\lesssim 7.5\%$ in region ϵ and ζ, and $\lesssim 5\%$ in region η). Region δ covers the brightest and softest northern part of the X-ray knot, region ϵ and ζ correspond to the central part of the cloud, and region η is located at South, where we have higher values of temperature and of mean photon energy. I use the same spectral model described for setup Sph1 to analyze simultaneously the synthesized and the observed MOS spectra. The results are summarized in Table 4.2. As shown in the table and in Fig. 4.18, there is a remarkably good agreement between synthesized and observed spectra. If we compare the spectra of the brightest regions (i. e. region 4 and region δ) we obtain a good agreement. Notice that region δ and region 4 are the ones with the minimum mean photon energy. We obtain a satisfying agreement also if we compare regions with higher mean photon energy and lower surface brightness.

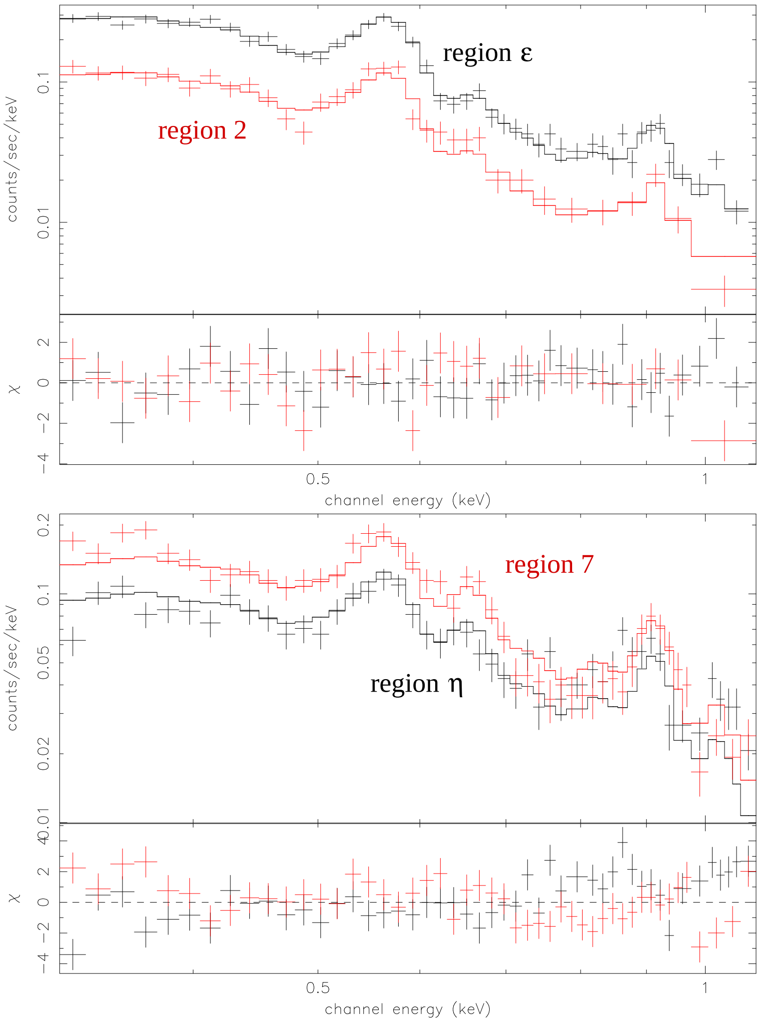

Figure 4.18: *Upper panel*: joint fit of the observed MOS spectrum in region 2 (in red) and of the synthesized MOS spectrum for setup Ell2 in region ϵ (in black). *Lower panel*: Same as above, for region η and region 7. The best fit models and residuals are also shown. For the localization of the regions see Fig. 4.3 and Fig. 4.9.

4.3 Discussion

I have pursued an accurate "forward" modeling of the interaction of the Vela SNR shock with an ISM cloud. The direct comparison of the observable synthesized from the hydrodynamic simulations with the data is a powerful tool to constrain the model and to obtain insight in the physical conditions of the Vela region.

The hydrodynamic model, set up from the analysis presented in Chapter 3, allows us to confirm that the bulk of the X-ray emission in the Vela FilD knot originates in the plasma behind the shock transmitted into an ISM cloud. It is now possible to confirm the important role of the thermal conduction between the shocked cloud and the intercloud medium and to demonstrate that thermal instabilities can explain the peculiar optical emission observed in the FilD region.

Thermal conduction induces the evaporation of the cloud (with a time-scale of a few 10^3 yr), while ~ 3000 yr after the impact of the shock front with the cloud, thermal instabilities develop determining the prompt (a few 10^2 yr) formation of optically emitting regions. We can also ascertain the physical origin of the two spectral components used to model the observed X-ray spectra and we can obtain information about the morphology of the ISM cloud. The hydrodynamic simulations show, in fact, how the pre-shock morphology of the ISM cloud influences the dynamics of the shock-cloud interaction and the corresponding X-ray and optical emission.

Setup Sph1 and Ell2 essentially differ for the shape of the ISM cloud (spherical vs. ellipsoidal), with physical parameters adapted so as to have similar post-shock temperature behind the transmitted shock, in spite of the different amount of cloud mass. Both in setup Sph1 and setup Ell2, the soft X-ray emission (below 0.5 keV) is associated with the cloud material heated by the transmitted shock front. In setup Sph1 a strong contribution to the X-ray emission above 0.5 keV comes from the intercloud material heated by the reflected shock and, in the end, the emission morphology and the spectral characteristics above 0.5 keV are not completely consistent with the *XMM-Newton* observation of FilD. In particular, as shown in Fig. 4.9, above 0.5 keV the bulk of the X-ray emission presents significant morphological differences from the softer emission (at odd with the observation) and the reflected shock emission is harder than the observed one (see lower panel of Fig. 4.13). Moreover, the optical filament is parallel to the plane of the shock front, at odd with the observation. Figure 4.19 (upper panel) shows the distribution EM vs. T of the three regions of the upper right panel of Fig. 4.9 for setup Sph1 (see also Tab. 4.2). In region α the emission measure peaks at $\sim 10^6$ K, that is the post-shock temperature of the cloud material, while the contribution of the intercloud material at $T \sim 4.6 \times 10^6$ K is about two orders of magnitude lower. In the central region β the peak of the EMD is at $\sim 1.5 \times 10^6$ K and the contribution of the plasma with higher temperatures to the synthesized emission becomes considerable. In the southern region γ all the emission originates in the hot intercloud plasma heated by the reflected shock front. We observe these features also for setup Sph2, which has the same shock temperature and cloud/intercloud density contrast as setup Ell2. Therefore, the models with a spherical cloud cannot explain all the spectral and morphological features we observe in FilD.

When the Vela blast wave shock impacts on an ellipsoidal cloud, the effects of the reflected shock on the X-ray emission are less significant. In this case, in fact, the extension of the X-ray emitting knot in the $0.3-0.5$ keV band is similar to the one in the $0.3-2$ keV band (see Fig. 4.9), just like in the Vela FilD cloud. Moreover, the spatial distribution of the thermal instabilities occuring in this model can explain the peculiar orientation of the FilD optical filament and its

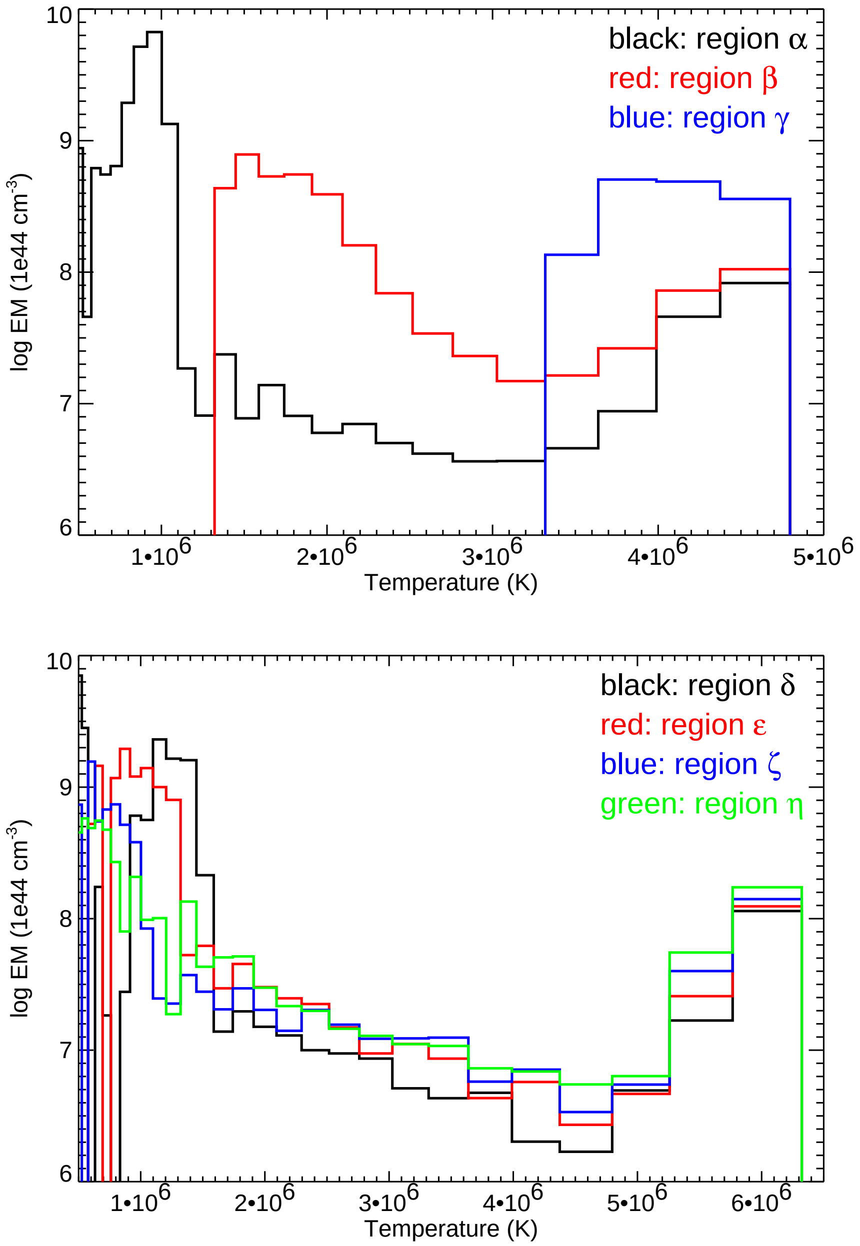

Figure 4.19: Distribution of the emission measure vs. temperature in the spectral regions of Fig. 4.9, for the spherical cloud (setup Sph1, *upper panel*) and the ellipsoidal cloud (setup Ell2, *lower panel*)

relationship with the X-ray emission. As for the X-ray surface brightness, all the setups yield higher values than the observed ones. This result may be partially due to distance effects[3]. However, while in setup Sph1 the higher count rates are observed above 0.5 keV, in setup Ell2 the brightest regions are those with

[3] I remind the reader that the distance D of the Vela SNR is known with a $\sim 30\%$ uncertainty and that the surface brightness scales as D^{-4}

the softest emission and the same happens in the FilD knot. The high surface brightness in setup Ell2 may be an artifact of the too perfect alignment of the cloud axis and the main shock velocity, since the brightest knot corresponds to the region where the transmitted and the lateral shocks simultaneously interact. The too extreme symmetry may also explain why in setup Ell2 we observe two vertical optical filaments, while in the FilD region the South-North filament is only one. In the case of the ellipsoidal cloud, all the synthesized spectra are remarkably in agreement with the observation. In all the spectral regions the soft component dominates and the surface brightness is related to its EM. These results are completely consistent with those obtained in Chapter 3. The lower panel of Fig. 4.19 shows the distribution EM vs. T of the four spectral regions selected for setup Ell2. In all the regions the contribution of the intercloud plasma heated by the reflected shock is constantly lower than that of the cloud material at lower temperature. It is worth noting that the spectral fittings performed on these four spectra have given results that are consistent with those obtained in Chapter 3. We conclude that setup Ell2 better describes the shock-cloud interaction processes in the Vela FilD region.

The model results lead us to new physical insight for the interpretation of the *XMM-Newton* data. In Sect. 3.2.3 I found that the FilD spectra are described well by two thermal components at $T_I \sim 1 \times 10^6$ K and $T_{II} \sim 3 \times 10^6$ K. I associated these components with two different phases of the cloud: the cloud core and the cloud corona respectively. We can now better understand the physical origin of these two components. The cooler component clearly originates in the cloud material heated by the transmitted shock front. The cloud core is, in fact, associated with the narrow peak of the EMD shown in the lower panel of Fig. 4.19. Since the X-ray flux is always dominated by the cooler component, we conclude that in the Vela FilD knot *the bulk of the X-ray emission originates behind the transmitted shock, which travels through an inhomogeneity of the ISM.* The corona is also related to the cloud. As shown in Fig. 4.19, we do not have a peak of the EMD at $\sim 3 \times 10^6$ K. The best-fit value T_{II} instead reflects a wide temperature distribution, approximatively between 1.5×10^6 K and 5×10^6 K. This is the cloud plasma (as shown in Fig. 4.14) that "evaporates" because of the thermal conduction with the hotter intercloud medium (which corresponds to the secondary peak of the DEM) and forms a hot halo around the cloud. The X-ray emission from the ambient medium heated by the main shock is always negligible with respect to the core and corona emission. The X-ray emission from the ambient medium heated by the reflected shock front is barely visible below 0.5 keV, and, although visible in the $0.5 - 1$ keV band, is always significantly lower than the emission associated with the cloud.

Although the modeling is focussed on a particular region of the Vela SNR, and I have not performed a wide exploration of the parameter space, I can give a few indications for the interpretation of other shock-cloud observations: i) the contribution to the broad band emission of the intercloud medium behind the main shock front is negligible in all the explored setups. Therefore, the X-ray emission (even the high temperature component) is associated with the inhomogeneities of the ISM; ii) it is possible to ascertain how much the transmitted and reflected shocks contribute to the X-ray emission through the comparison between the count rate image and the mean photon energy map in a wide energy band, even if the statistics is not enough for a spatially resolved spectral analysis: if the mean photon energy map (Fig. 4.12) has a minimum in the regions with the highest surface brightness, the emission behind the transmitted shock front dominates, otherwise the contribution of the plasma behind the reflected shock is significant; iii) a typical approach for the determination of the plasma density of the X-ray emitting plasma from the spectral analysis is based on the assumption of pressure equilibrium between the different spectral components (this allows us to derive, for each component, the filling factor and the density from EM and T). According to the results of the hydrodynamic model, this assumption may not be fully hold, as shown in Fig. 4.20, where I report the pressure 2-D cross-sections through the $(r,\ z)$ plane 3550 yr after the impact of the shock front with the ellipsoidal cloud (setup Ell2). However, the pressure variations are within a factor of 5, for the spherical cloud, and a factor of 10, for the ellipsoidal cloud.

We also obtained indications about the role of the different physical processes in the dynamics of the shock-cloud interaction. In particular, for example, the radiative losses determine the formation of thermal instabilities and the consequent optical emission, while thermal conduction between the cloud and the intercloud medium induces the evaporation of the cloud and the formation of the X-ray emitting "corona".

The efficiency of thermal conduction may be significantly reduced by the presence of a magnetic field (which is not taken into account in my model). If we assume an organized ambient magnetic field, the thermal conduction is anisotropic, because the conductive coefficient in the direction perpendicular to the field lines is several orders of magnitude lower than that parallel to the field lines, which coincides with the Spitzer's coefficient κ_{spi}. In the presence of a pre-shock uniform magnetic field, the ambient magnetic field is expected to envelope the shocked cloud during the shock-cloud interaction (Fragile et al. 2005, where the effects of thermal conduction are not taken into account) and this may prevent the evaporation of the cloud under the effect of thermal conduction and promote the formation of thermal instabilities.

However, Narayan & Medvedev (2001) have shown that, in the presence of a multiscale turbulent magnetic field, the efficiency of turbulent thermal conduction approaches the Spitzer's limit, the diffusion constant being $\sim \kappa_{spi}/5$. Since the conductive flux roughly scales as $T^{7/2}$, this reduction of the efficiency of thermal

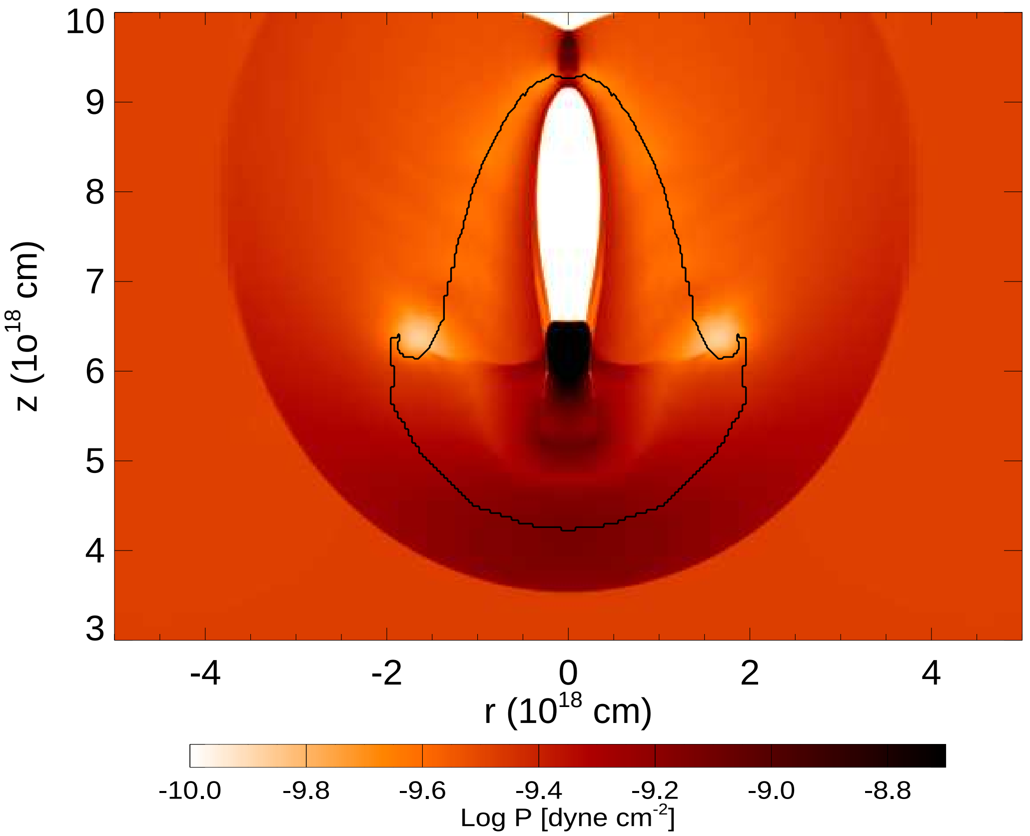

Figure 4.20: Pressure 2-D cross-sections through the $(r,\ z)$ plane 3550 yr after the impact of the shock front with the ellipsoidal cloud (setup Ell2). The tracer contour (in black) enclose the fluid cell whose content is the original cloud material by more than 90%.

conduction can be counterbalanced by increasing the shock temperature by a factor of $5^{2/7} \sim 1.58$, and/or by slightly reducing the cloud/intercloud density contrast. Since my model well reproduces the observed data, we can conclude that there is no need to include an organized ambient magnetic field, but the results substantially hold in the presence of a turbulent magnetic field.

Chapter 5

Large-scale view of the shock-cloud interaction in the northern rim of the Vela shell

In this chapter I show preliminary results of the analysis of two *XMM-Newton* EPIC observations of the northern rim of the Vela SNR, pointing the RegNE knot (introduced in Chapter 3) and the Vela FilE region (introduced in Sect. 1.6.2). The location of the two pointings is indicated in Fig. 1.11. Since these two observations, together with the Vela FilD pointing, cover an area of $\gtrsim 11$ pc^2 (at 250 pc), it is possible to study with high resolution the spatial distribution of the physical parameters of the plasma on this large scale. I also show the preliminary results of a hydrodynamic model to describe the X-ray spectral properties of RegNE (whose X-ray emission is harder than that of FilD, as explained in Chapter 3), and to explain the lack of optical emission in RegNE.

The chapter is organized as follows: in Sect. 5.1 I present the *XMM-Newton* data and describe the data processing procedure; Sect. 5.2 shows the X-ray analysis results in terms of imaging (Sect. 5.2.1) and the results of the spectral analysis of RegNE (Sect. 5.2.2). Section 5.3 is dedicated to the hydrodynamic forward modeling of the shock-cloud interaction in RegNE, while the conclusions are drawn in Sect. 5.4.

5.1 Data processing

The *XMM-Newton* EPIC observations presented here consist of two observation: i) Observation ID 0203960101 (PI F. Bocchino), with pointing coordinate α (2000) = $8^h35^m49^s$ and δ (2000) = $-42°35'28''$ (i. e. the RegNE region), obtained on the basis of the AO-3 proposal "The interaction between SNR shells and the interstellar medium" by F. Bocchino (PI), M. Miceli and A. Maggio

(COIs) and ii) Observation ID 0302190101 (PI M. Miceli), with pointing coordinate α (2000) $= 8^h34^m15^s$ and δ (2000) $= -42°55'40''$ (i. e. the FilE region), obtained on the basis of the approved AO-4 proposal "Multi-wavelength study of shock-cloud interactions in the Vela SNR", that I submitted as a PI, together with F. Bocchino, A. Maggio, and F. Reale (COIs). The observations have been performed with the EPIC MOS (Turner et al. 2001) cameras and with the EPIC pn (Strüder et al. 2001) camera on 31 October 2004 (0203960101) and on 14 November 2006 (0302190101). For a description of the *XMM-Newton* telescope and of the instrumental characteristics of the EPIC cameras see Appendix A. The relevant information about the two data sets are summarized in Table 5.1.

Table 5.1: Relevant information about the data.

OBS_ID	CAMERA	t_{exp} (ks)*	Mode	Filter
0203960101	MOS1	52.1/26.3	Large Window	medium
0203960101	MOS2	52.1/27.3	Large Window	medium
0203960101	pn	48.6/18.2	Ext. Full Frame	medium
0302190101	MOS1	39.8/32.7	Large Window	medium
0302190101	MOS2	40.0/28.5	Large Window	medium
0302190101	pn	35.8/23.7	Ext. Full Frame	medium

* Unscreened/Screened exposure time.

The data were processed using the Science Analysis System (SAS V7.0). Light curves, images, and spectra, were created by selecting events with PATTERN[1]$\leq$ 12 for the MOS cameras, PATTERN$\leq$ 4 for the pn camera, and FLAG$=0$ for both. To eliminate the contamination by soft proton flares, the data were screened by applying a count-rate limit on the light curves (binned at 100 s) at high energies ($10-12$ keV for MOS and $12-14$ keV for the pn camera). The count-rate limit is 0.18 counts per second for the MOS cameras, and 0.22 counts per second for the pn camera. The screened exposure times are given in Table 5.1.

All the images presented here are superpositions of the MOS1, MOS2, and pn images (obtained using the *EMOSAIC* task) of the two pointings and of the FilD pointing presented in Chapter 3 and are background-subtracted, vignetting-corrected, and adaptively smoothed (I used the task *ASMOOTH*). The contribution of the background was derived from the high signal-to-noise background event files E1_fm0000_M1.fits, E1_00fm00_M2.fits, E1_0000fm_PN.fits (obtained using the medium filter) described in detail by Read & Ponman (2003).

[1]For the definition of PATTERN and FLAG, see Appendix A

The exposure and vignetting corrections were performed by dividing the count images by the corresponding superposed exposure maps (obtained with the task $EEXPMAP$). Since the ratio between the MOS and pn effective area A_{rel} depends on the spectral distribution of the incoming photons, I have taken the thermal spectrum of the source into account when scaling the pn exposure maps by A_{rel}, to make MOS-equivalent superposed count rate images. In particular, since in Chapter 3 I found that in the FilD region the emission below 0.5 keV is associated with the soft component (at $\sim 10^6$ K), while above 0.5 keV dominates the hotter component (at $\sim 3 \times 10^6$ K), I assume an incoming thermal spectrum at 10^6 K for the images in the $0.3 - 0.5$ keV band ($A_{rel} = 0.16$) and at 3×10^6 K for the images in the $0.5 - 1$ keV ($A_{rel} = 0.2$), $0.85 - 0.98$ keV ($A_{rel} = 0.26$), and $1 - 1.24$ keV ($A_{rel} = 0.31$) bands. The background- and continuum-subtracted line images and the Ne equivalent width maps were produced by following the procedure described in Sect. 2.1.

Spectral analysis was performed in the energy band $0.3 - 1.5$ keV using XSPEC. The Ancillary Response Files were generated with the SAS $ARFGEN$ task, and the event files were processed using the $EVIGWEIGHT$ task (Arnaud et al. 2001) to correct vignetting effects. The background contribution was subtracted from the same regions as the source on the CCD (i. e. in the detector coordinates), in order to take into account the inhomogeneous response of the instruments across the field of view. Spectra were rebinned to achieve a signal-to-noise ratio per bin $> 5\sigma$ and the fittings were performed simultaneously on the two MOS spectra and on the single pn spectrum. All the reported errors are at 90% confidence, as calculated according to Lampton et al. (1976).

5.2 The data analysis

5.2.1 Image analysis

Figure 5.1 and Fig. 5.2 show the mosaiced count-rate image of the three observations of the northern rim of the Vela shell in the two bands chosen for the study of FilD: $0.3 - 0.5$ keV and $0.5 - 1$ keV (hereafter soft band and hard band).

The bulk of the X-ray emission of the RegNE knot is above 0.5 keV, although its brightest part, at the northern end of the knot, is also visible in the $0.3 - 0.5$ keV band. This bright "head" shows a bow-shaped morphology in the $0.5 - 1$ keV band and lies outside the field of view of the FilD observation discussed in Chapter 3. South of this head there is an elongated, sharp "tail" extending for about $15'$ (corresponding to ~ 1 pc, at 250 pc) towards the center of the remnant. North of RegNE a different faint, diffuse region is visible in the $0.5 - 1$ keV band. This region, labelled $Hreg$ in Fig. 5.2, does not present significant emission in the soft band. Figure 5.3 shows a combined optical (Hα, in red) and X-ray images of

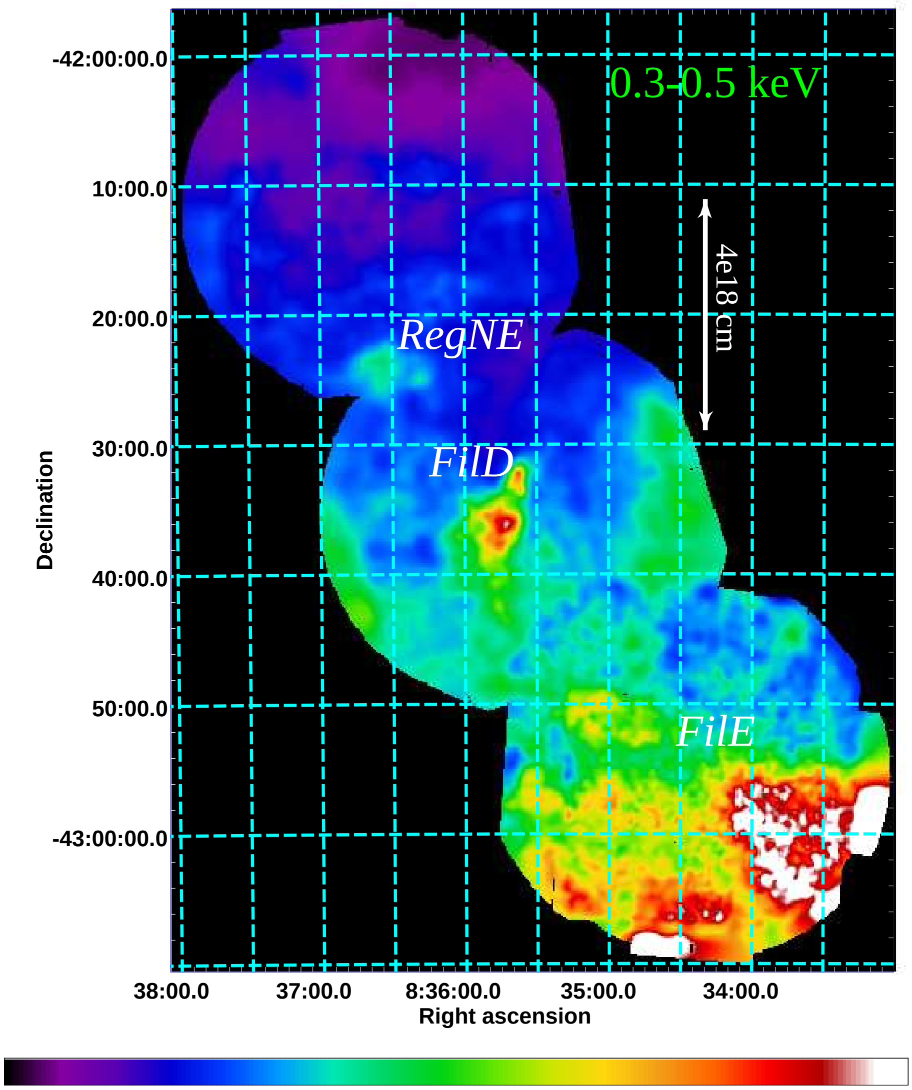

Figure 5.1: Mosaiced count-rate images (MOS equivalent) in the $0.3-0.5$ keV band (bin size= $8''$) of the northern rim of the vela SNR. The image is adaptively smoothed to a signal-to-noise ratio 25. The color bar has a linear scale and ranges between 0 and 2.5×10^{-4} s^{-1} per bin. The 4×10^{18} cm scale has been obtained assuming a distance $D = 250$ pc.

RegNE in the soft (in green) and hard (blue) X-ray bands. No significant optical emission is present in the wide region corresponding to the hard X-ray emitting knot (in blue, in Fig. 5.3) at odd with what happens in FilD where both soft X-ray and optical emission are present. A couple of optical filaments seem instead related to Hreg.

In the FilE region we instead observe significant emission both below and above 0.5 keV. In particular, in the Eastern side of the field of view there is a region (labelled *H FilE* in Fig. 5.2), where the surface brightness in the $0.5-1$ keV band is, on average, two times larger than that in the $0.3-0.5$ keV band. The

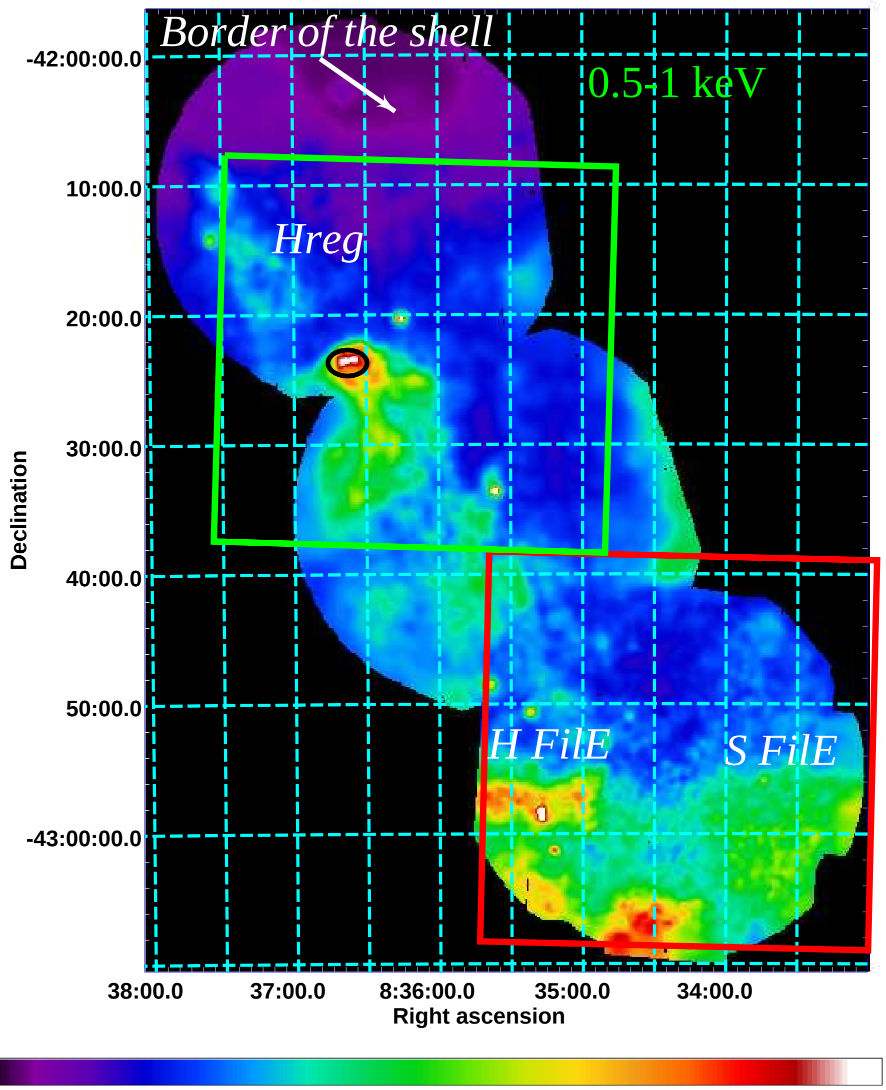

Figure 5.2: Same as Fig. 5.1 in the $0.5-1$ keV energy band. The color bar ranges between 0 and 6.7×10^{-4} s^{-1} per bin. The green box indicates the field of view of Fig. 5.3, while the red box indicates the field of view of Fig. 5.4. The black ellipse indicates the region selected for spectral analysis (see Sect. 5.2.2).

X-ray emission of this region is harder than that in the western part of the field of view (region *S FilE* in Fig. 5.2), where we observe a high surface brightness in the soft energy band. Figure 5.4 shows the intense Hα emission of the FilE region (in red), where I have superimposed the X-ray emission in the soft band (in green) and in the hard band (in blue). The H FilE structure with hard X-ray emission, lies clearly "behind" the optical filament. This configuration seems to indicate that we are observing in X-rays the plasma behind a reflected shock front. According to this interpretation, the reflected shock was generated by the impact of the main shock with a dense cloud, where the slow transmitted shock originates

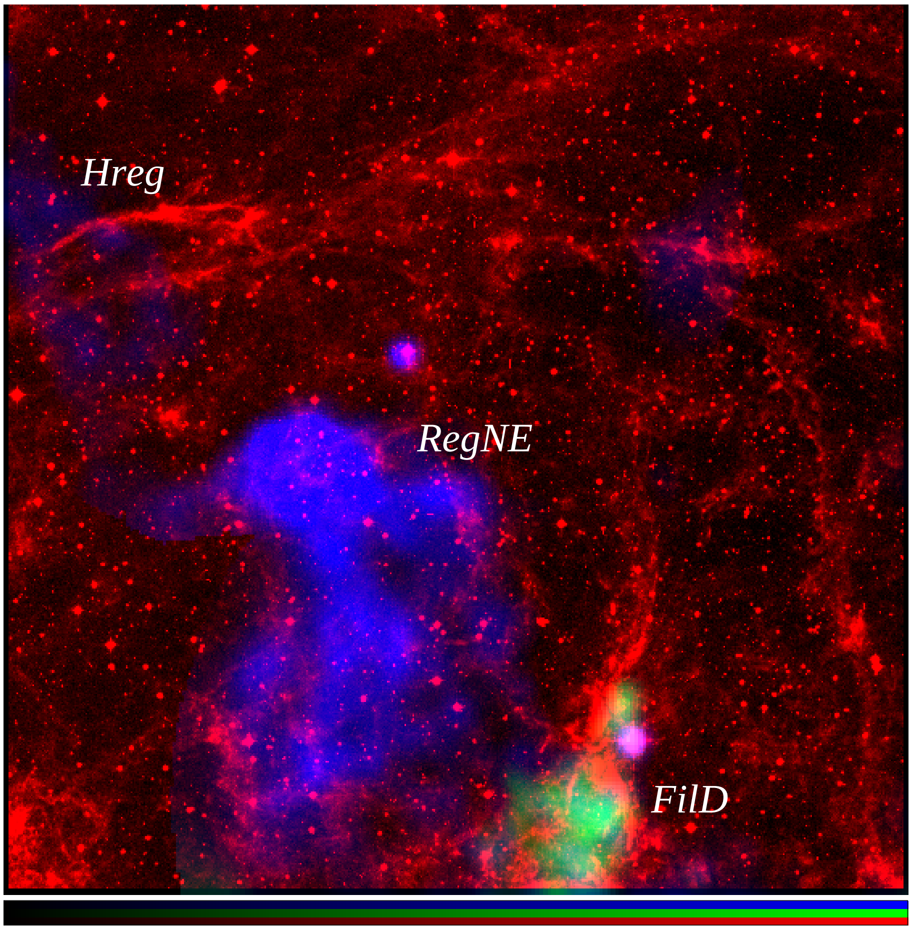

Figure 5.3: Combined optical and X-ray image of RegNE. The Hα emission (from AAO/UKST H-alpha survey) is indicated in red. I have superimposed, in green, the X-ray emission in the $0.3-0.5$ keV band (Fig. 5.1) and, in blue, the X-ray emission in the $0.5-1$ keV band (Fig. 5.2). The color bars have linear scales and range between 25% and 60% of the maximum count rate for the X-ray maps, while the optical image is scaled according to the IRAF zscale algorithm. The field of view of this image is indicated by the green box in Fig. 5.2.

the optical emission (in agreement with the scenario described in Sect. 1.4.3). The reflected shock scenario cannot be invoked for the S FilE region, where we observe both optical and soft X-ray emission, with narrow optical filaments that lie not behind, but "inside" the X-ray emitting region.

To obtain information about the thermal structure of the plasma in the wide region of the Vela shell covered by the three *XMM-Newton* pointings, I produce a MOS median photon energy map in the $0.3-2$ keV band, by following the procedure described in Sect. 2.2.2. I remind the reader that the MPE is an indicator of the hardness of the spectrum and then, if we assume an uniform N_H, it can be considered as an indicator of the temperature of the X-ray emitting plasma. I caution the reader that the median photon energy also depends on the local value of the $N_{\rm H}$, because where the interstellar absorption is higher

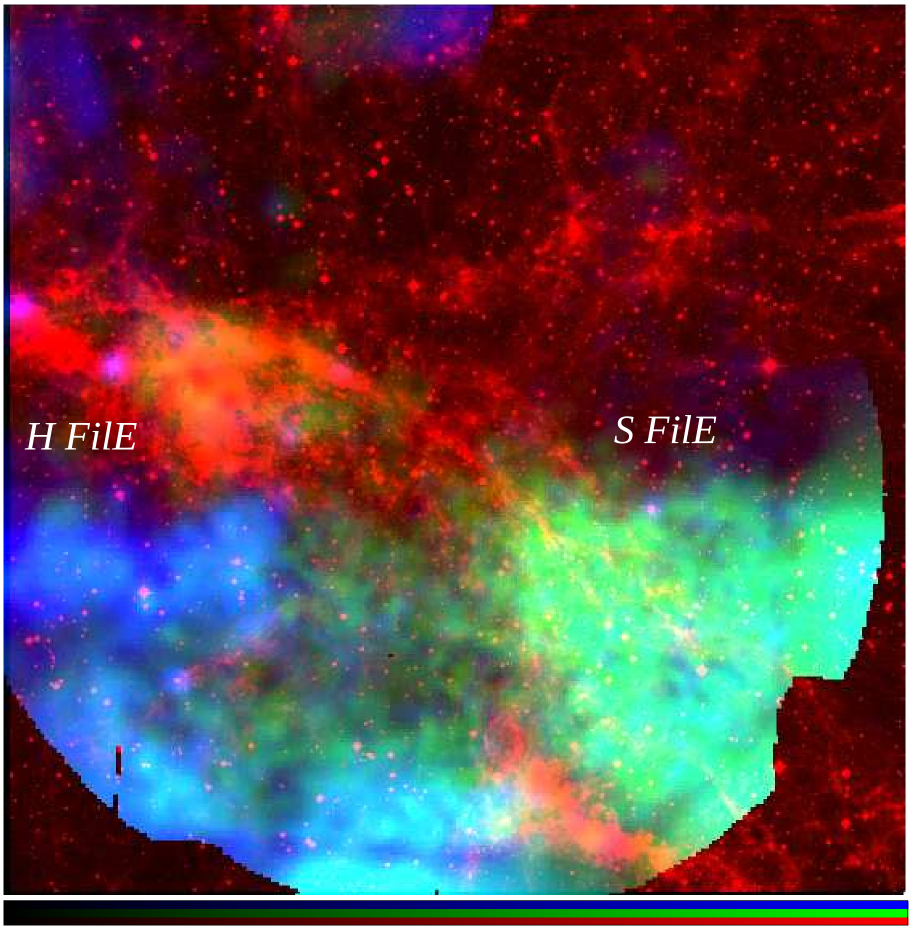

Figure 5.4: Same as Fig. 5.3 for FilE. The field of view of this image is indicated by the red box in Fig. 5.2.

we observe a hardening of the spectra. However, Lu & Aschenbach (2000) have shown that, in the region of the Vela shell covered by our set of observations, the $N_{\rm H}$ is quite uniform.

The median energy map is shown in Fig. 5.5 and has a bin size $12''$, so we can examine the different structures with high spatial resolution. The map clearly shows that very soft X-ray emission originates in the FilD and S FilE regions, where we observe relatively low values of MPE ($\lesssim 500$ eV). The H FilE region seems instead to be, on average, hotter than S FilE and FilD, thus supporting the possible association of this knot with interstellar material heated by a reflected shock. We observe the maxima of the median photon energy in RegNE and Hreg, (i. e. the regions where the bulk of X-ray emission is in the hard band). We then expect the plasma to be, on average, hotter in these two regions than in all the others.

We can also focus on the overall trend of the median photon energy on a large scale. Figure 5.5 clearly shows that two well-separate "regimes" (separated by

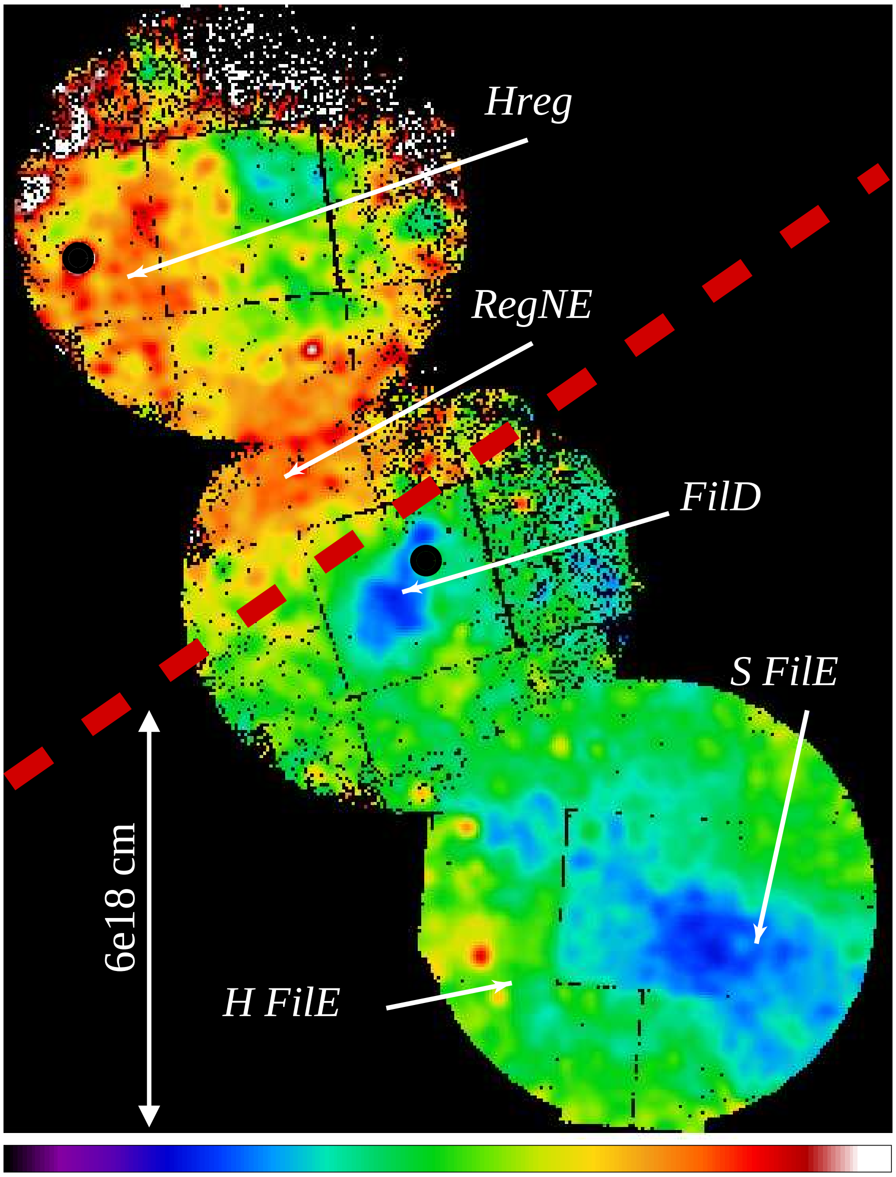

Figure 5.5: MOS median photon energy map in the $0.3-2$ keV band (bin size= $12''$). In each pixel the local median photon energy of the photons detected by the two MOS cameras is reported. The pixels where the median is computed with less than 5 photons have been masked out. The color bar has a linear scale and ranges between 415 eV and 750 eV. The red dashed line indicates the border between the two regimes discussed in Sect. 5.2.1.

the red dashed line in the figure) are present: a hard regime at North and a softer regime from FilD to the South. This may indicate that at North, in a large region behind the boundary of the shell, the filling factor of the soft component is very low and the shocked medium is, on average, less dense than in the FilD and FilE regions. In fact, the post-shock temperature of the plasma (and then the hardness of its X-ray emission) depends on the pre-shock density. The soft component at $\sim 10^6$ K that we observe also in the regions with low surface brightness in the FilD pointing (for example in region 12 of Fig. 3.2), may then be due to unresolved, small, dense clouds with a non-negligible volume filling factor. In the northern area of the shell this soft component (and then the dense cloudlets) seems to be absent, because of the high values of the median photon energy.

In Sect. 3.2.4 I showed that in the FilD region and in the tail of RegNE the Ne abundance is significantly higher than solar. In order to obtain information about the spatial distribution of the Ne abundance in the northern rim of the Vela SNR, I produce a Ne emission line image in the $0.85-0.98$ energy band. The continuum under the lines was estimated by scaling the flux in the adjacent band $1-1.24$ keV to the line emission, assuming for the continuum spectral slope a thermal bremsstrahlung model at 0.2 keV absorbed by a column density $N_H = 2.3 \times 10^{20}$ cm^{-2}. This phenomenological model for the continuum was chosen by taking the RegNE and FilD spectra into account. The image is shown in the left panel of Fig. 5.6. The Ne IX K line emission is particularly intense in RegNE and in H FilE. As for the case of W49B (Sect. 2.2.2), to disentangle higher element abundance in the line image from higher emission measure, I produce the Ne IX equivalent width map, as shown in the right panel of Fig. 5.6. I caution the reader that, as explained is Sect. 3.2.3, at ~ 0.9 keV, there is a blending between the Fe XVII L-lines and the Ne IX lines. The Fe lines, in particular, form a "false continuum" under the Ne line. The equivalent width map can then be considered as an indicator of the Ne/Fe abundance. The map clearly indicates that in RegNE there is a large Ne IX equivalent width, thus suggesting an enhanced Ne abundance in this region. We clearly observe low equivalent width in FilD, while in Hreg and in FilE the map appears patchy and shows no clear structures, except for a small knot near the southern border of the field of view.

An accurate study of the spatial distribution of temperature and of the chemical abundances will require an accurate spatially resolved spectral analysis. In what follows, I focus on RegNE, i. e. the brightest region with hard X-ray emission.

5.2.2 Spectral analysis of RegNE

In Sect. 3.2.3 I showed the results of the analysis of two spectra extracted from the tail of RegNE (regions 14 and 15 in Fig. 3.2). A single thermal component in CIE at $\lesssim 3\times10^6$ K describes well the observed spectra, but also a non-equilibrium of ionization model can be appropriate to describe the spectra.

To overcome this ambiguity and to obtain more detailed information on RegNE, I analyze the pn and MOS spectra extracted from the head of RegNE (the spectral region is indicated by the black ellipse in Fig. 5.2), where the statistics are significantly better than in the tail. I model the spectra with a single MEKAL model of an optically-thin thermal plasma in collisional ionization equilibrium

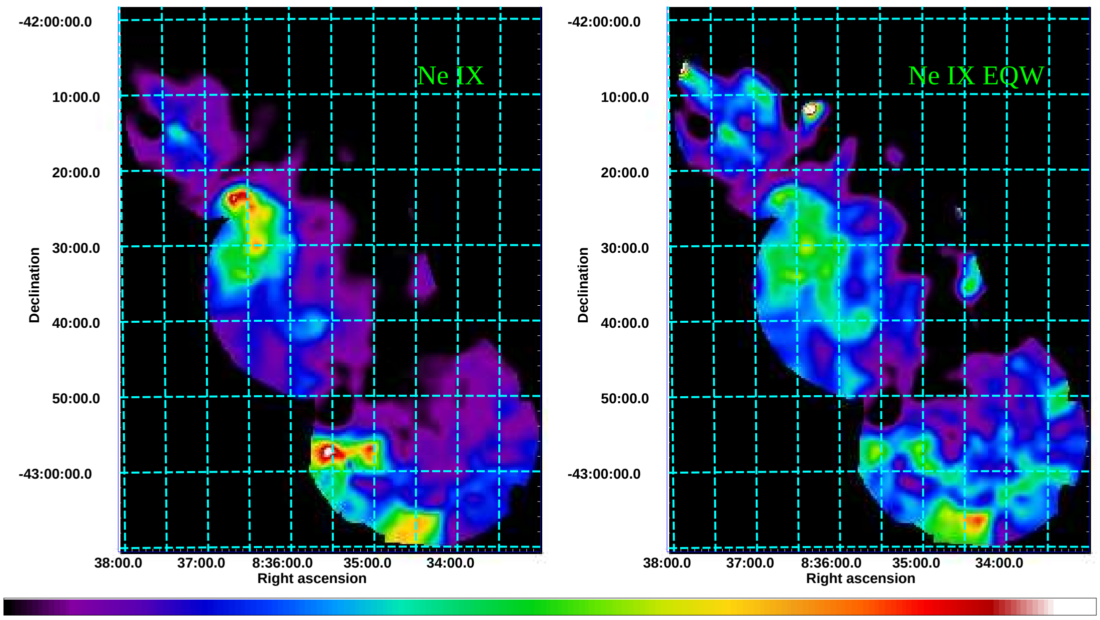

Figure 5.6: *Left panel* vignetting-corrected and continuum-subtracted EPIC count-rate images in the energy band of the Ne IX emission line ($0.85 - 0.98$ keV). The image is adaptively smoothed to a signal-to-noise ratio 25. The color bar has a linear scale and ranges between 0 and 6.63×10^{-5} s^{-1} per bin (bin size 8″). *Right panel:* equivalent-width maps of the Ne line image shown in the left panel. The color bar has a linear scale and ranges between 0 and 0.52 keV.

and with the non-equilibrium of ionization XSPEC NEI model. For both models I fix the N_H parameter to 1×10^{20} cm^{-2} (as done in Chapter 3) and I let the Fe, Ne, and Mg abundances as free parameters. I find no significant improvement of the quality of the fit (according to the F-test) by letting the O abundance free, so I tie it to 1. I find slight differences between the MOS and pn spectra, specially at ~ 1.3 keV (i. e. the energy of the Mg XI K emission blend), where, for all the attempted models, the joint pn+MOS spectral fitting gives pn residuals systematically below the best-fit model, while the MOS1 and MOS2 residuals are above it. In particular, according to the F-test, there is no need to let the Mg abundance free in the modeling of the single pn spectrum, which can be satisfyingly fitted by a model with solar Mg abundance (as shown in Table 5.2). The MOS spectra are instead described significantly better by a model with overabundant Mg[2]. I therefore perform a joint fit of the two MOS spectra and a separate fit of the pn spectrum. The results are summarized in Table 5.2.

I already pointed out (Sect. 3.2.3) that, in case of non-equilibrium of ionization, the post-shock temperature of the RegNE cloud assume high values, being

[2]The F-test gives the probability that the improvement of the fit is insignificant as $\sim 10^{-4}$ in CIE and $\sim 5 \times 10^{-3}$ in NEI.

Table 5.2: Best-fit parameters of the spectral analysis of the head of RegNE with the MEKAL CIE model and with the NEI model.

MEKAL model	MOS	pn
Temperature (10^6 K)	$2.67^{+0.1}_{-0.09}$	2.73 ± 0.1
n^2L (10^{18} cm^{-5})*	$1.20^{+0.05}_{-0.06}$	1.19 ± 0.06
$Fe/Fe_{\odot}$	$0.4^{+0.2}_{-0.1}$	$0.5^{+0.1}_{-0.2}$
$Ne/Ne_{\odot}$	3.1 ± 0.6	$3.0^{+0.7}_{-0.5}$
$Mg/Mg_{\odot}$	6^{+3}_{-2}	1^{**}
reduced χ^2(d.o.f.)	1.29 (106)	1.09 (141)
n^* (cm^{-3})	$0.98^{+0.02}_{-0.03}$	$0.92^{+0.02}_{-0.04}$
NEI model	MOS	pn
Temperature (10^6 K)	$6.0^{+2}_{-0.8}$	6.7^{+2}_{-1}
n^2L (10^{18} cm^{-5})*	$0.23^{+0.6}_{-1}$	$0.24^{+0.08}_{-0.05}$
$Fe/Fe_{\odot}$	$0.5 \pm 0,1$	0.4 ± 0.1
$Ne/Ne_{\odot}$	$2.5^{+0.4}_{-0.3}$	2.6 ± 0.3
$Mg/Mg_{\odot}$	$2.3^{+0.8}_{-0.6}$	1^{**}
τ_{NEI} (10^{10}s/cm^3)	$2.7^{+0.9}_{-0.7}$	3 ± 1
reduced χ^2(d.o.f.)	1.38 (105)	1.11 (140)
n^* (cm^{-3})	$0.43^{+0.05}_{-0.1}$	$0.42^{+0.6}_{-0.05}$

* Assuming $L = 1.25 \times 10^{18}$ cm.

** Frozen.

comparable with that inferred for the intercloud medium. The spectral analysis performed in the head of RegNE clearly indicates that the collisional ionization equilibrium model should be preferred for RegNE, given the lower χ^2 values obtained in CIE conditions. Figure 5.7 shows the two MOS spectra together with the MEKAL best-fit model and residuals.

While the emission measure per unit area is slightly larger in the head than in the tail (thus explaining its higher surface brightness), the best-fit values of temperature, Fe abundance, and τ_{NEI} in the head of RegNE are in quite good agreement with those found in the tail (see Table 3.3). The physical conditions of the X-ray emitting plasma are therefore fairly uniform across the whole RegNE, although the Ne abundance is slightly (but not significantly, considering the 90% confidence error bars) larger in the head than in the tail. Moreover, the good statistics allow us to resolve the Mg emission line and to highlight the possible Mg overabundance in RegNE. Notice, however, that the pn spectrum does not show the presence of overabundant Mg. As explained in Sect. 3.2.4, while the Ne overabundance in RegNE with respect to the solar value may be the result of a poor determination of the Ne abundance in the Sun, it is difficult to explain the observed values of Fe abundance. These values are, in fact, much larger than those typically observed in the ISM, where the Fe abundance is very low ($Fe/Fe_\odot \sim 0.02$), since metals are locked up in the interstellar dust grains (see Sect. 3.2.4). It is even more difficult to explain the Mg overabundance if we assume the X-ray emission to be originated in a shocked ISM cloud. The observed ratios O:Ne:Mg:Fe $\sim 2.5 : 7.8 : 15 : 1$ are quite similar to those observed by Katsuda & Tsunemi (2005) in the Vela Shrapnel D, i. e. $4.5 : 9.8 : 10 : 1$ (see also Sect. 1.6.2). This may indicate that Vela RegNE is a shrapnel generated during the explosion of the progenitor star. Notice, however, that, despite the similarity of the abundance ratios, the chemical abundances in the Vela Shrapnel D are much higher than that in RegNE ($O/O_\odot \sim 6.4$, $Ne/Ne_\odot \sim 13.7$ $Mg/Mg_\odot \sim 14$, and $Fe/Fe_\odot \sim 1.4$, as reported in Katsuda & Tsunemi 2005) and clearly prove the association with a shrapnel of ejecta. In our case, instead, the abundances are much closer to the solar values and the Mg overabundance is still not certain, because it is not consistent with the analysis of the pn spectrum. Notice, moreover, that, except for Mg, the abundances in RegNE do not differ very much from those of the interstellar FilD cloud.

As for the plasma density, the estimates in Table 5.2 have been obtained assuming the extension of RegNE along the line of sight to be comparable with that in the plane of the images. RegNE is indeed significantly less dense than the core of FilD, as suggested by the median photon energy map.

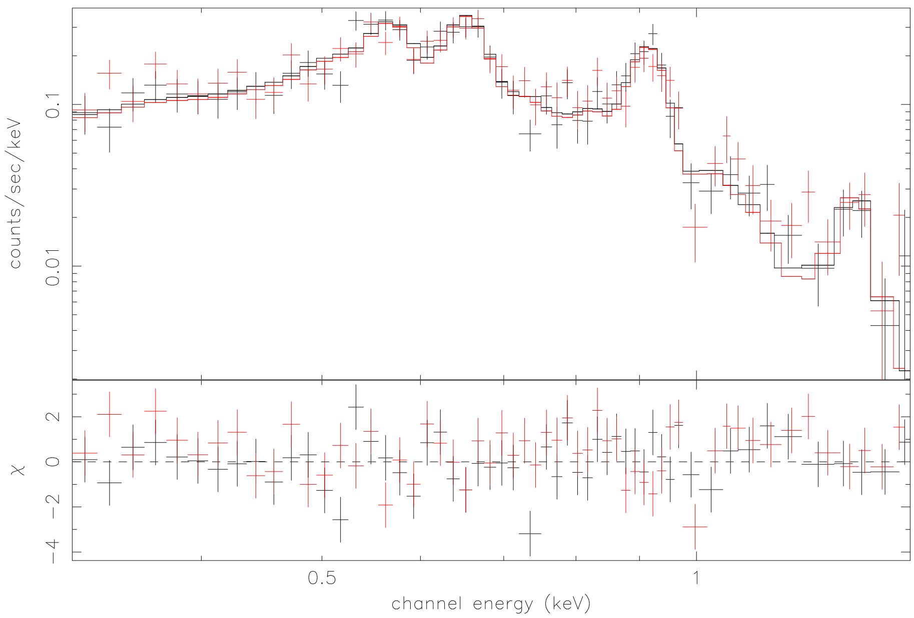

Figure 5.7: MOS1 (black) and MOS2 (red) spectra of the head of RegNE with the corresponding best-fit model and residuals obtained with one thermal component in collisional ionization equilibrium.

Figure 5.8 shows the χ^2 contour levels in the parameter spaces (Ne, τ_{NEI}), (Mg, τ_{NEI}), (Fe, τ_{NEI}), and (kT, τ_{NEI}), for the MOS spectra in collisional ionization equilibrium. While the best-fit temperature strongly depends on the ionization time-scale, we invariably observe overabundant Ne and Mg for a very large range of τ_{NEI}.

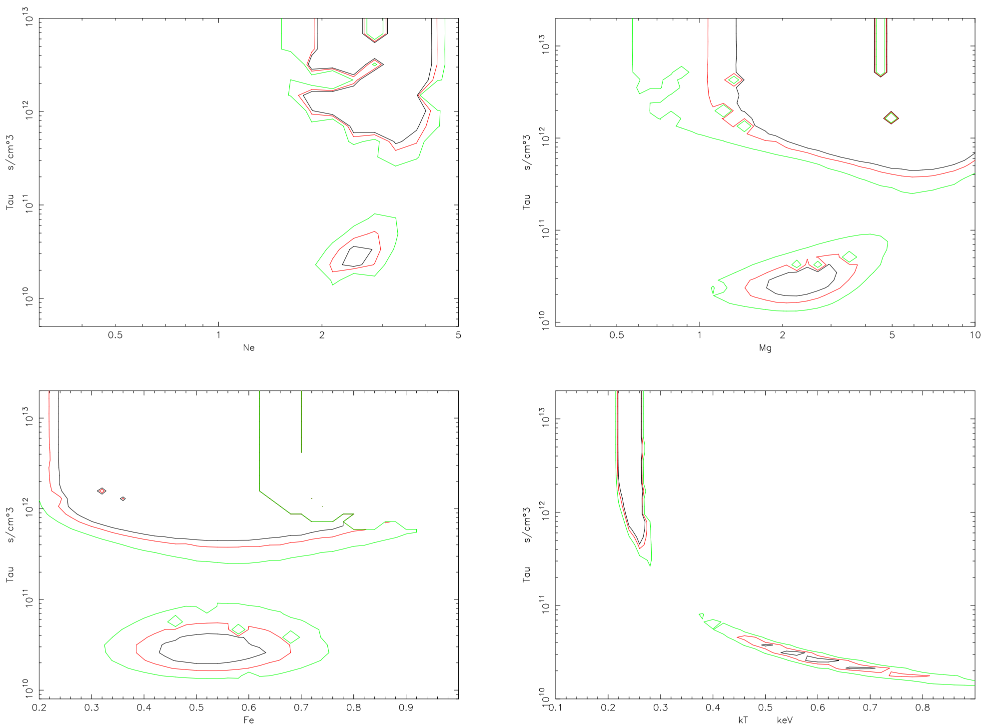

Figure 5.8: χ^2 contour levels (68%, 90%, 99%) in the parameter spaces (Ne, τ_{NEI}) (*upper left panel*) (Mg, τ_{NEI}) (*upper right panel*), (Fe, τ_{NEI}) (*lower left panel*), and (kT, τ_{NEI}) (*lower right panel*). The contour have been obtained by fitting the MOS spectra with the MEKAL model.

5.3 Hydrodynamic modeling of the shock-cloud interaction in RegNE

In this section I present preliminary results of the modeling of the interaction of the Vela SNR shock front with the RegNE cloud.

On the basis of the results of our preliminary imaging and spectral analysis, we have obtained indications that the RegNE X-ray knot can be the result of:

1. The interaction of the Vela shock with an ISM inhomogeneity. In particular, the spectral analysis results and the high values of the median photon energy North from FilD both suggest that, in RegNE and in the northernmost part of the Vela SNR, the inhomogeneities are less dense than FilD and FilE.

2. The propagation of a supersonic shrapnel of ejecta in the ISM medium. There are weak indications of non-interstellar metal abundances in RegNE that may be explained by this scenario.

I here focus on the first point, while point 2 will be investigated in future work (see Chapter 6).

I therefore model the impact of the Vela shock front with an interstellar cloud. The methodological approach, the model equations, the code used for the numerical solution of the equations, and the procedure for the synthesis of the observables are the same as those adopted for the modeling of FilD (see, in particular, Sect. 4.1.1, Sect. 4.1.3, and Sect. 4.1.5).

5.3.1 The model setup

As in Chapter 4, I model the impact of a plane-parallel SNR shock front on an isolated, uniform, cloud in pressure equilibrium with the intercloud isothermal medium. In the preliminary setup described here (hereafter setup Sph3) the cloud is spherical. The shock temperature is the same as that of the model that best describes the X-ray and optical emission of FilD (Setup Ell2 with $T_{sh} = 6 \times 10^6$ K, see Table 4.1). Since the RegNE post-shock temperature is about three times larger than that of the FilD core (see Table 5.2 and Fig. 3.7), I set the pre-shock cloud/intercloud density contrast in setup Sph3 at a value three times lower than in setup Ell2[3]. The cloud radius is 3.09×10^{18} cm, so the cloud volume is slightly larger that that of setup Ell2 (used in Chapter 4 to model FilD), given the larger extension of RegNE in the plane of the sky. Table 5.3 shows the values of the relevant initial physical parameters for setup Sph3. Notice that, according to the results of Orlando et al. (2005), for these setup values, thermal conduction dominates over radiative cooling (see Fig. 1.7). We therefore do not expect the formation of thermally unstable structures during the shock-cloud interaction. This setup provides only a preliminary description of the physical scenario in RegNE. In the future work it will be interesting to perform a parameter space exploration, by changing the initial geometry of the cloud, its density and its dimension. It is important to note that we now have one more constraint to the model than in the case of FilD (Chapter 4), since we have fixed the shock temperature.

Also in this case, the simulation is performed in a cylindrical 2-D coordinate system (r, z), assuming axial symmetry and with reflection boundary conditions at $r = 0$ and zero-gradient boundary conditions (for $\mathbf{v}$, ρ, and p) elsewhere. The

[3] I remind the reader that the post-shock temperature behind the transmitted shock linearly increases with the decreasing of the pre-shock density, see Eq. 1.12 and Eq. 1.7-1.8.

Table 5.3: Physical parameters of the model setup. The intercloud pre-shock temperature is 10^4 K and the intercloud pre-shock density is 0.05 cm^{-3}.

Model setup	Sph3
Cloud morphology	Sphere
Cloud Radius/semiaxis (10^{18} cm)	$R_{cl} =$ 3.09
Cloud density (cm^{-3})	$n_{cl} = 0.5$
Density contrast	10
Cloud mass ($M_\odot$)	$M_{cl} = 0.065$
Shock temperature (10^6 K)	$T_{sh} = 6.6$
Mach number	57

computational domain extends over 1.5×10^{19} cm in the r direction and over 2×10^{19} cm in the z direction. The shock velocity is parallel to the z axis, which corresponds to the North direction in the *XMM-Newton* observations. The post-shock initial conditions are given in the strong shock limit (Zel'Dovich & Raizer 1967). The finest spatial resolution is $\sim 1.95 \times 10^{16}$ cm, therefore we have more than 150 zones per cloud radius.

5.3.2 The model results

Fig. 5.9 shows the 2D cross-sections through the (r, z) plane of temperature and density (and the velocity field of the plasma) resulting from hydrodynamic modeling, 5000 yr after the impact of the shock front with the cloud. At this time (hereafter t_{best}) we obtain the stage of the interaction which best approaches the observed data, according to the criterion described in Sect. 4.1.6. Since RegNE is closer to the shock front than FilD, we expect, for RegNE, an interaction time $t \lesssim 4000$ yr, which is the upper limit for the interaction time of FilD, according to the results showed in Chapter 3 and 4. Notice, however, that by changing the geometry of the cloud, we can obtain lower values of t_{best}. For example, by reducing the cloud radius, we would reduce of the same factor also the cloud crushing time[4], thus obtaining a lower t_{best}. In this preliminary model I only address the main features of the shock-cloud interaction in RegNE, therefore I will not focus on this specific issue here.

At this stage of the interaction the two lateral shocks are interacting with each other and with the transmitted shock. The shocked cloud has temperature $T \gtrsim 3 \times 10^6$ K and density $1 - 2$ cm^{-3}, in good agreement with the results of spectral analysis (see Table 5.2). The cloud pressure is $1 - 2 \times 10^{-9}$ dyne cm^{-2}, while the pressure of the intercloud medium behind the main shock front

[4]For the definition of the cloud crushing time, see Sect. 1.4.2.

is $\gtrsim 3\times10^{-10}$ dyne cm^{-2}. In all the evolution of the shock-cloud interaction there are no conditions for optical emission of the plasma (I solved the time-dependent model equations over a time range of $\sim$ 8000 yr). In this case, therefore, there is no thermal instability and the plasma does not cool off to the characteristic temperatures of the optically emitting regions. This is in good agreement with what we observe in RegNE, where no optical filaments are present in the region of the X-ray knot, as shown in Fig. 5.3.

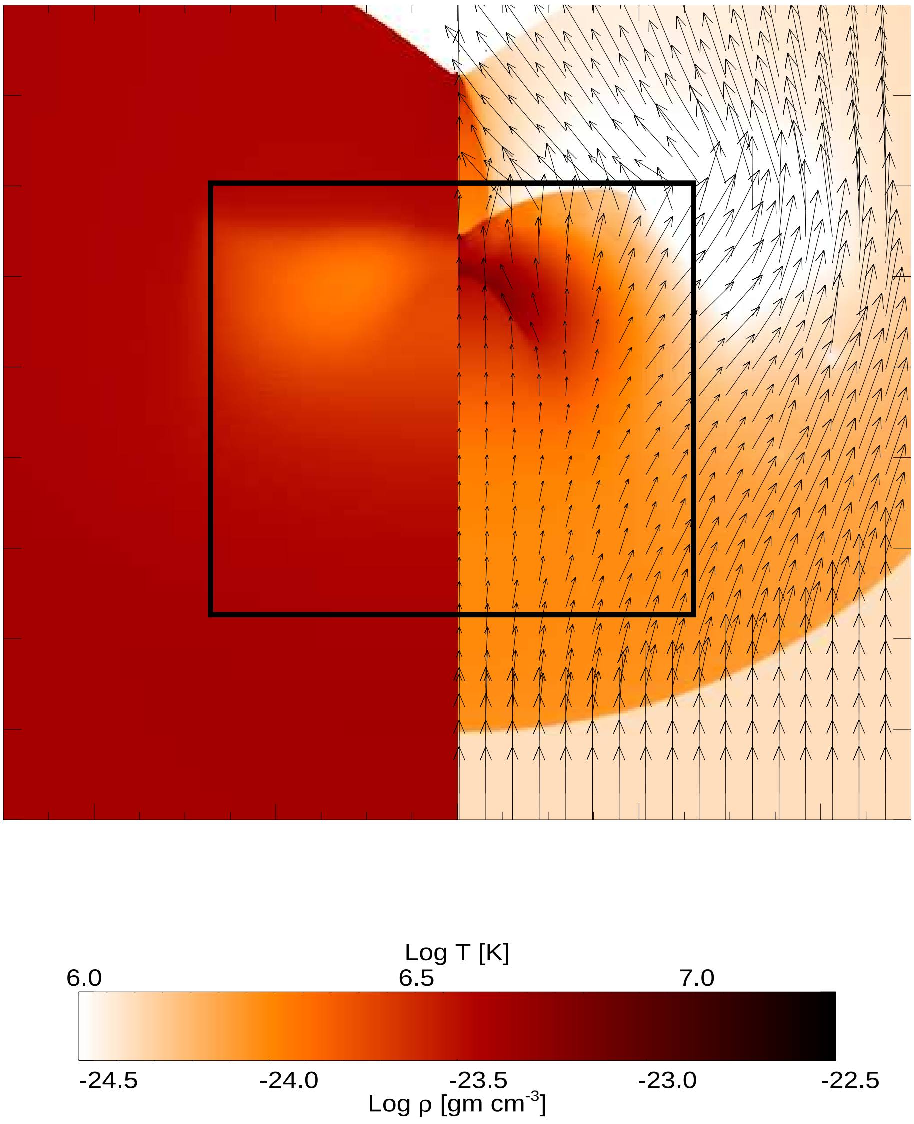

Figure 5.9: Temperature (on the left) and density (on the right) 2D cross-sections through the $(r,\ z)$ plane 5000 yr after the impact of the shock front with the cloud (setup Sph3). On the right panel I have superimposed the velocity field. The velocity arrows scale linearly with respect to the maximum velocity (1000 km/s). The black box indicates the field of view of the X-ray count-rate maps showed in Fig. 5.10.

The upper panels of Fig. 5.10 show the synthesized EPIC MOS X-ray maps, at the same epoch of Fig. 5.9, derived in the $0.3-0.5$ keV and $0.5-1$ keV energy bands. These images have been produced by taking into account the same instrumental response of the EPIC cameras, distance of the source, and interstellar absorption as in Chapter 4. The bulk of the X-ray emission is associated with the region where the two lateral shocks have "merged" and the emission of the plasma behind the reflected bow shock is negligible. The lower panels of the figure show, for comparison, the observed MOS count-rate maps for RegNE in the soft and hard energy bands (with the same bin size as the synthesized maps). The overall morphology of the synthesized emission in both the energy bands reproduces well the characteristic bow-shaped head of RegNE, but not its tail. The synthesized X-ray surface brightness is higher than that observed by about a factor of 3.5, although the relative flux in the two energy bands is consistent with the observations. The extension of the synthesized X-ray head is larger than that observed, therefore the high synthesized count rate may be the result of a too large volume of the emitting model cloud.

As done in Chapter 4, I also perform spatially resolved spectral analysis. In particular, I synthesize the spectrum from the region indicated in the upper right panel of Fig. 5.10 as it would be observed with the MOS1 camera with the same exposure time as that of the *XMM-Newton* observation of RegNE. I perform the spectral fitting simultaneously on the synthesized and the observed MOS spectra. In agreement with the findings of Sect. 5.2.2, I adopt a single thermal model of an optically-thin plasma in CIE with the same abundances as that reported in the first column of Table 5.2 for the MEKAL fits. I fix $N_H = 1 \times 10^{20}$ cm^{-2} and I add to the model an energy-independent multiplicative factor to take into account the differences in surface brightness between the synthesized and the observed spectra and the different areas of the spectral regions. Figure 5.11 shows the synthesized and the observed spectrum of the head of RegNE together with the corresponding best-fit model and residuals. Although thee are small differences at ~ 0.56 keV (i. e. O VII K line complex), the agreement between the observed and the synthesized spectra is remarkable, and the joint fit yields a reduced $\chi^2 = 1.86$ (with 177 d.o.f.).

5.4 Discussion

The combined analysis of the three *XMM-Newton* observations of the northern part of the Vela shell allowed us to obtain a high-resolution description of a large area ($\gtrsim 11$ pc^2) of the remnant.

The median photon energy map reveals the presence of a double regime in the shocked interstellar medium. In particular, as shown in Fig. 5.5, the region at less than $\sim 6 \times 10^{18}$ cm from the northern border of the shell shows, on average, a higher median photon energy than that observed at larger distances from the

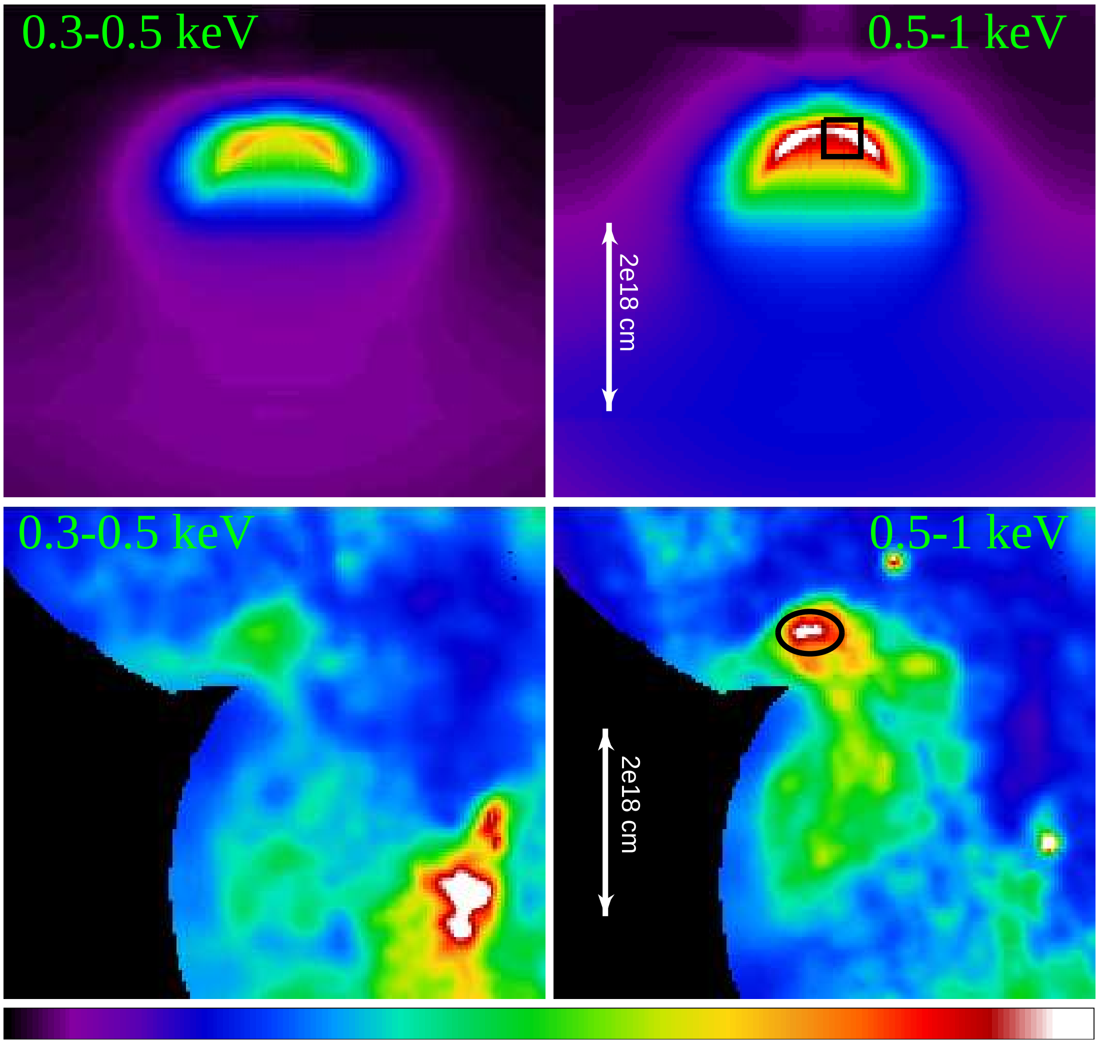

Figure 5.10: *Upper panels:* synthesized *XMM-Newton* EPIC MOS count rate images in the $0.3-0.5$ keV energy band (on the *left)* and in the $0.5-1$ keV band (on the *right*), at $t = 5000$ yr after the first impact of the shock with the cloud. The bin-size is 3.9×10^{16}, the color bar has a linear scale and ranges between 0 and 2.2^{-3} $\mathrm{s^{-1}}$ $\mathrm{bin^{-1}}$, in the $0.3-0.5$ keV image, and between 0 and 4.4^{-3} $\mathrm{s^{-1}}$ $\mathrm{bin^{-1}}$, in the $0.5-1$ keV image. The field of view of these image is indicated by a black box in Fig. 5.9. The black box in the upper right panel indicates the region selected for the spectral analysis. *Lower panels: XMM-Newton* EPIC MOS count rate images of the Vela RegNE knot, observed in the $0.3-0.5$ keV and $0.5-1$ keV bands. I smoothed the images adaptively to a signal-to-noise ratio 25. The bin size is $10.4''$, corresponding to 3.9×10^{16} cm, assuming a distance $D = 250$ pc. The color bar has a linear scale and the count rates range between 0 and 6×10^{-4} $\mathrm{s^{-1}}$ $\mathrm{bin^{-1}}$, in the $0.3-0.5$ keV band, and between 0 and 1.2×10^{-3} $\mathrm{s^{-1}}$ $\mathrm{bin^{-1}}$, in the $0.5-1$ keV images.

main shock front. This hardening of the X-ray spectrum can be interpreted as a consequence of the lack of dense inhomogeneities. Both the bright and the faint structures behind the northern border of the shell are, in fact, characterized by hard X-ray emission and this is a clear signature of the presence of hot plasma,

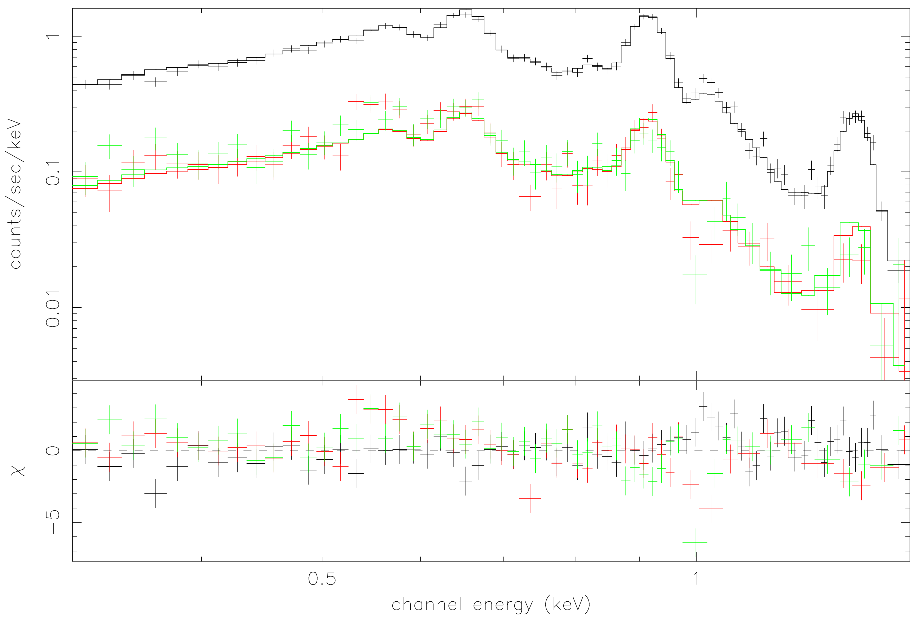

Figure 5.11: Joint fit (with best-fit model and residuals) of the observed MOS1 and MOS2 spectra of the head of RegNE (in red and green) and of the synthesized spectrum (in black) for setup Sph3 in the region indicated by the black ellipse in Fig. 5.10.

heated at relatively high temperatures because of its low density.

The spectral analysis of RegNE confirms this scenario: its temperature is three time larger than that of FilD and its density is $\lesssim 1$ cm^{-3} (while in FilD we find densities of a few cm^{-3}). However, the possibility that RegNE is a shrapnel of ejecta cannot be definitely ruled out. The boomerang-like shape of the head of RegNE and the evidence that its central axis intersects with those of the other shrapnels near the center of the remnant both support this association. Nevertheless, it is reasonable to assume that, in this case, an efficient mixing between the ejecta and the ISM has occurred, because of the relatively low chemical overabundances in RegNE with respect to the solar values. This kind of mixing has been recently invoked by Katsuda & Tsunemi (2006) to explain the observed abundances in the Vela Shrapnel A (see Sect. 1.6.2). A more natural explanation of the physical origin of the X-ray emission in RegNE is provided by considering the impact of the Vela shock front with a low-density ISM cloud. The preliminary hydrodynamic model I performed to describe this interaction clearly shows that the spectral properties of RegNE and a few morphological features of its X-ray emission can be the result of the interaction of a shock front at $T^* = 6 \times 10^6$ K with a cloud only 10 times denser than the intercloud medium. Even the lack of optical emission associated with the X-ray knot is explained by such a model, because the high efficiency of thermal conduction inhibits the occurrence of thermal instabilities that can originate optical emission, as shown in Chapter 4. The model needs to be upgraded so as to explain a few open issues (e. g. the presence of the RegNE tail and the determination of the evolutionary stage of the interaction), but it is worth noting that, by assuming that the shock at RegNE and at FilD has temperature T^*, the main morphological features, the spectral properties and the relationship between optical and X-ray emission in FilD *and* in RegNE can be naturally explained as the result of the interaction between the shock and two inhomogeneities with different density. Notice, moreover that the T^* value is perfectly consistent with the results of the observation analysis.

At larger distance from the border of the shell, closer the center of the remnant, we instead find large, dense, shocked clouds and small, unresolved cloudlets that determine the presence of a soft diffuse and faint emission. The spectral analysis confirms that also in these faint regions we observe a cold, thermal component with temperature comparable with that reached behind the shock transmitted through the FilD cloud. Finally, in the FilE knot (although a more accurate and detailed analysis is required) the median photon energy map and the relationship between optical and X-ray emission provide indications for X-ray emission associated with reflected (H FilE) and transmitted (S FilE) shocks.

Chapter 6

Summary and conclusions

In this thesis I have studied two different prototypes of SNR: W49B, which is a young, ejecta-dominated SNR, where the ejecta are interacting with a dense molecular cloud, and the Vela SNR, which is a middle-aged remnant where the main shock has expanded almost freely up to its actual radius and where the X-ray emission is associated with the shocked ISM inhomogeneities. The study of the X-ray emission in ejecta-dominated remnants provides important information on the dynamics of the explosion (energy, nucleosynthesis processes, etc). The study of middle-aged remnants, instead, allows us to probe the physical characteristics of the shocked ISM and to study the dynamics of the shock-cloud interaction.

6.1 The study of the SN ejecta: W49B

The study of the *XMM-Newton* observation of the galactic supernova remnant W49B shows that the X-ray emission can reveal interesting details on the dynamics of the supernova explosion and on the interaction of the shocked ejecta with ambient molecular clouds and wind residuals. The high effective area of *XMM-Newton* allows us to shed light on the open issues related to W49B. In particular, two important claims were proposed on the basis of the analysis of the *ASCA* observation of W49B: i) low-resolution *ASCA* line images of Si, S, and Fe K emission lines obtained by Fujimoto et al. (1995) seem to indicate a stratified radial distribution of the elements across the remnant, and ii) the analysis of the *ASCA* spectrum may suggest a possible overionization of the ejecta, as pointed out by Kawasaki et al. (2005). Moreover, preliminary analysis of *Chandra* and infrared observations of W49B have also suggested a possible association of the remnant with a GRB.

The *XMM-Newton* EPIC images of W49B presented in this thesis reveal many new details on the morphology of the X-ray emission. The remnant presents a complex X-ray morphology characterized by centrally barrel-shaped emission, terminated on the eastern side by an elongated perpendicular structure, and on the western side by a more diffuse, nearly aligned structure. The high quality of the data allows me to perform, for the first time, a spatially resolved spectral analysis on W49B. I do not find any indication of radial stratification of the abundances and of overionization. I confirm the association of the X-ray emission with the ejecta and I reveal a clear anisotropy in the physical and chemical properties of the ejecta. Lower temperatures and abundances are found in the western end of the remnant, while hotter regions with higher metal abundances are located in the center and at northeast. The good statistics of the EPIC observation allow me to highlight the presence of a high Ni overabundance ($Ni/Ni_{\odot} = 10^{+2}_{-1}$) in the central barrel, and to confirm the presence of Cr and Mn lines in the global spectrum.

Thanks to the results of the observation analysis, I find important constrains on the dynamics of the supernova explosion. The X-ray morphology of W49B may be attributed to pre-existing structures in the ambient medium, which may have produced an aspherical reverse shock or, more likely (according to our mass estimates), to a jet-like supernova explosion in a wind cavity, bounded by molecular clouds on the eastern side of the remnant. Because it has abundances similar to those in the central barrel, the eastern structure can be considered as the head of the jet. It is distorted and deviates mostly southward due to its impact with the infrared emitting, dense molecular wall that confines its expansion to the east. There is therefore evidence that W49B provides one of the few observed examples of a remnant of an asymmetric bipolar explosion.

I also investigate the possibility that W49B is a γ-ray burst remnant by comparing the observed abundances with yields derived from supernova and hypernova nucleosynthesis models. I find better agreement with the less energetic ($E \sim 10^{51}$ erg) models. The estimates of the energy of the ejecta concur in excluding the association of the remnant with a GRB. W49B seems then to be the result of an aspherical jet-like supernova explosion of normal energy. Notice that, in this case, we would have significant differences between the eastern arm of the jet, where high values of temperature and abundance have been found, and the western arm. It is, however, difficult to ascertain whether this East-West anisotropy is the result of an anisotropic explosion (like, for example, that produced by the instability of the accretion shocks described by Blondin & Mezzacappa 2006 and Blondin et al. 2003), or by the interaction of the jets with a complex, inhomogeneous ambient medium.

Although the data analysis provides indications of an aspherical explosion of normal energy, the spherical explosion scenario cannot be definitely ruled out. To discriminate between these scenarios and to obtain a more complete diagnostic, future work should then consist of detailed hydrodynamic modeling of aspherical and spherical explosions with a realistic description of the circumstellar medium

(e. g. molecular cloud and wind residuals).

6.2 The study of the shocked ISM: Vela

As for middle-aged SNRs, I study the Vela SNR. As explained in Chapter 1, shock-cloud interactions have been already extensively studied both analytically and numerically and three different physical scenarios have been proposed to explain the clumpy emission of middle-aged remnants. The discrimination between these different interpretations has been hampered by the poor instrumental characteristics of the past generations of X-ray satellites and by the lack of observable predictions derived from the models.

I then focus on the northern rim of the Vela SNR (where previous *ROSAT* observations have shown a clear signature of the interaction of the main shock front with ISM inhomogeneities). From the data analysis, I find a link between the optical and the X-ray emission in the FilD cloud. The optical filament lies between the two FilD regions with the highest X-ray surface brightness and this correlation clearly excludes that the X-ray emission originates behind the reflected shock front. However, it is difficult to explain the peculiar orientation of the optical filament in the FilD cloud as the result of a simple transmitted shock. The spectral analysis shows that two thermal components of an optically-thin plasma in CIE originate in the shocked clouds. The two components seem to be associated with two different phases of the clouds: the cloud core (which corresponds to the cooler component), and the hotter and less dense corona. The temperature of the cloud cores is quite uniform in the FOV ($\sim 1.14 \pm 0.02 \times 10^6$ K) and also all the cloud coronae have almost the same temperature ($3.0 \pm 0.1 \times 10^6$ K). The similarity of the temperatures indicates almost uniform densities among the cores and among the coronae. The inhomogeneous X-ray emission is instead determined by large variations of the emission measure of both components. There are therefore different volume distributions along the line of sight. The observed X-ray emission cannot be associated with the inter-cloud medium, and the reflected shock model does not seem to be compatible with the data. The ISM inhomogeneities are more likely heated by the transmitted shock which generates X-ray and optical emission, travelling through the clouds. The X-ray emission may be partially associated with the evaporation of the cloud heated by the hotter intercloud medium.

The data analysis results allow us to deepen our knowledge of the interaction of an SNR shock with a small ($\lesssim 1$ pc), isolated inhomogeneity and to obtain a much more precise description of the physical scenario with respect to that obtained with the past generation of X-ray telescopes. However, because of the complexity of the system, a higher level of diagnostic requires a detailed modeling of the shock-cloud interaction. The open issues are related, in particular, to the causes of the presence of the two X-ray emitting components and to their association with physical (pre-shock or post-shock) phases of the clouds and with specific heating processes (do both components originate in the plasma behind the transmitted shock, ore are they related with the cloud evaporation?) and to the physical origin of the optical emission.

To this end, I model the hydrodynamics of the interaction between a SNR blast wave shock and an isolated cloud, taking into account thermal conduction and radiative cooling effects. I explore four different model setups, choosing the values of the physical parameters on the basis of the preliminary analysis of the *XMM-Newton* X-ray data. Since I synthesize the X-ray emission filtered through the *XMM-Newton* EPIC-MOS instrumental response from the model, I can compare the model results directly to the data and derive detailed and quantitative information and deep insight. This study has shown that the dynamics of the shock-cloud interaction and the corresponding X-ray and optical emission are significantly influenced by the pre-shock morphology of the ISM cloud. In particular, if the Vela shock front impacts on a spherical cloud, both transmitted and reflected shocks contribute to the X-ray emission, while in the case of an ellipsoidal cloud, the reflected shock contribution is negligible. An ellipsoidal cloud 30 times denser than the intercloud medium, with the semimajor axis parallel to the shock velocity describes well the *XMM-Newton* observation of the Vela FilD knot in terms of X-ray spectral properties and morphology, and in terms of spatial relationship between optical and X-ray emission. The peculiar orientation of the FilD optical filament is naturally explained by this setup as a result of thermal instabilities. The model also allows us to understand the physical origin of the two thermal components used to describe the FilD observed spectra. The cooler component originates in the cloud material heated by the transmitted shock front, while the hotter component is the result of thermal conduction between the cloud and the hotter shocked intercloud medium. The heating of the cloud produces its evaporation and the formation of a hot diffuse halo. Moreover, I mark spectral and morphological characteristics of the emission from transmitted and reflected shocks, thus obtaining a key for the interpretation of other shock-cloud observations.

It is then interesting to verify if these conclusions can be generalized to other regions of the Vela shell. Many authors have pointed out that physical conditions of the Vela SNR environments are very non-uniform (e. g. the southwestern part vs. the northeastern part) and Lu & Aschenbach (2000) have shown that the temperatures and EMs of the two thermal components necessary to describe the X-ray spectra present significant inhomogeneities across the remnant (see Fig. 1.12). It is then reasonable to expect that the physical parameters I find in FilD may not be representative of the entire Vela SNR.

In this framework, I finally present a preliminary analysis of two new *XMM-Newton* observations of the northern rim of the Vela SNR. These observations (pointing two regions named RegNE and FilE), together with the FilD observation, cover an area $\gtrsim 11$ pc^2. The data analysis reveals a double regime in the shocked interstellar medium. A wide region at $\lesssim 6 \times 10^{18}$ cm from the border of the shell shows, on average, a higher median photon energy than that observed at larger distances from the main shock front. This seems to indicate the presence of hot, rarefied plasma, heated at relatively high temperatures (some million degrees). At larger distances, instead, we observe bright optical filaments and large, dense, X-ray emitting clouds, heated at lower temperatures, together with small, unresolved, dense cloudlets that determine the presence of a soft diffuse and faint emission. The spectral analysis of RegNE shows that a single thermal component at $\sim 3 \times 10^6$ K describes well the spectra, and preliminary hydrodynamic modeling shows that this result (and the lack of optical emission associated with RegNE) can be the explained with the interaction of a shock front at 6×10^6 K (i. e. the same temperature as that used for FilD) with an ISM cloud 10 times denser than the intercloud medium. There are, however, also indications of a possible association of RegNE with a shrapnel of ejecta. Future study should address this issue. In particular, a more complete analysis of the X-ray data is necessary and detailed hydrodynamic modeling of both the scenarios (shocked cloud vs. supersonic shrapnel) is required. Future study should also investigate the role of the magnetic field in the shock-cloud interaction in the Vela SNR.

Appendix A

The *XMM-Newton* satellite

In this appendix I review the main features of the *XMM-Newton* satellite. I focus in particular on the *XMM-Newton* European Photon Imaging Camera (EPIC), i. e. the instrument used to acquire the data discussed in Chapter 2, Chapter 3, and Chapter 5. The bibliographic sources for these appendix are the *XMM-Newton* web site (http://xmm.vilspa.esa.es), Turner et al. (2001), and Strüder et al. (2001).

A.1 The *XMM-Newton* telescope

The European satellite *XMM-Newton*, launched on December 10th, 1999, has been designed and developed by the European Space Agency and is equipped with three co-aligned X-ray telescopes. Each telescope is composed by 58 shells of co-axial and co-focal grazing incidence mirrors, disposed according to the Wolter-1 scheme, as shown in the left panel of Fig. A.1.

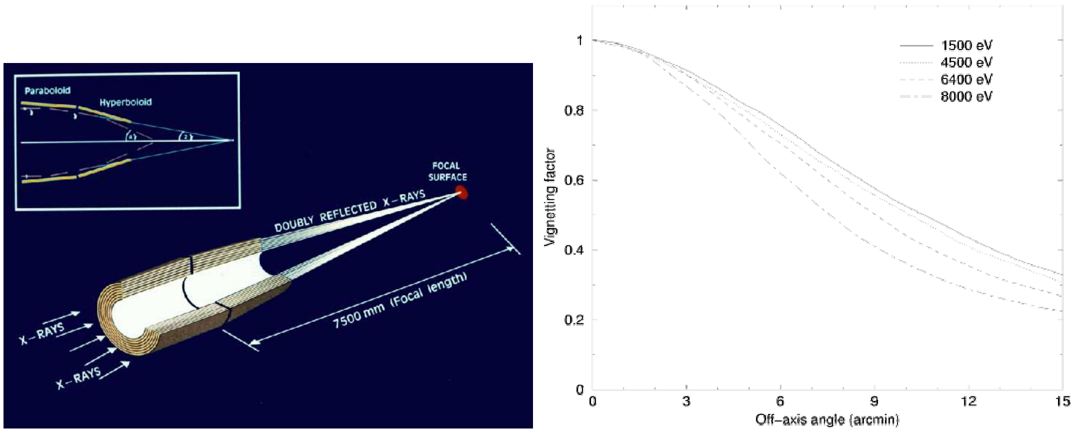

Figure A.1: *Left panel*: schematic configuration of the *XMM-Newton* telescope. *Right panel*: Vignetting function as a function of off-axis angle, at selected energies. From http://xmm.vilspa.esa.es.

The focal length of each telescope is 7.5 m and the geometric area is ~ 1550 cm^2, the highest ever obtained for an X-ray telescope. The mirror assembly is subject to vignetting, so there is a decrease in the effective area with increasing in off-axis angle. The decreasing in the effective area is quantified by the energy-dependent vignetting factor, as shown in the right panel of Fig. A.1.

The satellite hosts different X-ray detectors, the EPIC camera (see Sect. A.2) and the Reflection Grating Spectrometer (RGS). RGS is composed by two identical chains of reflection gratings which diffracts the X-rays to an array of dedicated CCD detectors. The RGS instruments achieve high resolving power over a range from 5 Å to 35 Å (0.33 – 2.5 keV), with $E/\Delta E \approx 100 - 500$. *XMM-Newton* is also equipped with a 30-cm optical/UV telescope with a microchannel-plate pre-amplified CCD detector in its focal plan (Optical Monitor). Table A.1 shows the main characteristics of the detectors

A.2 The EPIC camera

The EPIC camera consists of three CCD detectors (one for each X-ray telescope) designed to perform sensitive imaging observations over the field of view (FOV) of the telescope (diameter $30'$) and in the energy range from 0.15 to 15 keV with moderate spectral ($E/\Delta E \sim 20 - 50$) and angular resolution (PSF, $6''$ FWHM) and by the EPIC Radiation Monitor System (RMS), which provide information about the flux of ambient particles and turn off the detectors in case of high particle flux to protect the CCD cameras.

Two of the cameras are MOS (Metal Oxide Semi-conductor) CCD arrays (hereafter MOS cameras), installed in the focal plane of the X-ray telescopes that are equipped with the RGS gratings. The gratings divert about half of the telescope incident flux towards the RGS detectors such that (taking structural obscuration into account) about 44% of the original incoming flux reaches the MOS cameras. The EPIC instrument at the focus of the third X-ray telescope has an unobstructed beam and uses pn CCDs (pn camera). Figure A.2 shows the MOS and pn effective area as a function of energy.

There are seven front-illuminated CCDs in the focal plane of each MOS camera and central CCD is at the focal point on the optical axis of the telescope. The mosaic of the seven CCDs covers 28.4 arcmin. The imaging section has 600 x 600, 40 micron square, pixels. Each pixel covers 1.1 x 1.1 arcsec on the field of view. There are two read-out nodes for each CCD. The pn camera consists of a twelve 3 x 1 cm pn-CCDs on a single waver. There is a read-out node for each of the twelve CCDs. The imaging area is larger than that of the MOS and covers the 97% of the FOV. About 1/6 of the detector sensitive area is outside the FOV and is used to study the non-photonic background.

Table A.1: Main characteristics of the *XMM-Newton* detectors.

Detector	PN	MOS	RGS	OM
Bandpass	0.15 – 15 keV	0.15 – 12 keV	0.33 – 2.5 keV[1]	180 – 600 nm
Effective area[2]	$\sim$ 1400 cm^2	$\sim$ 450 cm^2	$\sim$ 55 cm^2	-
Field of view[3]	$30'$	$30'$	$5'$	$17'$
PSF[4]	$6''/15''$	$5''/14''$	–	$\sim 1.4'' - 2''$
Pixel size	150 μm ($4.1''$)	40 μm ($1.1''$)	81 μm[5]	$1''$
Timing resolution	0.03 ms[6]	1.5 ms[6]	16 ms[7]	500 ms[8]
Spectral resolution[9]	$\sim$ 80 eV	$\sim$ 70 eV	0.04 Å[1]	0.5/1.0 nm[5]

1. In the first grating order.
2. Optics+detector at 1 keV, without filter.
3. Diameter.
4. FWHM/HEW.
5. In spectroscopic mode.
6. In timing mode.
7. In high time resolution mode.
8. In fast mode.
9. At 1 keV.

Since the EPIC CCD detectors are sensitive to IR, visible and UV light, the three cameras include a set of four aluminised optical blocking filters (thin1, thin2, medium, thick), designed to reduce the contamination of the X-ray signal by those photons.

The spatial resolution of the EPIC instrument is limited by the Point Spread Function (PSF) of the telescope mirrors (see Table A.1). The PSF weakly depends on the energy of the incoming photons below 4 keV, while it slightly increases at higher energy.

The EPIC CCD detectors enable non-dispersive spectroscopy with moderate energy resolution. The energy resolution as a function of energy for the EPIC MOS and pn detectors is shown in Fig. A.3, for an on-axis point source.

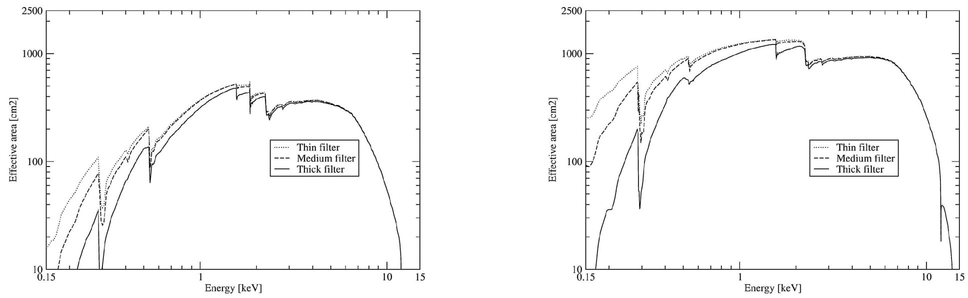

Figure A.2: EPIC MOS (*left panel*) and pn (*right panel*) effective area for different filters. From http://xmm.vilspa.esa.es.

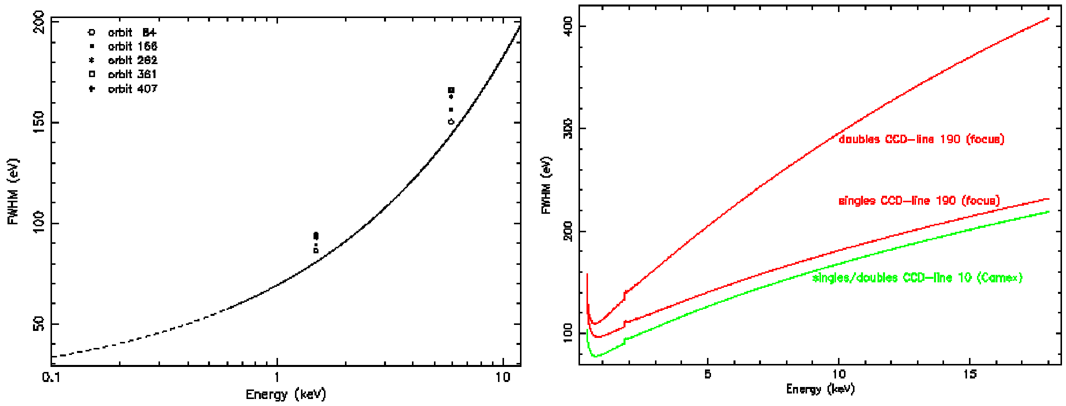

Figure A.3: *Left panel*: on-axis energy resolution of the MOS detectors as a function of energy obtained during the ground calibration (solid line) and on flight at different orbits of the satellite (points). *Right panel*: on-axis EPIC pn energy resolution as a function of energy as present in the most recent version of the response matrices, for single and double events (in full frame mode). The energy resolution at a position 10 pixels away from the readout node is also given. From http://xmm.vilspa.esa.es.

A.3 XMM-Newton data format

It is possible to produce an *XMM-Newton* event file in Flexible Image Transport System (FITS) format by processing the data set of the single EPIC cameras with the Science Analysis System software. The event files hold all the information about the position, energy, and detection time of the detected photons and about the instrumental response of the detector. At each photon is assigned a PATTERN value and a FLAG value. A significant number of X-ray events are expected to be split between pixels, and the PATTERN value codifies how many pixels have revealed a single event, as shown in Fig. A.4. PATTERN > 12 typically indicates non-photonic events (e. g. soft protons, cosmic rays). The FLAG value provides a bit encoding of various event conditions (e.g., near hot pixels, outside of the field of view, near a bad column). Setting FLAG=0 in the selection expression provides the most conservative screening criteria.

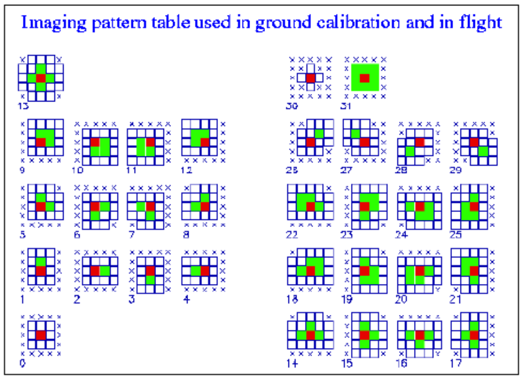

Figure A.4: PATTERN codification of the detected events. The pixels where the largest signal is detected are indicated in red, the pixels where the signal is over the detection threshold are indicated in green, and the pixels where the signal is below the detection threshold in white.

Appendix B

The FLASH code

The simulations described in Chapter 4 and Chapter 5 of this thesis have been performed by using the FLASH code (Fryxell et al. 2000) V2.5, developed at the FLASH Center of the University of Chicago.

FLASH is a 3-D astrophysical hydrodynamic code written mainly in FORTRAN 90 and made parallel with MPI directives for efficient execution on high performance computers. It solves the compressible Euler equations on a block-structured adaptive mesh, and its modular design permits the introduction of additional physics and different solvers.

B.1 PPM

The core of FLASH is based on a directionally split Piecewise-Parabolic Method (PPM, Woodward & Colella 1984) solver to handle compressible flows with shocks. PPM is an evolution of the Godunov method (Godunov 1959).

The hydrodynamic eulerian equations are approximated with a finite difference scheme on a discrete numerical grid. It is possible to demonstrate that, in a given grid cell, the solution at time $t + \delta t$ can be calculated from the solution at time t and the time-averaged fluxes across the cell of the relevant physical variables over the time δt.

According to the Godunov approach the time-averaged values are calculated by solving a collection of local Riemann shock-tube problems. In the Riemann shock-tube problem, a hot and dense gas is separated by a membrane from a more rarefied and cooler gas. Once the membrane is removed a rarefaction wave moves at local sound speed to the dense fluid, while a shock propagates in the rarefied gas (followed by the contact discontinuity). This problem can be solved analytically, as shown by Hawley et al. 1984 (and references therein). As a result of the discretization process, at every interface we have discontinuity of the physical variables (density, velocity, and pressure), therefore the time-averaged fluxes can be obtained from the analytic solutions of the Riemann problem, solved at each cell interface, as shown in the schematic representation of Fig. B.1. The way the

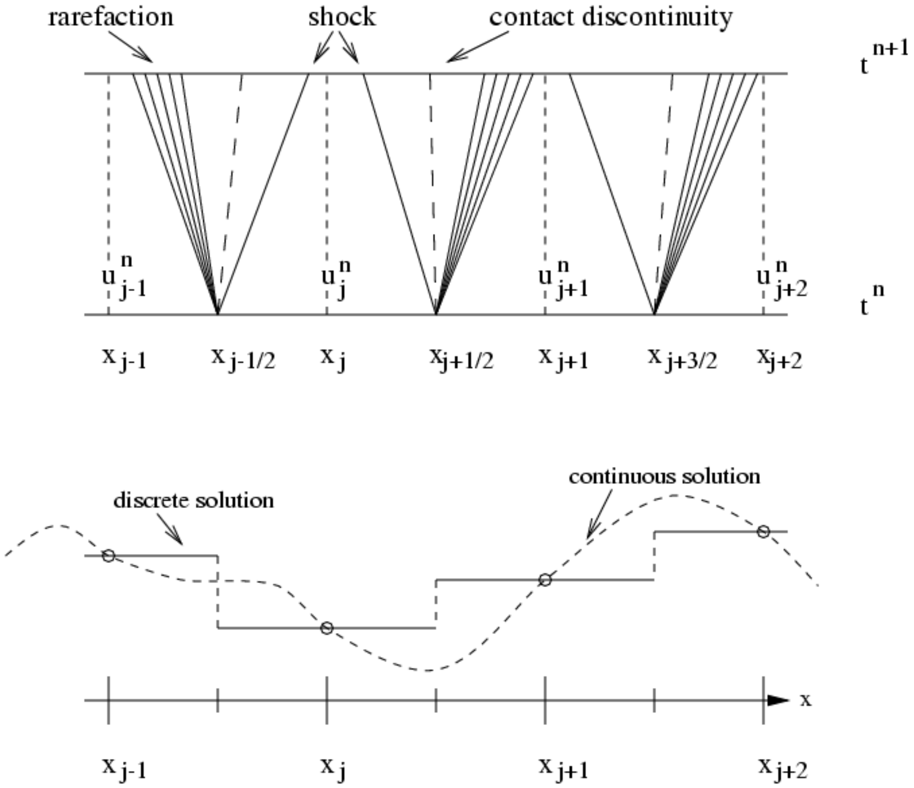

Figure B.1: Schematic representation of the Godunov scheme on an unidimensional spatial grid for a generic physical variable u. The subscript indexes indicate the position on the spatial grid, while the superscript indexes refer to the temporal grid.

variables necessary to set up the Riemann problem are computed determines the spatial order of accuracy of the numerical algorithm and controls the amplitude of the local jumps at every cell interface. With the Godunov method we have only first-order accuracy since we directly take the values in the adjacent cells.

PPM differs from the Godunov scheme because it yields second-order accuracy, since the constant values (of velocity, density, and pressure) used to set up the Riemann problem are obtained from a piecewise parabolic interpolation of the values in the three closest cells for each surface boundary of the cell. Therefore, PPM takes into account the influence of a wider spatial domain on a given computational cell.

B.2 Main modules

A key point is that the FLASH code is designed to allow users to configure initial and boundary conditions, to change algorithms, and to add new physics module.

In fact, the FLASH source code is a collection of components called FLASH modules, which can be combined in a variety of ways to form specific FLASH applications. In our work, the most important FLASH modules involved are:

- *The Driver module:* which controls the initialization, evolution, and output of a FLASH simulation. The Evolution submodule can use any of several different operator-splitting techniques to combine different physics operators and integrate them in time. In addition to these functions, the driver module supplies important simulation services to the rest of the FLASH framework, including Fortran modules to handle runtime parameters, physical constants, memory usage reports, and log file management.

- *The I/O module:* is controlled by the Driver module. The Output submodule involves the production of checkpoint files, plot files, and log files. Checkpoint files are the most important outputs of the code, since they contain all the values of the physical parameters and all the information necessary to restart the simulation from a given checkpoint.

- *Adaptive Mesh Refinement:* FLASH uses a package known as PARAMESH (MacNeice et al. 2000) for the parallelization and adaptive mesh refinement (AMR) portion of FLASH. PARAMESH consists of a suite of subroutines which handle refinement/derefinement of the mesh, distribution of work to processors, and flux conservation. AMR allows us to refine the computational grid where necessary. In particular, in an uniform unidimensional spatial grid, the error on a generic variable u can be estimated as:

$$E_i = \frac{|u_{i+1} - 2u_i + u_{i-1}|}{|u_{i+1} - u_i| + |u_i - u_{i-1}| + \epsilon(|u_{i+1}| - 2|u_i| + |u_{i+1}|)} \tag{B.1}$$

  where the subscript indexes indicate the position on the spatial grid and the denominator acts as a filter that avoids the refinement of small stochastic turbulence (the ϵ parameter can be set up by the user). Where E_i is larger than a given (user-defined) threshold E_{max}, the PARAMESH module refines the computational grid. On the other hand, where E_i is lower than a given threshold, E_{min}, the module reduces the refinement level.

- *Hydro module:* it solves all the plasma hydrodynamics and is based on a PPM solver, as shown in the previous section). PPM is particularly well-suited to flows involving discontinuities, such as shocks and contact discontinuities: it also performs extremely well for smooth flows. The high resolution and accuracy of PPM are obtained by the explicit nonlinearity of the scheme and through the use of intelligent dissipation algorithms, such as monotonicity enforcement, contact steepening, and interpolant flattening (Fryxell et al. 2000).

- *Thermal Conduction and Radiative Losses:* the non-linear thermal conduction equation with flux-limiting is added as an explicit finite difference term to the energy flux. Radiative losses are added as a source term (see Eq. 4.3).

Appendix C

Acronym and abbreviation list

ARF	Ancillary Response File
BH	Black Hole
CIE	Collisional Ionization Equilibrium
CSM	CircumStellar Material
DEC	DEClination
EPIC	European Photon Imaging Camera
FLOP	FLoating-point OPerations
FOV	Field Of View
FWHM	Full Width Half Maximum
GRB	Gamma-Ray Burst
HD	HydroDynamic
HE	Heating Efficiency
HEW	Half Energy Width
HST	Hubble Space Telescope
IR	InfraRed
ISM	InterStellar Medium
KH	Kelvin-Helmholtz
MC	McKee & Cowie 1975
MPE	Median Photon Ennergy
MPI	Message Passing Interface
NEI	Non-Equilibrium of Ionization
NS	Neutron Star
PPM	Piecewise-Parabolic Method
PSF	Point Spread Function
RA	Right Ascension
ROSAT	ROentgenSATellit

RT	Rayleigh-Taylor
SAS	Science Analysis System
SNR	SuperNova Remnant
UV	Ultra-Violet
VAN	VANcura et al. 1994
XMM	X-ray Multi-Mirror mission
WFPC2	Wide Field and Planetary Camera 2
XSPEC	X-ray SPECtral fitting package
ZAMS	Zero Age Main Sequence

Acknowledgements

I gratefully acknowledge the helpful and insightful support by F. Reale and F. Bocchino who have guided my work during all my PhD course with their suggestions and indications, and who have improved this thesis with their detailed comments. I express my gratitude to A. Decourchelle for her meaningful advices, insightful suggestions, and wise indications. I express special thanks to S. Orlando for his important support, his suggestions, and his worthy comments on this thesis. I also thank J. Ballet for his advices on the analysis of the W49B observation and J. P. Hughes, U. Hwang and R. Petre for their comments and suggestions on my work on W49B. I extend special thanks to A. Maggio, who contributed to some of the work presented and to G. Peres for his suggestions during all my PhD.

Finally, I want to express my gratitude to all the researchers and technicians at the INAF - Osservatorio Astronomico di Palermo and at the DSM/DAPNIA/ Service d'Astrophysique, CEA of Saclay for their assistance and kind hospitality.

Bibliography

Anders, E. & Grevesse, N. 1989, Geochim. Cosmochim. Acta, 53, 197

Arnaud, K. A. 1996, in ASP Conf. Ser. 101: Astronomical Data Analysis Software and Systems V, 17

Arnaud, M., Neumann, D. M., Aghanim, N., et al. 2001, A&A, 365, L80

Aschenbach, B., Egger, R., & Trumper, J. 1995, Nature, 373, 587

Bedogni, R. & Woodward, P. R. 1990, A&A, 231, 481

Bleeker, J. A. M., Willingale, R., van der Heyden, K., et al. 2001, A&A, 365, L225

Blondin, J. M. & Mezzacappa, A. 2006, ApJ, 642, 401

Blondin, J. M., Mezzacappa, A., & DeMarino, C. 2003, ApJ, 584, 971

Bocchino, F. & Bandiera, R. 2003, A&A, 398, 195

Bocchino, F., Maggio, A., & Sciortino, S. 1994, ApJ, 437, 209

Bocchino, F., Maggio, A., & Sciortino, S. 1997, ApJ, 481, 872

Bocchino, F., Maggio, A., & Sciortino, S. 1999, A&A, 342, 839

Bocchino, F., Maggio, A., Sciortino, S., & Raymond, J. 2000, A&A, 359, 316

Bock, D. C.-J., Turtle, A. J., & Green, A. J. 1998, AJ, 116, 1886

Borkowski, K. J., Lyerly, W. J., & Reynolds, S. P. 2001, ApJ, 548, 820

Borkowski, K. J., Shull, J. M., & McKee, C. F. 1989, ApJ, 336, 979

Brogan, C. L. & Troland, T. H. 2001, ApJ, 550, 799

Byun, D.-Y., Koo, B.-C., Tatematsu, K., & Sunada, K. 2006, ApJ, 637, 283

Cha, A. N., Sembach, K. R., & Danks, A. C. 1999, ApJ, 515, L25

Charles, P. A., Kahn, S. M., & McKee, C. F. 1985, ApJ, 295, 456

Chen, Y., Su, Y., Slane, P. O., & Wang, Q. D. 2004, ApJ, 616, 885

Cowie, L. L. & McKee, C. F. 1977, ApJ, 211, 135

Cox, D. P. 1972, ApJ, 178, 143

Cox, D. P. & Smith, B. W. 1974, ApJ, 189, L105+

Craig, W. W., Hailey, C. J., & Pisarski, R. L. 1997, ApJ, 488, 307

Cunha, K., Hubeny, I., & Lanz, T. 2006, ApJ, 647, L143

Dalton, W. W. & Balbus, S. A. 1993, ApJ, 404, 625

Damiani, F., Maggio, A., Micela, G., & Sciortino, S. 1997a, ApJ, 483, 350

Damiani, F., Maggio, A., Micela, G., & Sciortino, S. 1997b, ApJ, 483, 370

Decourchelle, A., Sauvageot, J. L., Ballet, J., & Aschenbach, B. 1997, A&A, 326, 811

Drake, J. J. & Testa, P. 2005, Nature, 436, 525

Dwarkadas, V. V. 2005, ApJ, 630, 892

Dwarkadas, V. V. 2006, Ap&SS, 537

Fesen, R. A., Blair, W. P., & Kirshner, R. P. 1982, ApJ, 262, 171

Field, G. B. 1965, ApJ, 142, 531

Filippenko, A. V. 1997, ARA&A, 35, 309

Fragile, P. C., Anninos, P., Gustafson, K., & Murray, S. D. 2005, ApJ, 619, 327

Fragile, P. C., Murray, S. D., Anninos, P., & van Breugel, W. 2004, ApJ, 604, 74

Fryxell, B., Olson, K., Ricker, P., et al. 2000, ApJS, 131, 273

Fujimoto, R., Tanaka, Y., Inoue, H., et al. 1995, PASJ, 47, L31

Galama, T. J., Vreeswijk, P. M., van Paradijs, J., et al. 1998, Nature, 395, 670

Giuliani, J. L. 1984, ApJ, 277, 605

Godunov, S. K. 1959, Mat. Sbornik, 47, 271

Graham, J. R., Levenson, N. A., Hester, J. J., Raymond, J. C., & Petre, R. 1995, ApJ, 444, 787

Gwinn, C. R., Moran, J. M., & Reid, M. J. 1992, ApJ, 393, 149

Hamilton, A. J. S. 1985, ApJ, 291, 523

Hamilton, A. J. S. & Sarazin, C. L. 1984, ApJ, 284, 601

Hashimoto, M., Iwamoto, K., & Nomoto, K. 1993, ApJ, 414, L105

Hawley, J. F., Wilson, J. R., & Smarr, L. L. 1984, ApJ, 277, 296

Heathcote, S. R. & Brand, P. W. J. L. 1983, MNRAS, 203, 67

Hwang, U., Decourchelle, A., Holt, S. S., & Petre, R. 2002, ApJ, 581, 1101

Hwang, U., Petre, R., & Hughes, J. P. 2000, ApJ, 532, 970

Iwamoto, K., Mazzali, P. A., Nomoto, K., et al. 1998, Nature, 395, 672

Jun, B.-I., Jones, T. W., & Norman, M. L. 1996, ApJ, 468, L59+

Kahn, S. M., Gorenstein, P., Harnden, F. R., & Seward, F. D. 1985, ApJ, 299, 821

Kane, J., Drake, R. P., & Remington, B. A. 1999, ApJ, 511, 335

Katsuda, S. & Tsunemi, H. 2005, PASJ, 57, 621

Katsuda, S. & Tsunemi, H. 2006, ApJ, 642, 917

Kawasaki, M., Ozaki, M., Nagase, F., Inoue, H., & Petre, R. 2005, ApJ, 631, 935

Keohane, J. W., Reach, W. T., Rho, J., & Jarrett, T. H. 2004, American Astronomical Society Meeting Abstracts, 204,

Keohane, J. W., Reach, W. T., Rho, J., & Jarrett, T. H. 2006, ArXiv Astrophysics e-prints

Khokhlov, A. M., Höflich, P. A., Oran, E. S., et al. 1999, ApJ, 524, L107

Klein, R. I., Colella, P., & McKee, C. F. 1990, in ASP Conf. Ser. 12: The Evolution of the Interstellar Medium, 117–136

Klein, R. I., McKee, C. F., & Colella, P. 1994, ApJ, 420, 213

Lacey, C. K., Lazio, T. J. W., Kassim, N. E., et al. 2001, ApJ, 559, 954

Lampton, M., Margon, B., & Bowyer, S. 1976, ApJ, 208, 177

Landau, L. D. & Lifshitz, E. M. 1959, Fluid mechanics (Course of theoretical physics, Oxford: Pergamon Press, 1959)

Levenson, N. A. & Graham, J. R. 2005, ApJ, 622, 366

Levenson, N. A., Graham, J. R., & Walters, J. L. 2002, ApJ, 576, 798

Levenson, N. A., Graham, J. R., & Walters, J. L. 2003, in Revista Mexicana de Astronomia y Astrofisica Conference Series, 252–257

Liedahl, D. A., Osterheld, A. L., & Goldstein, W. H. 1995, ApJ, 438, L115

Lu, F. J. & Aschenbach, B. 2000, A&A, 362, 1083

MacFadyen, A. I. & Woosley, S. E. 1999, ApJ, 524, 262

MacNeice, P., Olson, K. M., Mobarry, C., de Fainchtein, R., & Packer, C. 2000, Computer Physics Communications, 126, 330

Maeda, K. & Nomoto, K. 2003, ApJ, 598, 1163

Mazzali, P. A., Deng, J., Nomoto, K., et al. 2006, Nature, 442, 1018

Mazzali, P. A., Nomoto, K., Patat, F., & Maeda, K. 2001, ApJ, 559, 1047

McKee, C. F. 1974, ApJ, 188, 335

McKee, C. F. & Cowie, L. L. 1975, ApJ, 195, 715

McKee, C. F. & Hollenbach, D. J. 1980, ARA&A, 18, 219

Mellema, G., Kurk, J. D., & Röttgering, H. J. A. 2002, A&A, 395, L13

Mészáros, P. 2006, Reports of Progress in Physics, 69, 2259

Mewe, R., Gronenschild, E. H. B. M., & van den Oord, G. H. J. 1985, A&AS, 62, 197

Mewe, R., Lemen, J. R., & van den Oord, G. H. J. 1986, A&AS, 65, 511

Miceli, M., Bocchino, F., Maggio, A., & Reale, F. 2005a, A&A, 442, 513

Miceli, M., Bocchino, F., Maggio, A., & Reale, F. 2005b, Advances in Space Research, 35, 1012

Miceli, M., Decourchelle, A., Ballet, J., et al. 2006a, A&A, 453, 567

Miceli, M., Reale, F., Orlando, S., & Bocchino, F. 2006b, A&A, 458, 213

Miyata, E. & Tsunemi, H. 2001, ApJ, 552, 624

Miyata, E., Tsunemi, H., Aschenbach, B., & Mori, K. 2001, ApJ, 559, L45

Moffett, D. A. & Reynolds, S. P. 1994, ApJ, 437, 705

Moriguchi, Y., Yamaguchi, N., Onishi, T., Mizuno, A., & Fukui, Y. 2001, PASJ, 53, 1025

Morrison, R. & McCammon, D. 1983, ApJ, 270, 119

Myers, P. C. 1978, ApJ, 225, 380

Nakamura, T., Umeda, H., Nomoto, K., Thielemann, F.-K., & Burrows, A. 1999, ApJ, 517, 193

Narayan, R. & Medvedev, M. V. 2001, ApJ, 562, L129

Nomoto, K., Maeda, K., Umeda, H., et al. 2003, in IAU Symposium, 395–+

Nomoto, K., Tominaga, N., Umeda, H., Kobayashi, C., & Maeda, K. 2006, ArXiv Astrophysics e-prints

Orlando, S., Bocchino, F., Peres, G., et al. 2006, ArXiv Astrophysics e-prints

Orlando, S., Peres, G., Reale, F., et al. 2005, A&A, 444, 505

Park, S., Hughes, J. P., Slane, P. O., et al. 2004, ApJ, 602, L33

Patnaude, D. J. & Fesen, R. A. 2005, ApJ, 633, 240

Patnaude, D. J., Fesen, R. A., Raymond, J. C., et al. 2002, AJ, 124, 2118

Pye, J. P., Thomas, N., Becker, R. H., & Seward, F. D. 1984, MNRAS, 207, 649

Radhakrishnan, V., Goss, W. M., Murray, J. D., & Brooks, J. W. 1972, ApJS, 24, 49

Rakowski, C. E. 2005, Advances in Space Research, 35, 1017

Raymond, J. C., Cox, D. P., & Smith, B. W. 1976, ApJ, 204, 290

Raymond, J. C. & Smith, B. W. 1977, ApJS, 35, 419

Read, A. M. & Ponman, T. J. 2003, A&A, 409, 395

Rho, J. & Petre, R. 1998, ApJ, 503, L167

Sasaki, M., Stadlbauer, T. F. X., Haberl, F., Filipović, M. D., & Bennie, P. J. 2001, A&A, 365, L237

Sedov, L. I. 1959, Similarity and Dimensional Methods in Mechanics (New York: Academic Press, 1959)

Sgro, A. G. 1973, BAAS, 5, 434

Silk, J. & Solinger, A. 1973, Nature Physical Science, 244, 101

Smith, A., Peacock, A., Jones, L. R., & Pye, J. P. 1985, ApJ, 296, 469

Spitzer, L. 1962, Physics of Fully Ionized Gases (Physics of Fully Ionized Gases, New York: Interscience (2nd edition), 1962)

Stone, J. M. & Norman, M. L. 1992, ApJ, 390, L17

Strüder, L., Briel, U., Dennerl, K., et al. 2001, A&A, 365, L18

Taylor, J. H., Manchester, R. N., & Lyne, A. G. 1993, ApJS, 88, 529

Thielemann, F.-K., Nomoto, K., & Hashimoto, M.-A. 1996, ApJ, 460, 408

Thornton, K., Gaudlitz, M., Janka, H.-T., & Steinmetz, M. 1998, ApJ, 500, 95

Turner, M. J. L., Abbey, A., Arnaud, M., et al. 2001, A&A, 365, L27

van den Bergh, S. 1971, ApJ, 165, 457

Vancura, O., Raymond, J. C., Dwek, E., et al. 1994, ApJ, 431, 188

Wang, L., Baade, D., Höflich, P., & Wheeler, J. C. 2003, ApJ, 592, 457

Weiler, K. W. & Panagia, N. 1980, A&A, 90, 269

Weiler, K. W. & Sramek, R. A. 1988, ARA&A, 26, 295

White, R. L. & Long, K. S. 1991, ApJ, 373, 543

Willingale, R., Bleeker, J. A. M., van der Heyden, K. J., Kaastra, J. S., & Vink, J. 2002, A&A, 381, 1039

Woodward, P. & Colella, P. 1984, Journal of Computational Physics, 54, 115

Xu, J. & Stone, J. M. 1995, ApJ, 454, 172

Zel'Dovich, Y. B. & Raizer, Y. P. 1967, Physics of shock waves and high-temperature hydrodynamic phenomena (New York: Academic Press, 1966/1967, edited by Hayes, W.D.; Probstein, Ronald F.)